# MANIPULATING LIGHT IN TWO-DIMENSIONAL LAYERED MATERIALS

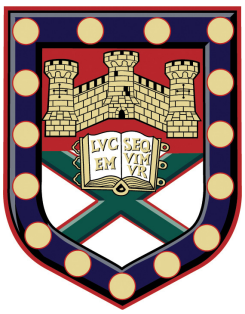

Submitted by Adolfo De Sanctis to the University of Exeter as a thesis for the degree of Doctor of Philosophy in Physics

December 2016



I certify that all material in this thesis which is not my own work has been identified and that no material has previously submitted and approved for the award of a degree by this or any other university.

Adolfo De Sanctis

# ABSTRACT

Graphene and layered two-dimensional (2D) materials have set a new paradigm in modern solid-state physics and technology. In particular their exceptional optical and electronic properties have shown great promise for novel applications in light detection. However, several challenges remain to fully exploit such properties in commercial devices. Such challenges include the limited linear dynamic range (LDR) of graphene-based photodetectors (PDs), the efficient extraction of photoexcited charges and ultimately the environmental stability of such atomically-thin materials.

In order to overcome the aforementioned limits, novel approaches to tune the properties of graphene and semiconducting $HfS_2$ are explored in this work, using chemical functionalisation and laser-irradiation. Intercalation of graphene with $FeCl_3$ is shown to lead to a highly tunable material, with unprecedented stability in ambient conditions. This material is used to define photo-active junctions with an unprecedented LDR via laser-irradiation. Intercalation with $FeCl_3$ is also used to demonstrate the first all-graphene position-sensitive photodetector (PSD) promising for novel sensing applications. Finally, laser-irradiation is employed, to perform controlled oxidation of ultra-thin $HfS_2$, which leads to induced strain in the material and a consequent spatially-varying bandgap. Such structure is used to demonstrate, for the first time, efficient extraction of photogenerated carriers trough the so-called "charge-funnel" effect, paving the way to the development of ultra-thin straintronic devices.

# ACKNOWLEDGEMENTS

This work would not have been possible without the help and support from many. First of all I would like to thank my supervisors: Prof. Saverio Russo and Prof. Monica Craciun for providing guidance and allowing me to explore the subtle notes of research with freedom and support. Thanks for being there, for pushing me when I needed it and for giving me the opportunity to travel and expand my knowledge and horizons.

A big thank you to all my colleagues and friends, who provided great support inside and outside the lab: time spent with you is always precious! I would like to thank Matt for being a great colleague, collaborator and a fantastic flatmate; Gareth for the important scientific advice, collaboration, help with measurements and for the delicious roast dinners and barbecues; Dominique for being an amazing mentor during my first year and for all the big parties in Bike Shed; Tom and Dave for teaching me their fabrication secrets and for the great nights in Firehouse; Jake for his help with the optoelectronic measurements and for all the interesting chats at lunch time; Iddo for his help with the AFM and electrical measurements, for the interesting discussions and for the good days out; Nicola for always being there to help while moving home twice, for the nice chats and the stargazing trips; Ana for the good advice and the lively dinners. Thanks also to Adam, Paul and Nick, from the mechanical workshop, for being able to cope with my never-ending requests for crazy things to make, your work is always great!

A special thank goes to my Mum, who patiently waited for me to go back home to visit and constantly sent emergency food packages to enjoy with my friends.

Finally, and most importantly, I wish to thank the person who, for the last two years, shared her life with me, with infinite patience and care, filling it with happiness and love. Thank you Lauren, the best is yet to come!

# CONTENTS

**Abstract** iii

**Acknowledgments** v

**List of Figures** xi

**List of Tables** xiii

**Acronyms** xiv

**1 Introduction** 1

## I Background concepts 7

**2 Theoretical background** 9

2.1 Graphene . . . . . 9

2.1.1 Brief history . . . . . 9

2.1.2 Crystal structure of graphite and graphene . . . . . 10

2.1.3 Band structure . . . . . 14

2.1.4 DOS and Fermi Level . . . . . 18

2.1.5 Bilayer and multilayer graphene . . . . . 20

2.1.6 Transport properties: ambipolar effect and mobility . . . . . 23

2.2 Optical properties of graphene . . . . . 26

2.2.1 Absorption and transmittance . . . . . 26

2.2.2 Optical contrast . . . . . 28

2.3 Transition metal dichalcogenides and $HfS_2$ . . . . . 30

2.3.1 Crystal structure and phases . . . . . 31
2.3.2 Electronic and optical properties . . . . . 33

**3 Experimental methods and characterisation 39**
3.1 Raman spectroscopy . . . . . 40
3.1.1 Classical theory of Raman scattering . . . . . 40
3.1.2 Quantum theory of Raman scattering . . . . . 43
3.1.3 Luminescence spectroscopy . . . . . 45
3.2 Raman spectrum of Graphene . . . . . 46
3.2.1 Layer-dependence of the 2D band . . . . . 48
3.3 Absorption spectroscopy . . . . . 49
3.3.1 Absorption in thick samples . . . . . 49
3.3.2 Absorption in thin films . . . . . 50
3.3.3 Absorption edge and bandgap determination . . . . . 52
3.4 Light detection in atomically-thin optoelectronic devices . . . . . 52
3.4.1 Photoconductive devices . . . . . 53
3.4.2 Junction devices . . . . . 55
3.4.3 Photothermoelectric (PTE) devices . . . . . 56
3.4.4 Local illumination and scanning photocurrent microscopy (SPCM) 57
3.5 SPCM and spectroscopy experimental apparatus . . . . . 60
3.5.1 Instrumentation . . . . . 62
3.5.2 Performance of multi-purpose microscope system . . . . . 69
3.5.3 Final remarks and outlook . . . . . 76
3.6 Atomic force microscopy (AFM) . . . . . 77
3.6.1 Experimental setup . . . . . 77
3.6.2 This work . . . . . 79

**4 $FeCl_3$-intercalated graphene 85**
4.1 Intercalation of graphene with $FeCl_3$ . . . . . 86
4.2 Characterisation of $FeCl_3$-FLG . . . . . 88
4.2.1 Electrical and optical properties . . . . . 88
4.2.2 Raman spectroscopy . . . . . 89
4.2.3 Determination of the stacking order in $FeCl_3$-FLG . . . . . 92

4.3 Large-area $FeCl_3$-FLG . . . 93
4.3.1 Characterisation of Ni-grown CVD graphene . . . 95
4.3.2 Intercalation and Raman study of large-area $FeCl_3$-FLG . . . 95
4.3.3 Electrical and optical properties of Ni-CVD $FeCl_3$-FLG . . . 99
4.4 Final remarks and outlook . . . 99

**II Functionalised graphene optoelectronics 105**

**5 Laser-defined photodetectors in $FeCl_3$-intercalated graphene 107**
5.1 Introduction . . . 107
5.2 Sample preparation and intercalation of FLG . . . 108
5.2.1 Stacking order of $FeCl_3$-FLG . . . 109
5.3 Laser-defined junctions in $FeCl_3$-FLG . . . 110
5.4 Optoelectronic response of laser-defined $p - p'$ junctions . . . 113
5.4.1 Bandwidth, noise and extraordinary linear dynamic range . . . 116
5.4.2 Spectral photoresponse . . . 119
5.5 Below the diffraction limit . . . 120
5.6 Summary and outlook . . . 120

**6 Hexagonal-domain $FeCl_3$-FLG for PSDs 127**
6.1 Introduction . . . 127
6.2 Samples preparation . . . 128
6.3 Characterisation of functionalised hexagonal-domains of graphene . . . 128
6.3.1 APCVD graphene photodetectors . . . 131
6.3.2 Towards position-sensitive light-detection in intercalated graphene 134
6.4 Summary and outlook . . . 135

**III Transition-metal dichalcogenides optoelectronics 139**

**7 Strain-engineered photodetectors in ultrathin $HfS_2$ 141**
7.1 Introduction . . . 141
7.2 Basic properties of $HfS_2$ . . . 143
7.2.1 AFM and Raman spectroscopy of $HfS_2$ . . . 144

7.3 Laser-irradiated $HfS_2$ . . . 144
7.4 Photo-oxidation mechanism in $HfS_2$ . . . 147
7.4.1 Charge-transfer and photo-oxidation: semiconductors in ambient conditions . . . 148
7.4.2 MGT theory of CT reaction . . . 152
7.5 Photoresponse and strain in photo-oxidised $HfS_2$ . . . 152
7.6 Charge-funnel effect in strained $HfS_2$ . . . 156
7.7 Summary and outlook . . . 157

**8 Final remarks and outlook 161**

**IV Appendices 163**

**A Materials preparation and sample fabrication 165**
A.1 Graphene preparation and transfer . . . 165
A.2 Devices fabrication . . . 166

**B Correction of responsivity spectra for substrate reflections 169**

**Publications 173**

# LIST OF FIGURES


2.1 The $sp^2$ hybridization of carbon . . . . . 11
2.2 Graphene's crystal lattice . . . . . 12
2.3 Stacking order of graphite . . . . . 13
2.4 Energy dispersion of graphene $\pi$ bands . . . . . 15
2.5 Band structure and DOS of graphene . . . . . 18
2.6 Band structure of bilayer graphene . . . . . 21
2.7 Ambipolar effect in graphene FET . . . . . 24
2.8 Optical transmittance graphene . . . . . 27
2.9 Optical contrast of graphene . . . . . 29
2.10 Crystal structure of TMDs . . . . . 31

3.1 Raman processes . . . . . 42
3.2 Raman spectrum of graphene . . . . . 46
3.3 Layer-dependent 2D band of graphene . . . . . 48
3.4 Absorption in thin films . . . . . 51
3.5 Photodetectors principles and characterisation . . . . . 53
3.6 Experimental setup diagram . . . . . 61
3.7 Experimental setup 3D model . . . . . 64
3.8 Agile optical path configurations . . . . . 65
3.9 Custom PCB chip-carrier boards . . . . . 69
3.10 Characterization of a graphene-based PD . . . . . 70
3.11 Absorption spectroscopy characterisation . . . . . 72
3.12 Polarized Raman characterisation . . . . . 73
3.13 PL spectroscopy characterisation . . . . . 76
3.14 AFM operating principle and modes . . . . . 77

4.1 Intercalation of FLG with $FeCl_3$ . . . . . 86
4.2 Electrical and optical properties of $FeCl_3$-FLG . . . . . 89
4.3 Raman spectroscopy of $FeCl_3$-FLG . . . . . 90
4.4 Raman estimation of charge density in $FeCl_3$-FLG . . . . . 92
4.5 Stacking order of $FeCl_3$-FLG . . . . . 94
4.6 Characterisation of Ni-CVD graphene . . . . . 96
4.7 Charge density estimation in large-area $FeCl_3$-FLG . . . . . 98

5.1 Inferred stacking order of four-layer $FeCl_3$-FLG. . . . . 109
5.2 Raman spectroscopy study of changes in laser-irradiated $FeCl_3$-FLG . . 111
5.3 Calibration of laser-induced displacement of $FeCl_3$ . . . . . 112
5.4 Formation of of p-p' junctions in $FeCl_3$-FLG . . . . . 114
5.5 SPCM study of laser-irradiated $FeCl_3$-FLG p-p' junctions . . . . . 115
5.6 Photoresponse characterisation at p-p' junctions in $FeCl_3$-FLG . . . . . 116
5.7 BW and NEP of a laser-written $FeCl_3$-FLG junction device . . . . . 117
5.8 High-resolution photo-active junctions in $FeCl_3$-FLG defined using SNOM 121

6.1 Raman characterisation of intercalated APCVD graphene. . . . . 129
6.2 AFM characterisation of intercalated APCVD graphene. . . . . 131
6.3 Multi-terminal hexagonal graphene device . . . . . 132
6.4 SPCM maps of hexagonal graphene device . . . . . 132
6.5 Raman maps of the hexagonal graphene device . . . . . 134
6.6 PSD characterization . . . . . 135

7.1 Crystal and band structure of $HfS_2$ . . . . . 143
7.2 AFM and Raman of ultra-thin $HfS_2$ . . . . . 145
7.3 Laser-induced oxidation of ultra-thin $HfS_2$ . . . . . 146
7.4 Characterisation of laser-irradiated $HfS_2$ . . . . . 147
7.5 Photo-oxidation dynamics study . . . . . 149
7.6 Charge-Transfer model and crystal structures of $HfO_2$ . . . . . 151
7.7 Photo-response characterisation of $HfS_2/HfO_2$ device . . . . . 153
7.8 Photo-oxidation-induced strain in $HfS_2$ . . . . . 154
7.9 Electrical characteristic of $HfS_2/HfO_2$ devices . . . . . 155
7.10 Charge funnel effect in $HfS_2/HfO_2$ photodetectors . . . . . 156

A.1 Electron-beam lithography . . . . . 166

B.1 Correction of spectral responsivity for substrate reflections . . . . . 170

## LIST OF TABLES

2.1 Properties of selected TMDs . . . . . 32

3.1 Photodetector parameters . . . . . 55
3.2 Laser spot diameters . . . . . 68

4.1 Intercalation heating cycle . . . . . 87

5.1 LDR of graphene and functionalized graphene devices . . . . . 118

7.1 Properties of $HfS_2$ . . . . . 144
7.2 Raman fit results of photo-oxidised $HfS_2$ . . . . . 148
7.3 Reactions energetics . . . . . 151

B.1 Corrections to responsivity . . . . . 170

# ACRONYMS

**2D** two-dimensional.
**AC** alternate-current.
**ACEL** alternating current electroluminescent.
**AFM** atomic force microscopy.
**APCVD** atmospheric pressure chemical vapour deposition.
**BLG** bilayer graphene.
**BO** Born-Oppenheimer.
**BP** band-pass.
**BS** beam-splitter.
**BW** bandwidth.
**CCD** charge-coupled device.
**CMOS** complementary metal-oxide semiconductor.
**CNP** charge neutrality point.
**CNTs** carbon nanotubes.
**CT** charge-transfer.
**CVD** chemical vapour deposition.
**CW** continuous-wave.
**DC** direct-current.
**DFT** density-functional theory.
**DiF** drop-in filter.
**DOS** density of states.
**e-beam** electon-beam.
**EDXMA** energy-dispersive X-ray microanalysis.
**EL** electroluminescence.
**EM** electromagnetic.
**EQE** external quantum efficiency.
**FBZ** first Brillouin zone.
**FET** field effect transistor.
**FGR** Fermi's golden rule.
**FIR** far-infrared.
**FLG** few-layer graphene.
**FM** flip mirror.
**FTO** Fluorine-doped Tin Oxide.
**FWHM** full-width at half-maximum.
**GICs** graphite intercalation compounds.
**hBN** hexagonal boron nitride.
**HRTEM** high-resolution transmission electron microscopy.
**IPA** isopropanol.
**IQE** internal quantum efficiency.
**IR** infrared.
**ITO** Indium-Tin Oxide.
**LCAO** linear combination of atomic orbitals.
**LDR** linear dynamic range.
**LED** light emitting device.
**LEDs** light emitting devices.
**LN2** liquid nitrogen.

**MEK** methyl ethyl ketone.
**MGT** Marcus-Gerischer theory.
**MIBK** methyl isobutyl ketone.
**MIR** mid-infrared.
**MLG** monolayer graphene.
**ND** neutral-density.
**NEBW** noise-equivalent bandwidth.
**NEP** noise-equivalent power.
**NFPN** near-field photocurrent nanoscopy.
**Ni-CVD** CVD-grown graphene on Nickel.
**NIR** near-infrared.
**OBIC** optical beam-induced current.
**OLED** organic light emitting device.
**OLEDs** organic light emitting devices.
**PCB** printed-circuit board.
**PD** photodetector.
**PDs** photodetectors.
**PL** photoluminescence.
**PMMA** poly(methyl methacrylate).
**PSD** position-sensitive detector.
**PSDs** position-sensitive detectors.
**PTE** photothermoelectric.
**PV** photovoltaic.
**RMS** root-mean-square.
**RRS** resonant Raman scattering.
**SdHO** Shubnikov-de Haas oscillations.
**SEM** scanning electron microscope.
**SIP** single-in-line package.
**SKPM** Scanning Kelvin probe microscopy.
**SNOM** scanning near-field optical microscopy.
**SNR** signal-to-noise ratio.
**SPCM** scanning photocurrent microscopy.
**TLG** trilayer graphene.
**TMD** transition metal dichalcogenide.
**TMDs** transition metal dichalcogenides.
**UV** ultra-violet.
**WF** work function.
**WL** white light.
**XRD** X-Ray diffraction.

# 1

# INTRODUCTION

In 1959, in his famous lecture entitled *There's plenty of room at the bottom*, Richard P. Feynman envisaged that the ability to create structures at the atomic and molecular scale, to manipulate and to control their arrangement, would have been the ultimate way to access novel physical properties of materials and to store information[1]. Since then, the field of nanotechnology thrived and, nowadays, graphene[2] and layered two-dimensional (2D) materials[3] are setting a new paradigm in nano-scale science and technology.

The interaction of light with matter is one of the most important topics in modern solid-state physics: the development of the theory of optical properties of materials had a striking effect on applications and devices. Modern technology, from light bulbs to mobile phones, strongly relies on the combination of optical and electrical properties of materials. Presently, optoelectronic applications are largely based on inorganic semiconductors such as Si, GaAs, AlGaAs, GaP and InP. Each of these materials is used in different devices such as solar cells, photodetectors (PDs), light emitting devices (LEDs), lasers and optical modulators. Some of these devices need to work in a very broad frequency range, others need to be sensible only to a very narrow band: therefore the properties of the materials need to be tailored in accordance to the application. This tailoring has currently reached a limit due to technological and physical limits, such as miniaturization, power consumption and speed[4].

Such limits started to fall with the advent of graphene, thanks to the realisation of new and exciting applications in optoelectronics[5], plasmonics[6], telecommunications[7], solar energy harvesting[8] and sensing[9]. Graphene also pushed forward the field of wearable and flexible electronics and of the so-called "internet of things"[10]. All these

discoveries rely on the extraordinary properties of this material such as broadband absorption and field effect tunability[11]. However, the lack of a bandgap and the intrinsic low absorption of graphene still present challenges for its use in practical applications. To this end, chemical functionalisation[12], that is the attachment of chemical species on the surface of graphene, has been proposed as a new route to engineer physical properties at the nano-scale and to overcome the aforementioned limits. In particular, intercalation with $FeCl_3$[13] has already shown good performance in a range of applications[14;15] and resilience to ambient conditions[16].

Alongside graphene, atomically-thin layered semiconducting transition metal dichalcogenides (TMDs)[17] have shown great versatility and promising applications in electronics and optoelectronics[18]. TMDs are compounds with chemical formula $MX_2$, where M is a transition metal from group IV-B, V-B or VI-B, and X is a chalcogen (S, Se or Te). The crystals have a lattice structure of the form X-M-X, with the chalcogen atoms disposed in hexagonal planes, where layers are held together by van der Waals forces[17]. Such materials have been known for decades in bulk form[19], but only in recent years the isolation of few- and single-layers allowed to fully exploit their unique electrical and optical properties. Such properties include: layer-dependent indirect-to-direct bandgap transition[20], strong optical anisotropy[21] and valley dichroism[22]. However, several challenges remain for the use of such semiconductors in real applications, such as the lack of efficient extraction of photogenerated carriers, low quantum yield due to strong excitonic effects[23] and, ultimately, the limit imposed by the principle of detailed balance in p-n junction devices[24].

In this work novel photodetectors based on functionalised graphene and semiconducting $HfS_2$ are reported, addressing the aforementioned limits in order to push the field forward. After a brief review of the fundamental properties of graphene and TMDs (chapter 2), such as band structure, optical and electronic properties, the most relevant techniques for the characterisation of these materials are reviewed. These include Raman and absorption spectroscopy, scanning photocurrent microscopy (SPCM) and transport measurements and atomic force microscopy (AFM) (chapter 3). During the investigations reported in this thesis, a system for the characterisation of optoelectronic devices based on graphene and 2D materials was developed and characterised and its working principles and implementations are detailed in section 3.5. A study of $FeCl_3$-intercalated graphene is presented in chapter 4, including the most important

results related to the characterisation of this material using non-destructive techniques. Intercalated graphene is then used in two types of PDs: a purely photovoltaic (PV) laser-written photoactive junction (chapter 5) and a position-sensitive detector (PSD) based on hexagonal single-domains of chemical vapour deposition (CVD)-grown $FeCl_3$-intercalated graphene (chapter 6). In the former case an unprecedented extended linear dynamic range (LDR) is reported for the first time in a purely PV graphene-based photodetector (PD). In the latter case, the first application of single-domain graphene for PSD is demonstrated. In both works, the use of $FeCl_3$-intercalated graphene demonstrates the great versatility of this functionalisation technique, which goes beyond the most conventional doping technique of electrostatic gating. Finally, a study of laser-assisted oxidation in ultra-thin $HfS_2$ is presented (chapter 7). This technique is used to induce strain in the $HfS_2$ which results in a spatially-varying bandgap. Such structure leads to the so-called "charge-funnel" effect, which is measured and demonstrated in a photodetector configuration for the first time, opening a new door to the development of ultra-thin straintronic devices.

# BIBLIOGRAPHY

[1] Richard P. Feynman. There's plenty of room at the bottom. *Engineering and Science*, 23(5):22–36, 1960.

[2] A. K. Geim. Graphene: Status and prospects. *Science*, 324(5934):1530–1534, 2009.

[3] Qing Hua Wang, Kourosh Kalantar-Zadeh, Andras Kis, Jonathan N. Coleman, and Michael S. Strano. Electronics and optoelectronics of two-dimensional transition metal dichalcogenides. *Nat Nano*, 7(11):699–712, Nov 2012.

[4] Y. Taur. Cmos design near the limit of scaling. *IBM Journal of Research and Development*, 46(2.3):213–222, March 2002.

[5] F. H. L. Koppens, T. Mueller, Ph Avouris, A. C. Ferrari, M. S. Vitiello, and M. Polini. Photodetectors based on graphene, other two-dimensional materials and hybrid systems. *Nat Nano*, 9(10):780–793, 2014.

[6] Z. Fei, A. S. Rodin, G. O. Andreev, W. Bao, A. S. McLeod, M. Wagner, L. M. Zhang, Z. Zhao, M. Thiemens, G. Dominguez, M. M. Fogler, A. H. Castro Neto, C. N. Lau, F. Keilmann, and D. N. Basov. Gate-tuning of graphene plasmons revealed by infrared nano-imaging. *Nature*, 487(7405):82–85, 2012.

[7] Thomas Mueller, Fengnian Xia, and Phaedon Avouris. Graphene photodetectors for high-speed optical communications. *Nat Photon*, 4(5):297–301, 2010.

[8] Chang-Hua Liu, You-Chia Chang, Theodore B. Norris, and Zhaohui Zhong. Graphene photodetectors with ultra-broadband and high responsivity at room temperature. *Nat Nano*, 9(4):273–278, 2014.

[9] Chang Oh Kim, Sung Kim, Dong Hee Shin, Soo Seok Kang, Jong Min Kim, Chan Wook Jang, Soong Sin Joo, Jae Sung Lee, Ju Hwan Kim, Suk-Ho Choi, and Euyheon Hwang. High photoresponsivity in an all-graphene p-n vertical junction photodetector. *Nature Communications*, 5:3249, 2014.

[10] A. I. S. Neves, T. H. Bointon, L. V. Melo, S. Russo, I. de Schrijver, M. F. Craciun, and H. Alves. Transparent conductive graphene textile fibers. *Scientific Reports*, 5:9866, 2015.

[11] K. S. Novoselov, A. K. Geim, S. V. Morozov, D. Jiang, Y. Zhang, S. V. Dubonos, I. V. Grigorieva, and A. A. Firsov. Electric field effect in atomically thin carbon films. *Science*, 306:666, 2004.

[12] M F Craciun, I Khrapach, M D Barnes, and S Russo. Properties and applications of chemically functionalized graphene. *Journal of Physics: Condensed Matter*, 25(42):423201, 2013.

[13] Ivan Khrapach, Freddie Withers, Thomas H. Bointon, Dmitry K. Polyushkin, William L. Barnes, Saverio Russo, and Monica F. Craciun. Novel highly conductive and transparent graphene-based conductors. *Advanced Materials*, 24(21):2844–2849, 2012.

[14] Thomas H. Bointon, Gareth F. Jones, Adolfo De Sanctis, Ruth Hill-Pearce, Monica F. Craciun, and Saverio Russo. Large-area functionalized CVD graphene for work function matched transparent electrodes. *Scientific Reports*, 5:16464, 2015.

[15] Elias Torres Alonso, George Karkera, Gareth F. Jones, Monica F. Craciun, and Saverio Russo.

Homogeneously bright, flexible, and foldable lighting devices with functionalized graphene electrodes. *ACS Applied Materials & Interfaces*, 8(26):16541–16545, 2016.

[16] Dominque J. Wehenkel, Thomas H. Bointon, Tim Booth, Peter Böggild, Monica F. Craciun, and Saverio Russo. Unforeseen high temperature and humidity stability of $FeCl_3$ intercalated few layer graphene. *Scientific Reports*, 5:7609, 2015.

[17] Manish Chhowalla, Hyeon Suk Shin, Goki Eda, Lain-Jong Li, Kian Ping Loh, and Hua Zhang. The chemistry of two-dimensional layered transition metal dichalcogenide nanosheets. *Nat Chem*, 5(4):263–275, Apr 2013.

[18] Andreas Pospischil and Thomas Mueller. Optoelectronic devices based on atomically thin transition metal dichalcogenides. *Applied Sciences*, 6(3):78, 2016.

[19] J.A. Wilson and A.D. Yoffe. The transition metal dichalcogenides discussion and interpretation of the observed optical, electrical and structural properties. *Advances in Physics*, 18(73):193–335, 1969.

[20] Kin Fai Mak, Changgu Lee, James Hone, Jie Shan, and Tony F. Heinz. Atomically thin $mos_2$: A new direct-gap semiconductor. *Phys. Rev. Lett.*, 105:136805, Sep 2010.

[21] Ozgur Burak Aslan, Daniel A. Chenet, Arend M. van der Zande, James C. Hone, and Tony F. Heinz. Linearly polarized excitons in single- and few-layer $res_2$ crystals. *ACS Photonics*, 3(1):96–101, 2016.

[22] Y. J. Zhang, T. Oka, R. Suzuki, J. T. Ye, and Y. Iwasa. Electrically switchable chiral light-emitting transistor. *Science*, 344(6185):725–728, 2014.

[23] Kin Fai Mak and Jie Shan. Photonics and optoelectronics of 2D semiconductor transition metal dichalcogenides. *Nat Photon*, 10(4):216–226, Apr 2016.

[24] William Shockley and Hans J. Queisser. Detailed balance limit of efficiency of p-n junction solar cells. *Journal of Applied Physics*, 32(3):510–519, 1961.

# Part I

# Background concepts

# 2

# THEORETICAL BACKGROUND

In this chapter the most relevant theoretical concepts for the understanding of the following chapters are reviewed. The chapter opens with an overview of the crystal structure of graphene (section 2.1.2), followed by a description of its electronic properties in section 2.1.3, with particular attention to the band structure and density of states of mono-layer and few-layer graphene (sections 2.1.4 and 2.1.5). The transport properties of graphene, in the absence of magnetic fields, are reviewed in section 2.1.6. As this work focuses on the interaction of light with 2D materials, the optical properties of graphene are of crucial importance and they are reviewed in section 2.2. Finally, the chapter closes with an overview of transition metal dichalcogenides (TMDs) with particular focus to the basic electrical and optical properties of $HfS_2$ (section 2.3).

## 2.1 GRAPHENE

Graphene is made of a single layer of carbon atoms arranged in an honeycomb crystal structure which form a planar structure considered to be effectively two-dimensional (2D). In 2004, Geim and Novoselov isolated graphene on a $SiO_2$ substrate[1] and measured its extraordinary electrical properties for the first time in a transistor configuration.

### 2.1.1 *Brief history*

The word "graphene" has been used for the first time[2] in 1987 to describe a monoatomic (1 atom thick) layer of graphite as one of the constituents of graphite intercalation compounds (GICs). Graphite is an abundant material on Earth (in 2013 the

world production of natural graphite was estimated to be 1110000 tons[3]), known as a mineral for more than 500 years and employed, since the industrial revolution, in different sectors of industry for multiple applications, such as: refractory coatings, brake linings and lubricants and many more[4].

The word "graphene" has been also used in the description of carbon nanotubes (CNTs) and of thin films of graphite which have been growth epitaxially upon different substrates since 1970[5]. Although "epitaxial graphite" is made of a 1 atom thick hexagonal crystal lattice of $sp^2$-hybridized carbon atoms, the strong interaction between the substrate and the layer hides the peculiar properties of graphene.

The forces between carbon atoms in graphite are highly anisotropic, in fact those between adjacent basal planes are about two orders of magnitude smaller than those between neighbouring atoms in the same plane. This property allows facile cleavage of graphite from its [001] faces[6;7], which suggested that a single layer of graphite could be mechanically "exfoliated" from a bulk crystal. Attempts began in 1990, but it was not possible to find films thinner than 50-100 layers until 2004, when Geim and Novoselov from the Manchester University succeeded in isolating one mono-atomic layer of graphite[1] on top of a silicon dioxide $SiO_2$ substrate. The two researchers succeeded in doing so by employing the so-called "micro-mechanical cleavage" technique or, as better known, "tape method". The choice of $SiO_2$ as substrate was crucial to allow both the optical identification of monolayer graphene (MLG) and the measurement of its electrical properties, as it will be shown later in this chapter.

Theoretical studies on graphene started in 1947 by Philip R. Wallace[8] in order to understand its electrical properties. After the first isolation, research in graphene, and 2D layered materials in general, has seen relentless growth[9;10].

### 2.1.2 *Crystal structure of graphite and graphene*

Carbon is the fourth most abundant element in the solar system[11]. Its chemical properties make it the most common element in composites and at the base of any known living form. It is present in different allotropic forms in the condensed state: the better known are diamond, amorphous carbon and graphite. Graphite has a layered structure of single planes of carbons arranged in an honeycomb crystal lattice.

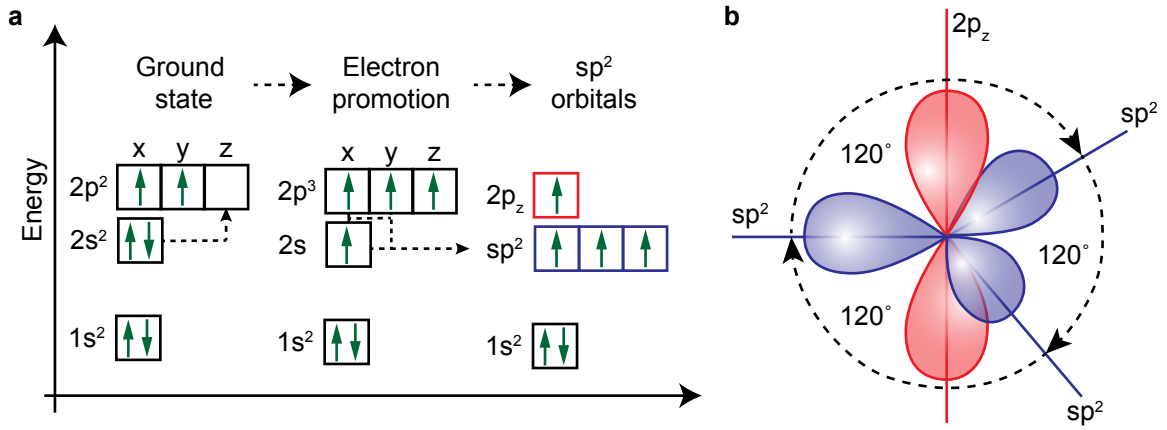


**Figure 2.1: The $sp^2$ hybridization of carbon.** **a**, Schematic representation of the atomic orbitals and associated electrons filling (green arrows) in the ground state and in the $sp^2$ hybrid orbitals. **b**, Spatial schematic representation of the in-plane $sp^2$ (blue) and out-of-plane $2p_z$ (red) orbitals.

#### 2.1.2.1 *The carbon atom*

Carbon is the sixth element in the periodic table and has two stable isotopes: $^{12}C$ and $^{13}C$ with natural abundances of 98.9% and 1.1% respectively[12]. Carbon has six electrons arranged in the atomic orbitals $1s^2$, $2s^2$ and $2p^2$. Since the difference in energy between the 2s and 2p orbitals is much lower than their bond energy, their wave functions can combine in a process called hybridization, forming the three hybrid orbitals *sp*, $sp^2$ and $sp^3$.

The *sp* hybridization occurs when carbon is bound to two other atoms (two double bonds or one single plus one triple bond). This results in a linear arrangement of atoms with an angle of 180° between the bonds. This hybridization is not common in solid crystals.

When carbon is bonded to four other atoms, the hybridization is $sp^3$ and the arrangement is tetrahedral with an angle of 109°27′ between the bonds. This gives rise to the tetrahedral structure of diamond, where each atom forms four $\sigma$ bonds with the neighbours.

A carbon atom bound to three atoms (two single bonds, one double bond) is $sp^2$ hybridized and forms a flat trigonal arrangement with 120° angles between the bonds.

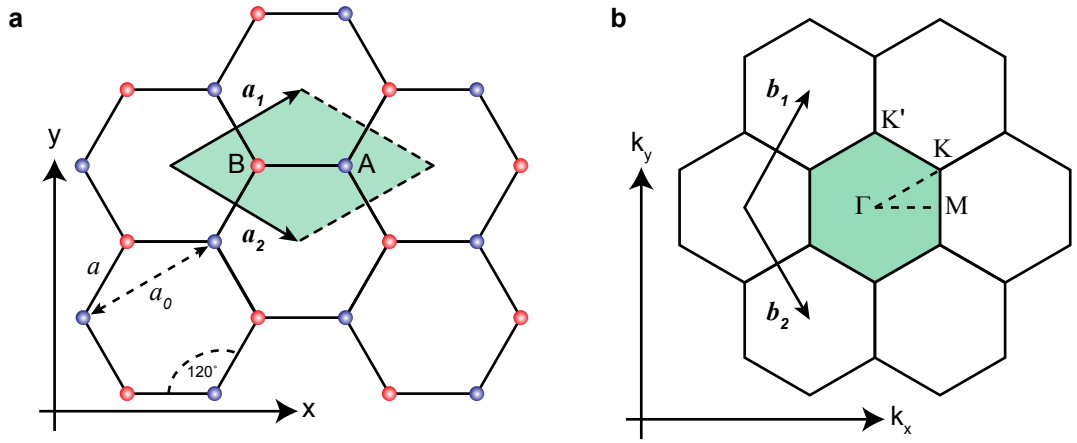


**Figure 2.2: Graphene's crystal lattice. a**, Crystal lattice in real space. Carbon atoms are arranged at the vertices of regular hexagons forming a honeycomb crystal lattice which can be decomposed into two triangular Bravais sub-lattices, A (blue) and B (red). $a = 1.42\,\text{Å}$ is the C-C distance and $a_0 = 2.46\,\text{Å}$ is the length of the primitive vectors $\boldsymbol{a}_1$ and $\boldsymbol{a}_2$. The unit cell is highlighted in green. **b**, Reciprocal lattice in k-space, shaded green area represents the FBZ with the high symmetry points Γ, M, K, K' and reciprocal unit vectors $\boldsymbol{b}_1$ and $\boldsymbol{b}_2$.

In this case the orbital $2p_z$ does not combine with the others, as shown in figure 2.1. The other orbitals forms $\sigma$ bonds in the hexagonal structure of graphite. The $2p_z$ orbitals of neighbouring atoms form $\pi$ bonds, which allow a strong electron delocalisation.

#### 2.1.2.2 *The crystal lattice*

In graphene, the carbon atoms are arranged at the vertices of regular hexagons, as shown in figure 2.2a, in the so-called "honeycomb crystal structure". The Bravais lattice is trigonal and the unit cell is a rhombus containing two atoms (A and B) defined by the primitive vectors

$$\boldsymbol{a}_1 = \frac{a}{2}\left(3, \sqrt{3}\right) \quad \text{and} \quad \boldsymbol{a}_2 = \frac{a}{2}\left(3, -\sqrt{3}\right), \tag{2.1}$$

where $a = 1.42\,\text{Å}$ is the inter-atomic distance and $a_0 = \sqrt{3}a = 2.46\,\text{Å}$ is the lattice constant. The reciprocal lattice is also trigonal and described by the primitive vectors

$$\boldsymbol{b}_1 = \frac{2\pi}{3a}\left(1, \sqrt{3}\right) \quad \text{and} \quad \boldsymbol{b}_2 = \frac{2\pi}{3a}\left(1, -\sqrt{3}\right), \tag{2.2}$$

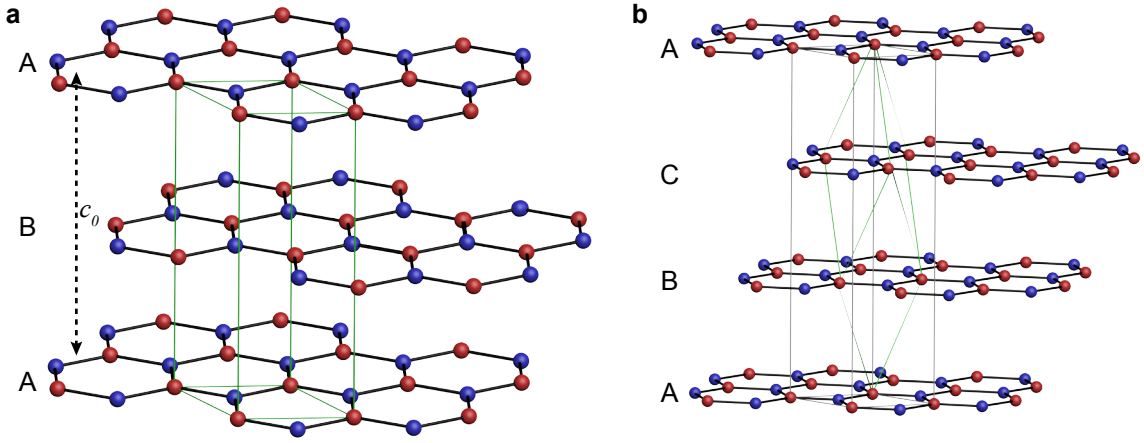


**Figure 2.3: Stacking order of graphite. a**, Hexagonal, or AB-stacked, graphite: atoms A of a plane are aligned with the atoms B of the nearest planes, while those B are aligned with the centres of the hexagons of the nearest planes. Interlayer spacing is $c_0/2 = 3.35\,\text{Å}$ **b**, Rhombohedral, or ABC-stacked, graphite which can be considered as an extended stacking fault in hexagonal graphite. Outline of the unit cells in green.

and the first Brillouin zone (FBZ) is hexagonal, as shown in figure figure 2.2b. Very important high symmetry points in the graphene FBZ are $K$ and $K'$, whose positions are given by:

$$\mathbf{K} = \left(\frac{2\pi}{3a}, \frac{2\pi}{3\sqrt{3}a}\right) \quad \text{and} \quad \mathbf{K}' = \left(\frac{2\pi}{3a}, -\frac{2\pi}{3\sqrt{3}a}\right), \tag{2.3}$$

as it will be discussed later, these points are associated with the peculiar properties of graphene arising from its band structure. Amongst the six vertices of the FBZ only two are not equivalent, the others are connected to one of them by a reciprocal lattice vector $\boldsymbol{G} = m\boldsymbol{b}_1 + n\boldsymbol{b}_2$, where $m$ and $n$ are integers.

Stacked planes of graphene form graphite which, in its natural form, contains a large percentage ($> 60\%$) of hexagonal, or *Bernal*-stacked, layers, where the second layer of carbons is rotated by 60° with respect to the first one and then repeated. In this way, the sublattices A of the two layers lie on top of each other, while the B ones are aligned with the centres of the hexagons of the nearest planes, see figure 2.3a. The distance between the planes is $c_0/2 = 3.35\,\text{Å}$. Up to 40% of natural graphite is rhombohedral[13], which has an ABCABC stacking sequence of the layers, as shown in

figure 2.3b. This allotrope of graphite is thermodynamically unstable: it is produced by shear deformation of hexagonal graphite and transforms progressively to the hexagonal modification on heating above 1600 K. Other types of graphite include turbostratic graphite[14], where the single stacked planes are rotated by a certain angle with respect to each other and artificially-made pyrolytic graphite, where some covalent bonding between the planes is present due to the production process. The stacking order affects the electronic properties of bulk graphite[15] as well as the interlayer potential[16], which ultimately determines the ability to exfoliate single layers of graphene.

### 2.1.3 *Band structure*

The tight-binding model, proposed by Bloch in 1929[17], is an approach to the calculation of electronic band structure using an approximate set of wavefunctions which are constructed as superposition of wavefunctions for isolated atoms located at each atomic site. The method is closely related to the linear combination of atomic orbitals (LCAO) method used in chemistry. Due to the translational symmetry of the crystal, these wavefunctions must satisfy Bloch theorem[18]: they must reflect the translational symmetry of the crystal. As a base to build the eigenfunction of the Hamiltonian it is possible to take the set of functions:

$$\Phi_m^{(v)}(\boldsymbol{r};\boldsymbol{k}) = \frac{1}{\sqrt{N}}\sum_t e^{i\boldsymbol{k}\cdot\boldsymbol{r}_{nv}}\chi_m^{(v)}(\boldsymbol{r}-\boldsymbol{r}_{tv}), \tag{2.4}$$

where $N$ is the number of primitive cells in the crystal, $\chi_m^{(v)}(\boldsymbol{r}-\boldsymbol{r}_{tv})$ is the normalized $m$-type atomic orbital wavefunction (for an isolated atom) centred on the atom $v$ in the cell $t$, pointed by the vector $\boldsymbol{r}_{tv}$. The Hamiltonian of the crystal can be written as:

$$\mathcal{H} = \frac{\boldsymbol{p}^2}{2m} + \sum_{t,v} V^{(a)}(\boldsymbol{r}-\boldsymbol{r}_{tv}), \tag{2.5}$$

where $V^{(a)}(\boldsymbol{r}-\boldsymbol{r}_{tv})$ is the atomic potential centred at $\boldsymbol{r}_{tv}$. Solving the consistent time-independent Schrödinger equation is equivalent to solving the secular equation:

$$\det|\mathcal{H}_{mv,m'v'}(\boldsymbol{k}) - E_n(\boldsymbol{k})S_{mv,m'v'}(\boldsymbol{k})| = 0, \tag{2.6}$$

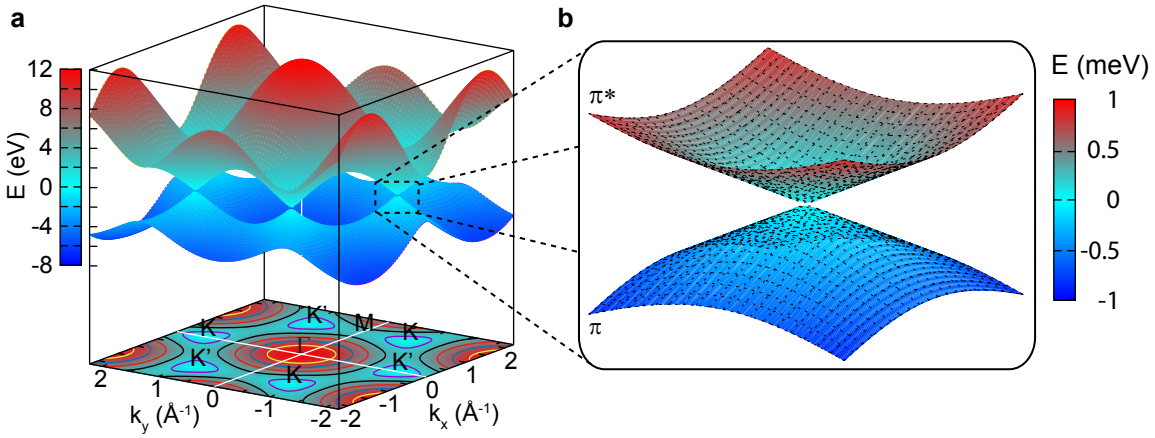


**Figure 2.4: Energy dispersion of graphene $\pi$ bands.** **a**, 3D plot of the energy dispersion of graphene $\pi$ bands in the FBZ calculated using equations (2.11) and (2.12) with $t = -2.8$ eV, $s = 0.1$ eV and $\epsilon_p = 0$ eV. **b**, Particular of the Dirac cone at the K point.

where $E_n(\boldsymbol{k})$ is the n$^{\text{th}}$ energy band in the point $\boldsymbol{k}$, $\mathcal{H}_{mv,m'v'}(\boldsymbol{k})$ the matrix elements of the Hamiltonian and $S_{mv,m'v'}(\boldsymbol{k})$ the elements of the superposition matrix, described by:

$$\begin{aligned} \mathcal{H}_{mv,m'v'}(\boldsymbol{k}) &= \langle \Phi_m^{(v)}(\boldsymbol{r};\boldsymbol{k}) | \hat{\mathcal{H}} | \Phi_{m'}^{(v')}(\boldsymbol{r};\boldsymbol{k}) \rangle, \\ S_{mv,m'v'}(\boldsymbol{k}) &= \langle \Phi_m^{(v)}(\boldsymbol{r};\boldsymbol{k}) | \Phi_{m'}^{(v')}(\boldsymbol{r};\boldsymbol{k}) \rangle. \end{aligned} \tag{2.7}$$

In graphene, in the low-energy bands, the index $m$ corresponds to the $2p_z$ orbital of carbon[8], while the index $v$ stands for the two atomic sites A and B. The matrix elements, in the first neighbours approximation, are given by:

$$\begin{aligned} &\mathcal{H}_{AA} = \mathcal{H}_{BB} = \varepsilon_p, \\ &\mathcal{H}_{AB}(\boldsymbol{k}) = \mathcal{H}^*_{BA}(\boldsymbol{k}) = t \left[ \mathrm{e}^{ik_x a} + 2\mathrm{e}^{-ik_x a/2} \cos\left( \frac{\sqrt{3}}{2} k_y a \right) \right] \equiv t f(\boldsymbol{k}), \\ &S_{AA} = S_{BB} = 1, \\ &S_{AB}(\boldsymbol{k}) = S^*_{BA}(\boldsymbol{k}) = s \left[ \mathrm{e}^{ik_x a} + 2\mathrm{e}^{-ik_x a/2} \cos\left( \frac{\sqrt{3}}{2} k_y a \right) \right] \equiv s f(\boldsymbol{k}), \end{aligned} \tag{2.8}$$

which can be re-written in matrix form as:

$$\mathcal{H}(\boldsymbol{k}) = \begin{pmatrix} \varepsilon_p & t\, f(\boldsymbol{k}) \\ t\, f^*(\boldsymbol{k}) & \varepsilon_p \end{pmatrix}, \quad S(\boldsymbol{k}) = \begin{pmatrix} 1 & s\, f(\boldsymbol{k}) \\ s\, f^*(\boldsymbol{k}) & 1 \end{pmatrix}, \tag{2.9}$$

where the parameters $\varepsilon_p$, $t$ (hopping) and $s$ (overlap) are described as:

$$\begin{aligned} \varepsilon_p &= \langle \chi_{p_z}(\boldsymbol{r} - \boldsymbol{r}_A) |\, \hat{\mathcal{H}}\, | \chi_{p_z}(\boldsymbol{r} - \boldsymbol{r}_A) \rangle\,, \\ t &= \langle \chi_{p_z}(\boldsymbol{r} - \boldsymbol{r}_A) |\, \hat{\mathcal{H}}\, | \chi_{p_z}(\boldsymbol{r} - \boldsymbol{r}_B) \rangle\,, \\ s &= \langle \chi_{p_z}(\boldsymbol{r} - \boldsymbol{r}_A) \mid \chi_{p_z}(\boldsymbol{r} - \boldsymbol{r}_B) \rangle\,. \end{aligned} \tag{2.10}$$

These parameters can be obtained from *ab-initio* calculations or from experimental data. Usually $\varepsilon_p = 0\,\text{eV}$ in order to centre the bands on the K points. Typical values[19] for $t$ are between $-2.5$ and $-3$ eV, while $s$ has values lower than 0.1 eV.

Solving equation (2.6) gives the two energy bands:

$$E_\pm(\boldsymbol{k}) = \frac{\varepsilon_p \pm t\,|f(\boldsymbol{k})|}{1 \mp s\,|f(\boldsymbol{k})|}, \tag{2.11}$$

where $E_-(\boldsymbol{k})$ and $E_+(\boldsymbol{k})$ correspond to the so-called $\pi$ and $\pi^*$ bands, respectively. The value of $|f(\boldsymbol{k})|$ is given by:

$$|f(\boldsymbol{k})| = \sqrt{3 + 2\cos\left(\sqrt{3}k_y a\right) + 4\cos\left(\frac{3}{2}k_x a\right)\cos\left(\frac{\sqrt{3}}{2}k_y a\right)}. \tag{2.12}$$

The energy dispersion for the two $\pi$ bands, calculated using equations (2.11) and (2.12), is shown in figure 2.4. These are degenerate in the K and K' points. Since there are two $\pi$ electrons per unit cell (one belongs to the $2p_z$ orbital of the A atom, the other to the B atom), the valence band is full while the conduction band is empty and the Fermi level lies in the degenerate point of the $\pi$ and $\pi^*$ bands. This makes graphene a semimetal, or a semiconductor with zero bandgap.

A further simplification is obtained by imposing the overlap parameter $s = 0$ in order to study the bands in the neighbourhood of the K and K' points. In this way the bands are symmetric with respect to the Dirac points and their dispersion is given by:

$$E_{\pm}(\boldsymbol{k}) = \varepsilon_p \pm t\,|f(\boldsymbol{k})|\,. \tag{2.13}$$

It is possible to expand the Hamiltonian $\mathcal{H}(\boldsymbol{k}) = \mathcal{H}(\boldsymbol{k} + \boldsymbol{K}(\boldsymbol{K}'))$ in equation (2.9) to the first order in $k_x$ and $k_y$ (where the momentum vector $\boldsymbol{k}$ is measured from the K or K' point) and obtain that $f(\boldsymbol{k}) \approx \sqrt{3}a(\lambda k_x - ik_y)/2\hbar$, where $\lambda = \pm 1$ in the vicinity of K and K' respectively. Therefore, the Hamiltonian can be rewritten as:

$$\mathcal{H}(\boldsymbol{k}) = \hbar v_{\mathrm{F}} \begin{pmatrix} 0 & \lambda k_x - ik_y \\ \lambda k_x + ik_y & 0 \end{pmatrix} = \hbar v_{\mathrm{F}}(\lambda \sigma_x k_x + \sigma_y k_y), \tag{2.14}$$

where we let $\varepsilon_k = 0$ and $v_{\mathrm{F}} = 3\,|t|\,a/(2\hbar) \approx 10^6\, m/s$ is the Fermi velocity, $\sigma_i$, $i = x, y$ are two Pauli matrices. The corresponding eigenvalues are given by:

$$E_{\pm} = \pm \hbar v_{\mathrm{F}} k. \tag{2.15}$$

Therefore, for small excitations above the Fermi level, the energy changes linearly with momentum and it is determined only by one parameter, the Fermi velocity $v_F$. This linearity is highlighted in figures 2.4 and 2.5.

The eigenfunctions of the Hamiltonian in equation (2.14) are:

$$\Phi_{e,h}^{(\boldsymbol{K})}(\boldsymbol{k}) = \frac{1}{\sqrt{2}} \begin{pmatrix} \exp(-i\phi_{\boldsymbol{k}}/2) \\ \pm\exp(i\phi_{\boldsymbol{k}}/2) \end{pmatrix},\ \Phi_{e,h}^{(\boldsymbol{K'})}(\boldsymbol{k}) = \frac{1}{\sqrt{2}} \begin{pmatrix} \exp(i\phi_{\boldsymbol{k}}/2) \\ \pm\exp(-i\phi_{\boldsymbol{k}}/2) \end{pmatrix}, \tag{2.16}$$

where $\phi_{\boldsymbol{k}} = \tan^{-1}(k_x/k_y)$ is the polar angle of the vector $\boldsymbol{k}$. The Hamiltonian in equation (2.14) is, therefore, a Dirac Hamiltonian for massless particles in which the role of the speed of light $c$ is replaced by $v_{\mathrm{F}} \simeq c/300$. This explains why we refer to K and K' as Dirac points, where the electrons act as massless Dirac fermions for which the spin degrees of freedom are replaced by the degrees of freedom due to the sublattice, known as pseudospin. In fact, the wavefunctions in equation (2.16) show how a rotation of $\phi_{\boldsymbol{k}} = 2\pi$ around the K point leads to a $\pi$ phase change in the wavefunction, typically known as Berry phase[20]. This phase is equivalent to the phase acquired by one electron during an adiabatic rotation of $2\pi$ in a magnetic field, therefore the name pseudospin.

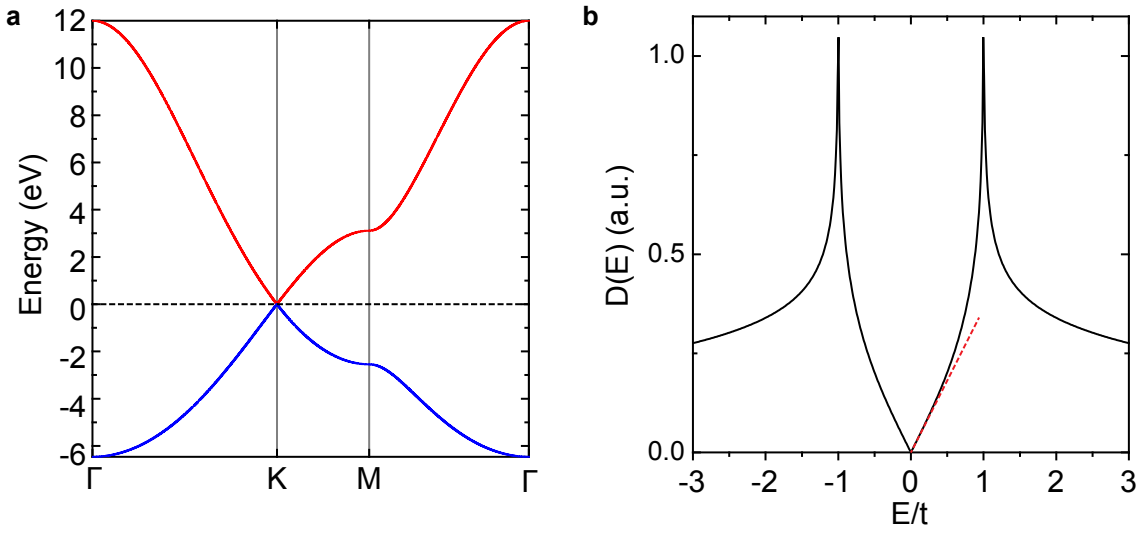


**Figure 2.5: Band structure and DOS of graphene.** **a**, $\pi$-band diagram of graphene calculated using equations (2.11) and (2.12) with $t = -2.8$ eV, $s = 0.1$ eV and $\epsilon_p = 0$ eV. $E_F = 0$ eV, occupied (empty) states are in blue (red). **b**, DOS of graphene as a function of $E/t$, calculated using equation (2.22). The divergences at $E = \pm t$ are Van Hove singularities. Dashed line marks the linear region for small energy excitations around the K points.

### 2.1.4 *DOS and Fermi Level*

The Fermi wavevector $k_{\mathrm{F}}$ for the conical bands described by equation (2.15), is linked to the carrier density $n$ and can be computed as:

$$n = g_s g_v \int_{E(\boldsymbol{k})=const} \frac{d\boldsymbol{k}}{(2\pi)^2} = \frac{g_s g_v}{4\pi} k_{\mathrm{F}}^2 \Rightarrow k_{\mathrm{F}} = \sqrt{\frac{4\pi n}{g_s g_v}}, \tag{2.17}$$

where the factors $g_s$ and $g_v$ are the spin and valley degeneracy respectively ($g_v = 2$ in graphene, due to the not equivalent points K and K'). The Fermi level $E_{\mathrm{F}}$ is therefore related to $n$ by:

$$E_{\mathrm{F}} = \hbar v_{\mathrm{F}} k_{\mathrm{F}} = \hbar v_{\mathrm{F}} \sqrt{\pi n}. \tag{2.18}$$

In 2D systems the electronic density of states (DOS) is given by[18]:

$$D(E) = \frac{g_s g_v}{(2\pi)^2} \int\limits_{E(k)=const} \frac{dl_E}{\left|\frac{dE}{dk}\right|}, \tag{2.19}$$

where the integral is computed on the line of $k$-space at constant energy. A simple expression for the electronic DOS can be derived considering only small energies ($E \to 0$). In this case the main contribution to the DOS comes from the points in the vicinity of K and K' ($\mathbf{k} \to \boldsymbol{K}$). Therefore, using equation (2.15) the DOS results:

$$D(|E|) \xrightarrow[\mathbf{k}\to\boldsymbol{K}]{} \frac{2|E|}{\pi\hbar^2 v_F^2}. \tag{2.20}$$

Therefore, $D(E)$ scales linearly with $E$ for $E \to 0$. The DOS at $E = E_F$ can be computed from equations (2.18) and (2.20):

$$D(E_F) = \frac{2\sqrt{n}}{\sqrt{\pi}\hbar v_F}, \tag{2.21}$$

which shows that intrinsic (undoped) graphene has zero density of carriers. The application of a gate voltage allows to shift $E_F$ inducing a tunable carrier density[1] and will be discussed in section 2.1.6.

A complete expression for the electronic DOS in MLG, in the nearest neighbour approximation, can be found following the derivation by Hobson *et al.*[21], as reported by Katsnelson[22]:

$$D(|E|) = \frac{2|E|}{\pi^2 t} \begin{cases} \frac{1}{\sqrt{\chi(|E|/t)}} F\left(\frac{4|E|/t}{\chi(|E|/t)}\right), & 0 < |E|/t < 1 \\ \frac{1}{\sqrt{4|E|/t}} F\left(\frac{\chi(|E|/t)}{4|E|/t}\right), & 1 < |E|/t < 3 \end{cases}, \tag{2.22}$$

where $F(\psi|k^2)$ is the complete elliptic integral of the first kind:

$$F(\psi|k^2) = \int_0^{\pi/2} \frac{d\psi}{\sqrt{1 - k^2 \sin^2\psi}}, \tag{2.23}$$

and $\chi(x)$ is given by:

$$\chi(x) = (1+x)^2 - \frac{\left(x^2-1\right)^2}{4}. \tag{2.24}$$

Equation 2.22 is plotted in figure 2.5b, where the linear behaviour of $D(E)$ for small

excitations around the K points, described by equation (2.20), is highlighted and shown to hold well for values of $E/t < 0.5$. The two infinite peaks at $E = \pm t$ have a logarithmic asymptotic behaviour[21]:

$$D(|E|) \simeq \frac{1}{2\pi^2}\log\left(\frac{1}{1-|\mathrm{E}|/\mathrm{t}}\right),\ |E| \to t. \tag{2.25}$$

These logarithmic divergences, associated with the saddle points at the M point in the band structure (figure 2.5a), correspond to Van Hove singularities and are responsible for the optical properties of graphene at high energies, as it will be discussed in section 2.2.

### 2.1.5 *Bilayer and multilayer graphene*

A stack of 2, 3 and $> 3$ layers are commonly referred to as bilayer graphene (BLG), trilayer graphene (TLG) and few-layer graphene (FLG), respectively.

The electronic properties of BLG are particularly interesting and can be derived using the same formalism used for MLG[23;22] (see section 2.1.3). Figure 2.6a shows the crystal structure of BLG in the *Bernal* stacking, as discussed in section 2.1.2.2. It is possible to identify four main hopping processes, described by the hopping parameters $\gamma_i$, $i = 0, 1, 3, 4$: $\gamma_0 = t$ represents the in-plane nearest-neighbour hopping, as in MLG; $\gamma_1$ is the interlayer hopping between two A sites; $\gamma_3$ and $\gamma_4$ represent the interlayer hopping between two B sites and between one A and one B site, respectively. From data on graphite[24], $\gamma_0 = -2.8$ eV and $\gamma_1 = 0.4$ eV. For simplicity, the on-site energy of the electrons residing on the A and B atoms can be fixed to be the same and equal to zero. Within the interlayer nearest-neighbour hopping approximation[22] the Hamiltonian for BLG can be written as:

$$\mathcal{H}(\boldsymbol{k}) = \begin{pmatrix} 0 & \gamma_0 f(\boldsymbol{k}) & \gamma_1 & 0 \\ \gamma_0 f^*(\boldsymbol{k}) & 0 & 0 & 0 \\ \gamma_1 & 0 & 0 & \gamma_0 f^*(\boldsymbol{k}) \\ 0 & 0 & \gamma_0 f(\boldsymbol{k}) & 0 \end{pmatrix}, \tag{2.26}$$

where $f(\boldsymbol{k})$ is given in equation (2.8) and the basis states are ordered as: $\{1\mathrm{A}, 1\mathrm{B}, 2\mathrm{A}, 2\mathrm{B}\}$, where the number indicates the layer and the letter the sublattice. Equation (2.26) can be diagonalized giving the four eigenvalues:

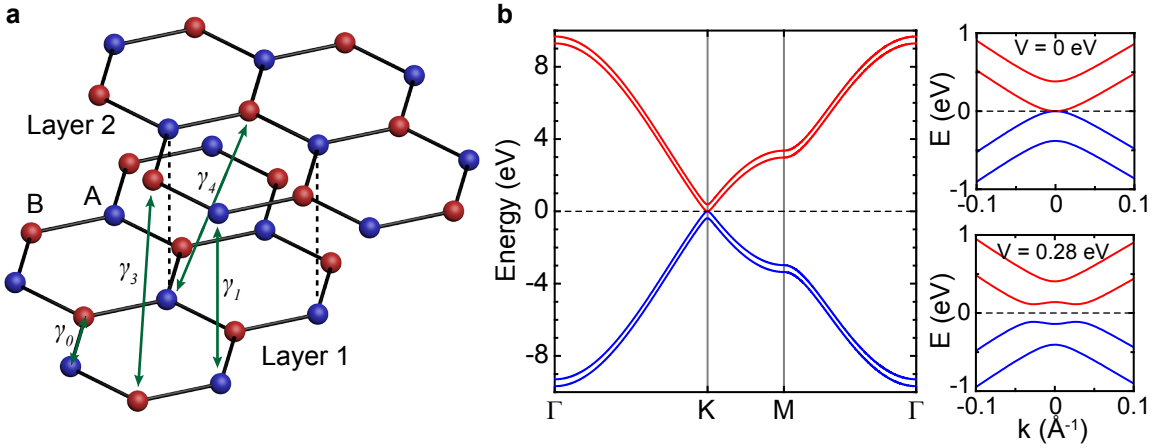


**Figure 2.6: Band structure of bilayer graphene.** **a**, *Bernal* (AB) stacked BLG. $\gamma_i$, $i = 0, 1, 3, 4$ represent the different hopping parameters in the tight-binding model. **b**, $\pi$-bands diagram of BLG calculated using equation (2.27) with parameters $\gamma_0 = -2.8$ eV, $\gamma_1 = 0.381$ eV without ($V = 0$) and with ($V = 0.28$ eV) a voltage applied perpendicular to the graphene layers. Occupied (empty) states are in blue (red).

$$E_i(\boldsymbol{k}) = \pm\frac{1}{2}\gamma_1 \pm \sqrt{\frac{1}{4}\gamma_1^2 + \gamma_0|f(\boldsymbol{k})|^2}, \tag{2.27}$$

where the two $\pm$ signs are independent. The spectrum in equation (2.27) is shown in figure 2.6b. The first feature to be noticed is that two of the four bands touch in the K and K' points. Expanding equation (2.27) for $\boldsymbol{p} \to 0$ ($\boldsymbol{p} = \boldsymbol{k} - \boldsymbol{K}^{(\prime)}$), in analogy with equation (2.14), the low-energy dispersion is:

$$E_{1,2} = -\frac{\gamma_1}{2}\left(\sqrt{\frac{4\lambda^2\gamma_0^2 p^2}{\gamma_1^2} + 1} \pm 1\right) \approx \pm\frac{\hbar p^2}{m^*}, \tag{2.28}$$

where the effective mass is $m^* = |\gamma_1|/(2v_F^2) \approx 0.054 m_e$ and $m_e$ is the rest mass of the electron[23]. Therefore, BLG is a gapless semiconductor, as MLG, with a parabolic band dispersion in the vicinity of the K (K') point, which results in massive carriers with effective mass $m^*$. The two other bands, at K (K'), are separated by a gap $2|\gamma_1|$ and play an important role in the optical properties and light scattering processes.

The application of a potential $V$ across the planes of carbon atoms removes the on-site energy symmetry between the A and B sublattices. In this case, the diagonal

terms of the tight binding Hamiltonian cannot all be set to zero and an energy gap opens in the energy dispersion of BLG[25]. More specifically, the Hamiltonian 2.26 takes the form:

$$\mathcal{H}(\boldsymbol{k}) = \begin{pmatrix} V/2 & \gamma_0 f(\boldsymbol{k}) & \gamma_1 & 0 \\ \gamma_0 f^*(\boldsymbol{k}) & V/2 & 0 & 0 \\ \gamma_1 & 0 & -V/2 & \gamma_0 f^*(\boldsymbol{k}) \\ 0 & 0 & \gamma_0 f(\boldsymbol{k}) & -V/2 \end{pmatrix}. \tag{2.29}$$

Diagonalizing equation (2.29) gives the following eigenvalues:

$$E_i(\boldsymbol{k}) = \pm\sqrt{\gamma_0^2|f(\boldsymbol{k})|^2 + \frac{\gamma_1^2}{2} + \frac{V^2}{4} \pm \sqrt{\frac{\gamma_1^4}{4} + (\gamma_1^2 + V^2)\,\gamma_0^2|f(\boldsymbol{k})|^2}}. \tag{2.30}$$

The spectrum given by equation (2.30) is shown in figure 2.6b for a value of $V = 0.28$ eV in the vicinity of the K point, where the bands have a "Mexican hat" dispersion. The first direct observation of a bandgap opening in bilayer graphene was reported by Ohta *et al.*[26] using angle-resolved photoelectron spectroscopy (ARPES).

The DOS of BLG can be easily computed for $E \to 0$ from equation (2.19) and equation (2.28):

$$D(|E|) \xrightarrow[\mathbf{k}\to\boldsymbol{K}]{} \frac{2m^*}{\pi\hbar^2}, \tag{2.31}$$

that is, the DOS is constant at small energies.

In the general case of multilayer graphene ($n \geq 2$), an equation has been derived by Wallace[8] for an infinite sequence of carbon layers in the ABAB (*Bernal*) stacking order. In this case, considering only $\gamma_0$ and $\gamma_1$ as the relevant hopping parameters, the energy spectrum is given by[8;22]:

$$E(\boldsymbol{k}, \theta) = \gamma_1 \cos(\theta) \pm \sqrt{\gamma_0^2|f(\boldsymbol{k})|^2 + \gamma_1^2\cos^2(\theta)}. \tag{2.32}$$

Here $\theta = 2k_z c$, where $k_z$ is the z-component of the wave vector and $c$ is the interlayer distance. In order to consider only $N$ layers of graphene ($N < \infty$), the boundary condition for which $E(\theta) = E(-\theta)$ has to be applied, therefore equation (2.32) still applies but with $\theta$ being a discrete number[22]:

$$\theta_n = (\pi n)/(N+1), \;\; n = 1, 2, ..., N. \tag{2.33}$$

Formally, equations (2.32) and (2.33), can be used to find the band diagram for an arbitrary number of graphene layers in *Bernal* stacking. For $N = 2$ (BLG), for example, $\cos(\theta) = \pm 1/2$ and, therefore, equation (2.27) is recovered. For $N = 3$ (TLG) there are six solutions to equation (2.32), with $\cos(\theta) = 0, \pm 1/\sqrt{2}$:

$$E(\boldsymbol{k}) = \begin{cases} \pm\gamma_0 |f(\boldsymbol{k})|, \\ \pm\frac{\sqrt{2}}{2}\gamma_1 \pm \sqrt{\frac{\gamma_1^2}{2} + \gamma_0^2 |f(\boldsymbol{k})|^2}, \end{cases} \tag{2.34}$$

where both conical (i.e. with a linear dispersion at $\boldsymbol{k} \to \boldsymbol{K}^{(\prime)}$) and parabolic bands touching at K and K' are found.

### 2.1.6 *Transport properties: ambipolar effect and mobility*

Owing to its gapless nature, graphene shows a strong ambipolar behaviour. The charge carrier type (e.g. electron, $e^-$, or hole, $h^+$) and concentration can be changed with the application of a gate voltage ($V_g$)[1]. A typical field effect transistor (FET) device is schematically depicted in figure 2.7a where a graphene layer is deposited on top of a heavily doped ($p$ or $n$) Si substrate capped with a layer of $SiO_2$, which acts as dielectric gate insulator. The application of a voltage $V_g > 0$ (figure 2.7a, top) to the Si gate induces positive charges at the interface with the oxide; to maintain charge neutrality, negative charges are induced at the other interface, that is, excess electrons will be present in the graphene layer, injected from the contacts. Conversely, the application of a voltage $V_g < 0$ (figure 2.7a, bottom) induces positive charges in the graphene layer, leaving it depleted of electrons. It is possible to relate the gate voltage to the induced charge concentration by[1]:

$$n_i = \frac{\epsilon_0 \epsilon V_g}{q\, d} = \alpha V_g, \;\; i = e, h \tag{2.35}$$

where $\epsilon_0$ and $\epsilon$ are the vacuum and gate oxide permittivities, respectively; $d$ is the thickness of the gate oxide and $q$ is the electron charge. The subscript $i$ is $e$ for electrons and $h$ for holes. For a typical device fabricated on 280 nm $SiO_2$ the value $\alpha = 7.698{\cdot}10^{10}$ cm$^{-2}$ V$^{-1}$. For values of $V_g \approx 100V$ it is possible to reach concentrations

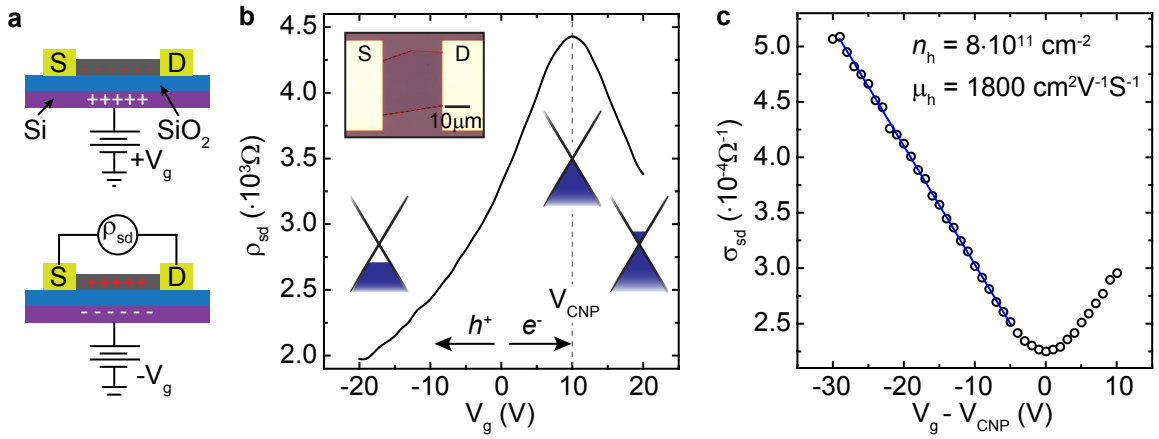


**Figure 2.7: Ambipolar effect in graphene FET. a**, Schematic of a graphene FET on $Si/SiO_2$ substrate. A positive, $V_g > 0$, gate bias induces excess electrons in the graphene channel (top), while a negative, $V_g < 0$, one induces holes (bottom). **b**, Resistivity, $\rho_{sd}$, as a function of $V_g$ for a typical graphene FET (inset). The CNP is at $V_g = V_{\text{CNP}} = 10$ V, indicating hole-doping of the graphene layer with a charge concentration $n_h \approx 8 \cdot 10^{11}$ cm$^{-2}$ (see main text). The illustrations represent the filling of the $\pi$ bands in the vicinity of the K point at different $V_g$. **c**, Conductivity, $\sigma_{sd}$, as a function of $V_g$ for the same device in **b**. The hole mobility, $\mu_h$, can be extrapolated from a linear fit (solid line).

of the order of $n \sim 10^{13}$ cm$^{-2}$.

Thanks to equation (2.18), therefore, the application of a gate voltage allows the shifting of the Fermi level of graphene between the valence and conduction bands. The absence of a bandgap makes this transition smooth, as shown in figure 2.7b. In a pristine, undoped, graphene sample the Fermi level lies at the charge neutrality point (CNP), where the two $\pi$ bands touch and there are no states available, see equation (2.21); at this point the resistivity $\rho_{sd}$ has a maximum. In general, however, contamination due to exposure to ambient conditions and fabrication processes induce a certain level of doping, due to charge-transfer between the contaminants and the surface of graphene[1;9;27]. In this case the CNP appears at $V_g \neq 0$, as shown in figure 2.7b, where $V_{\text{CNP}} = 10$ V. A positive, $V_{\text{CNP}} > 0$, indicates $p$-doping of graphene, that is, at $V_g = 0$ there is an excess concentration of holes $n_h$. Conversely, a negative, $V_{\text{CNP}} < 0$, indicates $n$-doping.

The conductivity of graphene, at high enough charge concentrations, follows the

standard equation given by the Drude model[1;28]:

$$\sigma_i = \frac{1}{\rho_i} = n_i \, q \, \mu_i, \;\; i = e, h, \tag{2.36}$$

where $\mu_i$ is the mobility of the charge carriers. Combining equations (2.35) and (2.36), a linear dependence of the conductivity with applied gate voltage is found:

$$\sigma_i = \alpha \, q \, \mu_i \, V_g, \;\; i = e, h. \tag{2.37}$$

This linear dependence is shown in figure 2.7c, where the linear fit of the experimental points gives a value of the mobility $\mu_h = 1800$ cm$^2$V$^{-1}$s$^{-1}$.

The electronic quality of graphene is remarkable: electrons and holes can cover sub-micron distances without being scattered, even at room temperature[1]. In fact, the carrier mobility can reach values[29] as high as 250000 cm$^2$V$^{-1}$s$^{-1}$ and ballistic transport can be observed in $\mu$m-scale samples[30]. The mobility in graphene does not depend on the temperature in the range $10 - 100$ K, suggesting that the dominant mechanism of scattering is due to defects[31;32]. At room temperature most samples obtained by mechanical cleavage and deposited on top of a substrate show mobilities of the order of $\mu_h = 2000$ cm$^2$V$^{-1}$s$^{-1}$. By improving the sample preparation through current annealing[33], values higher than 25000 cm$^2$V$^{-1}$s$^{-1}$ are reached. Furthermore, the mobility remains high even at high carrier concentrations and it is weakly influenced by chemical doping[34]. For supported devices, the most common substrate material for graphene is $SiO_2$ which is known to limit the performance of such devices and obscures interesting physics. This is thought to be caused by the roughness of the $SiO_2$ substrates, which induce corrugations in the graphene, as well as charge traps in the $SiO_2$ which results in inhomogeneous doping. In order to improve further the mobility it is necessary to shield or remove completely the substrate. In fact, for suspended graphene samples measured values of $\mu$ are as high as 250000 cm$^2$V$^{-1}$s$^{-1}$ [29;32]. Recently, the growth of high-quality hexagonal boron nitride (hBN) crystals[35] allowed a major improvement in the electronic quality of supported devices[36]. Encapsulation of graphene between two layers of hBN allowed full insulation of graphene from the environment and screening from the substrate, resulting in mobilities as high as 350000 cm$^2$V$^{-1}$s$^{-1}$, even higher that suspended devices[37].

## 2.2 OPTICAL PROPERTIES OF GRAPHENE

### 2.2.1 *Absorption and transmittance*

Graphene's unique electronic properties produce an unexpected high opacity for an atomic single layer. MLG, in fact has an absorption of $\sim 2.3\%$ across the whole spectrum, from far-infrared (FIR) to ultra-violet (UV) wavelengths[38]. This value is a universal constant, related to the fine-structure constant $\alpha \approx 1/137$ only[39]. An electromagnetic (EM) wave incident at normal angle on a free-standing MLG, with electric field $\mathbf{E}(\omega)$, where $\omega$ is the angular frequency, has an incident energy flux given by:

$$W_i = \frac{c}{4\pi} \left|\mathbf{E}(\omega)\right|^2, \tag{2.38}$$

where $c$ is the speed of light in vacuum. Due to momentum conservation, the electronic transition, excited by the incident photon, can be depicted as in figure 2.8a, where the initial $|i\rangle$ and final $|f\rangle$ states have the same momentum. Therefore, the absorbed energy flux is given by:

$$W_a = \eta\hbar\omega, \tag{2.39}$$

where $\eta$ is the quantum efficiency of the process, which can be derived using the Fermi's golden rule (FGR):

$$\eta = \frac{2\pi}{\hbar}|M|^2 D(\hbar\omega/2), \tag{2.40}$$

where $D(\hbar\omega/2) = \omega/\pi\hbar v_f^2$ is the density of states of graphene at $E = \hbar\omega/2$ and $|M|^2 = \left|\langle f|\,\mathcal{H}_{int}\,|i\rangle\right|^2$ is the matrix element of the interaction Hamiltonian. The Hamiltonian (2.14), in the presence of an EM field, can be re-written as:

$$\mathcal{H} = \hbar v_f \hat{\sigma}\cdot\mathbf{k} = v_f\hat{\sigma}\cdot\left(\mathbf{k} - \frac{q}{c}\mathbf{A}\right) = \mathcal{H}_0 + \mathcal{H}_{int}, \tag{2.41}$$

where the standard vector potential substitution $\hbar\mathbf{k} \to \hbar\mathbf{k} + q\mathbf{A}/c$ is used, with $\mathbf{A} = ic\mathbf{E}/\omega$ vector potential. Therefore, the matrix element can be computed as:

$$|M|^2 = \left|\langle f|\, v_f\hat{\sigma}\cdot\frac{q}{i\omega}\mathbf{E}\,|i\rangle\right|^2 = \frac{1}{8}\frac{v_f^2 q^2}{\omega^2}|E|^2, \tag{2.42}$$

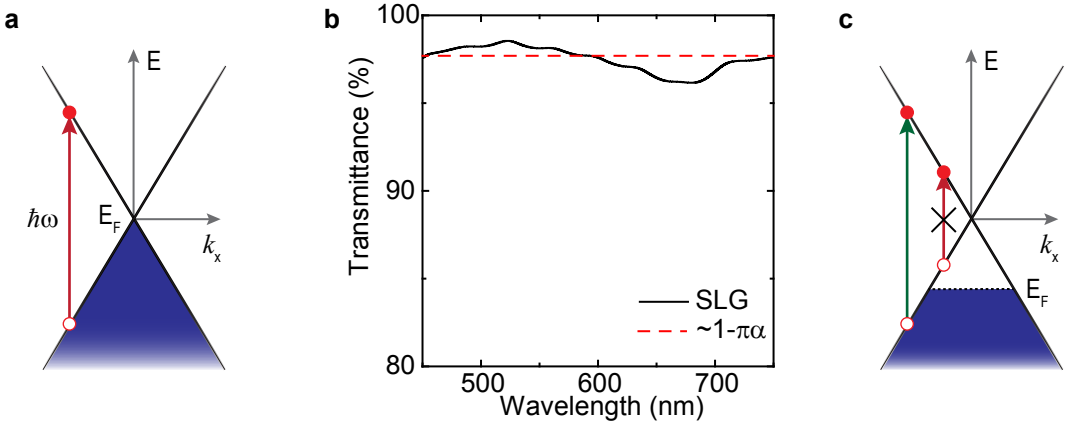


**Figure 2.8: Optical transmittance of graphene.** **a**, Schematic of a low-energy optical excitation in graphene: an $e-h$ pair is created by an incident photon of energy $E = \hbar\omega > 2E_{\mathrm{F}}$, where $E_{\mathrm{F}} \neq 0$ is the Fermi level. **b**, Measured optical transmittance of MLG graphene. Red line marks the value $T = 1 - \pi\alpha \approx 97.7\%$. **c**, Gate-tunable optical absorption: a photon of energy $E = \hbar\omega < 2E_{\mathrm{F}}$ is not able to excite an optical transition due to Pauli blocking, therefore making graphene transparent to photon energies $< 2E_{\mathrm{F}}$.

where the states $|i\rangle$ and $|f\rangle$ are given by equation (2.16) and both the spin and valley degeneracy are considered. Using equation (2.39) and equation (2.40), thus, $W_a = q^2|E|^2/4\hbar$ and, therefore, the absorption of MLG is:

$$A = \frac{W_a}{W_i} = \frac{\pi q^2}{\hbar c} = \pi\alpha \approx 2.3\%, \tag{2.43}$$

where $\alpha = q^2/\hbar c \approx 1/137$ is the fine structure constant. Given that the reflectivity of MLG is[39] $R \ll 1$ the transmittance of MLG can be approximated as:

$$T = 1 - A = 1 - \pi\alpha \approx 97.7\%. \tag{2.44}$$

In figure 2.8b, the measured transmittance of MLG across the visible spectrum is shown, with a value of $\sim 97.7\% \pm 0.5\%$. A similar derivation can be carried out for BLG[39], which gives $A = 2\pi\alpha$, highlighting the fact that the absorption of graphene is related to the gapless nature of the bands and the 2D nature of the carriers. Nair *et al.*[39] have shown that the absorption of graphene scales as $A = n\pi\alpha$, where $1 \leq n \leq 5$ is the number of graphene layers.

It is also possible to calculate the optical transmittance of graphene by calculating the conductance at frequency $\omega$ at $E_F = 0$, as done in ref. 40:

$$G_1(\omega) = \frac{\pi q^2}{\omega} |\mathbf{v}(\omega)|^2 D(\omega) \left[ f\left(-\frac{\hbar\omega}{2}\right) - f\left(\frac{\hbar\omega}{2}\right) \right], \tag{2.45}$$

where $G_1$ is the real part of the conductance, $\mathbf{v}(\omega)$ is the velocity matrix element between the initial and final state, $D(\omega)$ is the joint density of states and $f(E) = [\exp(E/T) + 1]^{-1}$ is the Fermi-Dirac distribution at temperature $T$. From equation (2.20) it can be seen that for small excitations $D(\omega) \propto \hbar^3\omega/v_F^2$ and $|\mathbf{v}(\omega)| \propto v_F$, giving $G_1(\omega) \propto q^2/\hbar$ at $T = 0$. Therefore, the optical transmittance is:

$$T(\omega) = \left(1 + \frac{2\pi G_1(\omega)}{c}\right)^{-2} = \left(1 + \frac{\pi\alpha}{2}\right)^{-2} \approx 1 - \pi\alpha, \tag{2.46}$$

and it is independent on the frequency $\omega$.

So far the situation of undoped, pristine graphene has been presented. Doping induces changes in the optical properties of graphene, resulting in a gate-tunable optical absorption[38]. As discussed in section 2.1.6, it is possible to modulate the concentration of the charge carriers is graphene by applying a gate voltage. As a consequence, the Fermi level $E_\mathrm{F}$ is shifted according to equation (2.18). Therefore, as incorporated in equation (2.45), transitions with energy $\hbar\omega < 2E_\mathrm{F}$ are suppressed (see figure 2.8c), this results in a transparency window at energies $< 2E_\mathrm{F}$, while it does not affect energies $> 2E_\mathrm{F}$, as shown experimentally in ref. 38.

### 2.2.2 *Optical contrast*

The high absorption per layer of graphene allows the identification of a single-layer of this material when it is deposited on a suitable substrate. This is due to the contrast that is created between the bare substrate and the portion covered by the graphene. The standard substrate used to fabricate graphene-based devices is highly-doped Si capped with a layer of thermally-grown $SiO_2$, typically $\sim$ 300 nm thick (see also section 2.1.6). This was, in fact, the first substrate on which MLG was identified[1]. Figure 2.9a,b shows optical micrographs of flakes of MLG, BLG and TLG on such substrate: it is remarkable that a single atomic layer has a contrast of $\sim 5\%$ under white light illumination. A simple model can be derived to explain the observed fea-

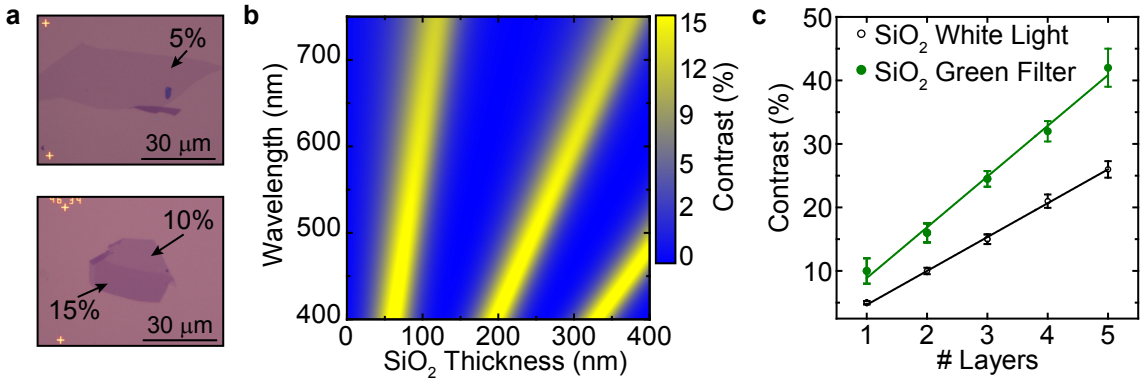


**Figure 2.9: Optical contrast of graphene.** **a**, Optical micrographs and contrast measurements of MLG (top), BLG and TLG (bottom) flakes on $Si/SiO_2$ (290 nm), under white light illumination. **b**, Optical contrast of MLG on $Si/SiO_2$ substrate as a function of incident wavelength and oxide thickness, calculated using equation (2.48). **c**, Optical contrast of different layers of graphene on $Si/SiO_2$ under white light illumination and with a green band-pass filter. Straight lines mark a slope of $(5.0 \pm 0.1)\%$ and $(8.0 \pm 0.2)\%$ per layer, respectively.

tures[41], starting by considering a stacked sequence of $Si/SiO_2/G/Air$. The bottom Si is treated as semi-infinite (in the vertical direction) with complex refractive index[42] $n_3(\lambda)$, which is function of the incident wavelength $\lambda$. The $SiO_2$ layer has thickness $d_2$ and refractive index[43] $n_2(\lambda)$. The thickness of the graphene layer is $d_1 = 0.34$ nm, which corresponds to the extension of the $\pi$ orbitals out of the plane[44]. The refractive index of graphene can be chosen as $n_1 \approx 2.6 - 1.3i$, which is the same as graphite (since the optical response of graphite, for normal incidence, is dominated by the in-plane EM response) and it is independent of $\lambda$. Finally, $n_0 = 1$ for air. In the described geometry the Fresnel coefficients can be used to derive the intensity of the reflected light by the stacked sequence[45]:

$$I^R_{n_1}(\lambda) = \left| \frac{r_1 e^{i(\phi_1+\phi_2)} + r_2 e^{-i(\phi_1-\phi_2)} + r_3 e^{-i(\phi_1+\phi_2)} + r_1 r_2 r_3 e^{i(\phi_1-\phi_2)}}{e^{i(\phi_1+\phi_2)} + r_1 r_2 e^{-i(\phi_1-\phi_2)} + r_1 r_3 e^{-i(\phi_1+\phi_2)} + r_2 r_3 e^{i(\phi_1-\phi_2)}} \right|^2 , \tag{2.47}$$

where $r_i = (n_{i-1} - n_i)/(n_{i-1} + n_i)$, $i = 1, 2, 3$, are the relative refractive indices and $\phi_i = 2\pi n_i d_i/\lambda$, $i = 1, 2$, are the phase shifts after each reflection. The contrast $C$ is

defined as the relative reflected intensity in the presence ($n_1 \neq 1$) and absence ($n_1 = 1$) of graphene:

$$C(\lambda) = \frac{I^R_{n_1=1}(\lambda) - I^R_{n_1}(\lambda)}{I^R_{n_1=1}(\lambda)}. \tag{2.48}$$

The results from equation (2.48) are shown in figure 2.9b, as a function of $SiO_2$ thickness $d_2$ and wavelength. It is notable the ability to enhance the contrast of MLG up to $\sim 15\%$ with the appropriate choice of substrate and illumination wavelength, although the windows of high contrast are narrow and a few nm of difference in the $SiO_2$ thickness can make graphene completely invisible. In figure 2.9c the optical contrast measured a function of the layers number of graphene on 285 nm $SiO_2$ is reported, under white light illumination and using a green ($\sim$ 550 nm) band-pass filter. A perfect linear relationship (up to 5 layers) can be seen, with slopes $(5.0 \pm 0.1)\%$ and $(8.0 \pm 0.2)\%$ per layer, respectively; as expected the green filter enhances the contrast. The layer thickness was confirmed with atomic force microscopy (AFM) and Raman spectroscopy (these techniques will be discussed in chapter 3). It is possible, therefore, to "count" the number of layers in FLG simply measuring the optical contrast, this is , in fact, the technique used in the rest of this work.

## 2.3 TRANSITION METAL DICHALCOGENIDES AND $HFS_2$

As complementary metal-oxide semiconductor (CMOS) technology is fast approaching its ultimate limit in the ability to scale down electronic devices[46;47], a new class of atomically-thin materials is emerging as a promising alternative. Two-dimensional (2D) layered materials[48;49] have been known for more than 40 years, but the recent successful isolation of single layers allowed the full exploitation of their broad spectrum of physical properties. Amongst these newly re-discovered 2D materials, semiconducting transition-metal dichalcogenides (TMDs) have shown great versatility in optoelectronic applications, spanning from solar energy harvesting[50] to sensing[51] and light-emission[52], thanks to their unique properties, such as: layer-dependent indirect-to-direct bandgap transition[53], strong optical anisotropy[54] and valley dichroism[55].

In this section the basic properties of TMDs are reviewed, starting from their crystal structure and polytypes (section 2.3.1) to the description of their main electronic and

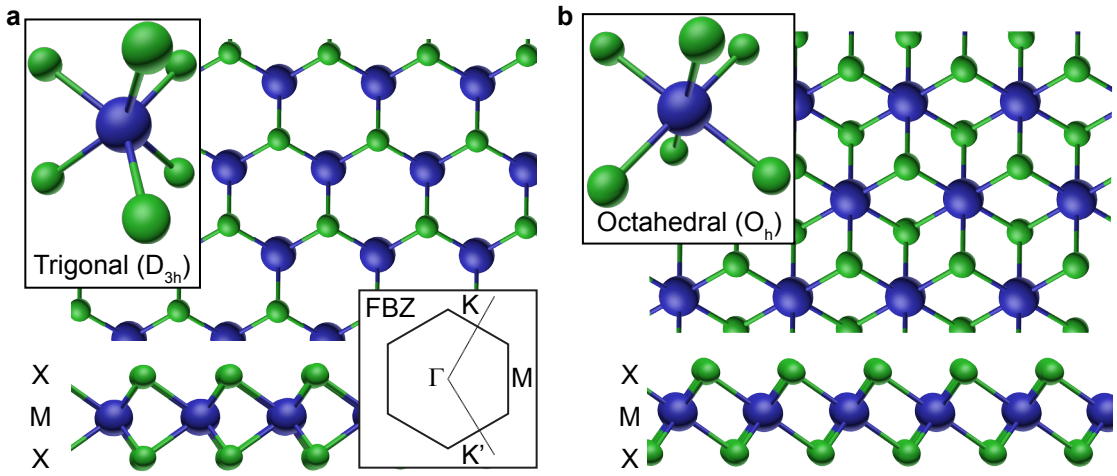


**Figure 2.10: Crystal structure of TMDs.** **a**, Trigonal prismatic ($D_{3h}$) symmetry in $H$-$MX_2$ TMDs. Inset: FBZ of $D_{3h}$ TMDs with high symmetry points. **b**, Octahedral ($O_h$), or trigonal anti-prismatic ($D_{3d}$) group of $O_h$, in $T$-$MX_2$ TMDs.

optical properties (section 2.3.2). Finally, the chapter closes with a description of the main properties of $HfS_2$, which is the transition metal dichalcogenide (TMD) used in this work (chapter 7) to realise novel optoelectronic devices.

### 2.3.1 *Crystal structure and phases*

TMDs are compounds with chemical formula $MX_2$, where M is a transition metal from group IV-B, V-B or VI-B, and X is a chalcogen (S, Se or Te)[49]. They crystallize in a graphite-like structure, with each layer $6 - 7$ Å thick, of the form X-M-X, with the chalcogen atoms disposed in hexagonal planes. The layers are held together by van der Waals forces which result in a strong anisotropy and the ability, as in graphite, to exfoliate TMDs in thin layers simply by micro-mechanical cleavage.

The crystalline phase of TMDs depends on the coordination of the metal atoms, which can be either trigonal prismatic ($D_{3h}$) or octahedral ($O_h$, sometimes referred to as trigonal anti-prismatic $D_{3d}$), as illustrated in figure 2.10. Depending on the kind of atoms involved, one of the two coordination is thermodynamically more stable than the other. The coordination dictates the polymorph of the specific TMD that is naturally found. The most common polymorphs are 1T (trigonal), 2H (hexagonal) and 3R (rhombohedral), where the digit indicates the number of X–M–X units in the unit cell.

**Table 2.1: Properties of selected TMDs.** Electronic properties of different TMDs and associated polymorphs.

| Metal | Chalcogen | Type (Phase) | Bandgap (eV) | References |
|---|---|---|---|---|
| Mo | $S_2$ | Semiconductor (2H)<br>Metal (1T) | 1.8 (1L)/1.2 (Bulk) | 48;56 |
| | $Se_2$ | Semiconductor (2H)<br>Metal (1T) | 1.5 (1L)/1.1 (Bulk) | 48;58 |
| | $Te_2$ | Semiconductor (2H)<br>Metal (1T) | 1.1 (1L)/1.0 (Bulk) | 48;58 |
| W | $S_2$ | Semiconductor (2H)<br>Metal (1T) | 1.51 (1L) | 57;59 |
| | $Se_2$ | Semiconductor (2H)<br>Semimetal (1T) | 1.22 (1L) | 57;59 |
| | $Te_2$ | Semiconductor (2H)<br>Semimetal (1T) | 0.7 (1L) | 60 |
| Re | $S_2$ | Semiconductor (1T) | 1.43 (1L)/1.35 (Bulk) | 61 |
| Hf | $S_2$ | Semiconductor (2H)<br>Semiconductor (1T) | 2.93 (1L)<br>2.96 (1L) | 62;59 |
| | $Se_2$ | Semiconductor (2H)<br>Semiconductor (1T) | 2.49 (1L)<br>2.95 (1L) | 59 |
| | $Te_2$ | Semiconductor (2H)<br>Metal (1T) | 1.62 (1L) | 59 |

Depending on its phase, that is its polymorph, a TMD can have very different electronic properties, such as for $MoS_2$ and $WSe_2$ which have a semiconducting behaviour in the 2H phase and a metallic one in the 1T phase[56;57].

The FBZ of a monolayer TMD in the trigonal prismatic structure, is hexagonal, as in graphene, with high symmetry points K and K' which show a peculiar behaviour, as in graphene (see figure 2.10a, inset). For instance, in the bulk form most TMDs are indirect semiconductors, with an indirect gap between the Q and Γ points, while in the monolayer limit it is found that they become direct gap semiconductors, with the gap located at the K (K') points. This effect is related to the increase in quantum confinement in the out-of-plane direction (given by the layered nature), which causes an increase in the indirect gap, without affecting the direct gap at K (K')[53].

### 2.3.2 *Electronic and optical properties*

Table 2.1 summarizes the main electronic properties of selected TMDs. With more than 40 materials, layered TMDs offer the best platform for a large class of applications[63;64]. The bandgap of semiconducting TMDs spans from mid-infrared (MIR) to UV wavelengths and careful combinations of several stacked layers[65], can be used to create novel optoelectronic devices.

The optical absorption of most TMDs is dominated by the direct transitions at K (K'), in the near-infrared (NIR) and visible regions of the EM spectrum. The absorption is characterized by strong excitonic effects in monolayer TMDs, which appear as sharp peaks in the absorption spectrum near the band edge, also at room temperature[53]. Theoretical[66;67] and experimental[68;69;70] results shown that the exciton binding energy in some TMDs is as high as $0.5 - 1.0$ eV, indicating an exciton Bohr radius (that is, the distance of the electron-hole pair) exceeding 1 nm. Indeed, these strong excitonic effects have been used to enhance the emission of an LED, by fabricating a stacked structure based on $WSe_2$[52].

Excitonic effects could be at the base of the observed single-photon emission in point-emitters in $WSe_2$, where local strain or structural defects are introduced[71;72;73;74]. These emitters show very narrow lines ($< 0.1$ meV, in contrast with excitonic lines which are $\sim 10$ meV) and single-photon character.

#### 2.3.2.1 *Band structure calculation*

As for graphene, knowledge of the band structure allows the computation of the electronic and optical properties of TMDs. In section 2.1.3 the tight binding method for the calculation of the band structure of crystals was presented and applied to graphene. In general, this procedure can be repeated for TMDs, although the amount of calculations to be performed makes it a formidable task[75;76]. The approach usually followed is to perform numerical simulations of the band structure based on density-functional theory (DFT)[18]. In chapter 7, data obtained using this method are presented. The description of such approach is beyond the scope of this work, and the DFT calculations were performed by Dr. Steven Hepplestone in the University of Exeter using the density functional by Perdew, Burkeand and Ernzerhof (PBE)[77], as implemented in the QUANTM ESPRESSO package[78].

# BIBLIOGRAPHY


[1] K. S. Novoselov, A. K. Geim, S. V. Morozov, D. Jiang, Y. Zhang, S. V. Dubonos, I. V. Grigorieva, and A. A. Firsov. Electric field effect in atomically thin carbon films. *Science*, 306:666, 2004.

[2] S. Mouras, A. Hamm, D. Djurado, and J. C. Cousseins. Synthesis of first stage graphite intercalation compounds with fluorides. *Revue de Chimie Minerale*, 24:572, 1987.

[3] Donald W. Olson. 2013 minerals yearbook: Graphite. *USGS*, 10/2015.

[4] G.R. Matos and D.W. Olson. Natural graphite end-use statistic. *USGS*, 2005.

[5] Chuhei Oshima and Ayato Nagashima. Ultra-thin epitaxial films of graphite and hexagonal boron nitride on solid surfaces. *Journal of Physics: Condensed Matter*, 9(1):1, 1997.

[6] J. Krumhansl and H. Brooks. The lattice vibration specific heat of graphite. *The Journal of Chemical Physics*, 21(10):1663–1669, 1953.

[7] J.C. Bowman and J.A. Krumhansl. The low-temperature specific heat of graphite. *Journal of Physics and Chemistry of Solids*, 6(4):367 – 379, 1958.

[8] P. R. Wallace. The band theory of graphite. *Phys. Rev.*, 71:622–634, May 1947.

[9] A. K. Geim and K. S. Novoselov. The rise of graphene. *Nat Mater*, 6(3):183–191, Mar 2007.

[10] A. K. Geim. Graphene: Status and prospects. *Science*, 324(5934):1530–1534, 2009.

[11] VV. AA. Tables of physical & chemical constants. *Kaye & Laby Online*, Version 1.0:3.1.3 Abundances of the elements, 1995.

[12] D.R. Lide, editor. *CRC Handbook of Chemistry and Physics 1999-2000*. CRC Press, 1998.

[13] A. D. McNaught and A. Wilkinson. Rhombohedral graphite. *IUPAC. Compendium of Chemical Terminology, 2nd ed. (the "Gold Book")*, 1997.

[14] R. Nicklow, N. Wakabayashi, and H. G. Smith. Lattice dynamics of pyrolytic graphite. *Phys. Rev. B*, 5:4951–4962, Jun 1972.

[15] J.-C. Charlier, X. Gonze, and J.-P. Michenaud. First-principles study of the stacking effect on the electronic properties of graphite(s). *Carbon*, 32(2):289 – 299, 1994.

[16] Aleksey N. Kolmogorov and Vincent H. Crespi. Registry-dependent interlayer potential for graphitic systems. *Phys. Rev. B*, 71:235415, Jun 2005.

[17] Felix Bloch. Über die quantenmechanik der elektronen in kristallgittern. *Zeitschrift für Physik*, 52(7):555–600, 1929.

[18] Giuseppe Grosso and Guseppe Pastori Parravicini. *Solid State Physics*. Academic Press, London, 2000.

[19] R. Saito, G. Dresselhaus, and M. S. Dresselhaus. *Physical properties of carbon nanotubes*. Imperial College Press, 1998.

[20] M. V. Berry. Classical adiabatic angles and quantal adiabatic phase. *Journal of Physics A: Mathematical and General*, 18(1):15, 1985.

[21] J. P. Hobson and W. A. Nierenberg. The statistics of a two-dimensional, hexagonal net. *Phys. Rev.*, 89:662–662, Feb 1953.

[22] Mikhail I. Katsnelson. *Graphene: Carbon in Two Dimensions*. Cambridge University Press, Cambridge, 2012.

[23] Edward McCann and Mikito Koshino. The electronic properties of bilayer graphene. *Reports on Progress in Physics*, 76(5):056503, 2013.

[24] M. S. Dresselhaus and G. Dresselhaus. Intercalation compounds of graphite. *Advances in Physics*, 51(1):1–186, 2002.

[25] Eduardo V. Castro, K. S. Novoselov, S. V. Morozov, N. M. R. Peres, J. M. B. Lopes dos Santos, Johan Nilsson, F. Guinea, A. K. Geim, and A. H. Castro Neto. Biased bilayer graphene: Semiconductor with a gap tunable by the electric field effect. *Phys. Rev. Lett.*, 99:216802, Nov 2007.

[26] Taisuke Ohta, Aaron Bostwick, Thomas Seyller, Karsten Horn, and Eli Rotenberg. Controlling the electronic structure of bilayer graphene. *Science*, 313(5789):951–954, 2006.

[27] Masa Ishigami, J. H. Chen, W. G. Cullen, M. S. Fuhrer, and E. D. Williams. Atomic structure of graphene on $SiO_2$. *Nano Letters*, 7(6):1643–1648, 2007.

[28] Neil W. Ashcroft and David N. Mermin. *Solid State Physics*. Holt, Rinehart and Winston, 1976.

[29] M. Orlita, C. Faugeras, P. Plochocka, P. Neugebauer, G. Martinez, D. K. Maude, A.-L. Barra, M. Sprinkle, C. Berger, W. A. de Heer, and M. Potemski. Approaching the dirac point in high-mobility multilayer epitaxial graphene. *Phys. Rev. Lett.*, 101:267601, Dec 2008.

[30] Luca Banszerus, Michael Schmitz, Stephan Engels, Matthias Goldsche, Kenji Watanabe, Takashi Taniguchi, Bernd Beschoten, and Christoph Stampfer. Ballistic transport exceeding 28 $\mu$m in CVD grown graphene. *Nano Letters*, 16(2):1387–1391, 2016.

[31] S. V. Morozov, K. S. Novoselov, M. I. Katsnelson, F. Schedin, D. C. Elias, J. A. Jaszczak, and A. K. Geim. Giant intrinsic carrier mobilities in graphene and its bilayer. *Phys. Rev. Lett.*, 100:016602, Jan 2008.

[32] Xu Du, Ivan Skachko, Anthony Barker, and Eva Y. Andrei. Approaching ballistic transport in suspended graphene. *Nat Nano*, 3(8):491–495, Aug 2008.

[33] J. Moser, A. Barreiro, and A. Bachtold. Current-induced cleaning of graphene. *Applied Physics Letters*, 91(16), 2007.

[34] F. Schedin, A. K. Geim, S. V. Morozov, E. W. Hill, P. Blake, M. I. Katsnelson, and K. S. Novoselov. Detection of individual gas molecules adsorbed on graphene. *Nat Mater*, 6(9):652–655, Sep 2007.

[35] Kenji Watanabe, Takashi Taniguchi, and Hisao Kanda. Direct-bandgap properties and evidence for ultraviolet lasing of hexagonal boron nitride single crystal. *Nat Mater*, 3(6):404–409, Jun 2004.

[36] Dean C. R., Young A. F., Meric I., Lee C., Wang L., Sorgenfrei S., Watanabe K., Taniguchi T., Kim P., Shepard K L., and Hone J. Boron nitride substrates for high-quality graphene electronics. *Nat Nano*, 5(10):722–726, Oct 2010.

[37] Luca Banszerus, Michael Schmitz, Stephan Engels, Jan Dauber, Martin Oellers, Federica Haupt, Kenji Watanabe, Takashi Taniguchi, Bernd Beschoten, and Christoph Stampfer. Ultrahigh-mobility graphene devices from chemical vapor deposition on reusable copper. *Science Advances*, 1(6), 2015.

[38] Kin Fai Mak, Long Ju, Feng Wang, and Tony F. Heinz. Optical spectroscopy of graphene: From the far infrared to the ultraviolet. *Solid State Communications*, 152(15):1341 – 1349, 2012. Exploring Graphene, Recent Research Advances.

[39] R. R. Nair, P. Blake, A. N. Grigorenko, K. S. Novoselov, T. J. Booth, T. Stauber, N. M. R. Peres, and A. K. Geim. Fine structure constant defines visual transparency of graphene. *Science*, 320(5881):1308–1308, 2008.

[40] A. B. Kuzmenko, E. van Heumen, F. Carbone, and D. van der Marel. Universal optical conductance of graphite. *Phys. Rev. Lett.*, 100:117401, Mar 2008.

[41] P. Blake, E. W. Hill, A. H. Castro Neto, K. S. Novoselov, D. Jiang, R. Yang, T. J. Booth, and A. K. Geim. Making graphene visible. *Applied Physics Letters*, 91(6), 2007.

[42] G.E. Jellison. Optical functions of silicon determined by two-channel polarization modulation ellipsometry. *Optical Materials*, 1(1):41 – 47, 1992.

[43] L. Gao, F. Lemarchand, and M. Lequime. Refractive index determination of $SiO_2$ layer in the UV/Vis/NIR range: spectrophotometric reverse engineering on single and bi-layer designs. *Journal of the European Optical Society - Rapid publications*, 8(0), 2013.

[44] Linus Pauling. *The nature of the chemical bond.* Cornell University Press, Ithaca, $3^{rd}$ edition, 1960.

[45] Antonín Vašíček. *Optics of thin films.* North-Holland publishing company, Amsterdam, $1^{st}$ edition, 1960.

[46] Y. Taur. CMOS design near the limit of scaling. *IBM Journal of Research and Development*, 46(2.3):213–222, March 2002.

[47] Denis Mamaluy and Xujiao Gao. The fundamental downscaling limit of field effect transistors. *Applied Physics Letters*, 106(19), 2015.

[48] Qing Hua Wang, Kourosh Kalantar-Zadeh, Andras Kis, Jonathan N. Coleman, and Michael S. Strano. Electronics and optoelectronics of two-dimensional transition metal dichalcogenides. *Nat Nano*, 7(11):699–712, Nov 2012.

[49] Manish Chhowalla, Hyeon Suk Shin, Goki Eda, Lain-Jong Li, Kian Ping Loh, and Hua Zhang. The chemistry of two-dimensional layered transition metal dichalcogenide nanosheets. *Nat Chem*, 5(4):263–275, Apr 2013.

[50] Yuka Tsuboi, Feijiu Wang, Daichi Kozawa, Kazuma Funahashi, Shinichiro Mouri, Yuhei Miyauchi, Taishi Takenobu, and Kazunari Matsuda. Enhanced photovoltaic performances of graphene/Si solar cells by insertion of a $MoS_2$ thin film. *Nanoscale*, 7:14476–14482, 2015.

[51] L. Britnell, R. M. Ribeiro, A. Eckmann, R. Jalil, B. D. Belle, A. Mishchenko, Y.-J. Kim, R. V. Gorbachev, T. Georgiou, S. V. Morozov, A. N. Grigorenko, A. K. Geim, C. Casiraghi, A. H. Castro Neto, and K. S. Novoselov. Strong light-matter interactions in heterostructures of atomically thin films. *Science*, 340(6138):1311–1314, 2013.

[52] F. Withers, O. Del Pozo-Zamudio, S. Schwarz, S. Dufferwiel, P. M. Walker, T. Godde, A. P. Rooney, A. Gholinia, C. R. Woods, P. Blake, S. J. Haigh, K. Watanabe, T. Taniguchi, I. L. Aleiner, A. K. Geim, V. I. Falko, A. I. Tartakovskii, and K. S. Novoselov. $WSe_2$ light-emitting

tunneling transistors with enhanced brightness at room temperature. *Nano Letters*, 15(12):8223–8228, 2015.

[53] Kin Fai Mak, Changgu Lee, James Hone, Jie Shan, and Tony F. Heinz. Atomically thin $MoS_2$: A new direct-gap semiconductor. *Phys. Rev. Lett.*, 105:136805, Sep 2010.

[54] Ozgur Burak Aslan, Daniel A. Chenet, Arend M. van der Zande, James C. Hone, and Tony F. Heinz. Linearly polarized excitons in single- and few-layer $ReS_2$ crystals. *ACS Photonics*, 3(1):96–101, 2016.

[55] Y. J. Zhang, T. Oka, R. Suzuki, J. T. Ye, and Y. Iwasa. Electrically switchable chiral light-emitting transistor. *Science*, 344(6185):725–728, 2014.

[56] Rajesh Kappera, Damien Voiry, Sibel Ebru Yalcin, Brittany Branch, Gautam Gupta, Aditya D. Mohite, and Manish Chhowalla. Phase-engineered low-resistance contacts for ultrathin $MoS_2$ transistors. *Nat Mater*, 13(12):1128–1134, Dec 2014. Article.

[57] Adriano Ambrosi, Zdenek Sofer, and Martin Pumera. 2H→1T phase transition and hydrogen evolution activity of $MoS_2$, $MoSe_2$, $WS_2$ and $WSe_2$ strongly depends on the mx2 composition. *Chem. Commun.*, 51:8450–8453, 2015.

[58] L. Liu, S. B. Kumar, Y. Ouyang, and J. Guo. Performance limits of monolayer transition metal dichalcogenide transistors. *IEEE Transactions on Electron Devices*, 58(9):3042–3047, 2011.

[59] Filip A. Rasmussen and Kristian S. Thygesen. Computational 2D materials database: Electronic structure of transition-metal dichalcogenides and oxides. *The Journal of Physical Chemistry C*, 119(23):13169–13183, 2015.

[60] Chia-Hui Lee, Eduardo Cruz Silva, Lazaro Calderin, Minh An T. Nguyen, Matthew J. Hollander, Brian Bersch, Thomas E. Mallouk, and Joshua A. Robinson. Tungsten ditelluride: a layered semimetal. *Scientific Reports*, 5:10013, Jun 2015. Article.

[61] Sefaattin Tongay, Hasan Sahin, Changhyun Ko, Alex Luce, Wen Fan, Kai Liu, Jian Zhou, Ying-Sheng Huang, Ching-Hwa Ho, Jinyuan Yan, D. Frank Ogletree, Shaul Aloni, Jie Ji, Shushen Li, Jingbo Li, F. M. Peeters, and Junqiao Wu. Monolayer behaviour in bulk $ReS_2$ due to electronic and vibrational decoupling. *Nature Communications*, 5:3252, Feb 2014. Article.

[62] D.L. Greenaway and R. Nitsche. Preparation and optical properties of group IV-VI chalcogenides having the $CdI_2$ structure. *Journal of Physics and Chemistry of Solids*, 26(9):1445 – 1458, 1965.

[63] Fengnian Xia, Han Wang, Di Xiao, Madan Dubey, and Ashwin Ramasubramaniam. Two-dimensional material nanophotonics. *Nat Photon*, 8(12):899–907, Dec 2014.

[64] Kin Fai Mak and Jie Shan. Photonics and optoelectronics of 2D semiconductor transition metal dichalcogenides. *Nat Photon*, 10(4):216–226, Apr 2016.

[65] Andres Castellanos-Gomez, Michele Buscema, Rianda Molenaar, Vibhor Singh, Laurens Janssen, Herre S J van der Zant, and Gary A Steele. Deterministic transfer of two-dimensional materials by all-dry viscoelastic stamping. *2D Materials*, 1(1):011002, 2014.

[66] Ashwin Ramasubramaniam. Large excitonic effects in monolayers of molybdenum and tungsten dichalcogenides. *Phys. Rev. B*, 86:115409, Sep 2012.

[67] Timothy C. Berkelbach, Mark S. Hybertsen, and David R. Reichman. Theory of neutral and

charged excitons in monolayer transition metal dichalcogenides. *Phys. Rev. B*, 88:045318, Jul 2013.

[68] Alexey Chernikov, Timothy C. Berkelbach, Heather M. Hill, Albert Rigosi, Yilei Li, Ozgur Burak Aslan, David R. Reichman, Mark S. Hybertsen, and Tony F. Heinz. Exciton binding energy and nonhydrogenic rydberg series in monolayer $ws_2$. *Phys. Rev. Lett.*, 113:076802, Aug 2014.

[69] Keliang He, Nardeep Kumar, Liang Zhao, Zefang Wang, Kin Fai Mak, Hui Zhao, and Jie Shan. Tightly bound excitons in monolayer $wse_2$. *Phys. Rev. Lett.*, 113:026803, Jul 2014.

[70] Ziliang Ye, Ting Cao, Kevin O'Brien, Hanyu Zhu, Xiaobo Yin, Yuan Wang, Steven G. Louie, and Xiang Zhang. Probing excitonic dark states in single-layer tungsten disulphide. *Nature*, 513(7517):214–218, Sep 2014. Letter.

[71] Philipp Tonndorf, Robert Schmidt, Robert Schneider, Johannes Kern, Michele Buscema, Gary A. Steele, Andres Castellanos-Gomez, Herre S. J. van der Zant, Steffen Michaelis de Vasconcellos, and Rudolf Bratschitsch. Single-photon emission from localized excitons in an atomically thin semiconductor. *Optica*, 2(4):347–352, Apr 2015.

[72] Yu-Ming He, ClarkGenevieve, SchaibleyJohn R., Yu He, ChenMing-Cheng, WeiYu-Jia, DingXing, Qiang Zhang, Wang Yao, Xiaodong Xu, Chao-Yang Lu, and Jian-Wei Pan. Single quantum emitters in monolayer semiconductors. *Nat Nano*, 10(6):497–502, Jun 2015. Letter.

[73] Chitraleema Chakraborty, Laura Kinnischtzke, Kenneth M. Goodfellow, Ryan Beams, and A. Nick Vamivakas. Voltage-controlled quantum light from an atomically thin semiconductor. *Nat Nano*, 10(6):507–511, Jun 2015. Letter.

[74] Ajit Srivastava, Meinrad Sidler, Adrien V. Allain, Dominik S. Lembke, Andras Kis, and A. Imamoğlu. Optically active quantum dots in monolayer $WSe_2$. *Nat Nano*, 10(6):491–496, Jun 2015. Letter.

[75] E. Cappelluti, R. Roldán, J. A. Silva-Guillén, P. Ordejón, and F. Guinea. Tight-binding model and direct-gap/indirect-gap transition in single-layer and multilayer $MoS_2$. *Phys. Rev. B*, 88:075409, Aug 2013.

[76] R B Murray, R A Bromley, and A D Yoffe. The band structures of some transition metal dichalcogenides. II. Group IVA: octahedral coordination. *Journal of Physics C: Solid State Physics*, 5(7):746, 1972.

[77] John P. Perdew, Kieron Burke, and Matthias Ernzerhof. Generalized gradient approximation made simple. *Phys. Rev. Lett.*, 77:3865–3868, Oct 1996.

[78] Paolo Giannozzi, Stefano Baroni, Nicola Bonini, Matteo Calandra, Roberto Car, Carlo Cavazzoni, Davide Ceresoli, Guido L Chiarotti, Matteo Cococcioni, Ismaila Dabo, Andrea Dal Corso, Stefano de Gironcoli, Stefano Fabris, Guido Fratesi, Ralph Gebauer, Uwe Gerstmann, Christos Gougoussis, Anton Kokalj, Michele Lazzeri, Layla Martin-Samos, Nicola Marzari, Francesco Mauri, Riccardo Mazzarello, Stefano Paolini, Alfredo Pasquarello, Lorenzo Paulatto, Carlo Sbraccia, Sandro Scandolo, Gabriele Sclauzero, Ari P Seitsonen, Alexander Smogunov, Paolo Umari, and Renata M Wentzcovitch. QUANTUM ESPRESSO: a modular and open-source software project for quantum simulations of materials. *Journal of Physics: Condensed Matter*, 21(39):395502, 2009.

# 3

# EXPERIMENTAL METHODS AND CHARACTERISATION

**NOTE:** The ideas and data presented in this chapter have been the subject of the following publication: Adolfo De Sanctis, Gareth F. Jones, Nicola J. Townsend, Monica F. Craciun and Saverio Russo. *An integrated and multi-purpose microscope for the characterization of atomically thin optoelectronic devices.* Review of Scientific Instruments 88, 055102 (2017).

Though theoretical studies of graphene and other 2D materials appeared more than 30 years ago, it was only in 2004 that the first graphene transistor was demonstrated experimentally. This is because it is difficult to identify, isolate and characterise a one-atom thick material. In section 2.2.2 it was shown how the optical contrast of monolayer graphene (MLG) can be enhanced. Atomic force microscopy (AFM) can be used to measure the thickness of a single layer of graphene and other 2D materials, however the main characterisation techniques used to study such materials are based on light-matter interaction, with Raman spectroscopy being the most used.

In this chapter the fundamentals of the characterization techniques used throughout this work are presented. The Raman effect is discussed in section 3.1, together with the Raman spectrum of graphene (section 3.2), highlighting its importance in the study of this novel material. Other spectroscopic techniques include photoluminescence (PL) and absorption, which are presented in sections 3.1.3 and 3.3 respectively. Both these techniques give important information on the properties of transition metal dichalcogenides (TMDs). Optoelectronic devices, such as photodetectors, are studied

in section 3.4, with focus on scanning photocurrent microscopy (SPCM) as the main characterization technique used in this work. Finally, the experimental apparatus used to perform these measurements is described in detail in section 3.5, this instrument was purposefully built during this work and represents a novel system explicitly dedicated to the characterization of optoelectronic devices based on graphene and 2D materials.

## 3.1 RAMAN SPECTROSCOPY

Raman spectroscopy is a technique based on Raman effect, discovered by Sir Chandrasekhra Venkata Raman, who first observed it in liquids[1;2] in 1928. This effect involves the scattering of a photon by an excitation in the examined material[3]. A photon impinging on a specimen will excite the transition of an electron from the highest occupied molecular orbital (HOMO), or valence band in crystalline solids, into an empty state, which could be a virtual state within the bandgap or a real state above the lowest unoccupied molecular orbital (LUMO) or conduction band. The excited electron-hole pair then undergoes inelastic scattering with an elemental vibration (phonon) of the material with energy $\hbar\Omega_k$, where $k$ designates a particular vibrational band. Therefore the scattered light will have a frequency shift given by $\Delta\omega = \omega_i \pm \Omega_k$, where $\hbar\omega_i$ is the excitation energy and the minus (plus) sign corresponds to the absorption (Stokes) or emission (anti-Stokes) of a phonon, respectively. In the case in which the final excited state is a real state, the effect is referred to as resonant Raman scattering (RRS).

### 3.1.1 *Classical theory of Raman scattering*

A classical approach to Raman scattering can explain the relationship between Raman effect and the dynamical properties of the system. This can also be used to explain qualitatively, and partially quantitatively, the Raman effect due to the vibrational modes of a molecule. In order to describe how rotational modes affect the inelastic scattering of light, specific discrete rotational frequencies have to be ascribed to a molecule. This can be done in the framework of a quantum theory, which will be briefly treated in section 3.1.2.

In solid crystals, where the rotational modes are absent, the theory of vibrations of a spatially fixed molecule can be easily applied (as they can be regarded as macromolecules infinitely extended). Therefore, a molecule in which the atoms, or ions, are

free to vibrate, but the rotational and translational degrees of freedom are frozen, can be used as a starting point. Such molecule, placed in an electric field **E** will be subject to an induced dipole, even in the absence a permanent one and the relationship between electric field and induced dipole moment $\hat{\mu}$ (to the first order) is given by:

$$\hat{\mu} = \hat{\alpha}\mathbf{E}, \tag{3.1}$$

where $\hat{\alpha}$ is the polarizability tensor in the chosen reference system, represented by an ellipsoid. If the Cartesian axes coincide with the principal axes of the ellipsoid, $\hat{\alpha}$ is represented by a diagonal matrix:

$$\mu_i = \alpha_{ii} E_i, \;\; i = x, y, z. \tag{3.2}$$

The vibrational modes of the atoms can be represented in terms of the normal modes of the system, which are related to the coordinates of the atoms, therefore the components of $\hat{\alpha}$ can be expanded in series:

$$\alpha_{ij} = (\alpha_{ij})_0 + \sum_k \left(\frac{\partial \alpha_{ij}}{\partial Q_k}\right)_0 Q_k + \frac{1}{2}\sum_{k,l}\left(\frac{\partial^2 \alpha_{ij}}{\partial Q_k \partial Q_l}\right)_0 Q_k Q_l + \ldots, \tag{3.3}$$

where the index 0 indicates that the derivatives are computed in the equilibrium configuration. Here, the vibration frequencies $\omega_k$, $\omega_l$, ... are associated to the normal coordinates $Q_k$, $Q_l$, and the incident radiation frequency is $\omega_0$. Considering the first order terms in $Q$ (harmonic approximation):

$$\hat{\alpha}_k = \hat{\alpha}_0 + \hat{\alpha}_k^{'} Q_k, \tag{3.4}$$

where the components of $\hat{\alpha}_k^{'}$ are given by:

$$\left(\alpha_{ij}^{\prime}\right)_k = \left(\frac{\partial \alpha_{ij}}{\partial Q_k}\right)_0. \tag{3.5}$$

In this approximation $Q_k = Q_{k_0}\cos(\omega_k t + \delta_k)$, where $\delta_k$ is a phase shift. Since the electric field of the electromagnetic (EM) radiation can be written as $\mathbf{E} = \mathbf{E}_0\cos(\omega_0 t)$, the induced dipole is given by:

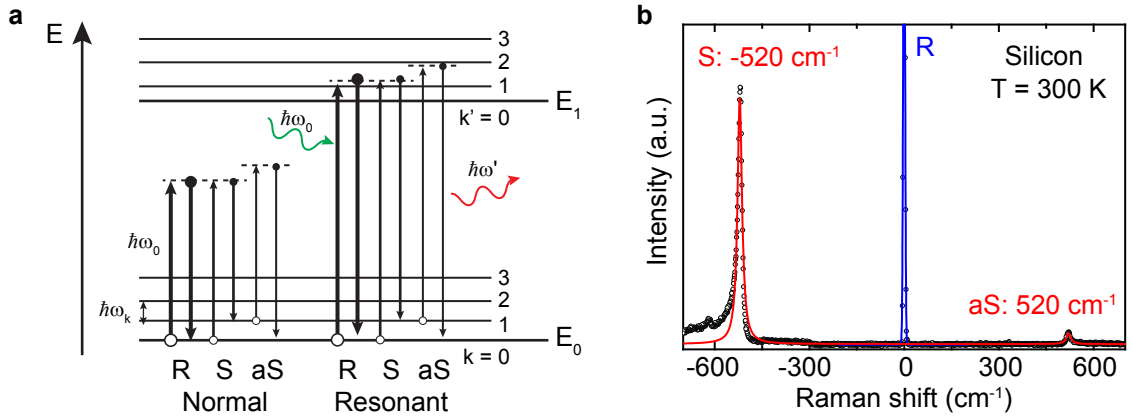


**Figure 3.1: Raman scattering.** **a**, Normal and resonant Raman processes in a simple diatomic molecule. The line thickness is proportional to the signal strength of the different transitions. R is the Rayleigh scattering and S and aS are the Stokes and anti-Stokes processes, respectively. Virtual states are shown by dashed lines. **b**, Sample Raman spectrum of crystalline Si at room temperature showing both Stokes and anti-Stokes bands at $\sim 520$ $\mathrm{cm}^{-1}$.

$$\begin{aligned}\hat{\mu} = \hat{\alpha}_0 \cdot \vec{E}_0 \cos(\omega_0 t) + \frac{1}{2} Q_{k_0} \hat{\alpha}'_k \cdot \vec{E}_0 \cos\{(\omega_0 + \omega_k)\, t + \delta_k\} \\ + \frac{1}{2} Q_{k_0} \hat{\alpha}'_k \cdot \vec{E}_0 \cos\{(\omega_0 - \omega_k)\, t - \delta_k\}\end{aligned} \tag{3.6}$$

Equation (3.6) shows that $\hat{\mu}$ consists of three oscillating terms which represent: (1) the elastic scattering of radiation with the same phase (Rayleigh scattering), (2) the inelastic scattering of radiation with an energy higher than the incident (Raman scattering in the anti-Stokes branch) and (3) the inelastic scattering of radiation with an energy lower than the incident (Stokes branch). It can be seen that, in order to have Rayleigh scattering $\hat{\alpha}_0 \neq 0$, which is always satisfied. For Raman scattering to occur, the $k^{\text{th}}$ vibrational mode at frequency $\omega_k$ is active only if $\hat{\alpha}'_k \neq 0$, which means that at least one of its components has to be non-zero ($(\partial \alpha_{ij}/\partial Q_k)_0 \neq 0$ at least for one $i, j$). This condition is not always satisfied and depends on the symmetry of the vibrational mode.

Figure 3.1a illustrates the Raman scattering in a simple diatomic model. In normal

Raman the exciting energy $\omega_0$ is usually chosen to be far below the first electronic excited state ($E_1$). Thus, the exciting energy leads to a transition to a virtual state. If the exciting energy is chosen so that it intercepts the manifold of an electronic excited state the Raman process is said to be resonant, this situation is referred to as RRS. The excitation of these transitions produces extremely strong enhancement of the bands, as observed in graphene[4] (this will be discussed in section 3.2). The lineshape of Raman peaks can be approximated very well using a Lorentzian profile:

$$I(x) = \frac{2A}{\pi} \frac{\Gamma}{4(x - x_0)^2 + \Gamma^2}, \tag{3.7}$$

where $A$ is the area under the curve, $\Gamma$ is the full-width at half-maximum (FWHM), that is the width of the peak at half its height and $x_0$ is the centre of the peak. The height of the peak can be expressed as $H = (2A)/(\pi\Gamma)$. This lineshape is the result of the interplay between the finite lifetime of the excited electrons and the dephasing (coherence time) induced by the inelastic scattering with the vibrational modes (phonons in solids). The classical theory predicts the same intensity for Stokes and anti-Stokes transitions. However, as shown in figure 3.1b for a crystalline Si, the Stokes (S) transitions are stronger than the anti-Stokes (aS) ones (under normal conditions, i.e. in thermal equilibrium). To explain such behaviour a quantum mechanical approach is therefore needed. Since both Stokes and anti-Stokes lines give the same information, it is customary to record only the Stokes side of the spectrum and label it with positive, instead of negative, wavenumbers.

### 3.1.2 *Quantum theory of Raman scattering*

A full treatment of the quantum theory of the Raman effect falls beyond the scope of this thesis. Such detail can be found, for example, in the wok of Ferraro *et. al.*[3], Long[5] and Lee[6]. In this section only the most important results, necessary for the understanding of the following chapters, are reviewed.

In a quantum mechanical framework, the Raman effect is treated by considering the transition of one electron from an initial to a final state which involves the interaction of a single-particle Hamiltonian with the EM field of the incident light. The molecular vibrations (phonons in crystal solids) play a role in the description of the interaction, when the scattering cross-section is calculated from the polarizability of the molecule,

akin to what discussed in the classical treatment. In general, the intensity of the Raman signal can be written as:

$$I_R \propto \sum_i \int \rho_G \left\| \hat{e_S} \cdot \mathbf{R_i} \cdot \hat{e_I}^{\mathrm{T}} \right\|^2 d\Omega_S, \tag{3.8}$$

where the integration is carried over the collection angle of the microscope objective $d\Omega_S$, $\rho_G$ is the population of the initial state, $\hat{e_I}$ and $\hat{e_S}$ are the incident and scattered photon vectors respectively, $c_1$ is a material dependent factor, T represents the transpose of a vector and $\mathbf{R_i}$ is the Raman tensor, which basis vectors are the crystallographic axes of the crystal (or molecule). Equation (3.8) is calculated using the Fermi's golden rule (FGR) applied to the described system, where the electronic and vibrational eigenfunctions of the system are separated (Born-Oppenheimer approximation) and the polarizability tensor becomes an Hermitian operator which depends only on the nuclear coordinates $\mathbf{R}$, treated as a parameter[6]. In the scattering processes described by this theory, the total energy and momentum of the system must be conserved, thus, the following must hold:

$$\begin{aligned} \hbar\omega_i &= \hbar\omega_s \pm \hbar\Omega, \\ \hbar\mathbf{k}_i &= \hbar\mathbf{k}_s \pm \hbar\mathbf{q}, \end{aligned} \tag{3.9}$$

where $\omega_i$ and $\mathbf{k}_i$ are the incident photon frequency and wavevector respectively, $\omega_s$ and $\mathbf{k}_s$ are the scattered photon frequency and wavevector respectively, $\Omega$ is the phonon frequency with wavevector $\mathbf{q}$, the sign "+" is for the creation of a phonon (Stokes) while the sign "−" is for the destruction of a phonon (anti-Stokes).

The difference in the intensity of the Stokes and anti-Stokes lines arises from the dependence of the Raman cross-section on the population of the initial state $\rho_G$. In thermodynamic equilibrium, the upper state will be less populated than the lower state. Therefore, the rate of transitions from the lower to the upper state (Stokes transitions) will be higher than in the opposite direction (anti-Stokes transitions). Correspondingly, Stokes scattering peaks are stronger than anti-Stokes scattering peaks (see figure 3.1b).

Equation (3.8) also shows that by changing the excitation and collection axes (directions) and the polarization of the light (that is $\hat{e_I}$ and $\hat{e_S}$) it is possible to determine the crystallographic orientation of the material and identify the different vibrational

modes[7].

The intensity of the Raman scattered light is dependent on the local temperature $T$ and the ratio between Stokes ($I_S$) and anti-Stokes ($I_{aS}$) intensities can be used as a temperature probe[8] using the following expression[9]:

$$\frac{I_S}{I_{aS}} = F \cdot C_{ex} \cdot \exp\left(\frac{h\omega_i}{k_B T}\right), \tag{3.10}$$

where $F$ is a parameter that depends on the optical constants of the material and $C_{ex}$ is a coefficient which accounts for the efficiencies of the optics and gratings at different wavelengths.

### 3.1.3 *Luminescence spectroscopy*

The radiative transition of electrons from an excited state to a lower level through the emission of light is known as luminescence[10]. Such transitions can be initiated by the absorption of a photon, known as PL fluorescence and phosphorescence, or by the application of an electric field through the material, known as electroluminescence (EL). In both cases, detailed measurement of the spectral intensity of the emitted light can give insight into the properties of the material and the performance of the examined device. In a typical PL experiment the excitation source is a laser, with a wavelength appropriate for exciting resonant electronic transitions. The emitted light from the material is then dispersed for spectral analysis. Usually a low-pass filter is used to reject the excitation wavelength. The detailed physical processes involved in PL are linked to the excitation and decay probabilities in the material[10]. The frequency-dependent intensity of a luminescence process can be written, in general, as:

$$I_L(h\nu) \propto \|M\|^2 \cdot g(\hbar\omega_0) \cdot \Gamma_e, \tag{3.11}$$

where $\|M\|^2$ is the matrix element of the transition, $g(\hbar\omega_0)$ is the density of states (DOS) at the excitation energy $\hbar\omega_0$ and $\Gamma_e$ represents the occupancy factors for the transition, which are related to the probability of the upper (lower) levels to be empty (occupied).

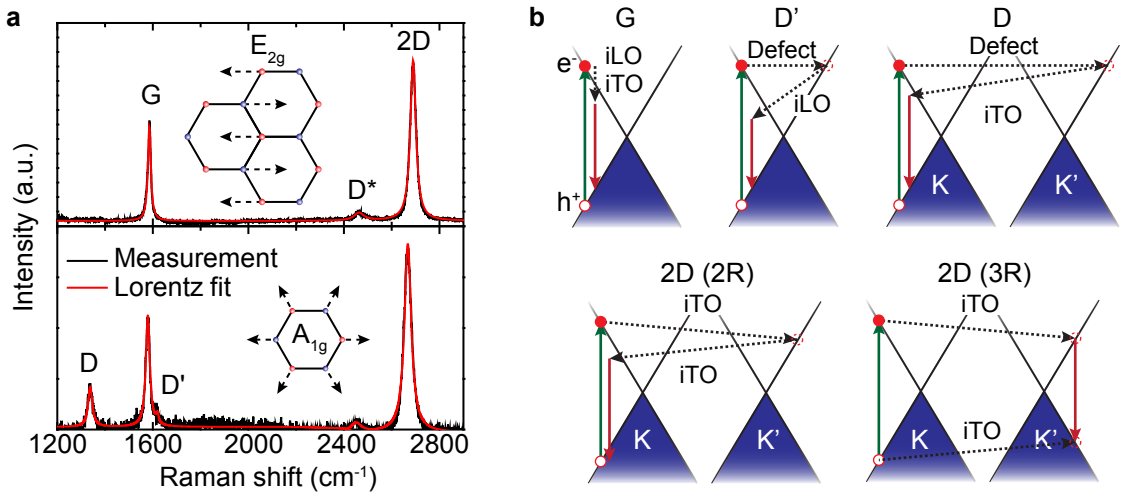


**Figure 3.2: Raman spectrum of graphene.** **a**, Sample spectra of pristine (top) and defective (bottom) MLG. Insets depict the Raman active modes. Red curve is a multi-Lorentzian fit to the experimental data (black). **b**, Raman processes in graphene: vertical arrows represent electronic transitions, dashed lines represents phonons or defects scattering events.

## 3.2 RAMAN SPECTRUM OF GRAPHENE

Raman spectroscopy has become the most powerful tool for the characterisation and understanding of the behaviour of phonons in graphene[4;11] and for the characterisation of defects[12;13], stacking order of layers[14] and doping[15;16]. The knowledge of the phonon dispersion bands in graphene is very important to understand its Raman spectrum and the information that can be extracted from its analysis.

The unit cell of graphene contains two atoms, therefore, there are six vibrational bands of which three are acoustic (A) and three optical (O). Two of them (one A and one O) represent vibrational modes perpendicular to the graphene plane (o), while the other four represent modes parallel to it (i). The propagation directions of vibrational modes are classified as transverse (T) or longitudinal (L) with respect to the directions which connects two carbon atoms in the unit cell. Hence, along the symmetry directions of the first Brillouin zone (FBZ) $\Gamma-$M and $\Gamma-$K, the six vibrational bands are named as iLO, iTO, ILA, iTA, oTA and oTO (see ref. 4). The Raman active modes are the iLO and iTO at both the $\Gamma$ and K points. These phonon branches originate from the

two fundamental vibrational modes of carbon, as shown in figure 3.2a: the $E_{2g}$ mode, which is the displacement of two carbon atoms in space, and the $A_{1g}$ mode, which is given by the breathing of an hexagonal ring. These modes are responsible for the observed peaks in the Raman spectrum of MLG, as shown in figure 3.2a, for a 514 nm laser excitation. The two most prominent peaks are the so-called G, at $\sim 1580$ cm$^{-1}$, and 2D, at $\sim 2670$ cm$^{-1}$. The G peak originates from the $E_{2g}$ mode at $\Gamma$, while the 2D peak originates from the $A_{1g}$ mode at K. In figure 3.2a, bottom panel, it is shown the Raman spectrum of defective graphene, i.e. acquired in the proximity of an edge. Two new peaks appear: the D peak, at $\sim 1330$ cm$^{-1}$, and the D', at $\sim 1620$ cm$^{-1}$, which originates from the $A_{1g}$ mode near $\Gamma$ and K, respectively, and require a defect to be active, as shown in figure 3.2b. In the same figure the origin of the other observed peaks is shown, in particular, the 2D peak is the result of a double (2R) and triple (3R) resonant process which involves two iTO phonons between the two non-equivalent K points. All the observed Raman modes in graphene are resonant, since the phonon wavevectors bring the electrons into real states.

Both the D and 2D peaks show a dispersive behaviour with respect to the excitation wavelength, where the position of the peaks shifts linearly with the energy of the incident light as $(\partial\omega_D\partial E_{exc}) \sim 50$ cm$^{-1}$eV$^{-1}$ for the D band and $(\partial\omega_{2D}/\partial E_{exc}) \sim 100$ cm$^{-1}$eV$^{-1}$ for the 2D band[4;17]. This dispersive behaviour is related to the fact that the process which originates the D and 2D bands is double-resonant (see figure 3.2b). In this case the wavevectors $\mathbf{q}$ of the iTO phonon, responsible for the D and 2D bands, would preferentially couple to the electronic states with wavevectors $\mathbf{k}$, such that $\mathbf{q} \simeq 2\mathbf{k}$. Therefore, as the incident photon energy is increased away from $E_F$, the wavevector $\mathbf{k}$ of the excited electronic states will move away from the K point, therefore also the wavevector $\mathbf{q}$ of the iTO phonon will increase, leading to the observed dispersive behaviour[18]. The position and FWHM of the G and 2D peaks also depend on the substrates on which the graphene is deposited[19] due to the strong interaction between the graphene layer(s) and the substrate, which has been proven to strongly affect both its optical and electrical properties.

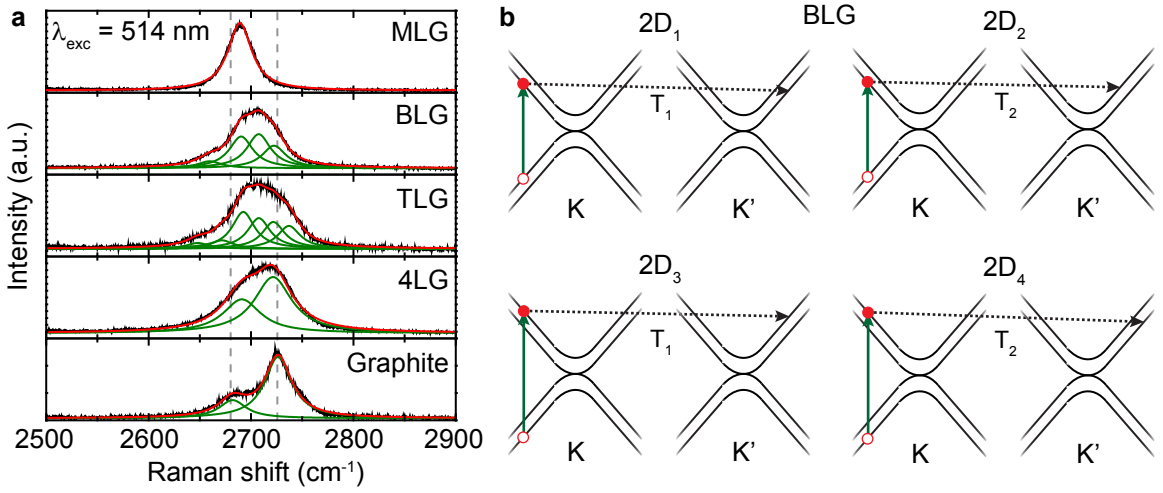


**Figure 3.3: Layer-dependent 2D band of graphene.** **a**, Sample spectra of graphene for different numbers of stacked layers, solid lines represent multi-Lorentzian fits to the experimental data. **b**, Raman processes in bilayer graphene (BLG) which originate the 2D band. $T_1$ and $T_2$ represent the active phonon modes.

### 3.2.1 *Layer-dependence of the 2D band*

The analysis of the 2D peak shape allows the quick identification of the thickness of a graphene flake, up to three layers. In figure 3.3a, the significant evolution of shape and intensity of the 2D peak as a function of the number of layers is shown. MLG is characterised by a single-Lorentzian 2D peak, whose intensity is higher than the G peak. In BLG the 2D peak has four Lorentzian components and a characteristic "square" shape with a small shoulder. In trilayer graphene (TLG) the 2D peak has six components and shows as well a characteristic square shape. Flakes with more than three layers are hardly distinguishable from bulk graphite which is characterised by a 2D peak with two components with intensities in a 1 : 3 ratio between them. The multi-Lorentzian shape of the 2D peak of BLG can be easily explained by considering all the double-resonant scattering processes (with different energies) between its four $\pi$ bands, as shown in figure 3.3b. A similar analysis gives 15 possible transitions in TLG but, since the energy of many of these transitions is too close to be resolved, only 6 can be fitted in the experimental spectrum[4]. Recently, it has been shown that the shear mode in few-layer graphene (FLG), that is, the relative motion of atoms

in adjacent planes responsible for the so-called "C" peak at $\sim 40$ cm$^{-1}$, can be used as a measurement of the interlayer coupling, and therefore to estimate the number of layers[20] in FLG.

## 3.3 ABSORPTION SPECTROSCOPY

The absorption coefficient, $\alpha(\lambda)$, is an important quantity for photoactive materials which can give important information for their use in optoelectronic devices. In particular, absorption spectroscopy can be used to determine the bandgap of a semiconductor and its nature, direct or indirect. In the specific case of 2D materials it has been shown, for example, that the bandgap of FLG can be tuned with an applied electric field[21] and in TMDs the bandgap energy changes with the number of layers and induced strain[22]. TMDs also show a transition of the bandgap from indirect to direct when they are thinned to single-layers[23]. This large variety of physical phenomena makes absorption spectroscopy an important tool for studying novel, atomically-thin materials.

In this section, the theory and the equations that allow the absorption coefficient of a thin film on a thick substrate to be measured will be reviewed. For clarity of notation the wavelength dependence of the defined quantities will be omitted, unless necessary to avoid confusion.

### 3.3.1 *Absorption in thick samples*

Light impinging on a slab of material of thickness $d$, immersed in a transparent medium of refractive index $n_0$, with intensity $I_0$, is partially reflected at the first surface and partially transmitted in the material. This is then partially reflected at the second surface and partially transmitted outside, as shown in figure 3.4a. Considering the complex refractive index $\mathbf{n_1} = n + i\kappa$, where $n$ is the real part (commonly known simply as refractive index) and $\kappa$ is the so-called extinction coefficient, the reflectivity can be written as[10]:

$$R = \frac{I_0}{I_R} = \left| \frac{\mathbf{n_1} - n_0}{\mathbf{n_1} - n_0} \right|^2, \tag{3.12}$$

where $I_R$ is the intensity of the reflected light. In the geometry shown in see figure 3.4a and assuming that $d \gg l_c$, where $l_c$ is the spatial coherence length of light (no inter-

ference effects), it is possible to write the intensity of transmitted light after the $n^th$ pass as:

$$I_n = I_1 \left(R_1 R_2 \exp(-2\alpha d)\right)^n , \tag{3.13}$$

where $I_1 = I_0(1-R_1)(1-R_2)\exp(-\alpha d)$ is the transmitted light after the first pass, $R_1$ and $R_2$ are the reflectivities of the two surfaces (assumed different), respectively, and $\alpha$ is the absorption coefficient, defined as the fraction of power absorbed per unit length into the material, such that the intensity at a distance $x$ in the material is given by the well-known Beer-Lambert law: $I(x) = I_0 \exp(-\alpha x)$. Therefore the total transmitted intensity is given by:

$$I_T = \sum_{n=1}^{\infty} I_n = \frac{I_0(1-R_1)(1-R_2)\exp(-\alpha d)}{1 - R_1 R_2 \exp(-2\alpha d)}, \tag{3.14}$$

since the term $(R_1 R_2 \exp(-2\alpha d)) < 1$ in equation (3.13). Therefore the transmittance $T$, defined as the ratio of the transmitted power to the incident one, is given by:

$$T = \frac{I_T}{I_0} = \frac{(1-R_1)(1-R_2)\exp(-\alpha\delta)}{1 - R_1 R_2 \exp(-2\alpha\delta)}. \tag{3.15}$$

Solving equation (3.15) for $\alpha$ allows the absorption coefficient to be computed from the measurement of the transmittance and reflectance of the material:

$$\alpha = -\frac{1}{d} \ln\left(\frac{L + \sqrt{L^2 + 4TM}}{M^2}\right), \tag{3.16}$$

where $L = (R_1 - 1)(R_2 - 1)$ and $M = TR_1R_2$. The absorption coefficient is directly related to the extinction coefficient by[10]:

$$\alpha = \frac{4\pi\kappa}{\lambda}, \tag{3.17}$$

where $\lambda$ is the free-space wavelength of the incident light.

### 3.3.2 *Absorption in thin films*

For a thin film deposited on a thick substrate, as with graphene or TMDs, it is possible to perform the same derivation as for the thick-film case. Since the measurements

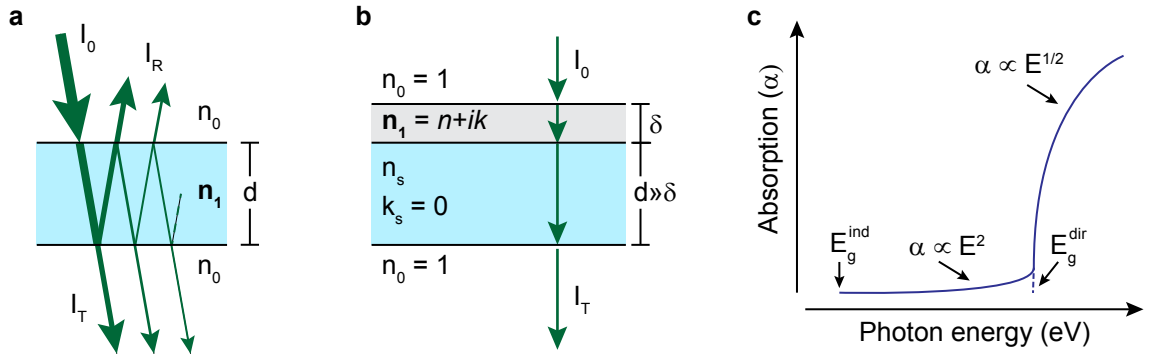


**Figure 3.4: Absorption in thin films and semiconductors.** **a**, Model of the transmittance through a thick sample with parallel sides considering multiple reflections. **b**, Transmittance trough a thin film on a thick transparent substrate. **c**, Schematic of a generic absorption coefficient ($\alpha$) measurement in an indirect-gap semiconductor.

presented in this thesis are performed using incoherent light sources, the effects of interference will be ignored. Such effects will introduce a wavelength-modulation of the absorption coefficient, similar to the fringes observed in a diffraction experiment, and a full derivation can be found in the work of Swanepoel[24]. With reference to figure 3.4b, assuming a film of thickness $\delta$ and complex refractive index $\mathbf{n_1}$ deposited on a thick, transparent, substrate of refractive index $n_s$ ($k_s = 0$), it is possible to derive a similar formula as in equation (3.16):

$$\alpha = -\frac{1}{\delta}\ln\left(\frac{P + \sqrt{P^2 + 2QT\left(1 - R_2R_3\right)}}{Q}\right), \tag{3.18}$$

where:

$$Q = 2T(R_1R_2 + R_1R_3 - 2R_1R_2R_3), \tag{3.19a}$$

$$P = (R_1 - 1)(R_2 - 1)(R_3 - 1), \tag{3.19b}$$

$$R_1 = \left|\frac{n_0 - \mathbf{n_1}}{n_0 + \mathbf{n_1}}\right|^2, R_2 = \left[\frac{\mathbf{n_1} - n_s}{\mathbf{n_1} + n_s}\right]^2, R_3 = \left[\frac{n_s - n_0}{n_s + n_0}\right]^2. \tag{3.19c}$$

In this case $R_1$ is the reflectance of the air/medium interface, $R_2$ is the reflectance of the substrate/medium interface and $R_3$ the reflectance of the substrate/air interface.

As for the previous case, each reflection coefficient $R_i$ can be either measured directly or computed from the knowledge of $\mathbf{n_1}$ and $n_s$.

### 3.3.3 *Absorption edge and bandgap determination*

Within the non-interacting single particle theory, absorption is related to the optical transitions of electrons from occupied to empty states. The absorption coefficient is zero for photon energies below the bandgap (in absence of mid-gap trap states), it increases sharply for energies close to the bandgap (band edge) and, in general, stays relatively constant, with the appearance of peaks related to resonant transitions, as shown in figure 3.4c. The band edge has a specific shape[10;25] (neglecting excitonic effects):

$$\alpha \propto (E_{ph} - E_g \pm \hbar\Omega)^m \quad \text{(indirect)}, \tag{3.20a}$$

$$\alpha \propto (E_{ph} - E_g)^{1/2} \qquad \text{(direct)}, \tag{3.20b}$$

where $E_{ph}$ is the incident photon energy, $E_g$ is the bandgap energy (direct or indirect), $\hbar\Omega$ is the associated phonon energy and $m$ is equal to 2 for allowed and 3 for forbidden indirect transitions. A typical spectral absorbance curve for an indirect bandgap semiconductor is shown in figure 3.4c, where the two band edges are highlighted. The presence of excitons, particle-hole pairs bound by coulomb interaction in the proximity of the band edges of the semiconductor, generally results in the appearance of peaks at the band edge in the absorption spectra. These peaks will be shifted to lower energies by the binding energy of the exciton $E_{\text{ex}}$.

## 3.4 LIGHT DETECTION IN ATOMICALLY-THIN OPTOELECTRONIC DEVICES

Optoelectronic devices work by converting an electric signal into light or *vice-versa* and divide into two main categories: light emitting devices (LEDs) and photodetectors (PDs). This work is primarily focused on the second category.

The basic experiment for the characterisation of a photodetector (PD) consists of shining light onto the device and recording its electrical response, such as measuring the current flow through it, the voltage drop across a load resistor or a change in

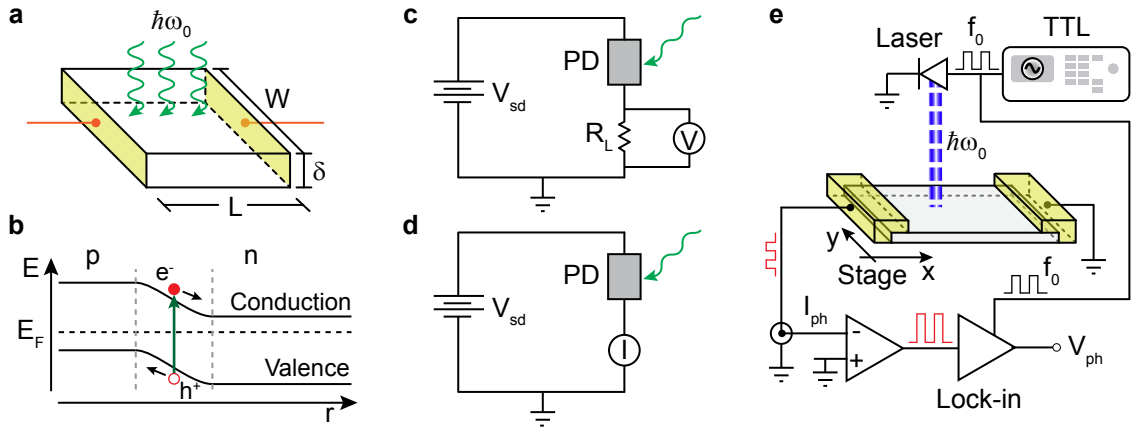


**Figure 3.5: Photodetectors principles and characterisation.** **a**, Model of a simple photoconductive device. **b**, Band diagram of a generic $p-n$ junction device. **c**, Circuit diagram of the operation of a photodetector in photovoltage configuration. **d**, Same as **c** in photocurrent configuration. In both cases the bias voltage $V_{\mathrm{sd}}$ can be set to 0 (short-circuit configuration). **e**, SPCM mapping configuration using a modulated laser light and lock-in amplifier, the focusing optics is omitted.

resistance[26], as shown in figure 3.5c-d. Light can impinge on the whole surface of the device, known as flood illumination, or it can be delivered with a focused laser onto a specific area to allow for a spatially resolved photo-response. Both techniques give insight on the physical nature of the observed photoresponse and on the efficiency of the device.

In semiconducting TMDs the main photoactive mechanism is the photovoltaic (PV) (or photoconductive) effect, which is discussed in detail in sections 3.4.1 and 3.4.2. In graphene, there are several possible mechanisms responsible for the observed photocurrent[27], however the dominant one has been shown to be the photothermoelectric (PTE) effect, which is discussed in section 3.4.3.

### 3.4.1 *Photoconductive devices*

The most basic PD is a photoconductive device: light with energy $\hbar\omega_0 > E_g$, impinging on its surface is able to excite an electron in the conduction band, creating an electron-hole $(e-h)$ pair. This extra charge causes a change in the conductivity of the material. Considering a slab of material of length $L$, width $W$ and thickness $\delta$, as shown in

figure 3.5a, the total number of $e-h$ pairs created is $\eta_i P_{opt} WL/\hbar\omega_0$, where $P_{opt}$ is the incident optical power density (or irradiance) and $\eta_i$ is the internal quantum efficiency (IQE) (number of $e-h$ pairs created per *absorbed* photon, per unit area). Therefore, the average generation rate $r_g$ of carriers per unit volume is given by:

$$r_g = \frac{\eta_i P_{opt} WL}{\hbar\omega_0 WL\delta} = \frac{\eta_i P_{opt}}{\hbar\omega_0 \delta}, \tag{3.21}$$

The recombination rate of the excess carriers is given by:

$$r_r = \frac{\Delta n}{\tau_c} = \frac{\Delta p}{\tau_c}, \tag{3.22}$$

where $\Delta n$ ($\Delta p$) is the excess electron (hole) population and $\tau_c$ is the minority carrier lifetime[26]. In equilibrium the two rates must be equal, therefore $\Delta n = \Delta p = r_g \tau_c$ and, by writing the conductivity as $\sigma = nq\mu_e + pq\mu_h$, where $\mu_e$ ($\mu_h$) is the electron (hole) mobility, it is possible to write the change in conductivity under illumination as:

$$\Delta\sigma = \Delta n q\mu_e + \Delta p q\mu_h = r_g \tau_c q \left(\mu_e + \mu_h\right). \tag{3.23}$$

A voltage $V_{sd}$, applied between the contacts, produces a photo-induced current (photocurrent) which is equal to:

$$I_{ph} = \frac{W\delta}{L}\Delta\sigma V_{sd} = \frac{\eta_i P_{opt}}{\hbar\omega_0}\frac{W}{L}\tau_c q \left(\mu_e + \mu_h\right) V_{sd}. \tag{3.24}$$

The IQE is related to the absorption coefficient $\alpha$, defined in section 3.3.1, by:

$$\eta_e = \left(1 - R - e^{-\alpha\delta}\right)\eta_i, \tag{3.25}$$

where $R$ is the reflectivity of the material and $\eta_e = (I_p h/q)/\phi_{in}$ is the external quantum efficiency (EQE), where $\phi_{in}$ is the incident photon flux. It is important to note that from equation (3.24), the observed photocurrent has a linear dependence with respect to the incident optical power: $I_{ph} \propto P_{opt}^{\alpha}$ with $\alpha = 1$.

Another important quantity used in the characterisation of PDs is the responsivity $\mathfrak{R} = I_{ph} S/P_{opt}$, defined as the ratio between the measured photocurrent (photovoltage) and the incident optical power and measured in units of A/W (V/W). Noise in photodetectors plays an important role in real-life applications, the main figure of merit

**Table 3.1:** Summary of parameters used to characterise PDs. Coupling Factors and wavelength dependence of all quantities are omitted for clarity of notation.

| Quantity | Symbol | Definition[a] | Units |
|---|---|---|---|
| External Quantum Efficiency | $\eta_e$, EQE | $(I_{ph}/q)/\phi_{in}$ | % |
| Internal Quantum Efficiency | $\eta_i$, IQE | $(I_{ph}/q)/\phi_{abs}$ | % |
| Responsivity | $\mathfrak{R}$ | $I_{ph}S/P_{opt}$ | A/W (V/W) |
| Noise Equivalent Power | NEP | $S_n/\mathfrak{R}$ | $\mathrm{W}/\sqrt{\mathrm{Hz}}$ |
| Specific Detectivity | $D^\star$ | $(S \cdot \Delta f)^{0.5}/\mathrm{NEP}$ | $\mathrm{cm}\sqrt{\mathrm{Hz}}/\mathrm{W}$ |

[a] $I_{ph}$ = Measured photocurrent, $\phi_{in}$ = Incident photon flux, $\phi_{abs}$ = Absorbed photon flux, $P_{opt} = \phi_{in}/S$ = Incident optical power density, $S$ = Device area, $\Delta f$ = Operating bandwidth, $S_n$ = Noise spectral density;

for the characterisation of noise is the noise-equivalent power (NEP), defined as the incident power necessary to produce a signal-to-noise ratio of 1 at 1 Hz bandwidth. It is given by the noise spectral density $S_n$ divided by the responsivity: $\mathrm{NEP} = S_n/\mathfrak{R}$ and measured in units of $\mathrm{W}/\sqrt{\mathrm{Hz}}$. The bandwidth $\Delta f$ of a PD is defined as the frequency at which its output power drops by 1/2, that is when the photocurrent drops by $\sim 70.7\%$ (known as $-3$ dB point). These quantities are used to define the main figure of merit in PDs performance, the specific detectivity $D^* = (S\Delta f)^{0.5}/\mathrm{NEP}$, where $S$ is the area of the device. $D^*$ is typically measured in *Jones* ($\mathrm{cm}\sqrt{\mathrm{Hz}}/\mathrm{W}$)[28]. Table 3.1 summarizes the main quantities used to characterise PDs.

### 3.4.2 *Junction devices*

Junction devices are usually made by two regions with different doping in a semiconductor material. Such $p-n$ junctions are responsible for the depletion of mobile charges in a region characterised by a strong electric filed. An $e-h$ pair generated by an incident photon will be, therefore, subject to the field and separated, as shown in figure 3.5b. The separated charges can be detected in two ways: by leaving the device in open-circuit and measuring the potential across a load resistor, known as PV mode (figure 3.5c) or by operating it in reverse bias (or short-circuit) and measuring the current flowing through the junction, known as photoconductive mode (figure 3.5d). In both cases the photocurrent generated in the device is given by equation (3.24)

and this is the measured photocurrent when the device is operated in photoconductive mode. In PV mode the current-voltage characteristic of a $p-n$ junction diode has to be taken into account[29]:

$$I = I_0 \left(e^{(qV)/(k_B T)} - 1\right), \tag{3.26}$$

where $I_0$ is the diode reverse-bias leakage current, $V$ is the voltage drop across the device, $k_B$ is the Boltzmann constant and $T$ the absolute temperature. Therefore the photocurrent is equal to:

$$I_{ph} = I_0 \left(e^{(qV)/(k_B T)} - 1\right) + \frac{V}{R} \rightarrow e^{(qV)/(k_B T)} \simeq \frac{I_{ph}}{I_0}, \tag{3.27}$$

assuming that $I_0 R \simeq V$, where $R$ is the resistance of the device. Therefore the measured voltage has a logarithmic dependence of the incident power:

$$V_{ph} = V_{sd} = \frac{k_B T}{q} \ln\left(\frac{I_{ph}}{I_0}\right) = \frac{k_B T}{q} \ln\left(\frac{\eta_i P_{opt}}{\hbar\omega_0} \frac{W}{L} \frac{V_{sd}}{I_0} \tau_c q \left(\mu_e + \mu_h\right)\right). \tag{3.28}$$

### 3.4.3 *Photothermoelectric (PTE) devices*

A junction between two materials with different Seebeck coefficients $S_1$ and $S_2$, in which the two sides are held at different temperatures, is subject to a voltage, known as thermoelectric voltage:

$$V_{\mathrm{PTE}} = (S_2 - S_1)\Delta T, \tag{3.29}$$

where $\Delta T = T_2 - T_1$ is the temperature difference between the two sides. The temperature difference can be induced by light, when the junction is illuminated, in fact, photogenerated carriers will have a temperature which depends on the microscopic dynamic of the specific material. The Seebeck coefficient can be expressed using the Mott relation[30;31]:

$$S = -\frac{\pi^2 k_B^2 T_h}{3q} \cdot \frac{1}{\sigma} \cdot \frac{\partial\sigma}{\partial\mu}, \tag{3.30}$$

where $T_h$ is the temperature of the hot carriers, $\sigma$ is the conductivity of the material and $\mu$ is the chemical potential. In general, the amount of energy taken by the hot carriers is given by:

$$C_h T_h \propto P_{\text{opt}}, \tag{3.31}$$

where $C_h$ is the heat capacity and $P_{\text{opt}}$ is the incident optical power. Assuming the hot carriers thermalise at a temperature far above that of the lattice, their specific heat is $C_h \propto T_h^2$ and, combining equations (3.29) and (3.30), the generated photocurrent is $I_{\text{PTE}} \propto T_h^2$. Therefore the proportionality between the generated photocurrent and the incident optical power results:

$$I_{\text{PTE}} \propto (P_{\text{opt}})^{\frac{2}{3}}. \tag{3.32}$$

This is the power exponent commonly measured in graphene photodetectors on $Si/SiO_2$ substrates.

### 3.4.4 *Local illumination and scanning photocurrent microscopy (SPCM)*

The study of spatially-resolved properties of semiconducting devices using localized excitation (injection) started in 1949 with the works of Haynes and Shockley[32] and Van Roosbroeck[33], while the use of localized illumination was first reported by Marek[34] in 1984. His work represents the birth of SPCM (also known as optical beam-induced current (OBIC)), a technique which uses a focused laser beam which is scanned across the device while the electrical response is recorded at each point, producing a two-dimensional map of its response[35], as shown in figure 3.5e. The spatial resolution is ultimately defined by the laser spot size which can be improved with the use of near-field techniques, such as scattering scanning near-field optical nanoscopy (s-SNOM)[27]. SPCM has been used, for example, to study the dynamics of hot carriers in graphene PDs[36], to demonstrate the role of defects in observed photocurrent signals[36] and to characterise the photoactive regions in TMDs junctions[37].

In order to describe how SPCM works, it is necessary to consider the mechanisms of generation, motion and collection of locally injected carriers. In a semiconductor it is possible to start from the charge continuity equation:

$$\frac{1}{q}\frac{\partial \rho}{\partial t} = G - R - \frac{1}{q}\boldsymbol{\nabla}\mathbf{j}, \tag{3.33}$$

where $\rho$ is the charge density, $G$ and $R$ are the carrier generation and recombination rates, respectively and $\mathbf{j}$ is the current density. It is possible to simplify the problem by choosing the excitation such that $G$ is a delta function in the point of injection, this is justified if the average carrier diffusion length is larger than the laser spot-size. The recombination rate can be written as:

$$R_i = -\frac{\Delta n_i}{\tau_i},\ i = e, h, \tag{3.34}$$

where $\tau_i$ is the carrier recombination lifetime and $\Delta n_i = n_i - n_i^{dark}$ is the excited carrier density, with $n_i$ total carrier density and $n_i^{dark}$ carrier density in the absence of illumination. In general, the carrier current density is comprised of a drift, a diffusion and a thermoelectric term (in the presence of a temperature gradient) in the form:

$$\mathbf{j} = qn_e\mu_e\mathbf{E} - qn_h\mu_h\mathbf{E} + qD_e\boldsymbol{\nabla}n_e - qD_h\boldsymbol{\nabla}n_h + \sigma S\boldsymbol{\nabla}T, \tag{3.35}$$

where $\mu_i$ is the mobility, $\mathbf{E}$ is the applied electric field, $\sigma = q(n_e\mu_e + n_h\mu_h)$ is the conductivity, $S$ is the Seebeck coefficient, $T$ the temperature and $D_i = (k_B T\mu_i)/q$ is the diffusion coefficient. If at least one of the contacts is Schottky-type, the photocurrent is dominated by on type of carrier[38] (since the drift and diffusion component of the majority carriers will cancel each other). It is therefore possible to recast equation (3.33), outside the illumination region, in terms, for example of holes:

$$\frac{\partial n_h}{\partial t} = -\frac{\Delta n_h}{\tau_h} - \frac{1}{q}\boldsymbol{\nabla}\cdot\mathbf{j_h}, \tag{3.36}$$

where $\mathbf{j_h} = -qn_h\mu_h\mathbf{E} - qD_h\boldsymbol{\nabla}n_h + \sigma S\boldsymbol{\nabla}T$ is the hole current density.

#### 3.4.4.1 *1D system*

From equations (3.35) and (3.36) it is possible to write the general continuity equation for a 1D system:

$$\frac{\partial n_h}{\partial t} = -\frac{\Delta n_h}{\tau_h} - n_h \mu_h \frac{\partial E}{\partial x} + q\mu_h E \frac{\partial n_h}{\partial x} + D_h \frac{\partial^2 n_h}{\partial x^2} - \\ + S\frac{\partial \sigma_h}{\partial x}\frac{\partial T}{\partial x} - \sigma_h S \frac{\partial^2 T}{\partial x^2} - \sigma_h \frac{\partial T}{\partial x}\frac{\partial S}{\partial x}, \tag{3.37}$$

where $\sigma_h = q n_h \mu_h$ is the hole conductivity. The simplest model which allows an analytical solution is given by considering no temperature gradient and no electric field applied (i.e. $\mathbf{E} = 0$ and $\boldsymbol{\nabla} T = 0$):

$$\frac{\partial n_h}{\partial t} = -\frac{\Delta n_h}{\tau_h} + D_h \frac{\partial^2 \Delta n_h}{\partial x^2}, \tag{3.38}$$

where $n_h$ can be substituted with $\Delta n_h$ since $n_h^{dark}$ is spatially uniform. Solving for the steady state $\partial n_h / \partial t = 0$:

$$D_h \frac{\partial^2 \Delta n_h}{\partial x^2} - \frac{\Delta n_h}{\tau_h} = 0 \rightarrow \Delta n_h = \Delta n_h^0 e^{\frac{x - x_0}{L_h}}, \tag{3.39}$$

where $x_0$ is the injection (illumination) point, $\Delta n_h^0$ is the excited hole density at $x = x_0$ and $L_h = \sqrt{D_h \tau_h}$ is the hole diffusion length. The current can be calculated considering the diffusion term, as:

$$j_h = -q D_h \frac{\partial \Delta n_h}{\partial x} = -q\sqrt{\frac{D_h}{\tau_h}} \Delta n_h^0 e^{\frac{x - x_0}{L_h}}. \tag{3.40}$$

Equation (3.40) shows that the observed photocurrent decays exponentially from the injection point with a decay constant equal to the carrier diffusion length. Knowledge of the carrier mobility allows the measurement of carrier lifetime using a SPCM measurement[38].

#### 3.4.4.2 *2D system*

In a 2D system it is possible to recast equation (3.38) using polar coordinates $(r, \theta)$ and assuming that the charge distribution is uniform in $\theta$:

$$\frac{\partial^2 \Delta n_h}{\partial r^2} + \frac{1}{r}\frac{\partial \Delta n_h}{\partial r} + \frac{\Delta n_h}{L_h} = 0, \tag{3.41}$$

where $r = \sqrt{x^2 + y^2}$. Equation (3.41) is in the form of the Emden-Fowler equation, which solution is given by[39]:

$$\Delta n_h(r,\theta) = \frac{\Delta n_h^0}{2\pi} K_0\left(\frac{r}{L_h}\right), \tag{3.42}$$

where $K_0$ is the modified Bessel function of the second kind. The current density can be therefore computed as:

$$j_h(r,\theta) = -qD_h\frac{\partial \Delta n_h}{\partial r} = -\frac{qD_h\Delta n_h^0}{2\pi L_h} K_1\left(\frac{r}{L_h}\right), \tag{3.43}$$

which, again, results in an exponential decay away from the excitation region with decay constant given by $L_h$.

## 3.5 SPCM AND SPECTROSCOPY EXPERIMENTAL APPARATUS

All the measurements presented so far require specific instrumentation in order to be performed. Commercially available instruments are traditionally employed, and they usually require the movement the samples from one instrument to the other, changing the environment and retrofitting to accommodate the different holders designed for each specific tool. These passages increase the chances of contamination and breakage of the samples. In order to solve such issues, I developed an experimental apparatus especially designed to characterise in one instrument optoelectronic devices based on graphene and other 2D materials.

Centred around an upright metallurgical microscope, the system allows one to perform multiple measurements in one instrument, with no need to remove the device from its holder, reducing the aforementioned risks. These measurements include: low frequency electrical transport, SPCM, absorption (transmittance and reflectance), micro-Raman and PL spectroscopy and mapping, with the possibility to analyse and change the polarization of light. A unique aspect of the developed design is the ability to concurrently perform both the electrical and optical measurements. The system is equipped with multiple laser sources, spanning from UV to red light and two white light sources used for transmission and reflection illumination. The laser light is delivered in enclosed paths and an interlock system is used to cut the laser light when access to individual parts is required, making the system extremely safe. High spatial

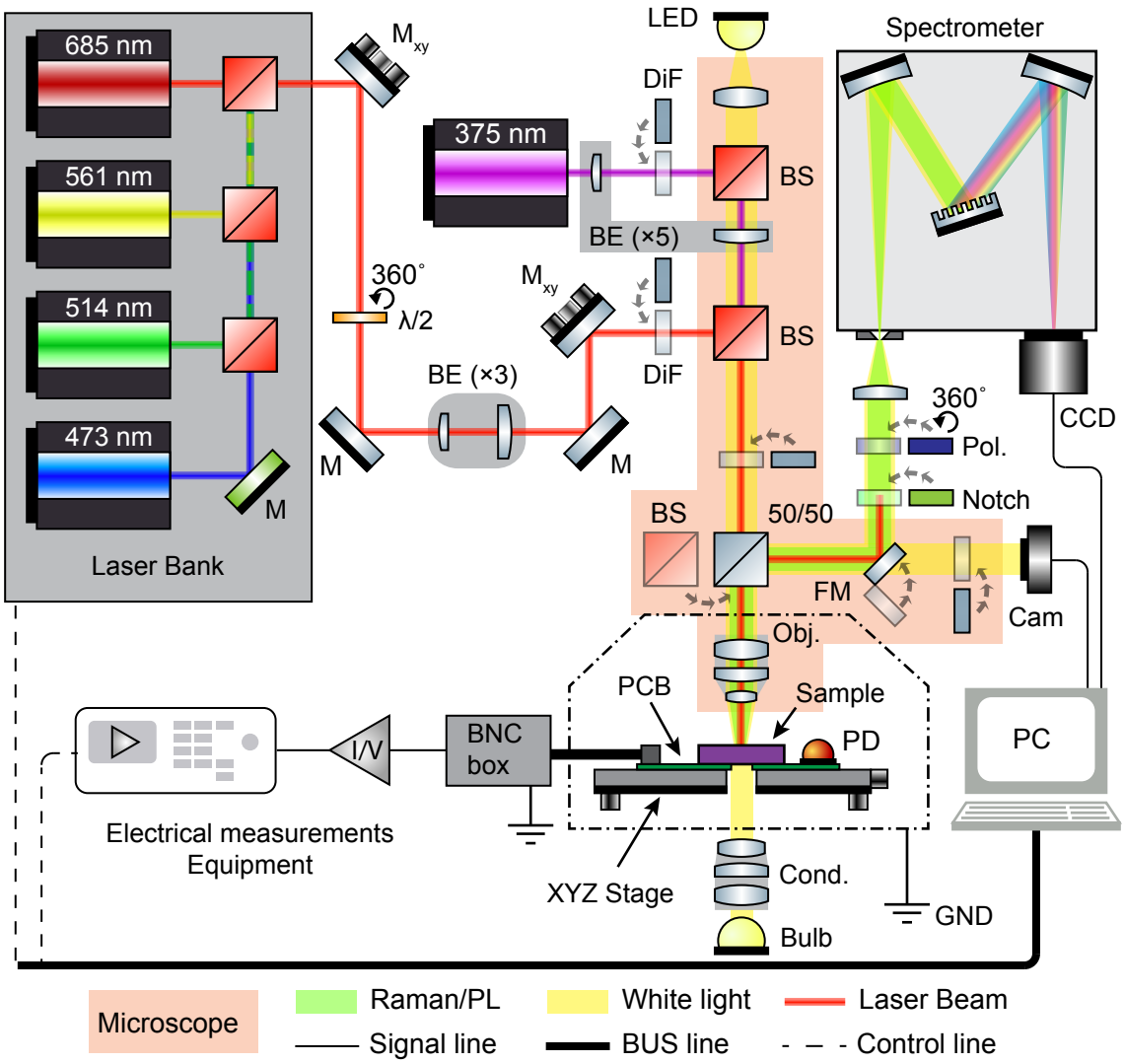


**Figure 3.6: Experimental setup diagram.** Laser light is used for scanning photocurrent mapping, Raman and PL spectroscopy. Four continuous-wave (CW) diode lasers are fitted in a laser enclosure while the ultra-violet (UV) laser source is directly attached to the microscope. White light from two different sources can be used for transmittance and reflectance measurements. An XYZ motorized microscope stage allows precise control of the sample position. The dash-dotted line represents the electrically screened light-tight enclosure of the sample stage. Signal lines carry electric/data signals to be measured, control lines carry the signals to configure the instruments, the lasers and the other sources, BUS line comprises USB and GPIB. Abbreviations: mirror (M), kinematic mirror ($M_{xy}$), half-wavelength plate ($\lambda/2$), beam expander (BE, followed by magnification), drop-in filter (DiF), beam splitter (BS, dichroic in red), Polariser/Analyser (Pol.), white light (WL), voltage (V) or current (I) sources/meters, flip mirror (FM), sample holder (PCB), photodetector (PD), condenser (Cond), microscope objective (Obj), imaging camera (Cam), spectroscopy camera (CCD), ground line (GND). Created with ComponentLibrary[40] symbols.

resolution in spectroscopy and SPCM measurements is achieved by diffraction-limited focusing of Gaussian laser beams and a high performance microscope stage. Electrical connections are secured by a custom-built printed-circuit board (PCB), designed to reduce electrical noise and allow easy access to the measured devices, without the need for long working distance microscope objectives.

### 3.5.1 *Instrumentation*

In this section the optical, mechanical and electrical part of the system are described, with particular attention to the solutions adopted in order to make the system multi-purpose and expandable, as well as safe and easy to use.

#### 3.5.1.1 *Optics*

Figure 3.6 shows a schematic diagram of the optical and electrical components of the system whilst a 3D model showing the actual implementation of the components is shown in figure 3.7. A set of visible wavelength CW laser diodes (*Coherent* 473LS, 514LX, 561LS and *Omicron* LuxX 685, with powers ranging from 30 to 50 mW) is fitted in an enclosure, which facilitates the alignment of each laser and can host up to 6 different wavelengths. Each laser is digitally modulated and the power is adjusted using an analog signal. Continuous modulation or TTL operation can be achieved by use of a digitally-controlled signal generator. Careful choice of dichroic mirrors inside the laser enclosure allows multiple wavelengths to be used at the same time. The laser light is then delivered with a series of kinematic and fixed mirrors into the illumination path of the optical microscope (*Olympus* BX51) after a $\times 3$ beam expansion. A dichroic beam-splitter (BS) is used to direct the light in the custom built Epi-illumination section of the microscope. A rotatable (360°) achromatic $\lambda/2$ waveplate (*ThorLabs* AHWP05M-600) is used to rotate the polarization of the laser light. A custom-built drop-in filter (DiF) system is used to introduce neutral-density (ND), polariser, notch and band-pass filters in the optical path of the lasers and the microscope: the same filter holders and housings are used throughout the system, ensuring full compatibility in each section. UV laser light (from a *Coherent* OBIS 375LX) is fed into the microscopy directly from the Epi-illumination BS cubes after a $\times 3$ beam expansion.

White light for reflection microscopy is provided by a white light emitting device

(LED) along the optical path of the laser beams, while transmittance illumination is achieved using the microscope's built-in lamp and condenser lens. Both the white and laser light are directed to the objective using either a 50%/50% BS or the appropriate dichroic band-pass (BP) mirror. The reflected light collected by the objective is directed to a charge-coupled device (CCD) imaging camera or, by using a flip mirror (FM), to the entrance slit of the spectrometer. The microscope is fitted with *Olympus* MPLanFL-N Semi-Apochromat infinity-corrected lenses with ×5, ×10, ×20 and ×50 magnification.

The spectroscopy section comprises an achromatic lens (*ThorLabs* AC254-150-A) with x/y and focus adjustment, a *Princeton Instruments* Acton SP2500 spectrometer equipped with three dispersion gratings (1200 g/mm with 500 nm and 750 nm blaze, and 1800 g/mm with 500 nm blaze) and a *Princeton Instruments* PIXIS400-eXcelon back-illuminated, peltier cooled, CCD camera. In this multi-purpose instrument, each grating is used for different measurements as they differ by number of grooves and blaze wavelength (which is the wavelength at which the efficiency is at maximum and the same for both S and P polarizations). In white light spectroscopy applications, corrections to account for the optics and gratings efficiencies, at different wavelengths, can be applied using *Princeton Instruments* "IntelliCal" system.

The microscope stage is a *Prior Scientific* OptiScan ES111 with ProScan III controller. The minimum step size is 10 nm. Focus control is also achieved trough the same controller.

The whole system is built on a vibration-isolated $120 \times 90\,\mathrm{cm}^2$ optical table. The laser light delivery system is enclosed within *ThorLabs* stackable tube lens system, allowing a light-tight connection. The microscope stage, foot and objective turret is covered with a light-tight enclosure, formed by a metal frame and a conductive fabric curtain connected to the ground of the electrical circuit to ensure shielding from electro-magnetic noise (see figure 3.7). The front of the curtain can be lifted to allow access to the stage and it is fitted with laser interlocks. The light-tight delivery system and enclosure, together with the magnetic interlocks, make the system a Class 1 laser product. The same light-tight tubes are used also to deliver light to the spectrometer, enabling the use of this instrument without the need of a darkened room.

The custom-built Epi-illumination system allows flexible and quick configuration of the microscope for different measurements. As shown in figure 3.8, the optical path can be configured for scattering, transmission/reflection spectroscopy and laser light

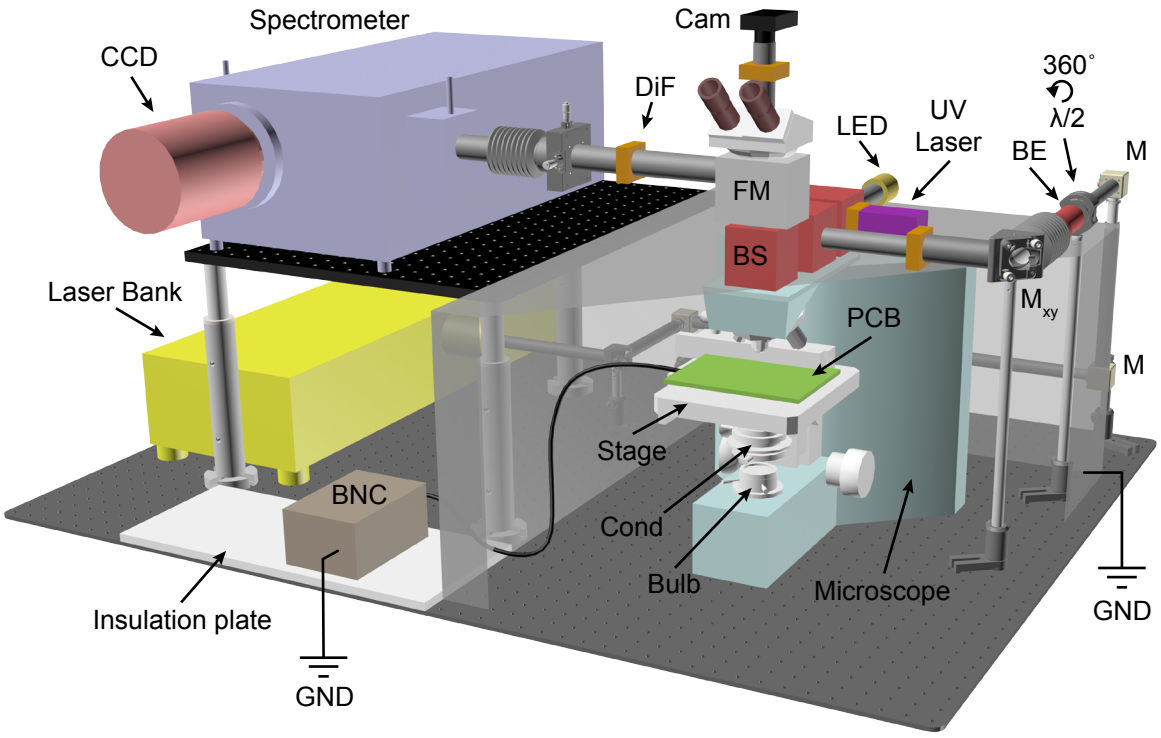


**Figure 3.7: Experimental setup 3D model.** The system is built on a vibration-isolated optical table ($120 \times 90$ cm$^2$). The electrically screened, light-tight, enclosure of the sample is shown in transparency and sectioned. Tube lenses are used to cover the light path of the laser beams, magnetic interlocks are located in the screen enclosure and in the BS cubes. Labels and abbreviations as in figure 3.6.

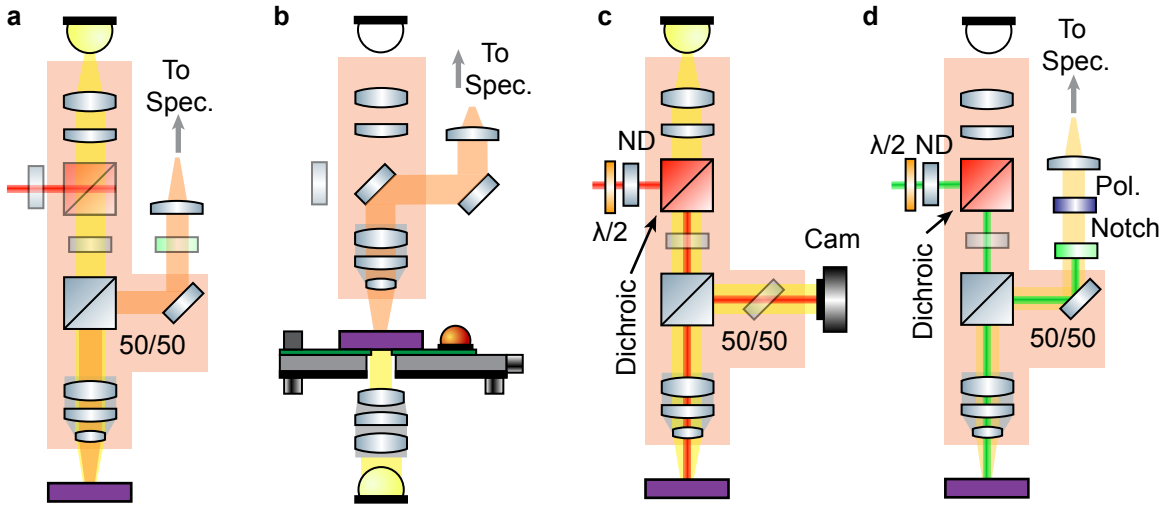


**Figure 3.8: Agile optical path configurations.** **a**, Reflectivity and **b**, Transmittance measurements using white light. **c**, SPCM mapping with laser light; **d**, Raman/Fluorescence/PL spectroscopy, including polarization. **c** and **d** can be combined and performed at the same time. UV laser delivery system is omitted. Symbols and abbreviations as in Figure 3.6.

illumination (as in SPCM) simply by replacing or removing the appropriate filters and BS. Each BS unit is fitted with magnetic interlocks for safety purposes. Figure 3.8a shows the configuration for reflectance measurements: light from the white LED travels freely (no laser BS fitted) after being collimated and reaches the objective though a 50%/50% BS; reflected light is collected by the same objective and partially transmitted by the BS to a FM which directs it into the spectrometer. A similar arrangement is used for transmittance spectroscopy, as shown in figure 3.8b. In this case the BS is replaced with a mirror and the white light from the incandescent bulb is collimated by the microscope condenser and, after travelling in the sample, collected by the objective and directed to the spectrometer. The configuration for laser-light illumination and SPCM is shown in figure 3.8c: in this case a dichroic BS is used to direct the laser light into the objective and the reflected light is partially transmitted to the imaging camera for direct assessment and focusing; the LED can be used at the same time for imaging. Figure 3.8d shows the configuration for Raman and PL spectroscopy: in this case the scattered light is collected by the objective and directed to the spectrometer via the

FM. Since the Raman signal is $\sim 10^6$ times smaller than the Rayleigh one, a very narrow notch filter, centred at the excitation wavelength, is typically used to reject the unwanted signal. ND and laser-line filters can be used to attenuate the beam power and clean it from spurious wavelengths. The latter two configurations can be used at the same time to perform Raman or PL mapping together with SPCM. Polarized Raman spectroscopy can be performed by interposing a polarizing filter (analyser) between the notch filter and the spectrometer, while the laser polarization is controlled by the $\lambda/2$ waveplate.

A PD is mounted on the stage, see figure 3.6, and used to automatically record the power of the laser light after a measurement, by programming the stage and the acquisition software accordingly. The ability to modulate the power of the lasers, both electrically and by introducing ND filters along the beam path, allows the system to span a power range (with the $\times 50$ objective) between $\sim 2$ nW and $\sim 20$ mW in steps of $0.4 \cdot 10^{-OD}$ mW, where $OD$ is the optical density.

#### 3.5.1.2 *Laser spot size*

Knowledge of the shape and size of the laser beams is paramount in the design of scientific optical systems. In this setup, solid-state diode lasers are used and all the optical components are chosen in order to minimize deviations from their $\mathrm{TEM}_{00}$ laser mode, which has a Gaussian intensity distribution:

$$I(r, r_b) = \sqrt{\frac{2}{\pi}} \frac{1}{r_b} e^{-\frac{r^2}{r_b^2}}, \tag{3.44}$$

where $r$ is the distance from the optical axis and $r_b$ is the radius of the beam, measured at the point at which the beam intensity falls by 50% (FWHM). As the beam is transmitted through a circular aperture of radius $r_a$, such as the pupil aperture of the objective lens, the transferred power is:

$$P_b = 1 - e^{-\frac{2r_a^2}{r_b^2}} = 1 - e^{-\frac{2}{T^2}}, \tag{3.45}$$

where $T = r_b/r_a$ is defined as the Gaussian beam truncation ratio. The focused beam profile is Gaussian for $T < 0.5$ and converges to the Airy pattern for $T \to \infty$. The focused spot size diameter ($d_s$) can be expressed as[41;42]:

$$d_s = \frac{K\lambda}{2\mathrm{NA}}, \tag{3.46}$$

where NA is the numerical aperture of the lens, $\lambda$ is the wavelength of the laser and $K$ is the $k$-factor for truncated Gaussian beams, which is a function of $T$ only. Urey[41] computed approximate expressions for $K$ for the two cases $T < 0.5$ (Gaussian) and $T > 0.4$ (Truncated Gaussian):

$$K(T) = \begin{cases} \frac{0.75}{T}, & T < 0.5 \\ 1.036 - \frac{0.058}{T} + \frac{0.156}{T^2}, & T > 0.4. \end{cases} \tag{3.47}$$

In the same work[41] an expression to determine the depth of focus, $\Delta z$ (i.e. the distance along the optical axis at which the irradiance drops by 50%), was determined:

$$\Delta z = K_2 \lambda f_{\#}^2, \tag{3.48}$$

where $f_{\#}$ is the ratio between the clear aperture diameter and the focal length of the lens (also called $f$-number) and $K_2$ is the focus $k$-factor, again a function of $T$ only[41]:

$$f_{\#} = \frac{1}{2\tan\left(\sin^{-1}\left(\frac{\mathrm{NA}}{n}\right)\right)}, \tag{3.49}$$

and

$$K_2(T) = \begin{cases} \frac{0.635}{T^2}, & T < 0.5 \\ 2.05 - \frac{0.12}{T} - \frac{0.28}{T^2} + \frac{0.22}{T^3}, & T > 0.4. \end{cases} \tag{3.50}$$

For the lenses used in this apparatus the computation gives: $T = 1.03$ for the UV laser and $T = 0.52$ for the visible lasers for all the objectives. The results obtained using equations (3.46) and (3.48) are shown in table 3.2. The calculated values show that the system is able to focus the laser light well in the diffraction-limit of the objective lens, allowing a high spatial resolution and that the very narrow depth of focus allows substrate contributions to be minimized.

#### 3.5.1.3 *Electronics*

Optoelectronic devices based on graphene and TMDs are usually fabricated from thin flakes deposited on a Si substrate capped with a $SiO_2$ layer, where electrical contacts

**Table 3.2:** Laser spot diameters $d_s$ and depth of focus $\Delta z$ of the lasers used in the experimental apparatus for different microscope objectives.

| | ×50 | | ×20 | | ×10 | |
|---|---|---|---|---|---|---|
| $\lambda$ (nm) | $d_s$ (nm) | $\Delta z$ (nm) | $d_s$ (nm) | $\Delta z$ (nm) | $d_s$ ($\mu$m) | $\Delta z$ ($\mu$m) |
| 375 | 264 | 158 | 469 | 420 | 0.7 | 0.7 |
| 473 | 445 | 268 | 792 | 710 | 1.1 | 1.1 |
| 514 | 484 | 291 | 861 | 770 | 1.3 | 1.2 |
| 561 | 528 | 320 | 940 | 840 | 1.4 | 1.3 |
| 685 | 645 | 390 | 1150 | 1025 | 1.7 | 1.6 |

are defined via lithography and metal evaporation. In order to allow versatile and easy electrical connections to such devices, a chip carrier has been purposefully designed. As shown in figure 3.9, the carrier is composed of a PCB board ($34 \times 29\,\mathrm{mm}^2$) with two standard 11-way pin strips, where 20 of these pins are connected to gold-coated pads and one to a central $15 \times 15\,\mathrm{mm}^2$ gold-coated pad (one pin is not connected). The central pad is used to contact, using silver-based conductive paint, the highly-doped silicon substrate which provides electrostatic gating. The other pads are used to connect the device's own pads to the PCB board using wire bonding. The design of the chip carrier differs from standard, commercially available, boards since the sample is not buried in a plastic or ceramic case, it is, instead, above the PCB and the soldering pads. In this way the objective lens cannot come into contact with parts of the chip carrier and long-working distance lenses are not required, thus improving the maximum achievable spatial resolution and minimum laser spot size. The chip carriers can also be fabricated with a central aperture, as shown in figure 3.9b, to allow the passage of light for transmission experiments with devices fabricated on transparent substrates.

Thanks to the use of standard single-in-line package (SIP) pins, the chip carrier is connected to a female socket on a second PCB board which is anchored on the microscope stage. This board is then connected through a shielded multi-core cable to a breakout BNC box, which enables connections with different measuring instruments, such as lock-in amplifiers, voltage/current amplifiers and multimeters, as shown in figures 3.6 and 3.7. In order to screen the devices from external electric fields, the light-tight enclosure surrounding the stage is made of conductive fabric and connected

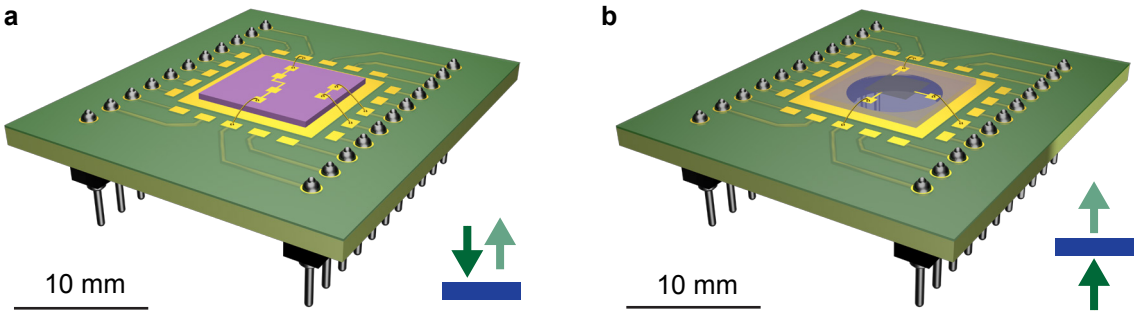


**Figure 3.9: Custom PCB chip-carrier boards.** **a**, Opaque substrates configuration where reflected and laser light is used. **b**, Transparent substrate configuration where transmitted light is used. Yellow areas are gold-coated pads.

to the ground of the circuit, together with the walls of the BNC box. All measuring instruments are decoupled from the rest of the electric instruments *via* insulating transformers, while signal and bus lines are kept isolated from the measuring PC *via* opto-electronic decouplers (*National Instruments* GPIB-120B).

Full automation of the system is achieved with a custom-made *National Instruments* LabView-based software which is able to communicate to all electronic instruments via GPIB/USB bus and modulate the lasers *via* digital-to-analog interface (DAC) (*National Instruments* NI-DAQ) while native software (*Princeton Instruments* LightField) is used to control the spectrometer and CCD camera, interfaced with the same LabView software.

### 3.5.2 *Performance of multi-purpose microscope system*

In this section a set of standard measurements are used to characterise the performance of the system. Such measurements include: SPCM on graphene-based photodetectors, absorption, Raman and PL spectroscopy of a range of 2D materials and organic semiconductors. These measurements prove the high functionality of the proposed design and demonstrate that the achieved resolution, both spatial and spectroscopic, and the overall performance, is equivalent to current commercial technologies, with the additional benefit of having a compact, multi-purpose, fully customizable, instrument with the potential for installation of additional features such as: vacuum chamber microscope stage with temperature control, multi-wavelength Raman spectroscopy, auto-

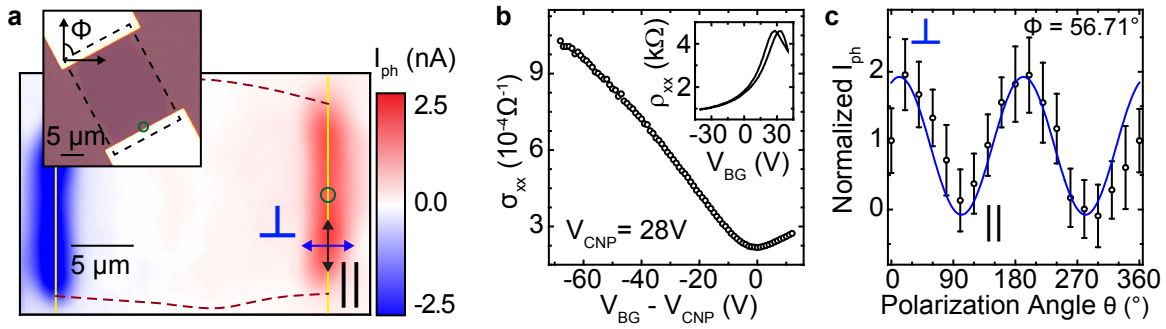


**Figure 3.10: Characterization of a graphene-based PD. a**, Optical micrograph of the single-layer graphene device in field effect transistor (FET) configuration (inset) and SPCM map at $\lambda_{\text{exc}} = 473$ nm; black-dashed box marks the mapped area, red-dashed lines mark the graphene flake boundary. **b**, Electrical characterisation of the graphene FET, acquired in the same setup, showing the conductivity as a function of back-gate voltage. **c**, Polarization dependence of the observed photocurrent $I_{ph}$ at the graphene-metal contact (green circle in panel **a**), maximum photocurrent is observed for light polarized $\perp$ to the metal contact. $\phi$ marks the angle between the vertical (y) axis of the microscope stage ($\theta = 0°$) and the graphene-metal interface, solid blue line is the expected curve.

focusing and high-frequency measurements.

#### 3.5.2.1 *Optoelectronic devices*

The ability of this instrument to perform measurements of optoelectronic devices is tested using a graphene-based photodetector[27;36;43;44]. The apparatus is setup as in figure 3.8c, where the white light (WL) source is used for imaging purposes and switched off during the measurements. The device is comprised of a single-layer exfoliated graphene flake, contacted in a two-terminal geometry with Cr/Au contacts, on a Si substrate capped with 295 nm $SiO_2$ gate oxide, as shown in figure 3.10a. The SPCM map is shown in figure 3.10a and it is acquired acquired with a 473 nm laser at 24 kW/cm$^2$ incident power in steps of 0.5 $\mu$m, under a source-drain bias $V_{SD} = 10$ mV and back-gate voltage $V_{BG} = 0$ V. The map shows strong photocurrent at the graphene/metal interface, in agreement with the expected behaviour[27;44]. The electronic response of the device is characterised directly on the microscope stage. Figure 3.10b shows the back-gate sweep (typical of a graphene FET) of the device under the same $V_{SD}$: from this it is possible to extrapolate the level of doping (holes in this case) $n \simeq 2.1 \cdot 10^{12}$ cm$^2$ and the field-effect hole mobility $\mu_h \simeq 650$ cm$^2$V$^{-1}$s$^{-1}$ using equations (2.35) and (2.37). All measurements are performed using a *DL* Model 1211 current amplifier, an *Ametek* 7270 DSP lock-in amplifier and a *Keithley* 2400 SourceMeter to provide both the source and gate bias.

The polarization capabilities of the apparatus are demonstrated by measuring the polarization dependence of the observed photocurrent in the graphene FET. The laser is focused at the graphene/metal interface and the $\lambda/2$ waveplate is used to change the polarization of the incident light, while recording the photocurrent. In this type of devices, hot-carriers dynamics in graphene, combined with the direct absorption of the metal contacts, lead to a polarization-dependent photocurrent[44], as will be discussed in greater detail in chapter 5. In figure 3.10c it is shown a plot of the photocurrent as a function of polarization angle $\theta$. Here, $I_{ph}$ is maximum when the polarization is orthogonal ($\perp$) to the metal contact and minimum when it is parallel ($\parallel$) to it, as expected[44]. The angle $\theta$ is defined as the angle between the polarization of the laser and the vertical (y) axis of the microscope stage. Since the device sits at an angle $\phi \simeq 57°$ with respect to y (see figure 3.10a), the polarization dependence should have

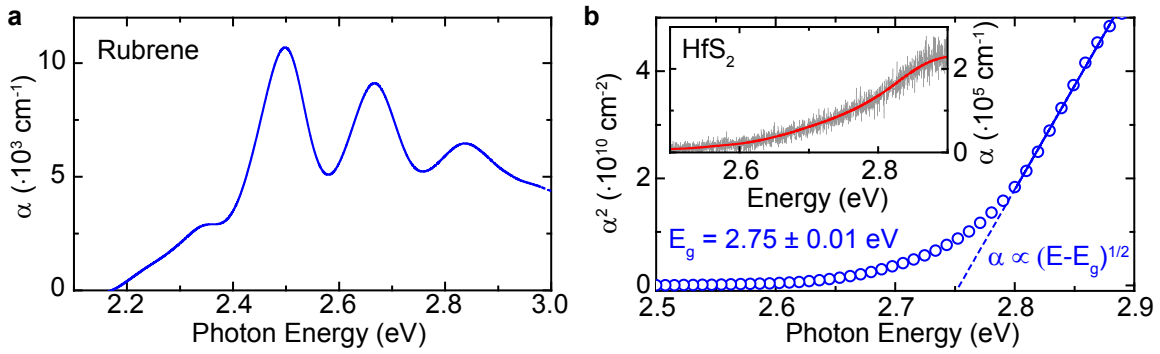


**Figure 3.11: Absorption spectroscopy characterisation.** **a**, Unpolarized absorption coefficient $\alpha$ of a Rubrene crystal, measured perpendicular to the ab facet; **b**, Absorption coefficient $\alpha$ of thin ($\sim 25$ nm) $HfS_2$ and direct-gap determination, $E_g = 2.75 \pm 0.01$ eV.

a "phase shift" of the same amount, i.e. $I_{ph} \propto \sin(2(\theta - \phi))$, as verified in figure 3.10c (solid blue line).

### 3.5.2.2 *Absorption spectroscopy*

In section 3.3 the absorption coefficient of a material was related to its transmittance and reflectance. To measure these quantities the optical configurations shown in figure 3.8a-b can be used.

Two examples of absorption coefficient measurements are shown, calculated using the results of section 3.3. The first example is a thin layer of organic crystalline semiconductor, Rubrene. The optical and electrical properties of this organic semiconductor have been intensively studied[45]. Therefore, it offers a good standard test the performance of the presented multi-purpose microscope system. Figure 3.11b shows the measured $\alpha(\lambda)$ of a Rubrene crystal on glass, using unpolarized light, perpendicular to the a-b facets and parallel to the c facet of the crystal (see ref. 45 for details). The measured spectrum is in very good agreement with literature, both in the intensity and position of the peaks. The second example is the absorption coefficient of ultra-thin $HfS_2$. This is a well known transition metal dichalcogenide (TMD) which was well characterised in the past as a bulk crystal[46] and recently as a thin flake on a substrate. Figure 3.11c, inset, shows the absorption coefficient of a $\sim 25$ nm thick flake of freshly-exfoliated $HfS_2$. The values agree well with literature[46;25]. Using equation (3.20b)

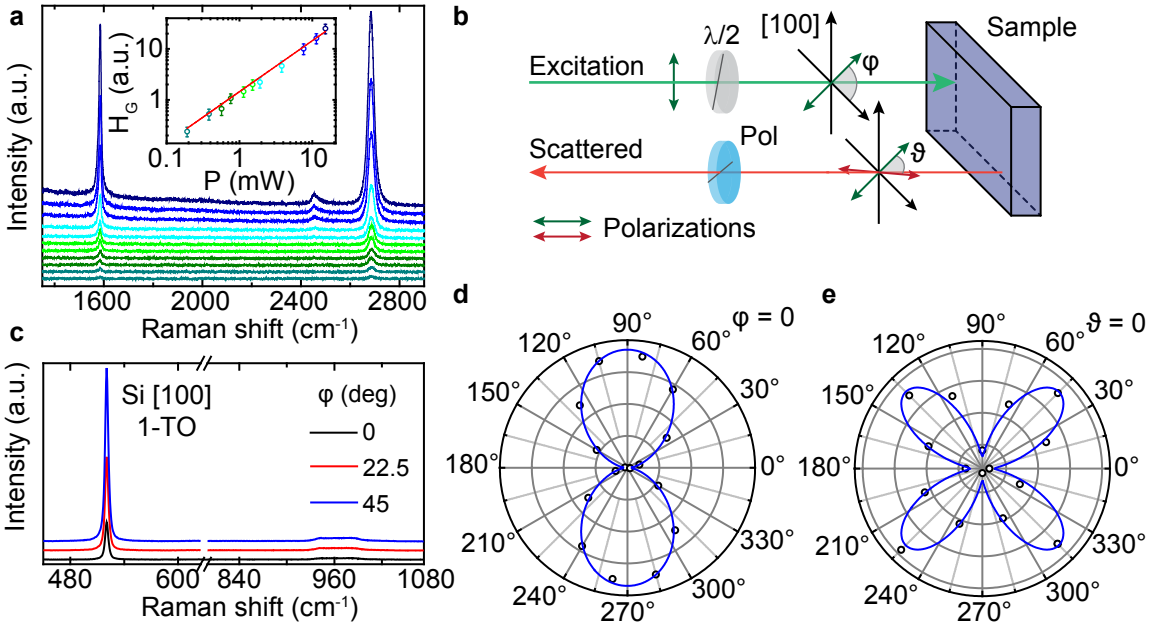


**Figure 3.12: Polarized Raman characterisation.** **a**, Raman spectrum of MLG as a function of incident optical power and power-dependence of the G-peak heigh (inset), solid line marks a slope of 1, curves shifted for clarity. **b**, Illustration of polarized Raman spectroscopy configuration for solid crystals. **c**, Raman spectra of Si showing the first-order (TO)-phonon mode at $\sim 520\,\mathrm{cm}^{-1}$ and two-phonon mode at $\sim 900-1000\,\mathrm{cm}^{-1}$. **d**, Polar plot of the height of the 1TO mode of Si as a function of $\vartheta$ ($\varphi = 0$) and **e**, Same plot as a function of $\varphi$ ($\vartheta = 0$). Solid lines are given by equation (3.53). All spectra are acquired with $\lambda_{\mathrm{exc}} = 514$ nm at 2.1 MW/cm$^2$ incident power and 2 s acquisition time.

the bandgap of the material can be extrapolated by plotting $\alpha^2$ as a function of $E$. The intercept of the extrapolated linear part mark the direct bandgap of the material $E_g = 2.75 \pm 0.01$ eV, in very good agreement with established values[46].

### 3.5.2.3 *Raman spectroscopy*

The inelastic light spectroscopy capabilities of the setup are characterised by studying two well-known materials: Si and graphene. In figure 3.1b the Raman spectrum of commercial-grade Si was presented. The spectrum was acquired with this setup using a $\lambda_{\mathrm{exc}} = 514$ nm laser at 1.0 MW/cm$^2$ incident power for 10 s. The first-order transverse-optical phonon (1TO) mode mode at $\sim 520\,\mathrm{cm}^{-1}$ is shown in both Stokes and anti-

Stokes regime in a single snapshot. The FWHM ($\Gamma$) of the Rayleigh line ($0\,\mathrm{cm}^{-1}$) is only $7\,\mathrm{cm}^{-1}$, and the Lorentzian fit of the Si modes gives $\Gamma = 17\,\mathrm{cm}^{-1}$. Using equation (3.10) for $T = 291$ K and $F = 0.97$ (see ref. 9 for details), the expected value of $I_S/I_{aS} = 11.92$; the experimental value extrapolated from figure 3.12a is $I_S/I_{aS} = 22 \pm 2$, giving an experimental correction factor $C_{ex} \simeq 1.84$.

As already discussed in section 3.2, the characterisation of graphene and other 2D materials relies strongly on Raman spectroscopy. The spectra presented in figures 3.2 and 3.3 were acquired with this setup. The ability of the system to resolve the multi-peak structures of the 2D band of graphene is clearly demonstrated in figure 3.3a. Furthermore, figure 3.12a shows the same spectrum of single-layer graphene acquired at different incident powers. The inset shows the height of the G peak as a function of incident power, adhering to the expected linear relationship. This serves to confirm that no artefacts are introduced in the spectra by the experimental apparatus. It is worth noting that it is possible to resolve clearly the G and 2D bands with an incident power density as low as 50 kW/cm$^2$ with an acquisition time of only 2 s for the whole spectral range, a performance already better than some commercial instruments.

Polarized Raman spectroscopy is another feature that can be accessed using the configuration shown in figure 3.8d. This technique has recently been applied to the investigation of graphene[47] and TMDs[48], where strong polarization dependence is given by valley anisotropy, highlighting the role of Raman spectroscopy in the study of electron-phonon coupling. As a benchmark test, the dependence of the Raman modes of Si upon incident polarization is measured. A diagram of the measurement is shown in figure 3.12b. Figure 3.12c shows the Raman spectrum of Si with the [100]-surface perpendicular to both the incident and the scattered light direction ($zxx\overline{z}$ and $zxy\overline{z}$ configurations). The spectra were acquired with $\lambda_{\mathrm{exc}} = 514$ nm at 2.1 MW/cm$^2$ incident power for 2 s. The 1TO mode at $520\,\mathrm{cm}^{-1}$ and a two-phonon mode at $\sim 900-1000\,\mathrm{cm}^{-1}$ are clearly visible. The Raman tensor of the 1TO mode in Si is[7]:

$$\mathbf{R} = \begin{pmatrix} 0 & c & 0 \\ c & 0 & 0 \\ 0 & 0 & 0 \end{pmatrix}, \tag{3.51}$$

where $c$ is a constant. The incident and scattered light polarizations, in the geometry of figure 3.12b, are:

$$\hat{e_I} = \begin{pmatrix} \cos(\vartheta - \varphi) \\ \sin(\vartheta - \varphi) \\ 0 \end{pmatrix}, \hat{e_S} = \begin{pmatrix} \cos(\varphi) \\ -\sin(\varphi) \\ 0 \end{pmatrix}. \tag{3.52}$$

Therefore, owing to equation (3.8), the Raman intensity of this mode is given by:

$$I_R(\vartheta, \varphi) = c^2 \sin^2(\vartheta - 2\varphi), \tag{3.53}$$

where $\vartheta$ is the polarization angle between the incident and scattered light and $\varphi$ is the angle between the incident polarization and the [100] axis. As this angle is varied, the 1TO peak is observed to decrease, while the two-phonon mode changes only slightly, as shown in figure 3.12c. Equation (3.53) is verified in figure 3.12d-e where the intensity of the 1TO mode is plotted as a function of $\vartheta$ and $\varphi$, respectively. The angle $\varphi$ is varied by rotating the polarization of the laser with a $\lambda/2$ waveplate, while the angle $\vartheta$ is defined by the angle of the analyser ("Pol" in figure 3.12b) with respect to the waveplate. In this way there is no need to rotate the sample, making it possible to have electrical connections to the devices. At the same time, this technique can be used to asses the orientation of the sample, since a measurement of the $\vartheta$ dependence will give a value of $\varphi \neq 0$ if the [100] axis is not aligned with the incident polarization angle.

#### 3.5.2.4 *Luminescence spectroscopy*

In this section the ability of the system to measure luminescence phenomena is demonstrated. Single-layer $WS_2$, a semiconducting TMD with good potential in optoelectronic applications[49;50] shows a strong PL spectrum, even at room temperature, as shown in figure 3.13a. This was acquired using the configuration shown in figure 3.8d, with $\lambda_{\text{exc}} = 514$ nm, $P = 5.1$ kW/cm$^2$ and 10 s acquisition time; the power is kept low to avoid causing damage to the sample. A strong peak is observed, centred at 2.02 eV and the Raman modes can be also observed in the same spectrum and expanded in figure 3.13b. Fit with Lorentzian curves of the Raman modes gives the following values: $2LA(M) = 353\,\text{cm}^{-1}$, $A_{1g}(\Gamma) = 420\,\text{cm}^{-1}$, $A_{1g}(M) + LA = 585\,\text{cm}^{-1}$ and $4LA(M) = 705\,\text{cm}^{-1}$. Both the PL and Raman spectra are in perfect agreement with the accepted values found in literature[51].

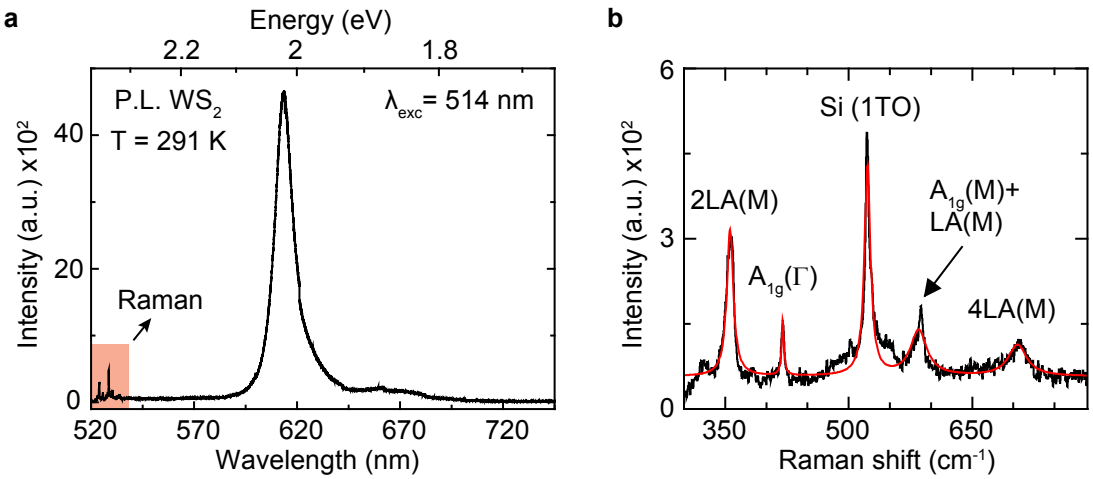


**Figure 3.13: PL spectroscopy characterisation.** **a**, Room temperature Photoluminescence of CVD-grown single-layer $WS_2$, $\lambda_{exc} = 514$ nm, $P = 5.1$ kW/cm$^2$, 10 s acquisition time. **b**, Zoom on the observed Raman modes.

### 3.5.3 *Final remarks and outlook*

I have presented the design of a new multi-purpose instrument for the characterization of optoelectronic devices based on 2D materials, including graphene. The instrument is capable of performing multiple electrical and optical measurements simultaneously with a performance at the level of the state-of-the-art commercial equipment. The ability to perform low-frequency electrical transport measurements, SPCM, Raman, absorption and PL spectroscopy, combined with full automation, high sensitivity and low noise, make this instrument ideal to face the challenges imposed by the advent of atomically-thin materials in optoelectronic devices.

Customization of each section allows multiple routes for future upgrades and expansion, these could include: a vacuum chamber microscope stage with temperature control, multi-wavelength Raman spectroscopy, auto-focusing and high-frequency (RF) measurements. The cost and size is very contained, making it suitable for small laboratories and the safety features introduced make it very easy to operate, with minimal training required.

All the data, involving optoelectronic measurements, presented in the rest of this work, except were explicitly stated, were acquired using this setup.

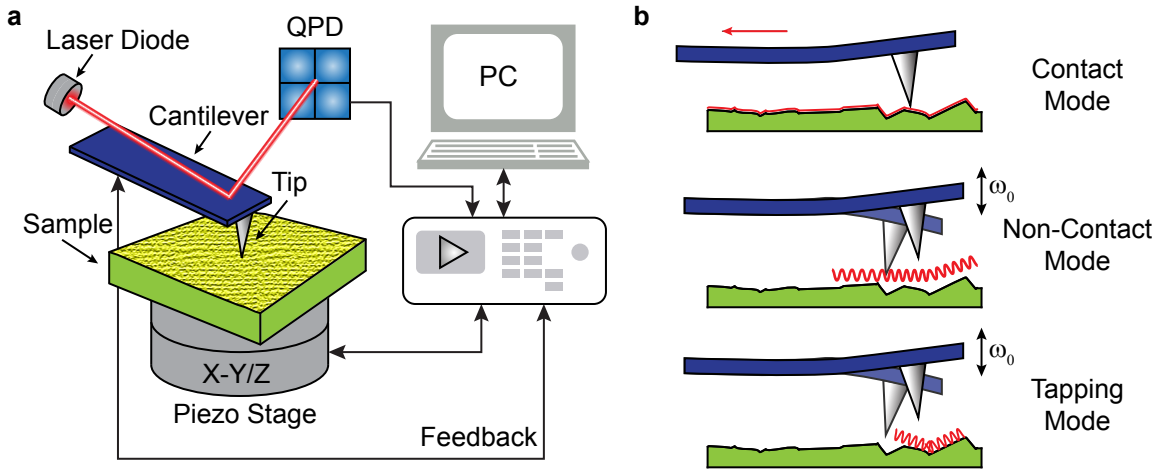


**Figure 3.14: AFM operating principle and modes.** **a**, Schematic illustration of an AFM setup. A quadrant photodetector (QPD) is used to measure the deviation of the cantilever due to the interaction between he tip and the sample. **b**, Common operation modes used in AFM topography. Red lines highlight the tip movements across the sample surface.

## 3.6 ATOMIC FORCE MICROSCOPY (AFM)

AFM is a technique which provides three-dimensional surface topography with nanometre resolution of a wide range of solid materials, including conductors, insulators or magnetic materials. AFM has been the first technique employed to establish if the graphene flakes were actually one atom thick. However, the thickness of a MLG on $SiO_2$ was first measured to be $0.8-1.2$ nm, instead of 0.4 nm as seen from X-ray diffraction and from AFM on bulk graphite[52]. The cause of this extra thickness is yet unclear, since the simple Van der Waals interaction between substrate and graphene cannot explain it. Even if AFM analysis is too slow to be employed as main identification and characterization technique for graphene and other 2D materials, the images obtained with this technique are the best way to inspect the morphological quality of small flakes.

### 3.6.1 *Experimental setup*

The basic principle of AFM operation is illustrate in figure 3.14a: a sharp tip is scanned on the sample surface, detecting the topography. Typical $Si_3N_4$ tips have a curvature

radius of $10 - 15$ nm and opening angle of about $20\,^{\circ}$. When the tip is brought very near to the surface to be analysed, the tip experiences attractive or repulsive forces, depending on the materials. The cantilever, on which the tip is located, is deflected accordingly and the tip movements are measured by mean of an optical lever. This consists of a laser beam focused on the cantilever, which reflection is projected into a quadrant photodetector (QPD). This kind of photodetector is able to register the position of a focused light spot by summing the signals from four PDs. While the sample is scanned, the tip-sample interaction is kept constant by a feedback loop usually involving a lock-in amplifier and a controlling PC.

AFM can be operated in different modes, that is the way the tip is driven across the surface and which kind of interaction is probed. The most common used in topography imaging are: contact mode, non-contact mode and "tapping" (or dynamic) mode. The first and foremost mode of operation, the contact mode, is very similar to a profiler: the tip-sample forces are maintained at a constant level and, with piezoelectric motion, the surface is scanned by the tip. In non-contact mode, the tip is driven at its resonant frequency $\omega_0$ and scanned across the surface without touching it. Using a feedback loop, the hight is kept constant. This mode belongs to a family of alternate-current (AC) modes, which refers to the use of an oscillating cantilever. In dynamic mode, the tip intermittently touches or taps the surface and the natural resonance frequency of the tip is shifted by the tip-sample force. This shift is proportional to the second derivative of the corresponding potential. This information is then converted in a topographical image of the surface. Furthermore, in this mode, the cantilever and the tip can be regarded as a (nearly) harmonic, damped oscillator, where the phase lag between tip motion and the driving force is characteristics of the viscoelastic properties of the surface, as well as adhesive forces due to different functional groups[53]. As an example, in reduced graphene oxide, phase images were shown to readily distinguish between reduced and oxidized flakes[54]. In AC modes, in order to filter out the thermal noise, a lock-in amplification is introduced and a more stable detection is allowed.

The forces acting between the tip and the surface are of different nature and depend on the tip-sample distance. The first interaction is the electrostatic force. It begins at $0.1 - 1$ nm and may be either attractive or repulsive depending on the material. At $10 - 100$ nm, surface tension effects result from the presence of condensed water vapour at the sample surface. The tip is pulled down toward the sample surface with attractive

force up to 200 pN. Van der Waals forces appear at the Å level above the surface: the atoms in the tip and sample undergo a weak attraction. Coming even closer, electron shells from atoms on both tip and sample repulse one another, preventing further intrusion by one material into the other (Coulomb forces, contact mode). Pressure exerted beyond this level leads to mechanical distortion and the tip or damage to the sample. The actual sharpness of a tip influences directly its ability to resolve surface features. Moreover, certain tip damages (e.g. double-pointed and cracked tips) occur very often. One obvious surface limitation is caused by deep grooves: the tip is not long enough, or thin enough, to reach the bottom of a recess. Furthermore, the tip cannot detect walls of the sample with an angle steeper than itself.

### 3.6.2 *This work*

The data shown in this work have been acquired with a *Bruker Innova* AFM system, operating in the dynamic mode to avoid damage to the sample while maintaining a high spatial resolution. The measurements were performed using a highly doped silicon tip from "Nanosensors" with a nominal resonance frequency of 330 kHz, and a sharp radius of curvature ($< 10$ nm).

# BIBLIOGRAPHY


[1] C. V. Raman. A new radiation. *Indian J. Phys.*, 2:387–398, 1928.

[2] C. V. Raman and K. S. Krishnan. A new type of secondary radiation. *Nature*, 121:501–502, 1928.

[3] J. R. Ferraro, K. Nakamoto, and C. W. Brown. *Introductory Raman Spectroscopy*. Elsevier, 2nd edition, 2003.

[4] L.M. Malard, M.A. Pimenta, G. Dresselhaus, and M.S. Dresselhaus. Raman spectroscopy in graphene. *Physics Reports*, 473(5-6):51 – 87, 2009.

[5] Derek A. Long. *The Raman Effect: A Unified Treatment of the Theory of Raman Scattering by Molecules*. John Wiley & Sons Ltd, 1st edition, 2002.

[6] Soo-Y. Lee. Placzek-type polarizability tensors for Raman and resonance Raman scattering. *The Journal of Chemical Physics*, 78(2):723–734, 1983.

[7] G. Kolb, Th. Salbert, and G. Abstreiter. Raman-microprobe study of stress and crystal orientation in laser-crystallised silicon. *Journal of Applied Physics*, 69(5):3387–3389, 1991.

[8] T. R. Hart, R. L. Aggarwal, and Benjamin Lax. Temperature dependence of Raman scattering in silicon. *Phys. Rev. B*, 1:638–642, Jan 1970.

[9] G. E. Jellison, D. H. Lowndes, and R. F. Wood. Importance of temperature-dependent optical properties for raman-temperature measurements for silicon. *Phys. Rev. B*, 28:3272–3276, Sep 1983.

[10] M. Fox. *Optical Properties of Solids*. Oxford University Press, 1st edition, 2010.

[11] Andrea C. Ferrari and Denis M. Basko. Raman spectroscopy as a versatile tool for studying the properties of graphene. *Nat Nano*, 8(4):235–246, Apr 2013.

[12] L. G. Cançado, A. Jorio, E. H. Martins Ferreira, F. Stavale, C. A. Achete, R. B. Capaz, M. V. O. Moutinho, A. Lombardo, T. S. Kulmala, and A. C. Ferrari. Quantifying defects in graphene via Raman spectroscopy at different excitation energies. *Nano Letters*, 11(8):3190–3196, 2011.

[13] Axel Eckmann, Alexandre Felten, Artem Mishchenko, Liam Britnell, Ralph Krupke, Kostya S. Novoselov, and Cinzia Casiraghi. Probing the nature of defects in graphene by Raman spectroscopy. *Nano Letters*, 12(8):3925–3930, 2012.

[14] Chun Hung Lui, Zhiqiang Li, Zheyuan Chen, Paul V. Klimov, Louis E. Brus, and Tony F. Heinz. Imaging stacking order in few-layer graphene. *Nano Letters*, 11(1):164–169, 2011.

[15] C. Casiraghi. Doping dependence of the Raman peaks intensity of graphene close to the Dirac point. *Phys. Rev. B*, 80:233407, Dec 2009.

[16] Chi-Fan Chen, Cheol-Hwan Park, Bryan W. Boudouris, Jason Horng, Baisong Geng, Caglar Girit, Alex Zettl, Michael F. Crommie, Rachel A. Segalman, Steven G. Louie, and Feng Wang. Controlling inelastic light scattering quantum pathways in graphene. *Nature*, 471(7340):617–620, Mar 2011.

[17] Istvan Pócsik, Martin Hundhausen, Margit Koós, and Lothar Ley. Origin of the D peak in the Raman spectrum of microcrystalline graphite. *Journal of Non-Crystalline Solids*, 227-230, Part 2:1083 – 1086, 1998.

[18] M. J. Matthews, M. A. Pimenta, G. Dresselhaus, M. S. Dresselhaus, and M. Endo. Origin of dispersive effects of the Raman D band in carbon materials. *Phys. Rev. B*, 59:R6585–R6588, Mar 1999.

[19] Ying ying Wang, Zhen hua Ni, Ting Yu, Ze Xiang Shen, Hao min Wang, Yi hong Wu, Wei Chen, and Andrew Thye Shen Wee. Raman studies of monolayer graphene: The substrate effect. *The Journal of Physical Chemistry C*, 112(29):10637–10640, 2008.

[20] P. H. Tan, W. P. Han, W. J. Zhao, Z. H. Wu, K. Chang, H. Wang, Y. F. Wang, N. Bonini, N. Marzari, N. Pugno, G. Savini, A. Lombardo, and A. C. Ferrari. The shear mode of multilayer graphene. *Nat Mater*, 11(4):294–300, Apr 2012.

[21] Tymofiy Khodkov, Ivan Khrapach, Monica Felicia Craciun, and Saverio Russo. Direct observation of a gate tunable band gap in electrical transport in ABC-Trilayer graphene. *Nano Letters*, 15(7):4429–4433, 2015.

[22] Rafael Roldan, Andres Castellanos-Gomez, Emmanuele Cappelluti, and Francisco Guinea. Strain engineering in semiconducting two-dimensional crystals. *Journal of Physics: Condensed Matter*, 27(31):313201, 2015.

[23] Qing Hua Wang, Kourosh Kalantar-Zadeh, Andras Kis, Jonathan N. Coleman, and Michael S. Strano. Electronics and optoelectronics of two-dimensional transition metal dichalcogenides. *Nat Nano*, 7(11):699–712, Nov 2012.

[24] R Swanepoel. Determination of the thickness and optical constants of amorphous silicon. *Journal of Physics E: Scientific Instruments*, 16(12):1214, 1983.

[25] K. Terashima and I. Imai. Indirect absorption edge of $ZrS_2$ and $HfS_2$. *Solid State Communications*, 63:315–318, July 1987.

[26] J. Wilson and J. F. B. Hawkes. *Optoelectronics: An introduction*. Prentice-Hall, 1st edition, 1942.

[27] F. H. L. Koppens, T. Mueller, Ph Avouris, A. C. Ferrari, M. S. Vitiello, and M. Polini. Photodetectors based on graphene, other two-dimensional materials and hybrid systems. *Nat Nano*, 9(10):780–793, Oct 2014.

[28] R. Clark Jones. Proposal of the detectivity D** for detectors limited by radiation noise. *J. Opt. Soc. Am.*, 50(11):1058–1059, Nov 1960.

[29] B. G. Streetman and S. K Banerjee. *Solid state electronic devices*. Pearson Prentice Hall, 6th edition, 2006.

[30] Melvin Cutler and N. F. Mott. Observation of anderson localization in an electron gas. *Phys. Rev.*, 181:1336–1340, 1969.

[31] E. H. Hwang, E. Rossi, and S. Das Sarma. Theory of thermopower in two-dimensional graphene. *Phys. Rev. B*, 80:235415, 2009.

[32] J. R. Haynes and W. Shockley. Investigation of hole injection in transistor action. *Phys. Rev.*, 75:691–691, Feb 1949.

[33] W. Van Roosbroeck. Injected current carrier transport in a semi-infinite semiconductor and

the determination of lifetimes and surface recombination velocities. *Journal of Applied Physics*, 26(4):380–391, 1955.

[34] J. Marek. Light-beam-induced current characterization of grain boundaries. *Journal of Applied Physics*, 55(2):318–326, 1984.

[35] R. Graham and D. Yu. Sanning photocurrent microscopy in semiconductor nanostructures. *Modern Physics Letters B*, 27(25):1330018, 2013.

[36] Achim Woessner, Pablo Alonso-Gonzalez, Mark B. Lundeberg, Yuanda Gao, Jose E. Barrios-Vargas, Gabriele Navickaite, Qiong Ma, Davide Janner, Kenji Watanabe, Aron W. Cummings, Takashi Taniguchi, Valerio Pruneri, Stephan Roche, Pablo Jarillo-Herrero, James Hone, Rainer Hillenbrand, and Frank H. L. Koppens. Near-field photocurrent nanoscopy on bare and encapsulated graphene. *Nat Commun*, 7, Feb 2016.

[37] Britton W. H. Baugher, Hugh O. H. Churchill, Yafang Yang, and Pablo Jarillo-Herrero. Optoelectronic devices based on electrically tunable p-n diodes in a monolayer dichalcogenide. *Nat Nano*, 9(4):262–267, Apr 2014.

[38] Christophe Raynaud, Duy-Minh Nguyen, Nicolas Dheilly, Dominique Tournier, Pierre Brosselard, Mihai Lazar, and Dominique Planson. Optical beam induced current measurements: principles and applications to SiC device characterization. *physica status solidi (a)*, 206(10):2273–2283, 2009.

[39] A.D. Polyanin and V.F. Zaitsev. *Handbook of Exact Solutions for Ordinary Differential Equations*. Chapman & Hall/CRC, 2nd edition, 2003.

[40] Franzen Alexander. Componentlibrary. *Licensed under CreativeCommons Attribution-NonCommercial 3.0 Unported License.*

[41] Hakan Urey. Spot size, depth-of-focus, and diffraction ring intensity formulas for truncated Gaussian beams. *Appl. Opt.*, 43(3):620–625, Jan 2004.

[42] Sidney A. Self. Focusing of spherical Gaussian beams. *Appl. Opt.*, 22(5):658–661, Mar 1983.

[43] Matt W. Graham, Su-Fei Shi, Daniel C. Ralph, Jiwoong Park, and Paul L. McEuen. Photocurrent measurements of supercollision cooling in graphene. *Nat Phys*, 9(2):103–108, Feb 2013.

[44] K J Tielrooij, M Massicotte, L Piatkowski, A Woessner, Q Ma, P Jarillo-Herrero, N F van Hulst, and F H L Koppens. Hot-carrier photocurrent effects at graphene-metal interfaces. *Journal of Physics: Condensed Matter*, 27(16):164207, 2015.

[45] Pavel Irkhin, Aleksandr Ryasnyanskiy, Marlus Koehler, and Ivan Biaggio. Absorption and photoluminescence spectroscopy of rubrene single crystals. *Phys. Rev. B*, 86:085143, Aug 2012.

[46] D.L. Greenaway and R. Nitsche. Preparation and optical properties of group IV-VI chalcogenides having the $CdI_2$ structure. *Journal of Physics and Chemistry of Solids*, 26(9):1445 – 1458, 1965.

[47] Duhee Yoon, Hyerim Moon, Young-Woo Son, G. Samsonidze, Bae Ho Park, Jin Bae Kim, Young-Pak Lee, and Hyeonsik Cheong. Strong polarization dependence of double-resonant Raman intensities in graphene. *Nano Letters*, 8(12):4270–4274, 2008.

[48] Daniel A. Chenet, O. Burak Aslan, Pinshane Y. Huang, Chris Fan, Arend M. van der Zande, Tony F. Heinz, and James C. Hone. In-plane anisotropy in mono- and few-layer $ReS_2$ probed by

raman spectroscopy and scanning transmission electron microscopy. *Nano Letters*, 15(9):5667–5672, 2015.

[49] Longhui Zeng, Lili Tao, Chunyin Tang, Bo Zhou, Hui Long, Yang Chai, Shu Ping Lau, and Yuen Hong Tsang. High-responsivity UV-Vis photodetector based on transferable $WS_2$ film deposited by magnetron sputtering. *Scientific Reports*, 6:20343, Jan 2016.

[50] Jiandong Yao, Zhaoqiang Zheng, and Guowei Yang. Layered-material $WS_2$/topological insulator $Bi_2Te_3$ heterostructure photodetector with ultrahigh responsivity in the range from 370 to 1550 nm. *J. Mater. Chem. C*, 4:7831–7840, 2016.

[51] Ana Laura Elías, Néstor Perea-López, Andrés Castro-Beltrán, Ayse Berkdemir, Ruitao Lv, Simin Feng, Aaron D. Long, Takuya Hayashi, Yoong Ahm Kim, Morinobu Endo, Humberto R. Gutiérrez, Nihar R. Pradhan, Luis Balicas, Thomas E. Mallouk, Florentino López-Urías, Humberto Terrones, and Mauricio Terrones. Controlled synthesis and transfer of large-area $WS_2$ sheets: From single layer to few layers. *ACS Nano*, 7(6):5235–5242, 2013.

[52] K. S. Novoselov, D. Jiang, F. Schedin, T. J. Booth, V. V. Khotkevich, S. V. Morozov, and A. K. Geim. Two-dimensional atomic crystals. *Proceedings of the National Academy of Sciences of the United States of America*, 102(30):10451–10453, 2005.

[53] Ricardo García and Ruben Perez. Dynamic atomic force microscopy methods. *Surface science reports*, 47(6):197–301, 2002.

[54] Juan Ignacio Paredes, Silvia Villar-Rodil, Pablo Solís-Fernández, Amelia Martínez-Alonso, and JMD Tascon. Atomic force and scanning tunneling microscopy imaging of graphene nanosheets derived from graphite oxide. *Langmuir*, 25(10):5957–5968, 2009.

# 4

# $FeCl_3$-INTERCALATED GRAPHENE

**NOTE:** Some of the ideas and data presented in this chapter have appeared previously in the following publication: Thomas H. Bointon, Gareth F. Jones, Adolfo De Sanctis, Ruth Hill-Pearce, Monica F. Craciun and Saverio Russo. *Large-area functionalized CVD graphene for work function matched transparent electrodes.* Scientific Reports, 5:16464 (2015).

The ability to manipulate and control the arrangement of atoms and molecules in a lattice is the ultimate way to engineer novel physical properties of materials[1]. For example, the chemical functionalisation of graphene[2] leads to radical modifications of its band structure and density of states, inducing an energy gap[3], intrinsic superconductivity[4] and magnetic properties[5]. Graphite intercalation compounds (GICs) have been known for decades[6] but only recently few-layer graphene (FLG) has been used and its properties investigated in depth. Amongst the different forms of functionalisation, intercalation with $FeCl_3$[7], is used to induce strong p-type doping in the graphene layers (up to $10^{14}$ charges/cm$^2$), making this material particularly suitable for transparent electrodes[8;9]. Indeed, it has been recently reported that $FeCl_3$-intercalated few-layer graphene ($FeCl_3$-FLG) gives an enhanced light emission of 60%, when employed in a light emitting device, compared to standard graphene electrodes and up to 40% enhancement compared to commercial conductive polymers[10]. At the same time, despite the hydrophobic nature of the intercalant, this material displays an unprecedented stability in ambient conditions[11]: it can sustain temperatures above 100 °C in air and up to 620 °C in vacuum, as well as exposure to 100 % humidity for weeks, without structural changes.

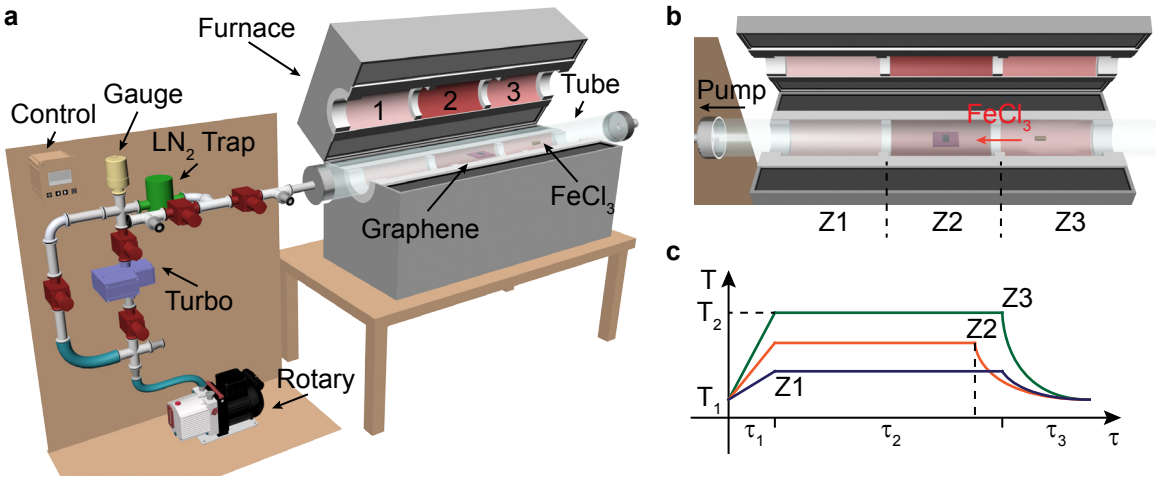


**Figure 4.1: Intercalation of FLG with $FeCl_3$.** **a**, Schematic of the setup used to perform the $FeCl_3$ intercalation of graphene. The main parts are a three-zones furnace equipped with glass tubes and a vacuum system able to evacuate the tube to a pressure of $< 10^{-5}$ mBar. **b**, Intercalation process using a three-zones furnace (Z1-3). **c**, Schematic diagram of the heating cycle during intercalation (see also table 4.1).

In this chapter the basic properties and fabrication methods of this extraordinary material are presented. Focus is put on its characterisation using Raman spectroscopy, as a non-destructive tool to estimate the charge concentration. Finally, a detailed study of large area $FeCl_3$-FLG prepared from chemical vapour deposition (CVD)-grown FLG is presented, as the base material used to demonstrate graphene-based light-emitting devices.

## 4.1 INTERCALATION OF GRAPHENE WITH $FeCl_3$

The procedure and the setup adopted in this work to intercalate FLG with $FeCl_3$ are illustrated in figure 4.1, and follow the work by Khrapach *et al.*[7]. The technique is a vapour-transport method[6], similar to CVD, in a sealed environment, without the use of dangerous carrier gasses, such as Chlorine. FLG is prepared on the desired substrate either by mechanical exfoliation from bulk graphite or by wet-transfer of CVD-grown graphene (see also section 4.3). After, the sample is loaded into a glass tube mounted in a three-zones furnace, as illustrated in figure 4.1a, with the sample placed in the

**Table 4.1: Intercalation heating cycle.** Heating cycle for the intercalation of FLG with $FeCl_3$. The transition between two temperatures is always linear except for the cooling stage in which it is exponential.

| | Zone 3[a] | Zone 2 | Zone 1 |
|---|---|---|---|
| $T_1$ (°C) | 20 | 20 | 20 |
| $\tau_1$ (min) | 40 | 40 | 31 |
| $T_2$ (°C) | 300 | 360 | 315 |
| $\tau_2$ (min) | 480 | 480 | 450 |
| $T_3$ (°C) | 300 | 360 | 315 |
| $\tau_3$ (min) | - | - | - |
| $T_4$ (°C)[b] | 20 | 20 | 20 |

[a] With reference to figure 4.1a,b; [b] Power OFF.

central zone. On the other end of the tube a small vial filled with anhydrous $FeCl_3$ (*Sigma-Aldrich*, powder, $\geq$ 99.99 % trace metals basis) is placed. The opposite end of the tube is connected to a vacuum system designed to evacuate the tube to a pressure $< 10^{-5}$ mBar (see figure 4.1a), using a turbo-molecular pump in combination with a liquid nitrogen (LN2) cold-trap. After reaching the desired vacuum the tube is sealed. The furnace is then programmed to perform the heating cycle illustrated in table 4.1 and figure 4.1c, where $\tau_2$ can be varied depending on the area to intercalate[8] (see also section 4.3). The first zone, containing the $FeCl_3$, is kept at the sublimation temperature of $FeCl_3$, in order to thermally decompose the powder into a gas. In this way the Chlorine gas developed by the sublimation reaction acts as carrier gas for the intercalation process. The second zone, containing the graphene sample, is kept at a higher temperature in order to drive the $FeCl_3$ gas towards it and facilitate the intercalation process by relaxing the FLG stacking. The third zone, which is empty, is kept below the sublimation temperature of $FeCl_3$, in order to crystallize the excess gas away from the sample during cooling.

The vacuum system shown in figure 4.1a has been purposefully designed and built as a part of this PhD project. All components are made of stainless steel, in order to avoid corrosion caused by residual $FeCl_3$ pumped in the system. A LN2 cold trap is used as a contamination barrier for the pumps, by freezing the incoming particles on

its internal surface, it also acts as a pumping system, which shortens the total process time. The furnaces can accommodate glass and quartz tubes up to 9 cm in diameter, making it possible to intercalate large-area FLG on rigid substrates up to areas of $\sim 80$ $cm^2$.

## 4.2 CHARACTERISATION OF $FeCl_3$-FLG

A schematic representation of the material resulting from the intercalation process described in section 4.1 is shown in figure 4.3c. A layer of linked $FeCl_3$ octahedra intercalates between the graphene layers, increasing the intra-layer distance from 3.4 Å to 9.2 Å, with the width of an individual layer of intercalant being 5.8 Å, as it was observed in the past on intercalated bulk graphite[12;13]. This structure gives exceptional properties to this material, resulting from the charge transfer between the $FeCl_3$ and the graphene.

The study of GICs and $FeCl_3$-intercalated graphite has been conducted in the past using a series of characterisation techniques, ranging from X-Ray diffraction (XRD)[13;14] to high-resolution transmission electron microscopy (HRTEM)[12]. Raman spectroscopy has been used as well[15;16], giving a series of information unavailable with the other techniques and nowadays is the main tool used to characterise this material. In this section the electrical and optical properties of intercalated graphene are reviewed together with the peculiarities of its Raman spectrum. Raman spectroscopy can be used to asses several remarkable effects of the intercalation on the pristine graphene and to estimate the amount of induced charge (doping) per layer.

### 4.2.1 *Electrical and optical properties*

Figure 4.2a shows an optical micrograph of two pristine flakes of FLG together with the same flakes after intercalation with $FeCl_3$. The intercalated flakes clearly show a different contrast and colouration of the substrate (the pictures are acquired in the same conditions). This can be easily attributed to the presence of the $FeCl_3$ molecules which modify the absorbance and reflectance of both the graphene and the substrate. As shown in figure 4.2b, the spectral transmittance of $FeCl_3$-FLG is different from pristine graphene. In particular, higher absorption at short wavelengths is observed but, in contrast, higher transparency is observed at longer wavelengths and in the

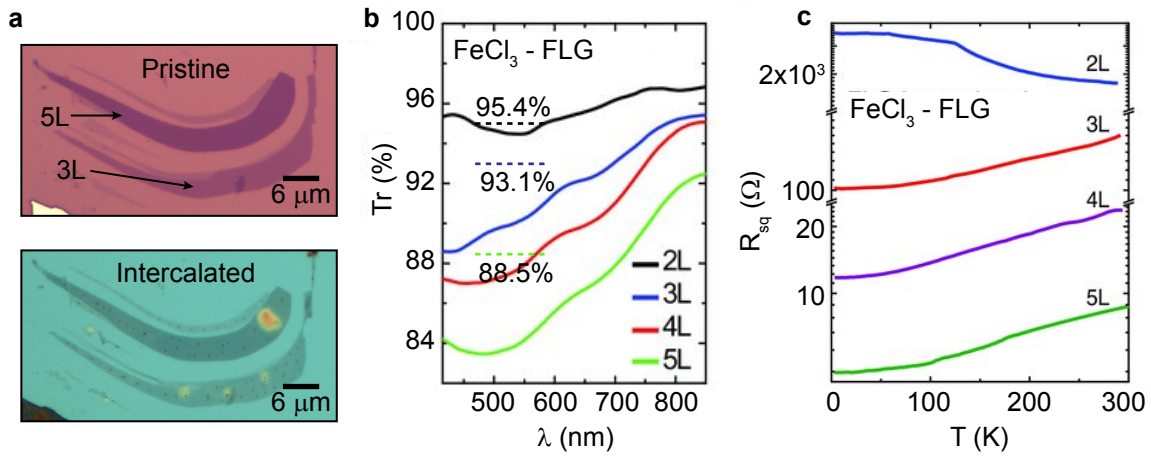


**Figure 4.2: Electrical and optical properties of $FeCl_3$-FLG. a**, Optical micrograph of pristine (top) and $FeCl_3$-FLG (bottom) flakes on $Si/SiO_2$ substrate. **b**, Transmittance spectra of $FeCl_3$-FLG for different number of layers. Dashed lines represent the literature values for pristine graphene. **c**, Square resistance of $FeCl_3$-FLG for different number of layers, as a function of temperature. Adapted with permission from Ref. 7 ©WILEY-VCH Verlag.

infrared (IR). The latter is given by the induced doping, which effectively opens an optical gap for photons with energy $\hbar\omega < 2E_F$ (see section 2.2.1).

The resistance of $FeCl_3$-FLG as a function of temperature is shown in figure 4.2c. It is observed that flakes thicker than bilayer graphene (BLG) show characteristic metallic behaviour, with a sheet resistance as low as $8\,\Omega/\square$ at 300 K for 5L intercalated graphene. This is due to the large charge transfer induced by the intercalant: Hall measurements on the same sample[7] show a charge density of $\sim 8.9 \cdot 10^{14}$ cm$^{-2}$. These charge densities exceed the highest values demonstrated so far by gating with other techniques[17;18] and, combined with the high transparency, make this material the best known transparent conductor. Therefore, $FeCl_3$-FLG holds the potential for its use in optoelectronic applications, in particular as a transparent conductor for display, photovoltaic (PV) and light emitting device (LED) applications.

### 4.2.2 *Raman spectroscopy*

The Raman spectrum of graphene intercalated with $FeCl_3$ shows two prominent features[7;19;20]: an upshift of the G-bands, with respect to pristine graphene, and a change

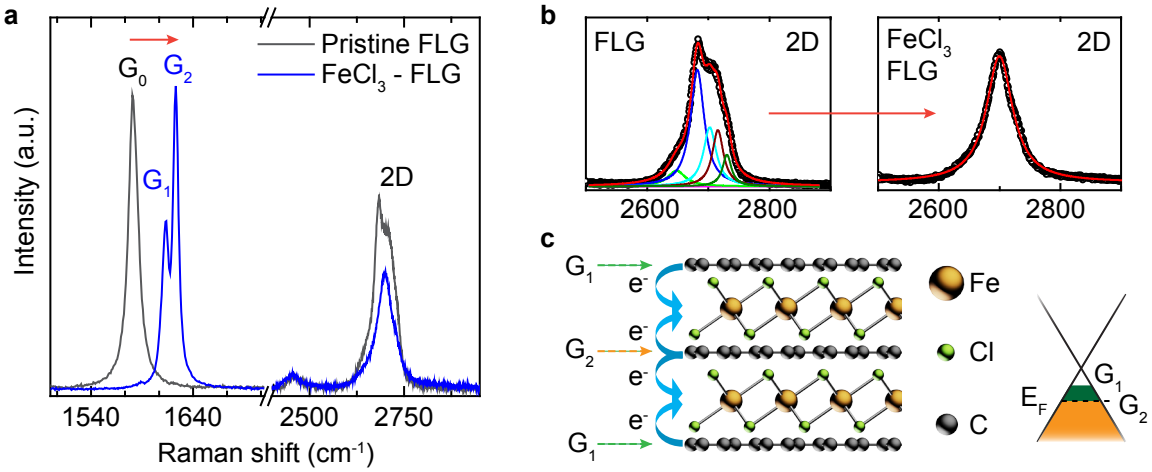


**Figure 4.3: Raman spectroscopy of $FeCl_3$-FLG. a**, Representative spectra of trilayer graphene (TLG), pristine (black) and $FeCl_3$-intercalated (blue). Upon doping with $FeCl_3$, the pristine $G_0$ peak at 1580 $cm^{-1}$ up-shifts and splits into two peaks $G_1$ and $G_2$, each corresponding to a different stage of intercalation. **b**, The reduced coupling within the layers transforms the double-resonant 2D band around 2650 $cm^{-1}$ from a multi-Lorentzian (6 in this case, right) to a single-Lorentzian peak (left). **c**, Schematic diagram of the structure and charge-transfer processes in $FeCl_3$-FLG, bond lengths and intra-layer distances are in scale.

in the shape of the 2D band, as shown in figure 4.3a,b. The charge-transfer induced by the $FeCl_3$ molecules induces hole doping in graphene, which results in the stiffening of the $E_{2g}$ mode[21], responsible for the resonant G-band at $\sim$ 1580 $cm^{-1}$ in the Raman spectrum. Two intercalation stages[12] are possible: when a graphene layer is in contact with $FeCl_3$ from one side (known as stage-2 intercalation) the charge doping shifts the G-band from $\sim$ 1580 $cm^{-1}$ to $\sim$ 1610 $cm^{-1}$, this is usually referred to as $G_1$ peak[7]. When a graphene layer is sandwiched between two $FeCl_3$ layers (known as stage-1 intercalation) the G band shifts up to 1625 $cm^{-1}$, which is usually called $G_2$ peak. The stage number indicates the number of graphene layers which are sandwiched between two $FeCl_3$ layers.

The increased distance between graphene layers reduces their coupling, causing the double-resonant 2D band, originating from the $A_{1g}$ mode, to change from a multi-peak band, characteristic for two and three layer graphene, to a single-Lorentzian peak, typical of stacked non-interacting graphene monolayers, as shown in figure 4.3b[7].

The different intercalation stages and the related charge-transfer effect are shown in figure 4.3c, where the shift in Fermi level due to the increased charge density is shown schematically.

As already mentioned, doping in graphene results in a stiffening of the $E_{2g}$ phonon mode. This is due to the presence of a Kohn anomaly in the phonon dispersion at the $\Gamma$ point. In general, the atomic vibrations in a solid are partially screened by electrons. This screening can change rapidly in a metal for vibrations associated with particular points of the first Brillouin zone (FBZ) which are determined by the shape of the Fermi surface. At these points, an anomalous behaviour of the phonon dispersion is observed, such as a discontinuity, and called Kohn anomaly[22]. Kohn anomalies may occur only for points in the FBZ such that there are two electronic states, with momenta $\boldsymbol{k}_1$ and $\boldsymbol{k}_2 = \boldsymbol{k}_1 + \boldsymbol{q}$, with $\boldsymbol{q}$ such that they both lie on the Fermi surface. As already discussed (see section 2.1.3), in graphene the two equivalent points K and K' are such that $\mathbf{K} = \mathbf{K}' + 2\mathbf{K}$ (the vectors $\mathbf{K}$ and $\mathbf{K}'$ are defined in equation (2.3)). Therefore, the two K points are connected by the vector $\mathbf{K}'$ and Kohn anomalies can occur for $\boldsymbol{q} = \Gamma$ or $\boldsymbol{q} = \mathbf{K}$[23]. Lazzeri *et al.*[21] calculated, from first principles, the frequency of the $E_{2g}$ mode of graphene at $\Gamma$, which is responsible for the G peak in the Raman spectrum, as a function of doing. Their model showed that, by treating the phonons as a dynamic perturbation and allowing for the increase of the graphene lattice spacing due to the increased charge density (expanded lattice) a strong dependence of the $E_{2g}$ phonon frequency with doping is observed, as shown in figure 4.4a. The key to they model is the treatment of the perturbation as dynamic, as opposed to the static Born-Oppenheimer (BO) approximation[24].

The aforementioned model has been verified experimentally by Das *et al.*[25] using a top-gated graphene transistor, with a maximum charge induced with this technique of $4 \cdot 10^{13}$ cm$^{-2}$, below the levels reached by $FeCl_3$ intercalation. To assess the accuracy with which the stiffening of the $E_{2g}$ phonon mode, and consequent up-shift of the G peak, can be reliably used to estimate the charge density in $FeCl_3$-FLG, a comparative study of the charge density obtained from the G peak shift and the period of the Shubnikov-de Haas oscillations (SdHO), presented in the work of Ref. 7, was conducted. Figure 4.4b shows the fit to Raman spectrum of a three-layer $FeCl_3$-FLG, from the data in Ref. 7. Using the model described above and the results shown in figure 4.4a, the $G_2$ peak at $1623.24 \pm 0.02$ cm$^{-1}$ gives a charge density of $n_h = (9.0 \pm 0.5) \cdot 10^{13}$ cm$^{-2}$, while

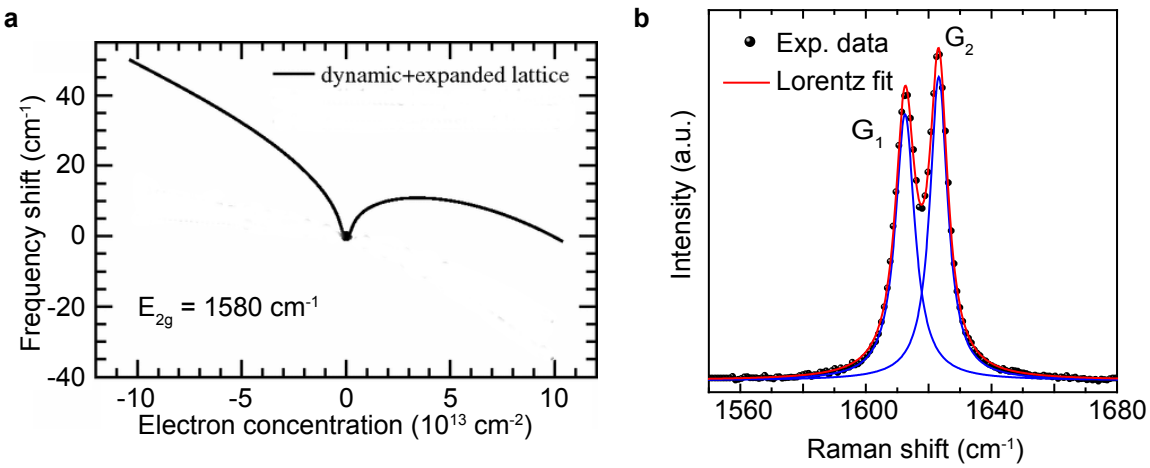


**Figure 4.4: Raman estimation of charge density in $FeCl_3$-FLG. a**, Frequency of the $E_{2g}$ $\Gamma$ phonon (Raman G band) as a function of charge concentration: shift with respect to the zero-doping frequency (1580 $cm^{-1}$). Adapted with permission from Lazzeri M. and Mauri F., Phys. Rev. Lett. 97, 266407 (2006), ©2017 by the American Physical Society[21]. **b**, Raman spectrum of 3L $FeCl_3$-FLG taken from the data in Ref. 7, where both stage-2 ($G_1$ peak) and stage-1 ($G_2$ peak) intercalation stages of graphene are present. Data courtesy of Monica F. Craciun.

the SdHO measurements on the same sample[7] report a value of $n_{SdHO} = (10.700 \pm 0.005) \cdot 10^{13}$ $cm^{-2}$. Given that Raman spectroscopy is a local probe (the laser spot-size is $< 1$ $\mu$m), it is possible to explain the discrepancy between the two measurements by small inhomogeneities of the sample under examination. Therefore, an uncertainty of $\pm 1 \cdot 10^{13}$ $cm^{-2}$ an be associated with the estimation of charge concentration using Raman spectroscopy, in $FeCl_3$-FLG. Given the small discrepancy between the two measurements it is possible to conclude that Raman spectroscopy is a valuable, non-destructive, tool to estimate the charge concentration in highly doped graphene, in particular over large areas.

### 4.2.3 *Determination of the stacking order in $FeCl_3$-FLG*

Using a combination of optical microscopy and Raman spectroscopy it is possible to determine the stacking order of $FeCl_3$-FLG. This information is very important in order to determine the total charge concentration of the whole stack and the associated

electrical and optical properties. In Ref. 7, the authors used magneto-transport measurement, together with Raman spectroscopy, to infer the stacking order of the measured flakes of $FeCl_3$-FLG, relying on the fact that the presence of a stage-1 BLG (i.e. a BLG which is sandwiched between to layers of $FeCl_3$) would result in the presence of massive Dirac fermions, whose mass was measured from the temperature dependence of the amplitude of magneto-conductivity oscillations[7]. In this section I will show how a careful analysis of the Raman spectrum and the knowledge of the thickness of the pristine flake, can be used to determine the stacking order, at least for BLG and TLG, in section 5.2.1 this technique is applied to a 4L graphene.

Figure 4.5a shows the optical micrograph of a pristine TLG flake, whose thickness was determined by optical contrast (see section 2.2.2). After intercalation with $FeCl_3$, the Raman maps, shown in figure 4.5b show a prominent $G_1$ peak and no $G_2$ or pristine $G_0$ peaks. These maps show the height of the G-band peaks normalized to the height of the Si peak at 520 $cm^{-1}$. Therefore, in this case the intercalation is of stage-2 and all graphene layers must be in contact with $FeCl_3$, resulting in a stacking structure in which one BLG is maintained, as shown schematically in figure 4.5a. The same analysis is shown in figure 4.5c and figure 4.5d, where a BLG flake is used. In this case the presence of a prominent $G_1$ peak across the whole flake, indicates that one layer of $FeCl_3$ intercalates between the graphene, leaving two decoupled monolayer graphene (MLG) in the stack.

Therefore, it is possible to use Raman spectroscopy to asses the stacking order in intercalated graphene across a large area: this is important for the study of the electronic and opto-electronic properties of this material, as it will be discussed in chapter 5.

## 4.3 LARGE-AREA $FeCl_3$-FLG

The development of flexible optoelectronic devices, such as PV cells and LEDs, depends on the availability of flexible and transparent electrodes and their compatibility with photoactive materials. At the same time, such electrodes should be scalable to large-area production. Currently used transparent conductors, i.e. Indium-Tin Oxide (ITO) and Fluorine-doped Tin Oxide (FTO), are brittle and degrade significantly under small applied strains[26;27]. Furthermore, the diffusion of Indium from ITO into the photoac-

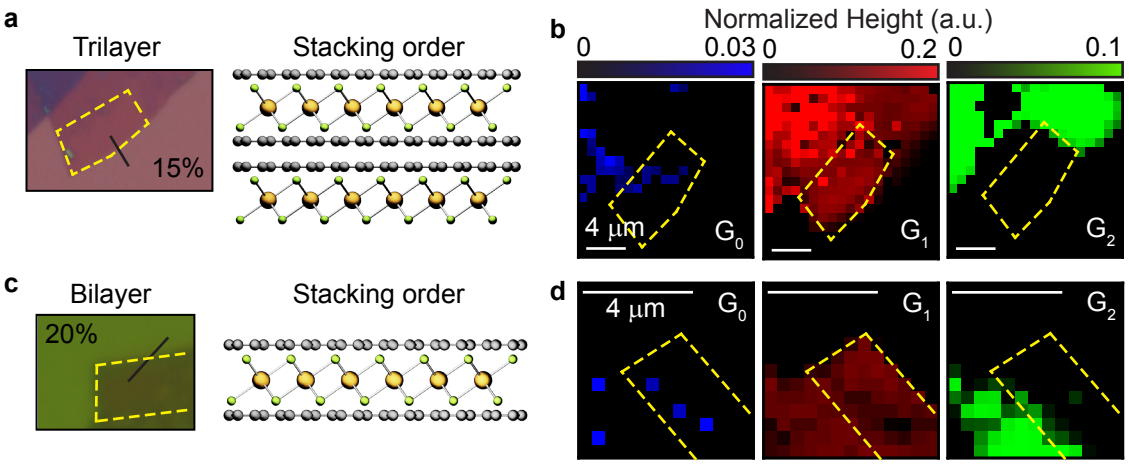


**Figure 4.5: Stacking order of $FeCl_3$-FLG. a**, Optical micrograph of a TLG flake on $Si/SiO_2$, with annotated contrast and schematic of the inferred stacking order. **b**, Raman maps of the same flake showing the height of the G-bands, normalized to the Si peak at 520 $cm^{-1}$. Yellow-dashed lines mark the region of the flake. **c** and **d**, Same micrograph and Raman maps for a BLG flake (a green filter is used to enhance the contrast).

tive layers of PV cells or organic light emitting devices (OLEDs) is a well-known cause of device degradation[28]. Other solutions have been proposed, such as meshes of metallic nano-wires, which have high optical transmission ($\sim 80\,\%$ at 550 nm) and low sheet resistance ($\sim 38\ \Omega/\square$)[29] even when subjected to 16 % strain[27]. However, scattering of light off nano-wires can introduce significant optical haze, limiting the applicability of these materials in real applications. As shown in section 2.1, graphene has a high optical transmission and does not suffer of haze, while its conductance is unchanged even when subject to strains up to 6.2 %[30]. Furthermore, contrary to ITO, no carbon migration has been reported in OLEDs that use graphene electrodes. However, the efficiency of these devices is still low due to the high sheet resistance of graphene ($> 500\ \Omega/\square$) and poor matching of its work function (WF) to that of the photoactive layer[31]. As already discussed, functionalisation of graphene[2] can lower its sheet resistance but for large-area applications, functionalised CVD-grown graphene still shows values greater than ITO ($8\ \Omega/\square$), causing excessive dissipation in electrical devices[32;33;34]. The high sheet resistance causes the potential drop across the area of a transparent electrode to result in gradients of light intensity over the surface of the organic light emitting

device (OLED). Furthermore, since the WF of pristine graphene is comparable to that of ITO (4.6 eV for graphene and 4.8 eV for ITO)[28], pristine graphene electrodes require electron or hole blocking layers for efficient PVs to account for the large WF mismatch between the electrode and the photoactive layers. Therefore, a transparent, flexible and highly conductive material that does not require charge blocking layers when embedded in PV would enable the development of more efficient optoelectronic devices.

To pursue this goal, CVD-grown graphene on Nickel (Ni-CVD)[35] was used in this work, since growth on Ni results in multilayer graphene with a continuous coverage over large areas (up to 100 $cm^2$). The intercalation of this kind of FLG was carried out as described in section 4.1, resulting in a highly doped material with high transparency, low sheet resistance and a WF comparable to that of gold. Its characterisation is presented in the following sections.

### 4.3.1 *Characterisation of Ni-grown CVD graphene*

Characterisation of commercially available Ni-CVD graphene transferred on $Si/SiO_2$ substrate is shown in figure 4.6 (see appendix A for details on growth and transfer of CVD graphene). The datasheet of commercially available Ni-CVD (100 mm diameter wafer from *Graphene-supermarket*) specify that this is a continuous film of FLG with thickness varying from 1 to $7-10$ layers. Figure 4.6a shows a false-colour map of an optical micrograph picture (shown in figure 4.6b) of such graphene transferred on a $Si/SiO_2$ (300 nm thick $SiO_2$) substrate using wet etching of Ni in 1M $FeCl_3$ solution. The variation in layer thickness of the different domains is clearly visible, while the size of such domains is consistent with previous studies[35]. A statistical analysis of the grain size shows that $\sim 35\,\%$ of the sample is 4 layers thick with and average domain area of $\sim 150\ \mu m^2$, see figure 4.6c.

### 4.3.2 *Intercalation and Raman study of large-area $FeCl_3$-FLG*

The intercalation of Ni-CVD graphene was conducted according to the method discussed in section 4.1, with an intercalation time $\tau_2$ of 8, 12 and 36 h. No significant differences were observed across the different samples.

Figure 4.6d shows an optical micrograph of a representative area of Ni-CVD after

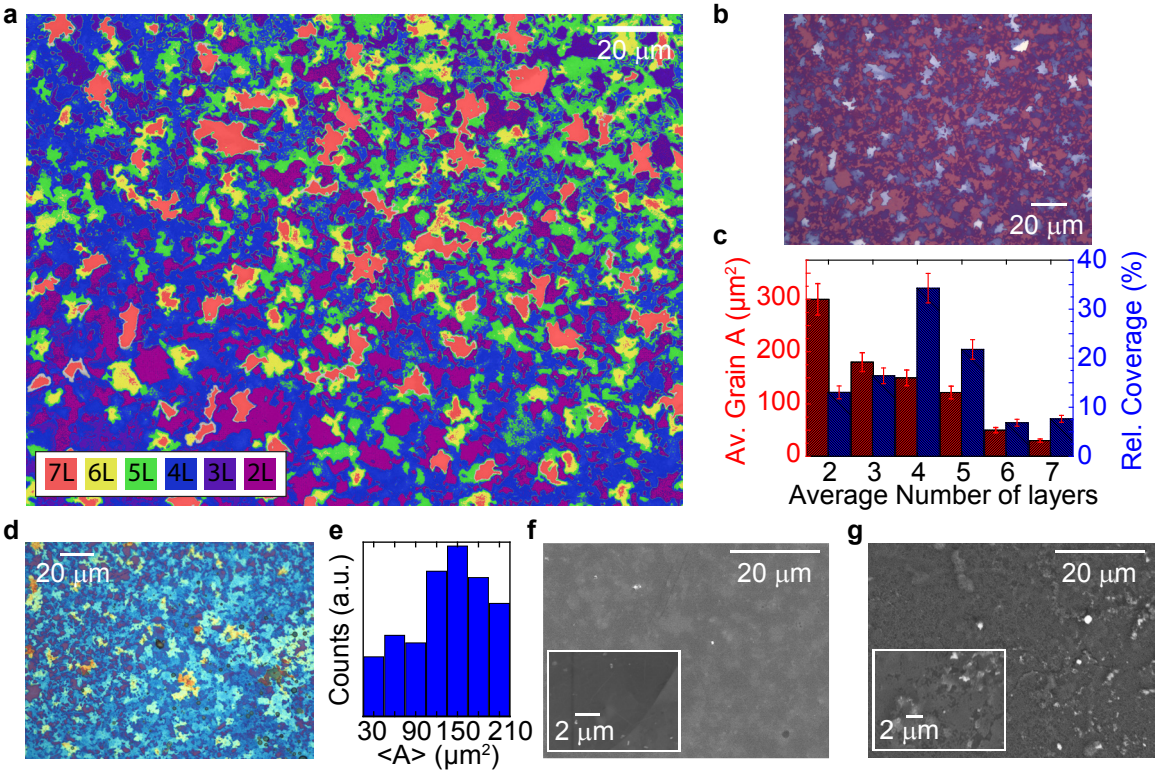


**Figure 4.6: Characterisation of Ni-CVD graphene.** **a**, False-colour map of pristine Ni-CVD graphene grains, masked according to the number of layers. **b**, Optical micrograph of the sample in **a**. **c**, Statistical study used to determine the relative coverage and average grain size of the multilayer islands in **a**. **d** Optical micrograph of large-area $FeCl_3$-FLG. **e**, Statistical study of average grain area $< A >$ of the sample in **d**. **f** and **g**, Scanning electron microscope (SEM) images of Ni-CVD and $FeCl_3$-FLG, respectively.

intercalation with $FeCl_3$. A statistical analysis of the micrograph images, figure 4.6e, shows no significant change of the average domain area upon intercalation, which is expected since the $FeCl_3$ is not etching the graphene during the intercalation process[7;11]. SEM images of Ni-CVD graphene on $SiO_2$ before and after $FeCl_3$ intercalation are shown in figure 4.6f-g respectively. After intercalation a better contrast is observed in the SEM image, given by the higher conductivity of the graphene. $FeCl_3$ residues are also present and appear as bright spots (since Fe has a higher Z than C) on the surface and at the boundaries of the islands.

Raman spectroscopy is employed to further characterise the material. Figure 4.7a shows a representative Raman spectrum of a 1 $cm^2$ multilayer graphene on $Si/SiO_2$ substrate intercalated for 36 h. The G-band can be fitted with four Lorentzian peaks, which, following the discussion in section 4.2.2, can be labelled as $G_0$ (1580 $cm^{-1}$), $G_1^*0$ (1600 $cm^{-1}$), $G_1$ (1611 $cm^{-1}$) and $G_2$ (1622 $cm^{-1}$). Upon doping the 2D-band is upshifted and its shape becomes the convolution of a smaller number of Lorentzian peaks, as compared to the pristine multilayer graphene, in agreement with previous reports[25]. In this case, four Lorentzian peaks are needed to obtain a good fit to the 2D-band, as shown in figure 4.7a, right, with maxima at 2637 $cm^{-1}$ ($2D_0$), 2684 $cm^{-1}$ ($2D_1^*$), 2700 $cm^{-1}$ ($2D_1$) and 2721 $cm^{-1}$ ($2D_2$). As discussed in section 4.2.2, the positions of G- and 2D- peaks are unique identifiers of the doping level in this intercalated compound. In this case, however, a new set of peaks appears which were labelled $G_1^*$-$2D_1^*$. It is reasonable, given the nature of large-area FLG, to attribute these peaks to graphene layers in direct contact to one adjacent $FeCl_3$ layer, as for the $G_1$ peak, but with a lower density of $FeCl_3$ molecules, which results in a lower charge transfer.

As discussed in section 4.2.2, the Fermi energy in $FeCl_3$-FLG can be measured using Raman spectroscopy. Estimates of $n_h$ over a representative surface area of $10^4$ $\mu m^2$ in this material show three different doping levels, as shown in figure 4.7b. Hence, the three corresponding charge concentrations are $n_h^0 = 0.3 \cdot 10^{13} \pm 1 \cdot 10^{12}$ $cm^{-2}$, $n_h^1* = 2.6 \cdot 10^{13} \pm 3 \cdot 10^{12}$ $cm^{-2}$ and $n_h^1 = 4.6 \cdot 10^{13} \pm 5 \cdot 10^{12}$ $cm^{-2}$, see figure 4.7c.

In a few-layer graphene system, such as the Ni-grown CVD graphene presented here, the total charge density in the system can reach values as high as $10^{15}$ $cm^{-2}$ for a sequence of 15 graphene layers. Since the exploitation of collective charge oscillations in graphene (i.e. plasmons) strongly relies on doping, $FeCl_3$-intercalation of multilayer graphene provides an attractive platform for pioneering studies of surface plasmons

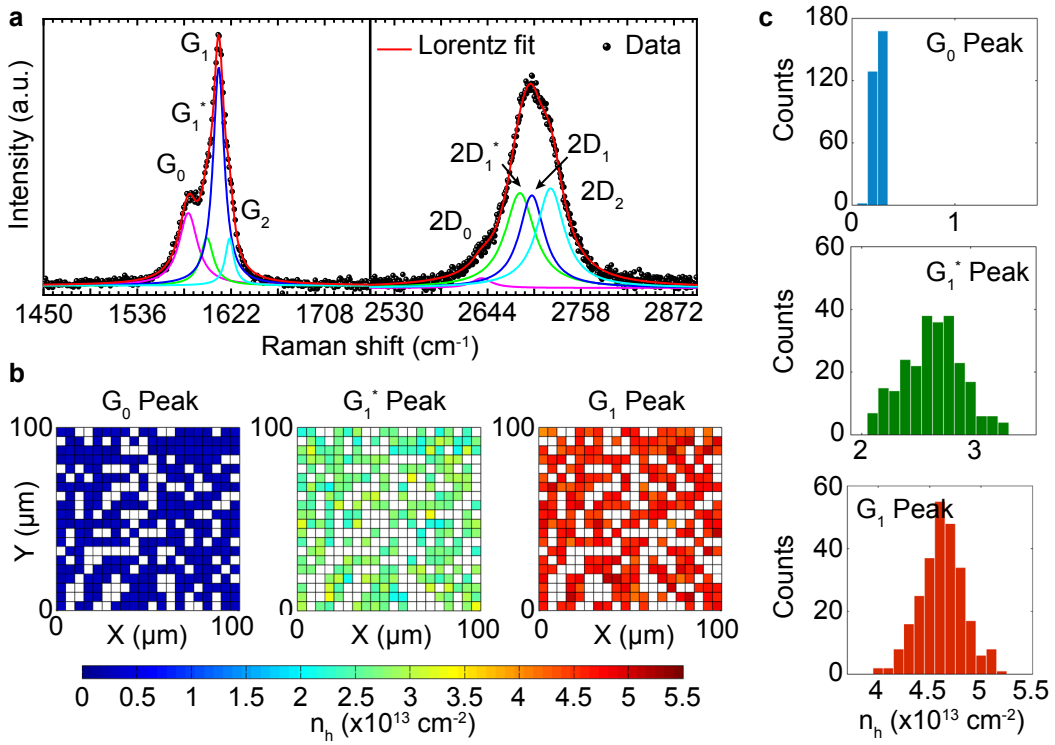


**Figure 4.7: Charge density estimation in large-area $FeCl_3$-FLG** **a**, Raman spectrum ($\lambda_{exc}$ = 532 nm) of $FeCl_3$-FLG showing the G- and 2D-band regions with the associated four-peaks fit ($G_0$-$2D_0$, $G_1^*$-$2D_1^*$, $G_1$-$2D_1$ and $G_2$-$2D_2$). **b**, Spatial distribution of the hole concentration $n_h$ for the first three intercalation stages, over an area of 100 × 100 $\mu m^2$. **c**, Statistical study of $n_h$ for each intercalation stage over the 400 points in **b**. Adapted with permission from Ref. 8.

at wavelengths of interest to the telecommunication industry (1 − 1.5 $\mu$m). More specifically, the plasmon frequency in graphene scales as[36]:

$$\hbar\omega_{pl} = \sqrt{\frac{E_F}{D}}, \tag{4.1}$$

where $E_F$ is the Fermi level and $D$ is the size of the resonant plasmonic structure. Therefore, ans $E_F \approx 1$ eV, which corresponds to a total charge density of $\sim 7 \cdot 10^{14}$ $cm^{-2}$ (see equation (2.18)), would result in a plasmon resonance at a photon wavelength of $\sim 1.4$ $\mu$m. Such high charge density can be easily obtained in $FeCl_3$-FLG.

### 4.3.3 *Electrical and optical properties of Ni-CVD $FeCl_3$-FLG*

The room temperature resistivity of the Ni-CVD $FeCl_3$-FLG was measured[8] to be $20.5 \pm 0.5\ \Omega/\square$, that is $\sim 1000$ times smaller than the resistivity of graphene at the neutrality point and more than 20 times smaller than the lowest values of resistivity reported in CVD-grown graphene.

The optical transmittance of Ni-CVD $FeCl_3$-FLG, deposited on a glass substrate, is larger than 74 % for the wavelength range $450 - 850$ nm, with a value of 77 % at 550 nm, which is comparable to the transmittance of a 10 $\mu$m thick ITO[37]. The optical transmittance was observed to increase monotonously up to 87 % at 850 nm incident wavelength.

The WF of Ni-CVD $FeCl_3$-FLG, $\Phi_{iFLG}$, was characterised using Scanning Kelvin probe microscopy (SKPM)[38;39] over a representative 20 $\mu m^2$ areas of the sample[8]. A distribution of $\Phi_{iFLG}$ was observed, with the most commonly occurring at 4.9 eV, 5 eV and 5.1 eV, with the majority of the surface area of the sample ($\sim 60$ %) showing a value $\Phi_{iFLG} = 5.1$ eV. The observed three dominant values of $\Phi_{iFLG}$ are to be expected in intercalated few-layer graphene and correlate very well with the three distinct intercalation stages observed in Raman spectroscopy (see section 4.3.2). Furthermore, while $\Phi_{iFLG}$ was observed to vary on the nano-scale between $4.8 - 5.2$ eV, the average value of 5 eV was observed to be uniform over a 1 $cm^2$ scale, that is the size of the sample.

## 4.4 FINAL REMARKS AND OUTLOOK

The unique properties of FLG intercalated with $FeCl_3$ have been reviewed and a comprehensive study of its Raman spectrum, and the information that can be extracted from it, has been shown. The ability to intercalate both exfoliated flakes and large-area CVD-grown graphene makes this material an attractive platform for novel applications, spanning different areas of technology. In particular, the unique combination of (1) large work function, (2) low electrical resistivity and (3) high optical transmittance make $FeCl_3$-FLG an attractive system for flexible optoelectronics. At the same time, a charge density per graphene layer of $\sim 5 \cdot 10^{13}$ $cm^{-2}$ makes it suitable for the study of plasmons in the infrared region, with potential applications to the telecommunication industry[40]. The application of $FeCl_3$-FLG in electroluminescent devices has been

recently demonstrated, showing an enhancement in the light-emission from alternating current electroluminescent (ACEL)-type devices, confirming that the low sheet resistance of this material, indeed, is the key[10]. In chapters 5 and 6 the use of $FeCl_3$-FLG in two different kind of photodetectors will be demonstrated.

# BIBLIOGRAPHY

[1] Richard P. Feynman. There's plenty of room at the bottom. *Engineering and Science*, 23(5):22–36, 1960.

[2] M F Craciun, I Khrapach, M D Barnes, and S Russo. Properties and applications of chemically functionalized graphene. *Journal of Physics: Condensed Matter*, 25(42):423201, 2013.

[3] Steven E. Martins, Freddie Withers, Marc Dubois, Monica F. Craciun, and Saverio Russo. Tuning the transport gap of functionalized graphene via electron beam irradiation. *New Journal of Physics*, 15(3):033024, 2013.

[4] B. M. Ludbrook, G. Levy, P. Nigge, M. Zonno, M. Schneider, D. J. Dvorak, C. N. Veenstra, S. Zhdanovich, D. Wong, P. Dosanjh, C. Straßer, A. Stöhr, S. Forti, C. R. Ast, U. Starke, and A. Damascelli. Evidence for superconductivity in Li-decorated monolayer graphene. *Proceedings of the National Academy of Sciences*, 112(38):11795–11799, 2015.

[5] Jeongmin Hong, Elena Bekyarova, Ping Liang, Walt A. de Heer, Robert C. Haddon, and Sakhrat Khizroev. Room-temperature magnetic ordering in functionalized graphene. *Scientific Reports*, 2:624, 2012. Article.

[6] M.S. Dresselhaus and G. Dresselhaus. Intercalation compounds of graphite. *Advances in Physics*, 30(2):139–326, 1981.

[7] Ivan Khrapach, Freddie Withers, Thomas H. Bointon, Dmitry K. Polyushkin, William L. Barnes, Saverio Russo, and Monica F. Craciun. Novel highly conductive and transparent graphene-based conductors. *Advanced Materials*, 24(21):2844–2849, 2012.

[8] Thomas H. Bointon, Gareth F. Jones, Adolfo De Sanctis, Ruth Hill-Pearce, Monica F. Craciun, and Saverio Russo. Large-area functionalized CVD graphene for work function matched transparent electrodes. *Scientific Reports*, 5:16464, 2015.

[9] Thomas H. Bointon, Monica F. Craciun, and Saverio Russo. Is graphene a good transparent electrode for photovoltaics and display applications? *IET Circuits, Devices and Systems*, 9:403–412, 2015.

[10] Elias Torres Alonso, George Karkera, Gareth F. Jones, Monica F. Craciun, and Saverio Russo. Homogeneously bright, flexible, and foldable lighting devices with functionalized graphene electrodes. *ACS Applied Materials & Interfaces*, 8(26):16541–16545, 2016.

[11] Dominque J. Wehenkel, Thomas H. Bointon, Tim Booth, Peter Böggild, Monica F. Craciun, and Saverio Russo. Unforeseen high temperature and humidity stability of $FeCl_3$ intercalated few layer graphene. *Scientific Reports*, 5:7609, 2015.

[12] J.M. Thomas, G.R. Millward, R.F. Schlögl, and H.P. Boehm. Direct imaging of a graphite intercalate: Evidence of interpenetration of "stages" in graphite: Ferric chloride. *Materials Research Bulletin*, 15(5):671 – 676, 1980.

[13] S. Hashimoto, K. Forster, and S. C. Moss. Structure refinement of an $FeCl_3$ crystal using a thin plate sample. *Journal of Applied Crystallography*, 22(2):173–180, 1989.

[14] J. M. Cowley and J. A. Ibers. The structures of some ferric chloride–graphite compounds. *Acta Crystallographica*, 9(5):421–431, 1956.

[15] N. Caswell and S.A. Solin. Vibrational excitations of pure $FeCl_3$ and graphite intercalated with ferric chloride. *Solid State Communications*, 27(10):961 – 967, 1978.

[16] C. Underhill, S.Y. Leung, G. Dresselhaus, and M.S. Dresselhaus. Infrared and raman spectroscopy of graphite-ferric chloride. *Solid State Communications*, 29(11):769 – 774, 1979.

[17] Dmitri K. Efetov and Philip Kim. Controlling electron-phonon interactions in graphene at ultrahigh carrier densities. *Phys. Rev. Lett.*, 105:256805, 2010.

[18] Jianting Ye, Monica F. Craciun, Mikito Koshino, Saverio Russo, Seiji Inoue, Hongtao Yuan, Hidekazu Shimotani, Alberto F. Morpurgo, and Yoshihiro Iwasa. Accessing the transport properties of graphene and its multilayers at high carrier density. *Proceedings of the National Academy of Sciences*, 108(32):13002–13006, 2011.

[19] Da Zhan, Li Sun, Zhen Hua Ni, Lei Liu, Xiao Feng Fan, Yingying Wang, Ting Yu, Yeng Ming Lam, Wei Huang, and Ze Xiang Shen. $FeCl_3$-based few-layer graphene intercalation compounds: Single linear dispersion electronic band structure and strong charge transfer doping. *Advanced Functional Materials*, 20(20):3504–3509, 2010.

[20] W. Zhao, P. H. Tan, J. Liu, and A. C. Ferrari. Intercalation of few-layer graphite flakes with $FeCl_3$: Raman determination of fermi level, layer by layer decoupling, and stability. *Journal of the American Chemical Society*, 133(15):5941–5946, 2011.

[21] Michele Lazzeri and Francesco Mauri. Nonadiabatic Kohn anomaly in a doped graphene monolayer. *Phys. Rev. Lett.*, 97:266407, 2006.

[22] W. Kohn. Image of the fermi surface in the vibration spectrum of a metal. *Phys. Rev. Lett.*, 2:393–394, 1959.

[23] S. Piscanec, M. Lazzeri, Francesco Mauri, A. C. Ferrari, and J. Robertson. Kohn anomalies and electron-phonon interactions in graphite. *Phys. Rev. Lett.*, 93:185503, 2004.

[24] Giuseppe Grosso and Guseppe Pastori Parravicini. *Solid State Physics*. Academic Press, London, 2000.

[25] Das A., Pisana S., Chakraborty B., Piscanec S., Saha S. K., Waghmare U. V., Novoselov K. S., Krishnamurthy H. R., Geim A. K., Ferrari A. C., and Sood A. K. Monitoring dopants by Raman scattering in an electrochemically top-gated graphene transistor. *Nat Nano*, 3(4):210–215, 2008.

[26] Darran R. Cairns, Richard P. Witte, Daniel K. Sparacin, Suzanne M. Sachsman, David C. Paine, Gregory P. Crawford, and R. R. Newton. Strain-dependent electrical resistance of tin-doped indium oxide on polymer substrates. *Applied Physics Letters*, 76(11):1425–1427, 2000.

[27] Zhibin Yu, Qingwu Zhang, Lu Li, Qi Chen, Xiaofan Niu, Jun Liu, and Qibing Pei. Highly flexible Silver nanowire electrodes for shape-memory polymer light-emitting diodes. *Advanced Materials*, 23(5):664–668, 2011.

[28] Junbo Wu, Mukul Agrawal, HÃ©ctor A. Becerril, Zhenan Bao, Zunfeng Liu, Yongsheng Chen, and Peter Peumans. Organic light-emitting diodes on solution-processed graphene transparent electrodes. *ACS Nano*, 4(1):43–48, 2010.

[29] Liangbing Hu, Han Sun Kim, Jung-Yong Lee, Peter Peumans, and Yi Cui. Scalable coating and properties of transparent, flexible, silver nanowire electrodes. *ACS Nano*, 4(5):2955–2963, 2010.

[30] Ved Prakash Verma, Santanu Das, Indranil Lahiri, and Wonbong Choi. Large-area graphene on polymer film for flexible and transparent anode in field emission device. *Applied Physics Letters*, 96(20):203108, 2010.

[31] Jens Meyer, Piran R. Kidambi, Bernhard C. Bayer, Christ Weijtens, Anton Kuhn, Alba Centeno, Amaia Pesquera, Amaia Zurutuza, John Robertson, and Stephan Hofmann. Metal oxide induced charge transfer doping and band alignment of graphene electrodes for efficient organic light emitting diodes. *Scientific Reports*, 4:5380, Jun 2014. Article.

[32] Yi Song, Wenjing Fang, Allen L Hsu, and Jing Kong. Iron (III) chloride doping of CVD graphene. *Nanotechnology*, 25(39):395701, 2014.

[33] T. Sun, Z. L. Wang, Z. J. Shi, G. Z. Ran, W. J. Xu, Z. Y. Wang, Y. Z. Li, L. Dai, and G. G. Qin. Multilayered graphene used as anode of organic light emitting devices. *Applied Physics Letters*, 96(13):133301, 2010.

[34] Lewis Gomez De Arco, Yi Zhang, Cody W. Schlenker, Koungmin Ryu, Mark E. Thompson, and Chongwu Zhou. Continuous, highly flexible, and transparent graphene films by chemical vapor deposition for organic photovoltaics. *ACS Nano*, 4(5):2865–2873, 2010.

[35] Keun Soo Kim, Yue Zhao, Houk Jang, Sang Yoon Lee, Jong Min Kim, Kwang S. Kim, Jong-Hyun Ahn, Philip Kim, Jae-Young Choi, and Byung Hee Hong. Large-scale pattern growth of graphene films for stretchable transparent electrodes. *Nature*, 457(7230):706–710, 2009.

[36] F. Javier García de Abajo. Graphene plasmonics: Challenges and opportunities. *ACS Photonics*, 1(3):135–152, 2014.

[37] Jung-Yong Lee, Stephen T. Connor, Yi Cui, and Peter Peumans. Solution-processed metal nanowire mesh transparent electrodes. *Nano Letters*, 8(2):689–692, 2008.

[38] Yves Martin, David W. Abraham, and H. Kumar Wickramasinghe. High resolution capacitance measurement and potentiometry by force microscopy. *Applied Physics Letters*, 52(13):1103–1105, 1988.

[39] Y. Rosenwaks, R. Shikler, Th. Glatzel, and S. Sadewasser. Kelvin probe force microscopy of semiconductor surface defects. *Phys. Rev. B*, 70:085320, 2004.

[40] Francisco J. Bezares, Adolfo De Sanctis, José M. Saavedra, Achim Woessner, Pablo Alonso-González, Iban Amenabar, Jianing Chen, Thomas H. Bointon, Siyuan Dai, Dimitri N. Basov, Rainer Hillenbrand, Monica F. Craciun, Javier García de Abajo, Saverio Russo, and Frank H.L. Koppens. Near-field imaging of plasmon-phonon interaction effects in highly-doped graphene. In preparation.

# Part II

# Functionalised graphene optoelectronics

# 5

# LASER-DEFINED PHOTODETECTORS IN $FeCl_3$-INTERCALATED GRAPHENE

**NOTE:** The ideas and data presented in this chapter have been the subject of the following publication: Adolfo De Sanctis, Gareth F. Jones, Dominque J. Wehenkel, Francisco Bezares, Frank H. L. Koppens, Monica F. Craciun and Saverio Russo. *Extraordinary linear dynamic range in laser-defined functionalized graphene photodetectors.* Science Advances 3, 1602617 (2017).

## 5.1 INTRODUCTION

The unique combination of electrical and optical properties of graphene, discussed in section 2.1, have been exploited in optoelectronic applications soon after its isolation. Graphene-based photodetectors[1] have demonstrated a unique range of properties, including mechanical flexibility[2], large operating bandwidth[3] and a broadband spectral response. However, state-of-the-art inorganic photodetectors (i.e. Si, Ga, GaAs, etc) currently exhibit a linear response over a larger range of optical powers compared to graphene. This is due to the comparatively small density of states at energies below 1 eV in graphene (see section 2.1.4). Furthermore, the thermal diffusion of photo-generated carriers has been found to dominate photocurrent signals measured in graphene-based photodetectors[4;5;6], leading to a strong photothermoelectric (PTE) effect, which enables multiplication of hot carriers but also cause photo-responsive regions to be smeared out over distances exceeding 2 microns[7;5]. The narrow linear dynamic range (LDR) and the size of the photoresponsive regions in graphene pho-

todetectors, ultimately, limits integration of graphene pixels in high resolution sensing and video imaging applications.

Chemical functionalisation[8] is a largely unexplored route to overcome the intrinsic limitations on sensing introduced by hot carrier dynamics in pristine graphene. Although attempts have been made to use chemical functionalisation to engineer p-n junctions in graphene[9;10] and selectively define photo-responsive regions[2;11;12], no major improvements have been shown compared to pristine graphene devices and several challenges remain. These include finding forms of functionalisation which give ultra-high values of charge doping and are also air-stable. As discussed in chapter 4, intercalation of graphene with $FeCl_3$ has been found to result in high levels of hole-doping, with a room temperature electrical conductivity up to 1000 times larger than pristine graphene whilst maintaining equivalent absorption over the visible wavelength range[13;14]. At the same time, an unforeseen stability to harsh environmental conditions[15], the ease of large-area processing[14] and the promise for efficient coupling of telecommunication wavelength light to electrical signals through surface plasmons[16], make this material uniquely suited to explore novel optoelectronic applications.

In this chapter, the use of $FeCl_3$-FLG to form micro-metre and nano-metre scale planar photo-responsive junctions is demonstrated. Such junctions are directly written in the host material simply by using focused laser light. The measured photocurrent signals reveal a purely photovoltaic (PV) response and a LDR as large as 44 dB, which is at least 4500 times larger than any previously reported graphene photodetector[3;17;18;19;20;21]. At the same time, these detectors exhibit remarkable stability in atmospheric conditions without any form of encapsulation and maintain a broad spectral response from UV-A to mid-infrared (MIR) wavelengths. Finally, the ability to surpass the diffraction-limited resolution of far-field methods is demonstrated by employing emerging nano-photonics tools such as near-field photocurrent nanoscopy (NFPN), which allow to define photo-responsive junctions smaller than half the laser wavelength used.

## 5.2 SAMPLE PREPARATION AND INTERCALATION OF FLG

Intercalation of $FeCl_3$ molecules into mechanically exfoliated few layer graphene on a $Si/SiO_2$ substrate was conducted using the method described in section 4.1. A typical

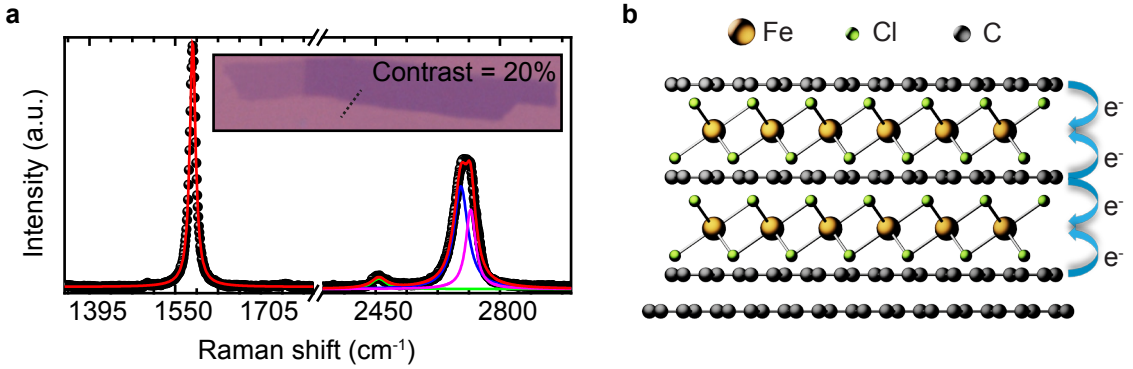


**Figure 5.1: Inferred stacking order of four-layer $FeCl_3$-FLG. a**, Raman spectrum of the four-layer graphene flake before intercalation with $FeCl_3$. Inset, Image analysis of an optical micrograph shows a 20% contrast between the flake and $SiO_2$/Si before intercalation. **b**, Schematic representation of the inferred stacking order.

Raman spectrum of the resulting system is shown in figure 5.2a, where the $G_0$ peak at $1580\,cm^{-1}$ is due to the $E_{2g}$ phonon mode of pristine graphene as well as the red-shifted $G_1 = 1615\,cm^{-1}$ and $G_2 = 1625\,cm^{-1}$ peaks of the same mode caused by the charge doping of $FeCl_3$ molecules adjacent to only one side of a graphene layer (stage-2) or sandwiching the carbon atoms (stage-1), as described in section 4.2.2.

### 5.2.1 *Stacking order of $FeCl_3$-FLG*

As described in section 4.2.3, using a combination of optical microscopy and Raman spectroscopy it is possible to determine the stacking order of the $FeCl_3$-FLG. The starting flake (before intercalation) used in the work presented in this chapter is a four-layer graphene, as inferred from the 20 % optical contrast relative to the Si/$SiO_2$ substrate, under white light illumination (see section 2.2.2), and the multi-peak structure of its Raman spectrum (figure 5.1a). Following $FeCl_3$ intercalation, the splitting of the G-band into three separate Lorentzian peaks is observed (figure 5.2b), as previously described. Hence, from the Raman spectrum it is possible to identify the configuration reported in figure 5.1b. Here one graphene layer remains isolated from $FeCl_3$. Two graphene layers are in contact with a single layer of intercalant and a fourth graphene layer at the centre of the structure is fully intercalated. It is highly improbable for $FeCl_3$ to remain on the top (or at the bottom) of the flake considering that any such

layer would be directly exposed to all solvents used during subsequent device fabrication processes. Furthermore, the $G_1$ peak intensity is indicative of a larger presence of stage-2 intercalated states, relative to stage-1, as expected for the structure shown in figure 5.1b.

## 5.3 LASER-DEFINED JUNCTIONS IN $FeCl_3$-FLG

Upon exposure of the intercalated flake to focused laser light with $\lambda_{\text{exc}} = 532$ nm at $P_{\text{opt}} = 15.3$ MW/cm$^2$ incident power for 3 s, a drastic modification of the Raman G-band is observed: with a pronounced down-shift of the G-peak positions; a reduction of their full-width at half-maximum (FWHM), the disappearance of the $G_2$ peak and the emergence of the $G_0$ peak, as shown in figure 5.2a. All of these changes indicate a reduction in hole doping caused by laser-induced displacement of $FeCl_3$, with the disappearance of the $G_2$ peak stemming from the complete removal of stage-1 intercalation.

The effectiveness of laser irradiation as a method for locally tailoring the intercalation of $FeCl_3$ in graphene, was tested by exposing a 5.5 $\mu$m wide section of the intercalated flake to a raster laser scan ($P_{\text{opt}} = 15.3$ MW/cm$^2$ for 3 s in 0.5 $\mu$m steps). The Raman spectra, collected at incrementally spaced locations across the laser-exposed region, are shown in figure 5.2b, both before and after laser-irradiation. Comparing the spectral profiles at each location, it is apparent that all irradiated regions undergo a substantial degree of de-intercalation. In figure 5.2c, the positions of the $G_1$ and $G_2$ peaks along a 21 $\mu$m line-scan are analysed. Uniform removal of the $G_2$ peak from the entirety of the rastered region clearly demonstrates that $FeCl_3$ molecules may be displaced from arbitrarily mapped areas. Importantly, the degree of intercalation remains unchanged away from the irradiated area, with the resolution of $FeCl_3$ displacement defined by the laser spot profile. The remarkable effectiveness of laser-induced de-intercalation over a significant fraction of the $FeCl_3$-FLG flake area presents an elegant method, akin to optical lithography, which can be used to locally customise the chemical functionalisation of graphene layers.

As shown in section 4.2.2, the shift of the Raman G-peak is quantitatively translated into a charge density. Adopting the same method, it can be seen that the laser irradiation of $FeCl_3$ causes a reduction in charge density of up to $\Delta p_{tot} \approx -0.6 \times 10^{14}$ cm$^{-2}$

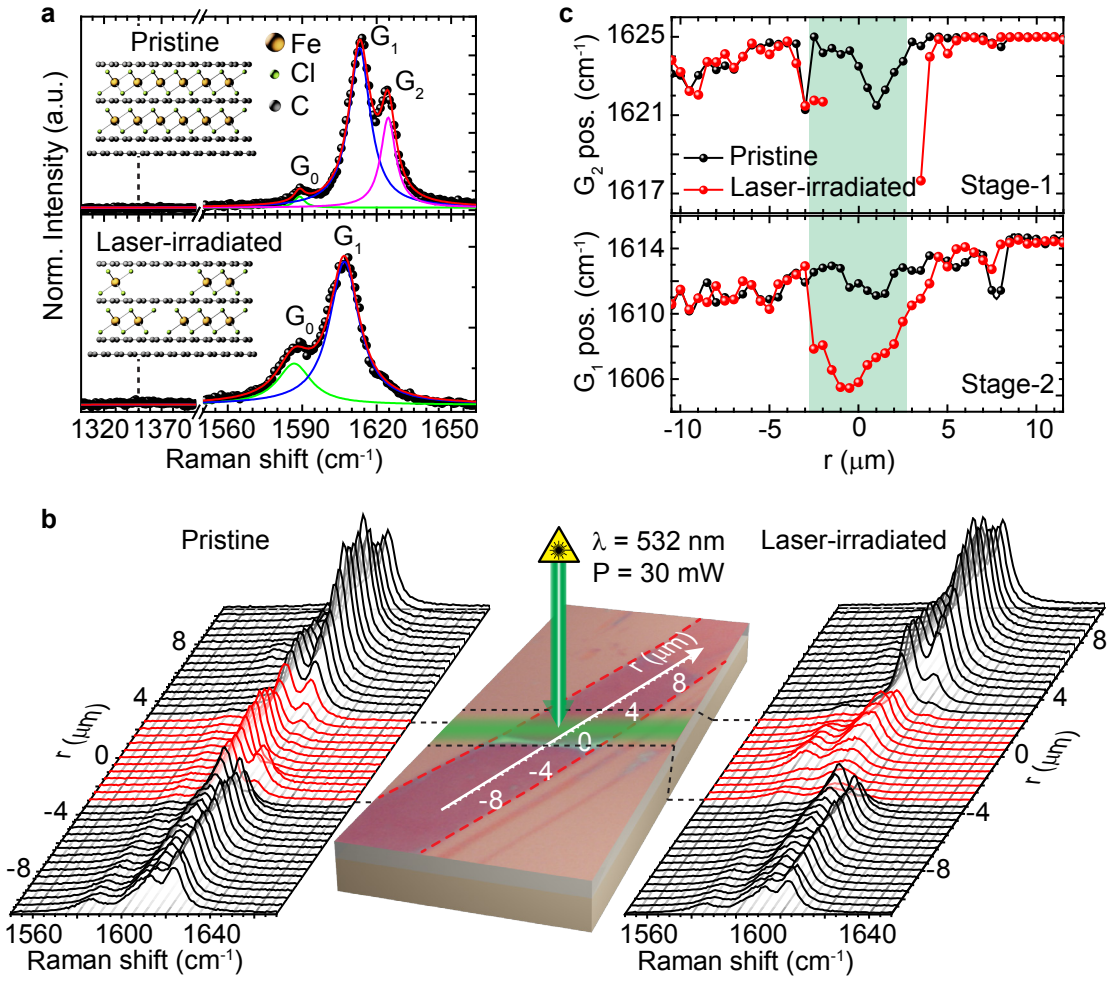


**Figure 5.2: Raman spectroscopy study of changes in laser-irradiated $FeCl_3$-FLG.** **a**, G-bands in $FeCl_3$-FLG before (top) and after (bottom) exposure to a 30 mW laser for 3 s ($\lambda = 532$ nm), with superimposed Lorentzian fits to the $G_0$, $G_1$ and $G_2$ peaks (continuous lines). **b**, Optical micrograph of the $FeCl_3$-FLG flake (delimited by red-dotted lines) with the laser-irradiated region highlighted in green. Raman spectra are acquired along $r$ before (left) and after (right) laser-irradiation. **c**, $G_2$ (top) and $G_1$ (bottom) peak positions representing stage-1 and stage-2 intercalation stages, respectively. Data points are extrapolated from the fit of the peaks in **b**.

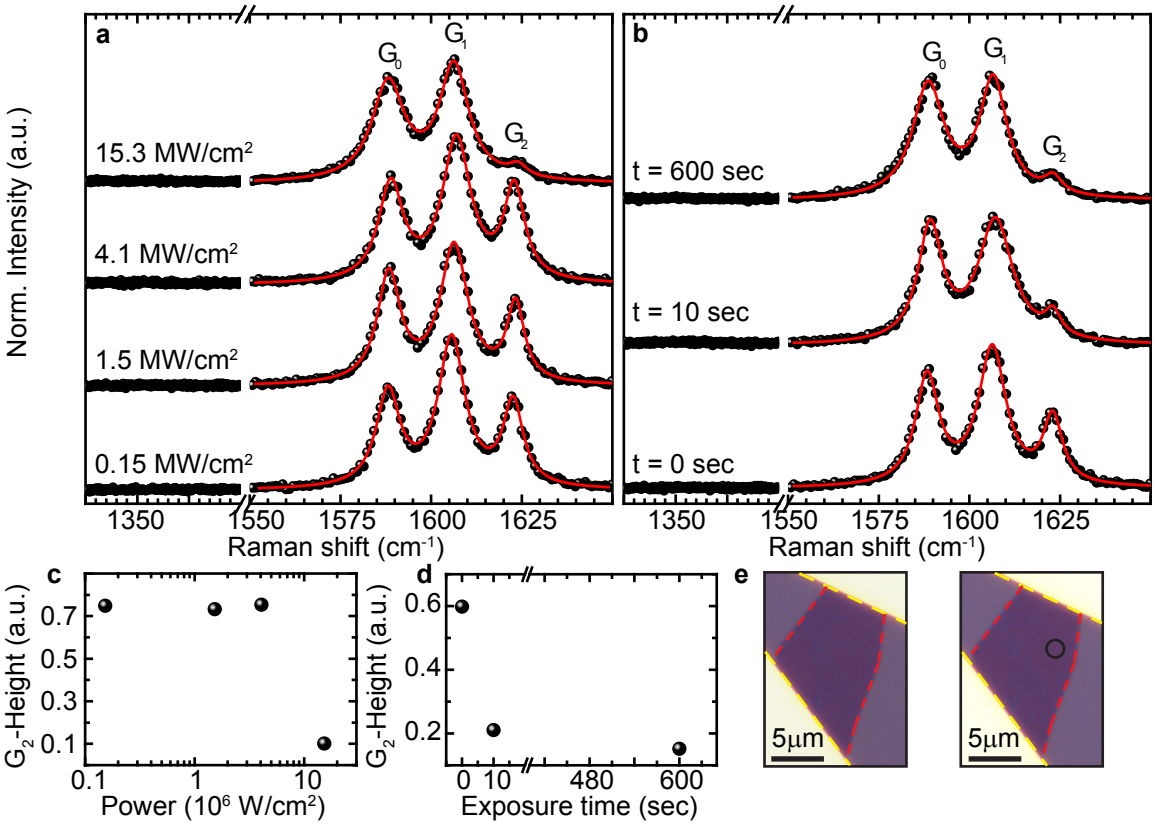


**Figure 5.3: Calibration of laser-induced displacement of $FeCl_3$** **a**, Raman spectra of $FeCl_3$-FLG acquired on the same location after irradiating with a $\lambda_{exc} = 532$ nm laser at different incident powers (0.15 MW/cm$^2$, 1.5 MW/cm$^2$, 4.1 MW/cm$^2$ and 15.3 MW/cm$^2$) for 20 seconds. **b**, Raman spectra of $FeCl_3$-FLG after irradiating with a power of 15.3 MW/cm$^2$ for 10 and 600 seconds compared with not-irradiated (t = 0 seconds). Each spectrum is acquired with the same laser at power of 0.15 MW/cm$^2$, red solid lines are Lorentzian fits. **c-d**, Summary of the $G_2$-peak Height (normalized to the Si peak at 520 cm$^{-1}$) versus incident power and exposure time, as extrapolated from the fits in panels **a-b**. **e** Optical micrography of the examined $FeCl_3$-FLG flake before (right) and after (left) laser irradiation on the highlighted spot (black circle), no optical modifications are visible in the flake.

(see figure 5.4a) which, also, agrees well with electrical measurements showing a 170% increase in resistivity over the modified area. Hence, the abrupt change in hole concentration at the boundaries of the laser-exposed region defines sharp p-p' junctions.

Finally, the effect of the laser power was analysed. In order to calibrate the laser-induced displacement of $FeCl_3$ with respect to the incident laser power and time, a Raman spectroscopy study on two spots of a representative flake (shown in figure 5.3) was performed. The effect of exposing $FeCl_3$-FLG to laser powers of 0.15 MW/cm$^2$, 1.5 MW/cm$^2$, 4.1 MW/cm$^2$ and 15.3 MW/cm$^2$ is shown in figure 5.3a-c: it is evident that a change in $G_2$-peak height, indicative of a reduction in doping, only occurs upon exposure to a high-power light source. The dependence upon time was examined by irradiating a spot on the flake with a fixed power of 15.3 MW/cm$^2$ for 0, 10 and 600 seconds (figure 5.3b-d). The doping modification happens very quickly, within the first 10 seconds, while a prolonged exposure causes no further effect. Optical micrographs of the flake before and after laser exposure are shown in figure 5.3e, no visible modifications to $FeCl_3$-FLG are observed. Notably, the absence of a defect-related Raman peak at $\sim 1350$ cm$^{-1}$ does not emerge, demonstrating that this functionalisation can sustain higher laser powers than pristine graphene.

## 5.4 OPTOELECTRONIC RESPONSE OF LASER-DEFINED $p - p'$ JUNCTIONS

In order to characterise the optoelectronic properties of these laser-defined junctions, scanning photocurrent microscopy (SPCM) was conducted on the device, as shown figure 5.4b, in short-circuit configuration (see section 3.4.4). The laser light was focused to a beam spot size of $1.0\,\mu$m at $P_{\text{opt}} = 300\,\mu W$. The acquired SPCM maps are shown in figure 5.5b-c for a variety of excitation wavelengths, together with an optical micrograph of the device (figure 5.5a). As expected for uniform doping, no significant photocurrent is observed in $FeCl_3$-FLG before laser patterning. However, when a p-p'-p junction is defined by laser-assisted displacement of $FeCl_3$, a photocurrent as large as 9 nA is measured at each of the lateral interfaces.

A multitude of physical mechanisms can give rise to a photoresponse. Of these, two play a major role in graphene-based photodetectors. They are the photothermoelectric PTE effect and the photovoltaic PV effect[1]. The PTE effect originates from a difference in Seebeck coefficients across a graphene junction formed by regions with a differing

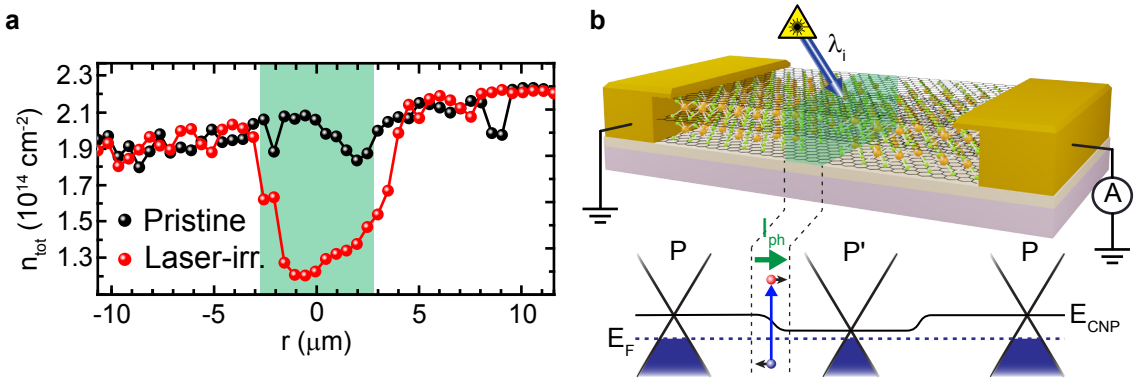


**Figure 5.4: Formation of p-p' junctions in $FeCl_3$-FLG. a**, Total charge carrier concentration before and after laser-assisted displacement of $FeCl_3$, estimated from G-peak positions in figure 5.2c. **b**, Short-circuit configuration (top) for scanning photocurrent measurements of a p-p'-p junction in (p' region in green). Schematic band structure (bottom) of each region illustrates of photo-generated carriers drifting under a chemical potential gradient.

density of states, as described in section 3.4.3. If the junction is illuminated, a local increase of temperature results in the diffusion of carriers and an opposing photovoltage is generated (see equation (3.29)). Hot carrier dynamics are generally recognised to dominate photocurrent generation in supported graphene devices due to inefficient cooling of electrons with the lattice[5;6]. For the PV effect, incident photons generate a density ($n_{ph}$) of carriers which, in the presence of an in-built electric field, are separated and induce current at the electrodes (see figure 5.4b). Other mechanisms such as the bolometric effect, photogating effect and Dyakonov-Shur effect require an externally applied voltage[1] and are therefore not active in the short circuit configuration adopted in these measurements.

A first insight on the microscopic mechanism behind the observed photocurrent can be gained by comparing the laser power dependence in pristine and intercalated graphene. Figure 5.6a shows a typical power dependence for photocurrent ($I_{PH} \propto P^{\alpha}$) generated in one of several measured monolayer graphene devices, where $\alpha = 2/3$ was obtained (see equation (3.32)). On the other hand, the photoresponse in $FeCl_3$-FLG is strikingly different from that of pristine graphene, exhibiting a linear dependence extending beyond three logarithmic decades of incident laser power. The observed difference originates from the charge carrier dynamics. More specifically, in pristine

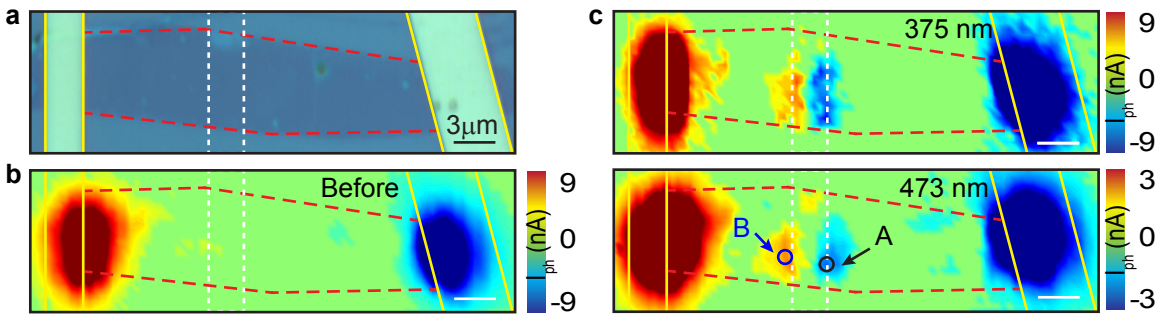


**Figure 5.5: SPCM study of laser-irradiated $FeCl_3$-FLG p-p' junctions.** **a**, Optical micrograph of a $FeCl_3$-FLG flake (red-dashed lines) with Au contacts (yellow lines). **b**, SPCM map of the photoresponse of the pristine device in **a**, measured at 473 nm incident wavelength. **c**, SPCM map after selective laser-assisted displacement of $FeCl_3$ (white dashed lines), measured at excitation wavelengths of 375 nm and 473 nm.

graphene the chemical potential ($\mu$) lies close to the charge neutrality point and the small Fermi surface imposes tight constraints on the maximum energy lost through momentum-conserving acoustic phonon emission ($\Delta E_{ac} < 2\hbar v_s k$, where $v_s \sim 2 \times 10^4\,\mathrm{m\,s^{-1}}$ is the acoustic phonon speed and $k$ is the hot carrier wavenumber)[22]. As a result, photo-excited carriers reach a steady state temperature far above that of the lattice ($T_h >> T_l$) and are cooled via short-range "supercollision" processes at sites of disorder[17;23]. If the PTE effect is similarly responsible for photocurrent in $FeCl_3$-FLG, the steady state temperature of hot carriers must lie significantly closer to that of the lattice ($T_h - T_l << T_l$) in order to justify the observed linear power dependence[17]. A reduction in $T_h$ can, indeed, be explained by the ultrahigh levels of charge density achieved through $FeCl_3$ intercalation; the expanded Fermi surface enhances $\Delta E_{ac}$ to as much as 60 times that of pristine graphene, accelerating the cooling of photo-generated charges. On the other hand, the small temperature gradients present at these highly doped junctions could diminish thermoelectric currents so much that they become negligible compared to signals generated by the PV effect. A linear power dependence would also be expected in this case, provided that the incident light intensity is sufficiently low so as to not affect the average lifetime of the photo-generated carriers. The observation of photocurrent with a linear dependence upon incident power therefore indicates enhanced cooling of hot carriers in $FeCl_3$-FLG but

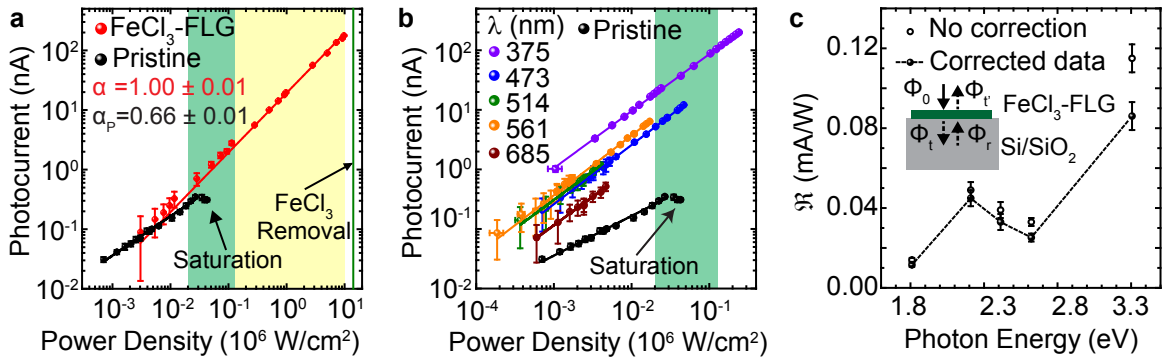


**Figure 5.6: Photoresponse characterisation at p-p' junctions in $FeCl_3$-FLG. a**, Photocurrent produced by $\lambda_{exc} = 473$ nm as a function of incident power density measured at a laser-defined p-p' junction and for pristine monolayer graphene (black). Power-law exponents ($I_{ph} \propto P^{\alpha}$) are detailed for each data set with fits shown as solid lines. Powers within the range at which photocurrent in pristine graphene has been reported to saturate are highlighted in green. Yellow-shaded area represents the extended range of $FeCl_3$-FLG. **b**, Photocurrent measured at the junction A in figure 5.5c using different excitation wavelengths, solid lines are linear fits. **c**, Spectral responsivity of a p-p' junction in $FeCl_3$-FLG shown with (filled circles) and without (open circles) correcting for reflections from the $SiO_2$/Si substrate. Dashed line is a guide to the eye. Inset: schematic of the model used to correct Re($\lambda$) for substrate reflections.

cannot, in contrast to what other studies have suggested[20], be used independently to distinguish between PTE and PV effect.

A careful analysis of the properties of the presented devices shows that these junctions are characterised by a pure PV response, thanks to the suppression of the temperature gradient at the $FeCl_3$-FLG junctions. Such analysis falls beyond the scope of this thesis, and it is detailed in Ref. 24.

### 5.4.1 *Bandwidth, noise and extraordinary linear dynamic range*

As discussed in section 3.4.1 and table 3.1, several parameters characterise the performance of a photodetector. Amongst those, the LDR defines the range in which the response of the detector is a linear function of the incident optical power, above the noise level. The LDR is expressed in decibels (dB) as:

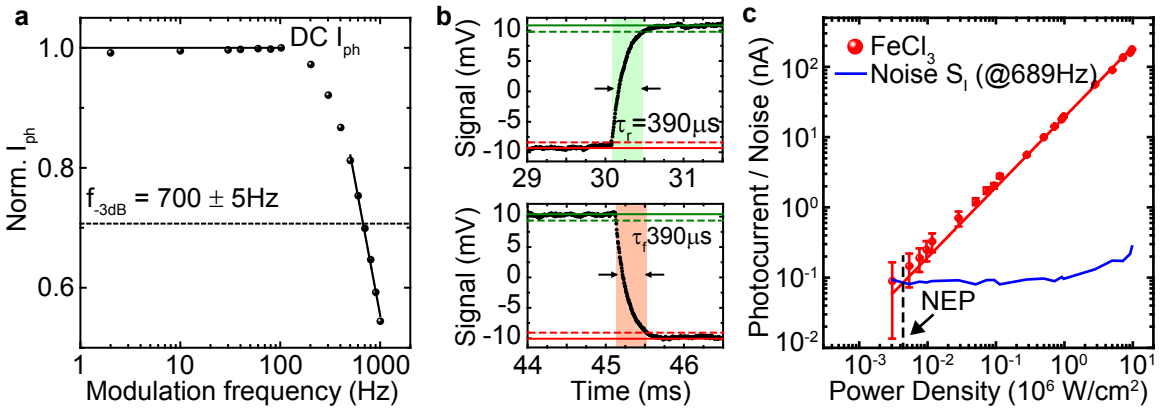


**Figure 5.7: BW and NEP of a laser-written $FeCl_3$-FLG junction device.** **a** Frequency-modulated photoresponse of the device measured in figure 5.6a: photocurrent is normalized to the DC value and the $-3$dB cut-off is marked by the dashed line. **b** Rise (top) and fall (bottom) time of the same device. Solid lines mark the steady state, dashed lines mark the $10\% - 90\%$ thresholds. **c**, Photoresponse as a function of laser power (red) together with the RMS noise measured during the same experiment (blue). The intersection marks the value of the NEP.

$$\mathrm{LDR} = 10 \times log_{10}\left(\frac{P_{\mathrm{sat}}}{\mathrm{NEP}}\right)\ [\mathrm{dB}], \tag{5.1}$$

where the noise-equivalent power (NEP) is defined as the power at which the signal-to-noise ratio (SNR) has a value of 1 and $P_{\mathrm{sat}}$ is the power at which the photoresponse deviates from linearity. The NEP can be measured directly or computed as:

$$\mathrm{NEP} = \frac{S_I}{R}\left[\frac{W}{\sqrt{\mathrm{Hz}}}\right], \tag{5.2}$$

where $S_I$ is the root-mean-square (RMS) current noise (in $\mathrm{A}/\sqrt{\mathrm{Hz}}$) and $R$ is the responsivity of the photodetector (in A/W). The operating bandwidth (BW), ultimately determines the speed at which the detector can record information. This is defined as the frequency at which the power of the detector is cut by 1/2, that is, when the photoresponse signal is depleted by $-3$ dB with respect to the direct-current (DC) value. The BW is related to the rise and fall time of the detector, which, ultimately, depend on the microscopic mechanisms which give rise to the observed photoresponse.

**Table 5.1: LDR of graphene and functionalized graphene devices.**

| Literature Reference | $P_{sat}$[a] | NEP[b] | LDR[c] |
|---|---|---|---|
| Kim *et al.*[18] | $10^{-3}$ W/cm$^2$ | - | - |
| Liu *et al.*[21] | 1.27 W/cm$^2$ | 0.03 W/cm$^2$ | 15 dB[d] |
| Tielrooij *et al.*[4] | 23 kW/cm$^2$ | - | - |
| Mueller *et al.*[3] | 51 kW/cm$^2$ | 10 kW/cm$^2$ | 7.5 dB[e] |
| Graham *et al.*[17] | 57 kW/cm$^2$ | - | - |
| Patil *et al.*[20] | 14 kW/cm$^2$ | - | - |
| Wang *et al.*[12] | 120 kW/cm$^2$ | 3.3 kW/cm$^2$ | 15 dB[e] |
| This work (Graphene) | 45 kW/cm$^2$ | - | - |
| **This work ($FeCl_3$-doped)** | **$> 10^4$ kW/cm$^2$** | **4 kW/cm$^2$** | **44 dB[d]** |

[a] Power density at which saturation of photocurrent is observed; [b] Noise Equivalent Power; [c] Linear Dynamic Range; [d] Measured; [e] Estimated.

The frequency-modulated photoresponse of the $FeCl_3$-FLG device is shown in figure 5.7a. The $-3$dB cut-off gives an operating BW of $700 \pm 5$ Hz, in good agreement with the rise and fall time measurements shown in figure 5.7b. To determine the NEP, RMS noise measurements were performed with a lock-in amplifier measuring the photocurrent directly (that is, with no current preamplifier in the circuit). The lock-in noise-equivalent bandwidth (NEBW) was set to be 16.6 Hz, the modulation frequency was 689 Hz, just below the operating BW of the device. Measured values are reported in figure 5.7c, together with values of the photocurrent, as a function of incident laser power. The NEP can be extrapolated and it is 4 kW/cm$^2$.

Using equation (5.1), the LDR of the laser-written $FeCl_3$-FLG device is 44 dB. This is 4500 times larger than previously reported graphene photodetectors (LDR $\approx$ 7.5 dB)[3] and $\sim$ 800 times larger than other functionalized graphene devices (LDR $\approx$ 15 dB)[12]. Furthermore, table 5.1 shows the saturation power density ($P_{sat}$) of graphene and functionalized graphene photodetectors reported in literature compared to the values measured in this work for $FeCl_3$-FLG junctions. Previous works have shown deviation from linear behaviour and saturation of photocurrent for power densities $< 57$ kW/cm$^2$ in graphene[17] and $< 120$ kW/cm$^2$ in functionalized graphene[12]. In contrast, $FeCl_3$-FLG junctions show a saturation level $> 10^4$ kW/cm$^2$, more than two orders of magnitude larger than other reports.

Equation (5.2) was used to calculate the NEP of different graphene-based photode-

tectors reported in literature[3;12]. Assuming a graphene photodetector operating at the same frequency as the device used in this work (689 Hz), it is possible to take as the main source of noise the $1/f$ contribution[25]. Using the results in Ref.s 25 and 26, the spectral noise for the examined device in table 5.1 is calculated to be $S_I = 1.0 \cdot 10^{-8}$ $A/\sqrt{Hz}$. The NEP for reference 21 is taken from the measured values and the LDR agrees well with the estimation made for the other reports.

### 5.4.2 *Spectral photoresponse*

Further assessment of the suitability of $FeCl_3$-FLG for optoelectronic applications is given by its spectral response, shown in figure 5.6b. The power dependence of photocurrent at a p-p' junction in $FeCl_3$-FLG is measured for various wavelengths of incident light ranging from UV-A (375 nm) to red (685 nm). Fits of the power exponent at each wavelength give: $\alpha_{375} = 0.99 \pm 0.01$, $\alpha_{473} = 1.05 \pm 0.06$, $\alpha_{514} = 0.97 \pm 0.03$, $\alpha_{561} = 0.99 \pm 0.01$ and $\alpha_{685} = 0.95 \pm 0.05$. Again, no deviation from a strictly linear power dependence in the whole measured power range is observed for each wavelength. This indicates that the ultra-high degree of charge carrier doping introduced by $FeCl_3$ intercalation acts as a uniquely stable method to fix the photo-generated carrier dynamics of graphene to an extended linear dynamic regime, avoiding the sensitivity to processing methods and environmental conditions which pristine graphene photodetectors[3;17] inevitably suffer from. In figure 5.6c, the spectral responsivity, $\mathfrak{R}(\lambda) = I_{ph}/P_{opt}(\lambda)$, of a p-p' junction is displayed with and without correcting for reflections from the $Si/SiO_2$ substrate (see appendix B). The photoresponse remains remarkably consistent across the entirety of the visible range, where $\mathfrak{R}(\lambda)$ varies by only one order of magnitude. Of particular interest is the increase in responsivity towards UV-A wavelengths, a region where the performance of silicon photo-diodes decreases. The extended LDR can be attributed to accelerated carrier cooling and the enhanced responsivity to an increased high energy density of states introduced by $FeCl_3$ intercalation[27]. This consistent proportionality between output electrical signal and incident optical power over a broad spectral range makes $FeCl_3$-FLG-based photodetectors ideally suited to radiometry and spectroscopy applications.

## 5.5 BELOW THE DIFFRACTION LIMIT

The spatial resolution of $FeCl_3$ displacement at the engineered p-p' junctions is determined by the profile of the laser spot used for patterning. In far-field optical microscopy, spot sizes are dictated by the Abbe diffraction-limit, $\sim \lambda/(2NA)$, where $NA$ is the numerical aperture of the objective (see also section 3.5.1.2). In order to explore the density to which graphene-based imaging pixels may be packed in the absence of hot carrier effects, a novel technique, that is scattering-SNOM, is employed to define photo-active junctions below the aforementioned limit. This technique has been used extensively to study the plasmonic[28] and optoelectronic[29] response of graphene-based devices and involves focusing a laser onto a metallised AFM tip which creates a strong, exponentially-decaying, field at its apex. The tip is then scanned across the sample, allowing parameters including topography, scattered light emission and local photo-current to be measured with sub-wavelength resolution[30].

Figure 5.8a-c show photocurrent maps, using a $\lambda_{exc} = 10\,\mu$m, from a tunable $CO_2$ laser, taken before and after displacement of $FeCl_3$ by a $\lambda_{exc} = 632\,$nm HeNe laser. The measurements were performed in short-circuit configuration. Planar junctions exhibiting a photovoltaic response are readily defined with a peak-to-peak separation of just 250 nm (figure 5.8f) whilst concurrent topography mapping (figure 5.8d-e) indicates that the flake surface remains undamaged. Importantly, the absorption of photons with energy $E << 2\mu$ in $FeCl_3$-FLG highlights the role of transitions to the $\pi$ band from localized states introduced by Fe, as predicted by density-functional theory (DFT) calculations[31]. This prevents Pauli blocking of long wavelengths and maintains a broadband spectral response in these novel photodetectors.

## 5.6 SUMMARY AND OUTLOOK

In conclusion, laser-patterning is an elegant method of creating photo-responsive junctions in intercalated few-layer graphene which is compatible with commercial roll-to-roll processes. Photo-responsive junctions in $FeCl_3$-FLG are engineered on the sub-micron scale and remain highly stable under atmospheric conditions and intense light exposure. This presents a unique opportunity relative to other methods of chemical functionalisation, whereby photocurrent mechanisms are reliably pinned to produce a linear

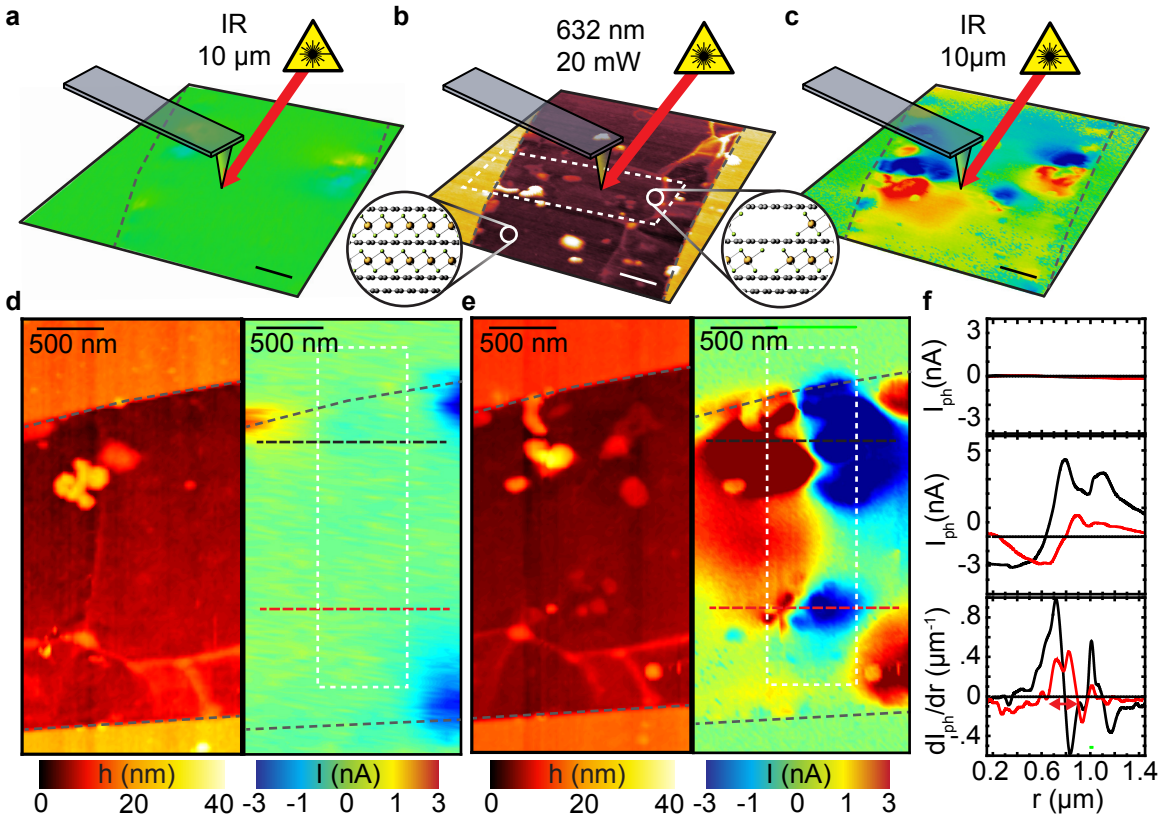


**Figure 5.8: High-resolution photo-active junctions in $FeCl_3$-FLG defined using scanning near-field optical microscopy (SNOM).** **a**, Spatial map of photocurrent in a uniformly-doped $FeCl_3$-flake before laser irradiation. **b**, Atomic force microscopy (AFM) topography and **c**, SPCM maps of the $FeCl_3$-FLG flake after laser irradiation with $\lambda_{exc}$ = 632 nm, scanned over a 500 nm region (white dashed lines). Insets: illustrations of the chemical structure in p- and p'-doped regions. Schematics of the excitation wavelength focussed on a metallized AFM tip in each measurement are included in **a-c**, outlines of the flake are superimposed (black dashed lines). Scale bars 500 nm. Magnified concurrent AFM topography and scanning photocurrent maps are shown before, **d**, and after, **e**, laser irradiation. **f**, Line profiles of photocurrent measured cross laser-defined p-p'-p junctions (**d** and **e**, red and black dashed lines) before (top panel) and after (middle panel) displacement of $FeCl_3$ molecules. First derivative plots of the photocurrent signal after $FeCl_3$ displacement (bottom panel) shows a peak-to-peak distance of 250 *nm* between adjacent p-p' junctions (red arrows).

response over broad ranges of power and wavelength with no requirement for encapsulation from the environment. These junctions show an extraordinary linear dynamic range up to 44 dB, more than 4500 times larger than other graphene photodetectors, that can operate at incident optical powers up to $10^4$ kW/cm$^2$ in the whole visible range and in the near-UV.

In order to exploit these findings in practical applications, future work will be required to achieve uniform intercalation of $FeCl_3$ in large-area few-layer graphene films of a consistent layer number. If this can be realized, these finds provide exciting prospects towards the development of novel light sensors with potential applications in imaging and spectroscopy.

# BIBLIOGRAPHY

[1] F. H. L. Koppens, T. Mueller, Ph Avouris, A. C. Ferrari, M. S. Vitiello, and M. Polini. Photodetectors based on graphene, other two-dimensional materials and hybrid systems. *Nat Nano*, 9(10):780–793, 2014.

[2] Nan Liu, He Tian, Gregor Schwartz, Jeffrey B.-H. Tok, Tian-Ling Ren, and Zhenan Bao. Large-area, transparent, and flexible infrared photodetector fabricated using p-n junctions formed by n-doping chemical vapor deposition grown graphene. *Nano Letters*, 14(7):3702–3708, 2014.

[3] Thomas Mueller, Fengnian Xia, and Phaedon Avouris. Graphene photodetectors for high-speed optical communications. *Nat Photon*, 4(5):297–301, 2010.

[4] K. J. Tielrooij, M. Massicotte, L. Piatkowski, A. Woessner, Q. Ma, P Jarillo-Herrero, N. F. van Hulst, and F. H. L. Koppens. Hot-carrier photocurrent effects at graphene-metal interfaces. *Journal of Physics: Condensed Matter*, 27(16):164207, 2015.

[5] Justin C. W. Song, Mark S. Rudner, Charles M. Marcus, and Leonid S. Levitov. Hot carrier transport and photocurrent response in graphene. *Nano Letters*, 11(11):4688–4692, 2011.

[6] Max C. Lemme, Frank H. L. Koppens, Abram L. Falk, Mark S. Rudner, Hongkun Park, Leonid S. Levitov, and Charles M. Marcus. Gate-activated photoresponse in a graphene p-n junction. *Nano Letters*, 11(10):4134–4137, 2011.

[7] Nathaniel M. Gabor, Justin C. W. Song, Qiong Ma, Nityan L. Nair, Thiti Taychatanapat, Kenji Watanabe, Takashi Taniguchi, Leonid S. Levitov, and Pablo Jarillo-Herrero. Hot carrier-assisted intrinsic photoresponse in graphene. *Science*, 334(6056):648–652, 2011.

[8] M F Craciun, I Khrapach, M D Barnes, and S Russo. Properties and applications of chemically functionalized graphene. *Journal of Physics: Condensed Matter*, 25(42):423201, 2013.

[9] Damon B. Farmer, Yu-Ming Lin, Ali Afzali-Ardakani, and Phaedon Avouris. Behavior of a chemically doped graphene junction. *Applied Physics Letters*, 94(21), 2009.

[10] Timm Lohmann, Klaus von Klitzing, and Jurgen H. Smet. Four-terminal magneto-transport in graphene p-n junctions created by spatially selective doping. *Nano Letters*, 9(5):1973–1979, 2009.

[11] Li Lin, Xiang Xu, Jianbo Yin, Jingyu Sun, Zhenjun Tan, Ai Leen Koh, Huan Wang, Hailin Peng, Yulin Chen, and Zhongfan Liu. Tuning chemical potential difference across alternately doped graphene p-n junctions for high-efficiency photodetection. *Nano Letters*, 16(7):4094–4101, 2016.

[12] S Wang, Y Sekine, S Suzuki, F Maeda, and H Hibino. Photocurrent generation of a single-gate graphene p-n junction fabricated by interfacial modification. *Nanotechnology*, 26(38):385203, 2015.

[13] Ivan Khrapach, Freddie Withers, Thomas H. Bointon, Dmitry K. Polyushkin, William L. Barnes, Saverio Russo, and Monica F. Craciun. Novel highly conductive and transparent graphene-based conductors. *Advanced Materials*, 24(21):2844–2849, 2012.

[14] Thomas H. Bointon, Gareth F. Jones, Adolfo De Sanctis, Ruth Hill-Pearce, Monica F. Craciun, and Saverio Russo. Large-area functionalized CVD graphene for work function matched transparent electrodes. *Scientific Reports*, 5:16464, 2015.

[15] Dominque J. Wehenkel, Thomas H. Bointon, Tim Booth, Peter Bøggild, Monica F. Craciun, and Saverio Russo. Unforeseen high temperature and humidity stability of $FeCl_3$ intercalated few layer graphene. *Scientific Reports*, 5:7609, 2015.

[16] F. Javier García de Abajo. Graphene plasmonics: Challenges and opportunities. *ACS Photonics*, 1(3):135–152, 2014.

[17] Matt W. Graham, Su-Fei Shi, Daniel C. Ralph, Jiwoong Park, and Paul L. McEuen. Photocurrent measurements of supercollision cooling in graphene. *Nat Phys*, 9(2):103–108, 2013.

[18] Chang Oh Kim, Sung Kim, Dong Hee Shin, Soo Seok Kang, Jong Min Kim, Chan Wook Jang, Soong Sin Joo, Jae Sung Lee, Ju Hwan Kim, Suk-Ho Choi, and Euyheon Hwang. High photoresponsivity in an all-graphene p-n vertical junction photodetector. *Nature Communications*, 5:3249, 2014.

[19] J. K. Tielrooij, L. Piatkowski, M. Massicotte, A. Woessner, Q. Ma, Y. Lee, S. K. Myhro, N. C. Lau, P. Jarillo-Herrero, F. N. van Hulst, and F. H. L. Koppens. Generation of photovoltage in graphene on a femtosecond timescale through efficient carrier heating. *Nat Nano*, 10(5):437–443, 2015.

[20] Vikram Patil, Aaron Capone, Stefan Strauf, and Eui-Hyeok Yang. Improved photoresponse with enhanced photoelectric contribution in fully suspended graphene photodetectors. *Scientific Reports*, 3:2791, 2013.

[21] Chang-Hua Liu, You-Chia Chang, Theodore B. Norris, and Zhaohui Zhong. Graphene photodetectors with ultra-broadband and high responsivity at room temperature. *Nat Nano*, 9(4):273–278, 2014.

[22] R. Bistritzer and A. H. MacDonald. Electronic cooling in graphene. *Phys. Rev. Lett.*, 102:206410, May 2009.

[23] Justin C. W. Song, Michael Y. Reizer, and Leonid S. Levitov. Disorder-assisted electron-phonon scattering and cooling pathways in graphene. *Phys. Rev. Lett.*, 109:106602, 2012.

[24] Adolfo De Sanctis, Gareth F. Jones, Dominque J. Wehenkel, Francisco Bezares, Frank H. L. Koppens, Monica F. Craciun, and Saverio Russo. Extraordinary linear dynamic range in laser-defined functionalized graphene photodetectorss. Under review.

[25] Alexander A. Balandin. Low-frequency 1/f noise in graphene devices. *Nat Nano*, 8(8):549–555, 2013.

[26] G. Liu, W. Stillman, S. Rumyantsev, Q. Shao, M. Shur, and A. A. Balandin. Low-frequency electronic noise in the double-gate single-layer graphene transistors. *Applied Physics Letters*, 95(3), 2009.

[27] Xingquan Zou, Da Zhan, Xiaofeng Fan, Dongwook Lee, Saritha K. Nair, Li Sun, Zhenhua Ni, Zhiqiang Luo, Lei Liu, Ting Yu, Zexiang Shen, and Elbert E. M. Chia. Ultrafast carrier dynamics in pristine and $FeCl_3$-intercalated bilayer graphene. *Applied Physics Letters*, 97(14), 2010.

[28] Z. Fei, A. S. Rodin, G. O. Andreev, W. Bao, A. S. McLeod, M. Wagner, L. M. Zhang, Z. Zhao, M. Thiemens, G. Dominguez, M. M. Fogler, A. H. Castro Neto, C. N. Lau, F. Keilmann, and

D. N. Basov. Gate-tuning of graphene plasmons revealed by infrared nano-imaging. *Nature*, 487(7405):82–85, 2012.

[29] Achim Woessner, Pablo Alonso-González, Mark B. Lundeberg, Yuanda Gao, Jose E. Barrios-Vargas, Gabriele Navickaite, Qiong Ma, Davide Janner, Kenji Watanabe, Aron W. Cummings, Takashi Taniguchi, Valerio Pruneri, Stephan Roche, Pablo Jarillo-Herrero, James Hone, Rainer Hillenbrand, and Frank H. L. Koppens. Near-field photocurrent nanoscopy on bare and encapsulated graphene. *Nature Communications*, 7:10783, 2016. Article.

[30] F. Keilmann and R. Hillenbrand. Near-field microscopy by elastic light scattering from a tip. *Philosophical Transactions of the Royal Society of London A: Mathematical, Physical and Engineering Sciences*, 362(1817):787–805, 2004.

[31] Da Zhan, Li Sun, Zhen Hua Ni, Lei Liu, Xiao Feng Fan, Yingying Wang, Ting Yu, Yeng Ming Lam, Wei Huang, and Ze Xiang Shen. Fecl3-based few-layer graphene intercalation compounds: Single linear dispersion electronic band structure and strong charge transfer doping. *Advanced Functional Materials*, 20(20):3504–3509, 2010.

# 6

# HEXAGONAL-DOMAIN $FeCl_3$-FLG FOR POSITION-SENSITIVE PHOTODETECTORS

**NOTE:** The ideas and data presented in this chapter have been the subject of the following publication: Adolfo De Sanctis, Matthew D. Barnes, Iddo Amit, Monica F. Craciun and Saverio Russo. *Functionalised hexagonal-domain graphene for position-sensitive photodetectors*. Nanotechnology, 28:124004 (2017).
The growth of the APCVD graphene here reported was carried out by Matthew D. Barnes with assistance from the author in the transfer stage.

## 6.1 INTRODUCTION

As discussed in chapter 5, the photoresponse of graphene-based photodetectors (PDs) has been investigated with many techniques. Graphene has been tested in many applications, such as: high-responsivity[1] and high-speed[2] broadband PDs, wave-guide coupling[3] and transparent and flexible electrodes[4]. However, so far, no reports have been made of its application in position-sensitive detectors (PSDs). Such devices traditionally consist of a semiconductor (Si or Ge) junction with four contacts, which exploits the so-called *lateral photoeffect*[5]. This consists of a photovoltage generated at the junction plane in the presence of localized illumination, in addition to the conventional photovoltage effect that is formed across the junction. This effect has been extensively studied in the past[6;7] and it is at the base of PSDs presently used in many applications, such as: laser alignment, motion control, automation and scanning probe microscopy. The detection of focussed X-rays *via* field-effect in a graphene transistor

has been shown[8], though no other uses of graphene for PSDs in the ultra-violet (UV), visible and near-infrared (NIR) spectral range have been reported. Furthermore, the use of functionalised graphene for such applications has not been demonstrated.

In this chapter, the first all-graphene position-sensitive detector (PSD) is presented. This is based on chemically functionalized multilayer hexagonal domains of graphene grown by atmospheric pressure chemical vapour deposition (APCVD)[9].

## 6.2 SAMPLES PREPARATION

Multilayer hexagonal domains of graphene were grown on copper by APCVD[10] using a melting/re-solidification pre-treatment step to reduce nucleation density and increase domain size. Growth was carried out at $\sim$ 1075°C using diluted $CH_4$ (1000 ppm) as the carbon precursor and a high $H_2/CH_4$ (50/25 sccm) to aid multilayer formation. The crystals where then transferred to highly doped Si substrate capped with 285 nm thermal $SiO_2$ using poly(methyl methacrylate) (PMMA)-supported electrochemical delamination[11;12]. The delamination step was performed using a 0.5M NaCl solution and glassy carbon anode at 0.5 A, followed by rinsing in de-ionised water. Intercalation with $FeCl_3$ was carried out using the method reported in section 4.1, with an intercalation time $\tau_2$ of 12 hours.

Devices were fabricated using standard electron-beam lithography, as described in appendix A.2 and characterised using the techniques and the apparatus described in chapter 3.

## 6.3 CHARACTERISATION OF FUNCTIONALISED HEXAGONAL-DOMAINS OF GRAPHENE

Figure 6.1a shows the optical micrographs and Raman spectra of a pristine, as-transferred, multi-layer hexagonal domain of graphene grown by APCVD. Each layer grows in a stacked sequence, where the multi-layers appear at the centre of the first single-layer sharing the same nucleation site[13]. The Raman spectrum of the first layer (1) shows the the G peak at $\sim$ 1585 $cm^{-1}$ and the 2D peak at $\sim$ 2700 $cm^{-1}$. The shape of the 2D band, a single Lorentzian peak, and intensity ratio $I_{2D}/I_G \sim 1.9$ confirm the single-layer nature of the crystal. The spectrum of the second layer (2) shows the same

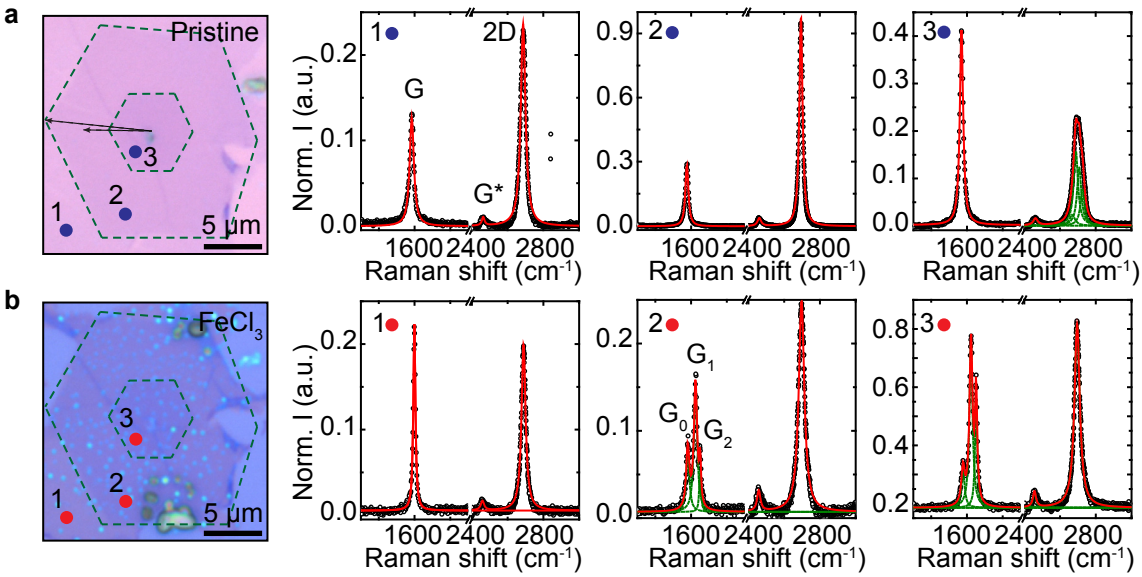


**Figure 6.1: Raman characterisation of intercalated APCVD graphene.** **a**, Optical micrograph (left) and Raman spectra (right) of pristine APCVD graphene hexagonal crystals on three different locations: (1) first crystal on substrate, (2) second layer grown on the first, (3) third layer. Dashed lines indicate the twisting of the hexagonal crystals. **b**, Optical micrograph and Raman spectra of the same crystals after intercalation with $FeCl_3$. Raman spectra are normalized to the height of the 1-TO mode of Si at 520 $cm^{-1}$.

features but with a ratio $I_{2D}/I_G \sim 3.36$, which deviates from the expected ratio for two AB-stacked graphene layers[14]. This is due to the rotation of the crystallographic axes with respect to the underlying layer, producing an effective decoupling of the two stacked layers[15;10]. The third layer (3) is slightly twisted with respect to the second, as shown by optical inspection, and the spectrum shows a 2D band that can be fitted with the convolution of 4 Lorentzian peaks, which is characteristic of twisted bilayer graphene with a twist angle $< 3°$, as reported in literature[10;16]. These observations are common to all examined crystals.

Figure 6.1b presents the optical micrograph and the Raman spectra of the intercalated flake. The Raman spectra are acquired in the same locations as in figure 6.1a and show the characteristic peaks of $FeCl_3$-FLG. The first layer (1) shows an upshift of the position of the G peak to 1600 $cm^{-1}$ and an increase in the height ($I_{2D}/I_G \sim 0.92$). The second (2) and third (3) layers show the expected split of the G band into three peaks,

each corresponding to different doping levels, as previously detailed in section 4.2.2: the $G_0$-peak is the signature of pristine graphene; the $G_1$-peak is given by a graphene layer in contact with one $FeCl_3$ layer (stage-2) and the $G_2$-peak is given by one layer of graphene sandwiched between two $FeCl_3$ layers (stage-1). The shape of the 2D-band also indicates the effective decoupling of the graphene layers by the intercalant. The peaks related to the $FeCl_3$ molecules lie at significant lower energies ($100-400\ cm^{-1}$)[17], therefore they do not interfere with the modes of graphene. These results confirm the successful intercalation of hexagonal-domains of APCVD graphene with $FeCl_3$.

Atomic force microscopy (AFM) was used to evaluate the quality of the intercalated APCVD graphene. Figure 6.2a-b show the topography image of a pristine crystal, with a second layer grown at the centre, as seen optically (inset). Here, a series of parallel wrinkles (green arrows) can be observed. These match the topography of the re-solidified copper used as metal catalyst during the growth. More interestingly, larger wrinkles running in the perpendicular direction with respect to the first ones, originating from the centre of the crystal (blue arrows) and ending close to the middle of the hexagon's side, are observed as well. Wrinkles in APCVD graphene have been previously reported[12;18] to form during the cooling stage due to the different thermal expansion coefficients of graphene and copper.

Intercalation with $FeCl_3$ also affects the surface of graphene. Figure 6.2c-d show the AFM topography and phase images of an intercalated crystal. In this case the image was acquired after fabrication of metal contacts. Focusing on the topographic features, the absence of the substrate-related wrinkles is apparent, while a number of bubble-like structures are still present and the cross-directional wrinkles can still be seen (blue arrows). The disappearance of small wrinkles is attributed to the intercalation process: by separating the graphene layers, the intercalant allows them to relax. The AFM phase image can readily distinguish between different materials, as it represents the phase lag between the tip excitation signal and its motion that is due to the (viscoelastic) damping properties of the sample[19]. In figure 6.2d it can be seen that the bubble-like structures observed in topography show a clear phase contrast. Their distribution and density is comparable with what is observed in the pristine crystals, suggesting that those structures can be attributed to PMMA residues from the transfer process[20].

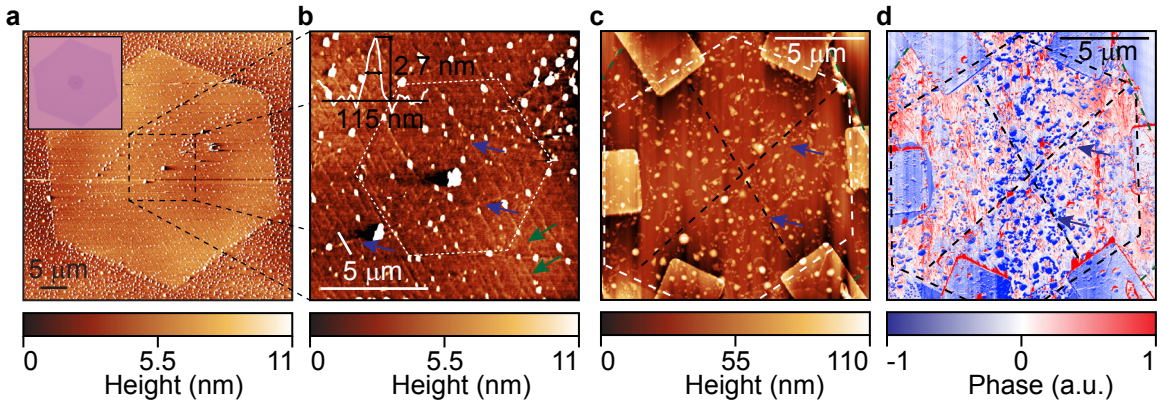


**Figure 6.2: AFM characterisation of intercalated APCVD graphene.** **a**, AFM topography of a pristine APCVD graphene hexagonal crystal after transfer on $Si/SiO_2$ substrate. Inset: optical micrograph of the same crystal. **b**, High resolution AFM topography of the central area. Blue and green arrows indicate wrinkles. Inset: profile of a wrinkle, height 2.7 nm and width 115 nm. **c**, AFM topography of a $FeCl_3$-FLG hexagonal crystal in a multi-terminal photodetector device. **d**, Tapping phase image of the same device. Dashed lines as in figure 6.3, blue arrows indicate the residual wrinkles after intercalation.

### 6.3.1 *APCVD graphene photodetectors*

The optoelectronic properties of intercalated hexagonal-domain of multi-layer graphene are now studied. Figure 6.3a shows a schematic representation of a multi-terminal device, where the contacts have been positioned in parallel to the sides of the top-layer hexagon, as shown in the optical micrograph (figure 6.3b). The resistance across two opposing pair of contacts, namely 1-4 and 3-6 in figure 6.3b, was measured to be $R_{1-4} = 660 \pm 2\,\Omega$ and $R_{3-6} = 670 \pm 2\,\Omega$, in agreement with the results in chapters 4 and 5. The photoresponse of the device was characterized using SPCM, employing, each time different pairs of contacts. Figure 6.4a,b show the SPCM maps acquired with contacts 1-4 and 3-6, respectively. Both SPCM maps show photocurrent $I_{\mathrm{ph}}$ being generated across the whole device, with a net change in sign appearing at the centre of it, in the direction orthogonal to the contacts. The dashed black lines in figure 6.4a,b mark the position of the maxima of the photocurrent. Measuring across both pair of contacts and summing the two signals, a SPCM map is obtained, which displays a clear four-fold symmetry of the photocurrent, as shown in figure 6.4c. where

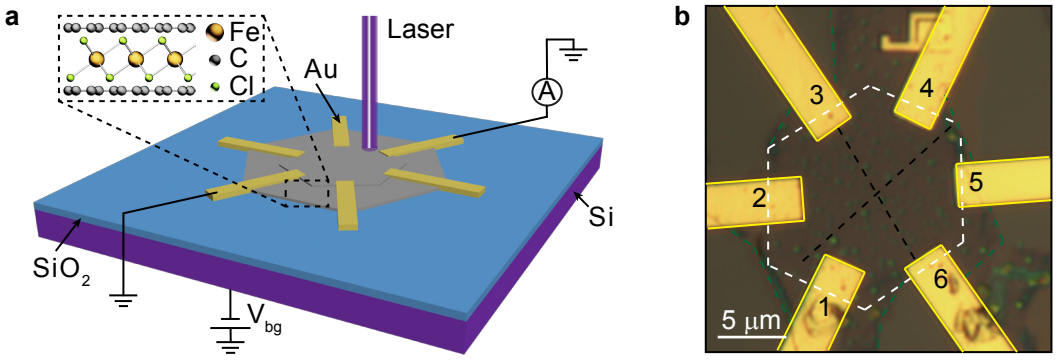


**Figure 6.3: Multi-terminal hexagonal graphene device.** **a**, Schematic of the multi-terminal device and scanning photocurrent microscopy (SPCM) measuring geometry. Inset: layer structure of $FeCl_3$-FLG. **b**, Optical micrograph of the device.

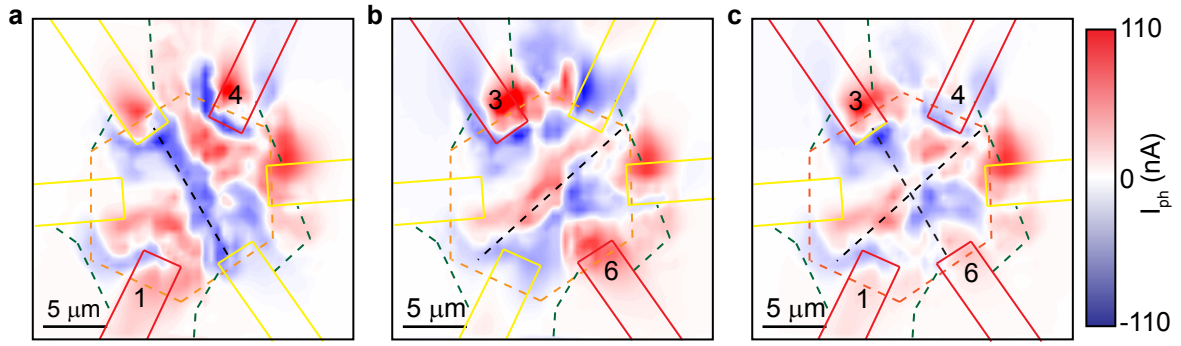


**Figure 6.4: SPCM maps of hexagonal graphene device.** **a**, SPCM map with contacts 1 and 4 connected. **b**, SPCM map with terminals 3 and 6. **c**, Sum of the SPCM maps shown in panels **a** and **b**. Dashed green lines mark the first graphene layer while dashed hexagons (white and orange) mark the second. Dashed black lines indicate the regions in the flake where $I_{ph}$ reverses sign.

the black dashed lines are the same as in figure 6.4a,b. Superimposing these lines, extrapolated from the SPCM map, onto the AFM maps of the same device, shown in figure 6.2c-d, it is clear that they match the observed crossed wrinkles in the graphene crystal.

The role of grain boundaries and wrinkles in graphene-based photodetectors has been studied using near-field photocurrent nanoscopy (NFPN), where the presence of grain boundaries was associated with a reversal in the sign of the photocurrent while enhanced photocurrent was observed in the presence of wrinkles[21]. The growth of hexagonal domains by APCVD is known to give high-quality, defect-free, graphene with no grain boundaries present across the device. The results presented so far, point towards the fact that the observed photocurrent is related to the intercalation spatial inhomogeneity, and thus to the doping inhomogeneity, of the graphene crystals. The presence of wrinkles is likely to create clusters of $FeCl_3$, increasing the level of doping in those regions, while sign reversal is related to a sharp change in doping, forming a p-$p^+$ junction in the highly doped graphene. These junctions can therefore act as photoactive centres giving the observed photoresponse for the overall device.

To confirm these hypotheses, a Raman map of the device was acquired. In figure 6.5a,d the fit of Lorentzian peaks to the G-band region are reported. Figure 6.5a,b show the height and position of the $G_0$ peak, respectively, while the $G_1$ band is shown in figure 6.5c,d. The presence of a blueshifted $G_0$ peak which agrees very well the boundaries of the crystal and indicates areas with partial intercalation of $FeCl_3$ within the graphene layers. The $G_1$ peak height decreases significantly in the region where a sign reversal in photocurrent is observed (the cross-shaped structure). This decrease in height is also accompanied by a redshift of the $G_1$ peak, from $\sim 1612\,cm^{-1}$ to $\sim 1605\,cm^{-1}$, in the same region, as shown in figure 6.5d. Using the model described in section 4.2.2 it is possible to extrapolate the total density of holes in doped graphene from the position of the G-band peaks. The results are shown in figure 6.6 (bottom insets) where a gradient of charge density is present along the two lines determined by the photocurrent maps, confirming our hypotheses. These doping gradients are discussed in the next section.

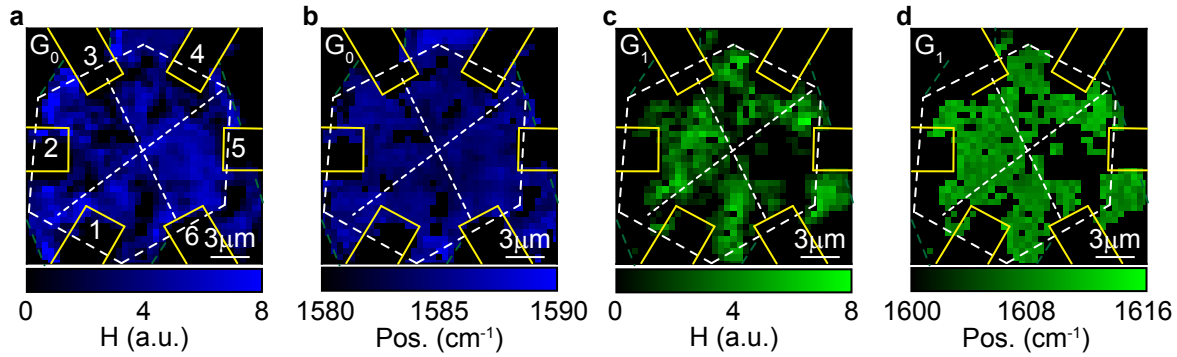


**Figure 6.5: Raman maps of the hexagonal graphene device.** **a**, $G_0$ peak height and **b**, $G_0$ peak position. **c**, $G_1$ peak height and **d**, $G_1$ peak position. Solid and dashed lines as in figure 6.4.

### 6.3.2 *Towards position-sensitive light-detection in intercalated graphene*

The unique photocurrent distribution, with a four-fold symmetry, observed in the examined device (figure 6.4c), can be used for position-sensitive applications. Commercial PSDs exploit the photovoltage generated parallel to a semiconductor junction in the presence of local illumination[5]. This effect has been extensively studied in the past[6;7] and is characterized by a bipolar linear photoresponse as a function of illumination position. Figure 6.6a,b (top panels) show the line profiles extrapolated from the SPCM maps in figure 6.4a,b, while in the bottom panels the same line profiles acquired on the charge density $n_h$ maps are reported. The mean value of the log-normal distribution of $n_h$ ($\overline{n_h} = (4.27 \pm 0.02) \cdot 10^{13}\,\mathrm{cm}^{-2}$) separates values $n_h < \overline{n_h}$ (low doping, p regions) and $n_h > \overline{n_h}$ (high doping, $p^+$ regions). It can be seen that the extremes of $I_{\mathrm{ph}}$ are located where $n_h$ crosses $\overline{n_h}$, i.e. in the presence of a p-$p^+$ junction. At the same time, bipolar linear regions are present (green lines), where the photocurrent changes sign at the centre of the photoactive junction. This behaviour is very similar to what is observed in a *lateral* photoactive junction[5]. In this case the junction is formed between areas of different doping in the functionalised graphene, induced by the inhomogeneity of the $FeCl_3$ intercalation driven by the wrinkles in the pristine APCVD crystals. Therefore, exploiting a multi-terminal geometry, as the one adopted here, it is possible to use these linear regions to determine the position of a focussed light spot on the device.

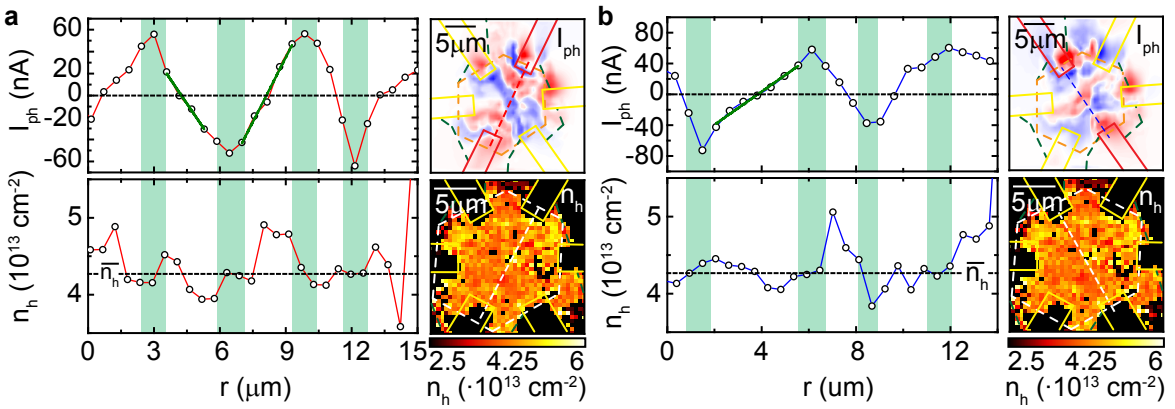


**Figure 6.6: PSD characterization.** **a**, Line profiles of photocurrent $I_{\mathrm{ph}}$ (top) and total hole density $n_h$ (bottom) taken along the dashed lines shown in the right panels, with contacts 3 and 6 connected. **b**, Same line profiles as in **a** with contacts 1 and 4. Green solid lines mark the linear regions, green-shaded areas mark the maxima and minima of the photocurrent and the corresponding hole density. $\overline{n_h}$ is the log-normal mean value of the reported data.

## 6.4 SUMMARY AND OUTLOOK

In summary, the successful intercalation of multilayer APCVD-grown hexagonal crystals of graphene has been demonstrated together with its use as a PSD. The degree of intercalation and the resulting doping of graphene was characterised, showing the formation of multiple p-p$^+$ junctions associated with the presence of wrinkles in the pristine APCVD crystals. At the same time, the photoresponse of a multi-terminal device shows a strong spatial correlation between the observed photocurrent and the p-p$^+$ junctions. The photoresponse is found to be a linear function of the laser spot position and changes sign at the centre of each junction. This behaviour, combined with a four-fold pattern in the spatially resolved photocurrent, make these devices ideal candidates for position sensitive detection of focussed light. Furthermore, all measurements have been repeated after $\sim$ 11 months exposure of the device to environmental conditions, showing no change in the photoresponse, in agreement with the previously reported stability of this material[22]. These findings pave the way to additional functionality in graphene-based optoelectronic devices and open a new route towards flexible, lightweight, transparent and highly stable PSDs, with possible employment in smart textile and wearable electronics[23].

# BIBLIOGRAPHY

[1] Chang-Hua Liu, You-Chia Chang, Theodore B. Norris, and Zhaohui Zhong. Graphene photodetectors with ultra-broadband and high responsivity at room temperature. *Nat Nano*, 9(4):273–278, 2014.

[2] Thomas Mueller, Fengnian Xia, and Phaedon Avouris. Graphene photodetectors for high-speed optical communications. *Nat Photon*, 4(5):297–301, 2010.

[3] Xiaomu Wang, Zhenzhou Cheng, Ke Xu, Hon Ki Tsang, and Jian-Bin Xu. High-responsivity graphene/silicon-heterostructure waveguide photodetectors. *Nat Photon*, 7(11):888–891, 2013.

[4] Elias Torres Alonso, George Karkera, Gareth F. Jones, Monica F. Craciun, and Saverio Russo. Homogeneously bright, flexible, and foldable lighting devices with functionalized graphene electrodes. *ACS Applied Materials & Interfaces*, 8(26):16541–16545, 2016.

[5] J. Torkel Wallmark. A new semiconductor photocell using lateral photoeffect. *Proc. IRE*, 45:474–483, April 1957.

[6] Gerald Lucovsky. Photoeffects in nonuniformly irradiated p-n junctions. *Journal of Applied Physics*, 31(6):1088–1095, 1960.

[7] T. G. Carr, J. C. Richmond, and R. G. Wagner. Position-sensitive schottky barrier photodiodes: Time-dependent signals and background saturation effects. *IEEE Transactions on Electron Devices*, 17(7):507–513, 1970.

[8] Edward Cazalas, Biddut K. Sarker, Michael E. Moore, Isaac Childres, Yong P. Chen, and Igor Jovanovic. Position sensitivity of graphene field effect transistors to X-rays. *Applied Physics Letters*, 106(22), 2015.

[9] Ali Mohsin, Lei Liu, Peizhi Liu, Wan Deng, Ilia N. Ivanov, Guoliang Li, Ondrej E. Dyck, Gerd Duscher, John R. Dunlap, Kai Xiao, and Gong Gu. Synthesis of millimeter-size hexagon-shaped graphene single crystals on resolidified copper. *ACS Nano*, 7(10):8924–8931, 2013.

[10] Rui He, Ting-Fung Chung, Conor Delaney, Courtney Keiser, Luis A. Jauregui, Paul M. Shand, C. C. Chancey, Yanan Wang, Jiming Bao, and Yong P. Chen. Observation of low energy raman modes in twisted bilayer graphene. *Nano Letters*, 13(8):3594–3601, 2013.

[11] Yu Wang, Yi Zheng, Xiangfan Xu, Emilie Dubuisson, Qiaoliang Bao, Jiong Lu, and Kian Ping Loh. Electrochemical delamination of CVD-grown graphene film: Toward the recyclable use of copper catalyst. *ACS Nano*, 5(12):9927–9933, 2011.

[12] Libo Gao, Wencai Ren, Huilong Xu, Li Jin, Zhenxing Wang, Teng Ma, Lai-Peng Ma, Zhiyong Zhang, Qiang Fu, Lian-Mao Peng, Xinhe Bao, and Hui-Ming Cheng. Repeated growth and bubbling transfer of graphene with millimetre-size single-crystal grains using platinum. *Nat Commun*, 3:699, 2012.

[13] Ali Mohsin, Lei Liu, Peizhi Liu, Wan Deng, Ilia N. Ivanov, Guoliang Li, Ondrej E. Dyck, Gerd Duscher, John R. Dunlap, Kai Xiao, and Gong Gu. Synthesis of millimeter-size hexagon-shaped graphene single crystals on resolidified copper. *ACS Nano*, 7(10):8924–8931, 2013.

[14] L.M. Malard, M.A. Pimenta, G. Dresselhaus, and M.S. Dresselhaus. Raman spectroscopy in graphene. *Physics Reports*, 473(5–6):51–87, 2009.

[15] Daniel R. Lenski and Michael S. Fuhrer. Raman and optical characterization of multilayer turbostratic graphene grown via chemical vapor deposition. *Journal of Applied Physics*, 110(1), 2011.

[16] Y. Cao, J. Y. Luo, V. Fatemi, S. Fang, J. D. Sanchez-Yamagishi, K. Watanabe, T. Taniguchi, E. Kaxiras, and P. Jarillo-Herrero. Superlattice-induced insulating states and valley-protected orbits in twisted bilayer graphene. *Phys. Rev. Lett.*, 117:116804, 2016.

[17] N. Caswell and S.A. Solin. Vibrational excitations of pure $FeCl_3$ and graphite intercalated with ferric chloride. *Solid State Communications*, 27(10):961 – 967, 1978.

[18] Yimin A. Wu, Ye Fan, Susannah Speller, Graham L. Creeth, Jerzy T. Sadowski, Kuang He, Alex W. Robertson, Christopher S. Allen, and Jamie H. Warner. Large single crystals of graphene on melted copper using chemical vapor deposition. *ACS Nano*, 6(6):5010–5017, 2012.

[19] Ricardo Garcıa and Ruben Perez. Dynamic atomic force microscopy methods. *Surface science reports*, 47(6):197–301, 2002.

[20] A. Pirkle, J. Chan, A. Venugopal, D. Hinojos, C. W. Magnuson, S. McDonnell, L. Colombo, E. M. Vogel, R. S. Ruoff, and R. M. Wallace. The effect of chemical residues on the physical and electrical properties of chemical vapor deposited graphene transferred to $SiO_2$. *Applied Physics Letters*, 99(12), 2011.

[21] Achim Woessner, Pablo Alonso-Gonzalez, Mark B. Lundeberg, Yuanda Gao, Jose E. Barrios-Vargas, Gabriele Navickaite, Qiong Ma, Davide Janner, Kenji Watanabe, Aron W. Cummings, Takashi Taniguchi, Valerio Pruneri, Stephan Roche, Pablo Jarillo-Herrero, James Hone, Rainer Hillenbrand, and Frank H. L. Koppens. Near-field photocurrent nanoscopy on bare and encapsulated graphene. *Nat Commun*, 7, 2016.

[22] Dominique J. Wehenkel, Thomas H. Bointon, Tim Booth, Peter Boggild, Monica F. Craciun, and Saverio Russo. Unforeseen high temperature and humidity stability of $FeCl_3$ intercalated few layer graphene. *Scientific Reports*, 5:7609, 2015.

[23] A. I. S. Neves, T. H. Bointon, L. V. Melo, S. Russo, I. de Schrijver, M. F. Craciun, and H. Alves. Transparent conductive graphene textile fibers. *Scientific Reports*, 5:9866, 2015.

# Part III

# Transition-metal dichalcogenides optoelectronics

# 7

# STRAIN-ENGINEERED PHOTODETECTORS IN ULTRATHIN $HFS_2$

**NOTE:** The ideas and data presented in this chapter have been the subject of the following publication: Adolfo De Sanctis, Iddo Amit, Steven Hepplestone, Monica F. Craciun and Saverio Russo. *Strain-engineered energy funneling in a layered semiconductor*. (Under review in *Advanced Materials*).
The first principles calculations here reported were carried out by Steven Hepplestone and Robert Keens. The AFM characterisation was carried out by Iddo Amit with the assistance of the author.

## 7.1 INTRODUCTION

In chapters 4,5 and 6 I showed how laser-irradiation of functionalised graphene can be used to realise novel optoelectronic devices, demonstrating that intercalation with $FeCl_3$ allows one to fix the carrier dynamics in this atomically-thin material to achieve a pure PV response. Similarly to graphene, other layered materials display unique optical and electrical properties which can be tuned in a similar way, using, for example, chemical functionalisation, strain or laser irradiation. Such materials are suitable for the realisation of novel optoelectronic devices as they display unique feature thanks to their layered structure. In particular, transition metal dichalcogenides (TMDs)[1] are attracting a growing attention in applications such as solar energy harvesting and sensing since they display a unique layer-dependent indirect-to-direct bandgap transition[3], strong optical anisotropy[4] and valley dichroism[5]. However, efforts to improve

the efficiency of such devices have been hampered by several factors, including the lack of efficient extraction of photogenerated carriers, low quantum yield due to strong excitonic effects[6] and, ultimately, the limit imposed by the principle of detailed balance in p-n junction devices[7]. It has been recently proposed[8;9] that a spatially varying bandgap, caused by a local strain field, could be used to "drive" excitons (particle-hole pairs bound within the bandgap of the material) towards the regions of least gap, where they can be efficiently separated. This "exciton funnel" effect has been experimentally demonstrated using photoluminescence experiments[10;11] while the electrical detection this phenomenon could be used to boost the efficiency of solar devices beyond the aforementioned limits. Furthermore, such effect is expected also in the presence of weakly bound excitons and free charges, allowing its use without low temperatures or ultra-pure samples[8].

Strain-engineering in traditional semiconductors (e.g. Si, Ge, etc.) has been used to tune and improve their performances[12]. Unfortunately, most bulk semiconductors fail at strains of $\sim 0.1 - 0.4\%$[13] with thin membranes able to sustain up to $\sim 1 - 2\%$[14]. On the contrary TMDs can sustain strains up to 25% without rupturing[15;16;9], with profound implications on their electronic structure. For instance, the bandgap of semiconducting black phosphorus depends sensitively on applied strain, to the point in which it vanishes for compressive strains above 2 %[17;18]. Furthermore, single-photon emission from localized excitons has been reported in TMDs, where structural defects or local strain is induced[19;20]. Therefore, strain-engineering of the optical and electrical properties of TMDs is a promising field with the potential to enable the development of conceptually new optoelectronic applications.

In this work a novel method for engineering strain in ultrathin $HfS_2$ is demonstrated. A focused laser beam is used to drive the controlled oxidation of the exposed areas of $HfS_2$. The complementary study of a wide range of experimental techniques (i.e. spatially resolve absorption and Raman spectroscopy, elemental analysis and atomic force microscopy) and theoretical modelling with density-functional theory (DFT) clearly demonstrate that the lattice mismatch between the $HfO_2$ and the pristine $HfS_2$ induces compressive strain in the $HfS_2$, resulting in the spatial modulation of the bandgap of this material away from the oxidised area. Scanning photocurrent microscopy (SPCM) reveals an enhanced signal in proximity of this interface, with a responsivity 350 % higher than in the pristine device, indicating efficient extraction of photogenerated

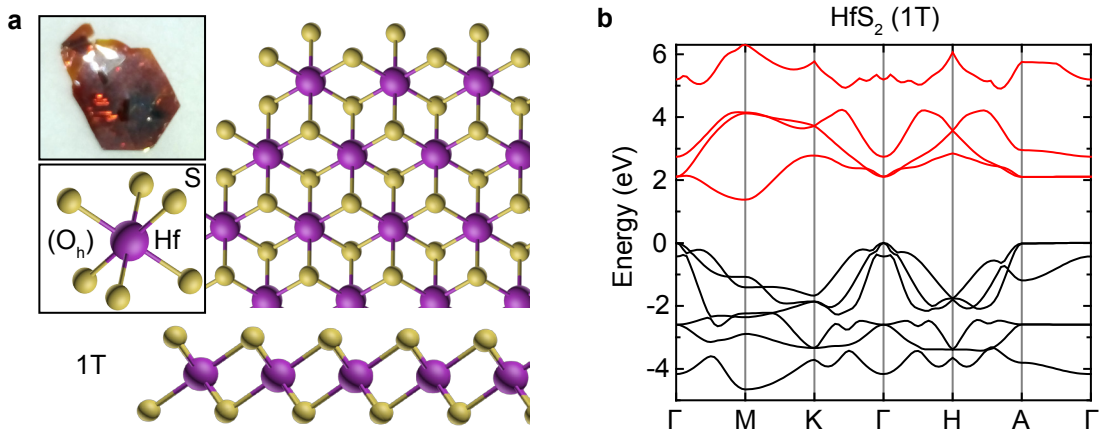


**Figure 7.1: Crystal and band structure of $HfS_2$.** **a**, Photograph of a commercial bulk $HfS_2$ crystal grown via vapour-transport method and its crystal structure. The stable polymorph at 300 K is the 1T phase, with octahedral coordination of the Hf atoms. **b**, Calculated band structure of bulk $HfS_2$, conduction (valence) bands in red (black). The energy scale is relative to the highest occupied state (0 eV).

carriers. The bias dependence of the photocurrent reveals the funneling of energy, also known as charge-funnel effect, which is measured electrically for the first time.

## 7.2 BASIC PROPERTIES OF $HFS_2$

Hafnium disulphide ($HfS_2$) is a semiconducting transition metal dichalcogenide (TMD) with an octahedral coordination of the Hf atoms at room temperature, therefore the crystal structure is 1T ($O_h$), as shown in figure 7.1a. This structure is also historically known as the $CdI_2$ structure. The first studies started in 1965 with the measurements of the optical[21] and electronic[22] properties of bulk samples grown by vapour transport technique[23].

The basic optical and electronic properties of $HfS_2$ are reported in table 7.1, from literature. The bulk crystal appears as dark red hexagonal plates with a metallic lustre, as shown in figure 7.1a, inset. Figure 7.1b shows the band structure of bulk $HfS_2$ computed *via* DFT. The indirect band gap is $\sim 1.38$ eV between Γ and M, while the direct gap at the Γ point is $\sim 2.1$ eV. These values are $\sim 40\%$ off the measured ones[21;26] but in line with other DFT calculations[27].

**Table 7.1: Properties of $HfS_2$.** Basic structural, electronic and optical properties of $HfS_2$.

| a (Å) | c (Å) | $E_g^{ind}$ (eV)[a] | $E_g^{dir}$ (eV)[b] | $\sigma$ ($\Omega^{-1}cm^{-1}$)[c] | Ref. |
|---|---|---|---|---|---|
| $3.625 \pm 0.005$ | $5.88 \pm 0.03$ | $1.96 \pm 0.02$ | $2.90 \pm 0.1$ | $3.0 \cdot 10^{-3}$ | 21;23 |

| Raman modes ($cm^{-1}$) | $A_{1g}$ | $E_g$ | $E_u$(TO) | $E_u$(LO) | |
|---|---|---|---|---|---|
| | 337 | 260 | 155-166 | 321 | 24;25 |

[a] Indirect bandgap (experimental); [b] Direct bandgap (experimental); [c] Room-temperature electrical conductivity;

### 7.2.1 *AFM and Raman spectroscopy of $HfS_2$*

Figure 7.2a shows the atomic force microscopy (AFM) topography of a thin flake of $HfS_2$ deposited on a $Si/SiO_2$ substrate (inset). The height profile across a "step" allows to measure the height of a single layer of $HfS_2$ to be $0.76 \pm 0.08$ nm.

$HfS_2$ has three atoms per unit cell, therefore it has 6 modes in the optical branch[25]: $A_{1g}+E_g+2A_{2u}+2E_u$, of which the $A_{1g}$ and $E_g$, depicted in figure 7.2b, are Raman active while the others are infrared (IR) active (although the $E_u$ modes are visible also in a typical Raman experiment[24]). The Raman spectrum of $HfS_2$ is shown in figure 7.2c, for flakes of different thickness, acquired with $\lambda_{ext} = 514$ nm. In the bulk material all the first order modes are observed: $A_{1g} = 337$ $cm^{-1}$, $E_g = 260$ $cm^{-1}$, plus the two other modes $E_u(LO) = 321$ $cm^{-1}$ and $E_u(TO) = 136$ $cm^{-1}$; All these modes are well described by a fit with a Lorentzian curve with a full-width at half-maximum (FWHM) $\sim 10$ $cm^{-1}$ and the peak positions agree well with previous studies[24;25], except for the $E_u(TO)$ mode which appears blue-shifted (literature value $\sim 155 - 166$ $cm^{-1}$). For thinner flakes, it becomes increasingly difficult to acquire a spectrum: spectra A and B in figure 7.2c show, in fact, that it is not possible to resolve the $E_u$ and $E_g$ modes for very thin flakes. At the time of printing this work, no reports have shown the isolation of single-layer $HfS_2$.

## 7.3 LASER-IRRADIATED $HFS_2$

Thin flakes of $HfS_2$ were deposited on $CaF_2$, Quartz and $Si/SiO_2$ substrates, using micro-mechanical exfoliation[28] from commercial bulk crystal (*HQ Graphene*). The

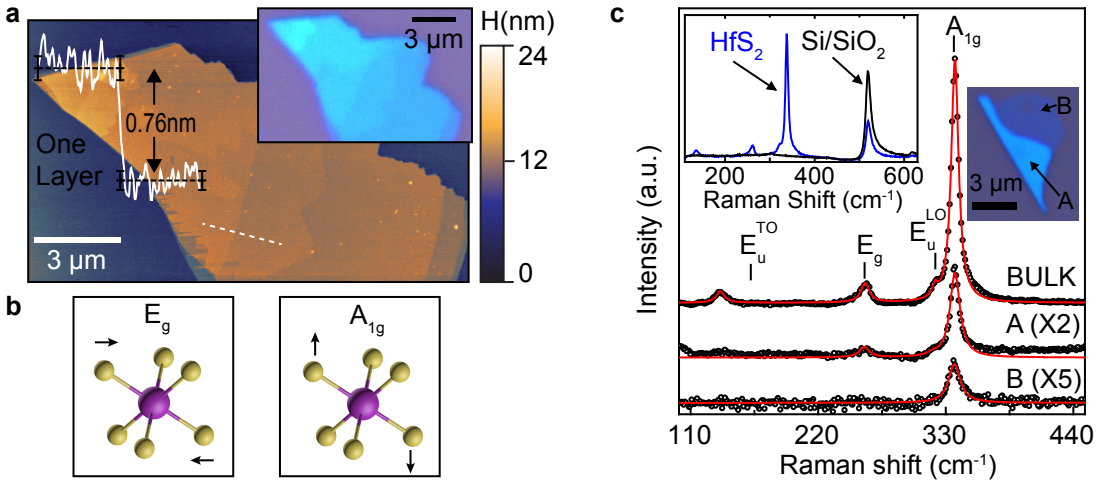


**Figure 7.2: AFM and Raman of ultra-thin $HfS_2$.** **a**, AFM topography and optical micrograph of an exfoliated flake of $HfS_2$ on top of a $Si/SiO_2$ substrate. The height of a single layer is measured to be $0.76 \pm 0.08$ nm. **b** Schematic representation of the main Raman active modes in $HfS_2$. **c**, Raman spectra of $HfS_2$ acquired on a bulk sample ($> 100$ $\mu$m thick) and on a thinner flake exfoliated on $Si/SiO_2$ (areas A and B in the optical micrograph), after subtraction of the pristine substrate spectrum (inset).

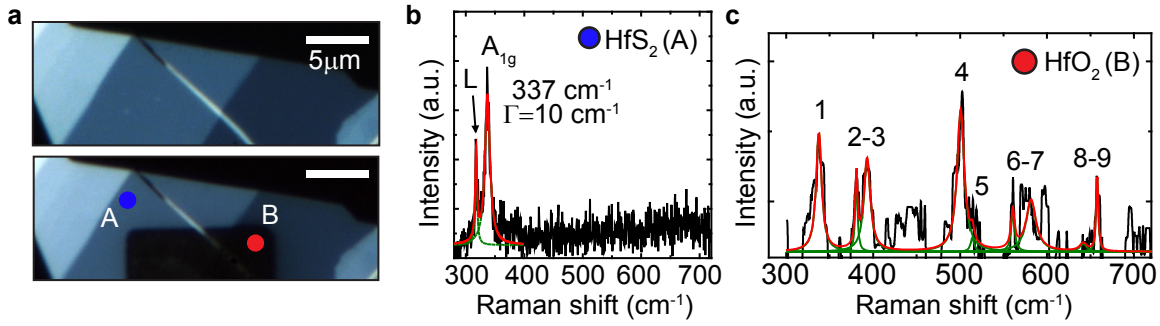


**Figure 7.3: Laser-induced oxidation of ultra-thin $HfS_2$.** **a**, Optical micrograph of an $HfS_2$ flake before (top) and after (bottom) laser exposure of a rectangular area in its centre. **b**, Raman spectrum acquired in location A (panel **a**), showing a Lorentzian peak corresponding to the $A_{1g}$ mode at 337 $cm^{-1}$ (FWHM 10 $cm^{-1}$) of $HfS_2$ (top), and in location B, showing nine Lorentzian peaks compatible with the modes of $HfO_2$ (bottom, after background subtraction and smoothing). The peak named L corresponds to a spurious laser line.

choice of substrate was dictated by the different characterizations performed.

Upon exposure to focused laser light ($\lambda$ = 375 nm, P = 1 MW/$cm^2$) for 1 s, the exposed area becomes transparent to the naked eye, possibly suggesting the ablation of $HfS_2$, see figure 7.3a. Surprisingly, topographic AFM measurements show no ablation of material in the exposed area. At the same time, the tapping phase image clearly reveals a change in the viscoelastic properties of the material, see figure 7.4a. To elucidate the nature of the laser-exposed $HfS_2$, energy-dispersive X-ray micro-analysis (EDXMA) was used. In this case the $HfS_2$ was deposited on $CaF_2$ since no oxygen can be detected in it with EDXMA and, at the same time, has a well defined Raman peak at 322 $cm^{-1}$, away from the $HfS_2$ features. The microanalysis reveals the absence of the S peaks (K lines) and the appearance of an O peak ($K_\alpha$ line) in this region, in contrast to the pristine area, as shown in figure 7.4b. No change was observed in the Hf and substrate peaks. A quantitative analysis shows that, upon laser irradiation, the weight ratio of S decreased from $\sim$ 20% to $\sim$ 1% of the total, while the O content increased from $\sim$ 1% to $\sim$ 20%, indicating the formation of $HfO_2$. Raman spectroscopy in the pristine region shows the characteristic $A_{1g}$ mode of $HfS_2$ at 337 $cm^{-1}$ (figure 7.3b while the Raman spectrum of the laser-irradiated area, figure 7.3c, shows a series of peaks in good agreement with the nine modes reported in literature for monoclinic $HfO_2$ [29],

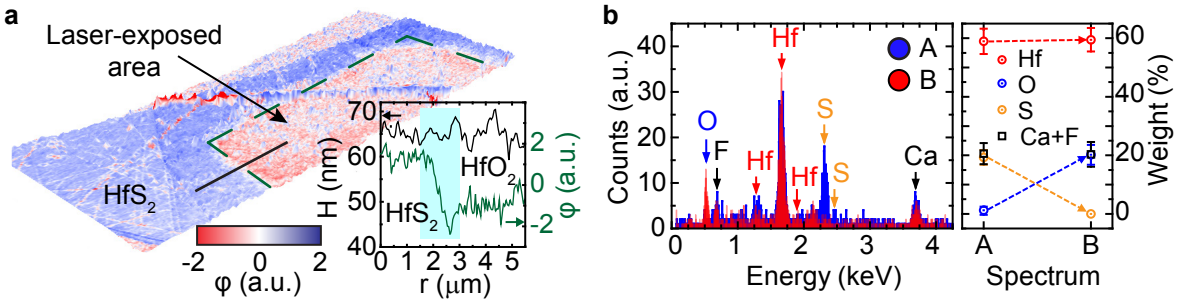


**Figure 7.4: Characterisation of laser-irradiated $HfS_2$.** **a**, AFM topography with phase contrast $\varphi$ signal superimposed of the flake shown in figure 7.3a, after laser irradiation. Bottom-right inset: height (H) and phase signal along a 5 $\mu$m line profile (black line). **b**, EDXMA spectra acquired in the regions A and B in figure 7.3a and quantitative analysis of the chemical elements (right).

as detailed in table 7.2. In particular, good agreement is observed for the relative intensities of the peaks, with the strongest being the $A_g$ mode at 500 $cm^{-1}$.

## 7.4 PHOTO-OXIDATION MECHANISM IN $HFS_2$

The oxidation mechanism, responsible for the observed changes, can be determined using three important experimental observations: (1) The oxidation process is found to be thickness-dependent. For thin flakes ($h \sim 6 - 20$ nm) it was found that short exposures, $\sim 1 - 2$ s, at relatively low power densities, $\sim 10^5$ W/$cm^2$, are sufficient to oxidise the flake. Thick flakes ($h > 60$ nm) showed that even after prolonged exposure at high powers, it was not possible make the entire flake transparent and, instead, ablation of the material was observed; (2) The oxidation area is compatible with the diffraction-limited spot size of the laser system used (see section 3.5.1.2), as shown in figure 7.5a. Here the AFM topography and tapping phase images of a thick ($h \sim 80$ nm) flake are shown. The flake was exposed to a 375 nm laser for 10 s at a power density of 1.5 MW/$cm^2$ in a single spot where it presents a bubble-like structure with a 25% increase in height (compatible with a previous report on the natural oxidation of $HfS_2$ [30]). This feature shows a Gaussian profile with a FWHM of 260 nm, as expected for the system used; (3) Exposing different areas of the flake, in the same conditions as in (2), for different lengths of time, no changes in the FWHM of the Gaussian

**Table 7.2:** Lorentzian fit results from figure 7.3c and comparison with literature values.

| Peak Number | $\omega_0$ ($cm^{-1}$) Exp. | $\omega_0$ ($cm^{-1}$) Lit.[a] | Intensity (Lit)[b] |
|---|---|---|---|
| 1 | 338 | 336 | 0.89 (m) |
| 2 | 381 | 384 | 0.54 (s) |
| 3 | 393 | 398 | 0.69 (s) |
| 4 | 500 | 500 | 1.00 (vs) |
| 5 | 513 | 522 | 0.06 (m) |
| 6 | 560 | 552 | 0.30 (m) |
| 7 | 580 | 580 | 0.47 (m) |
| 8 | 648 | 642 | 0.03 (s) |
| 9 | 658 | 672 | 0.37 (s) |

[a] From Ref. 29; [b] Normalized to peak 4. () s-strong, m-medium, w-weak, from Ref. 29;

profile was recorded, as shown in figure 7.5b. All these observations point towards a light-assisted oxidation process, as opposed to a thermally-driven one.

### 7.4.1 *Charge-transfer and photo-oxidation: semiconductors in ambient conditions*

The laser-induced doping of semiconducting TMDs in a dopant gas atmosphere has been recently reported[31], where the laser is used to create chalcogen vacancies in the TMD. At the same time, Favron et al.[32] demonstrated photo-oxidation in exfoliated black phosphorus, and related the process to the rate of charge-transfer (CT) between the black phosphorus and the aqueous oxygen present in air. Indeed, the work of Jaegermann and Schmeisser[33] also suggested that, in the presence of $H_2O$, oxidation occurs via the oxygen-water redox couple:

$$2H_2O \rightleftharpoons O_2(aq) + 4e^- + 4H^+, \tag{7.1}$$

where the $O_2$ binds to a metal site. Adopting the same model and supported by the EDXMA data, a model for the reaction is proposed, as illustrated in figure 7.6a. The intrinsic chemical potential of $HfS_2$ is $\mu_i = -5.2$ eV (calculated from the distance from the vacuum level to the top of the valence band, $\phi = -6.68$ eV and indirect bandgap $E_g = 1.96$ eV), while that of the oxygen acceptor state is $\mu^0_{redox} = -4.1$ eV. This induces a band-bending at the surface of the layered semiconductor such that an

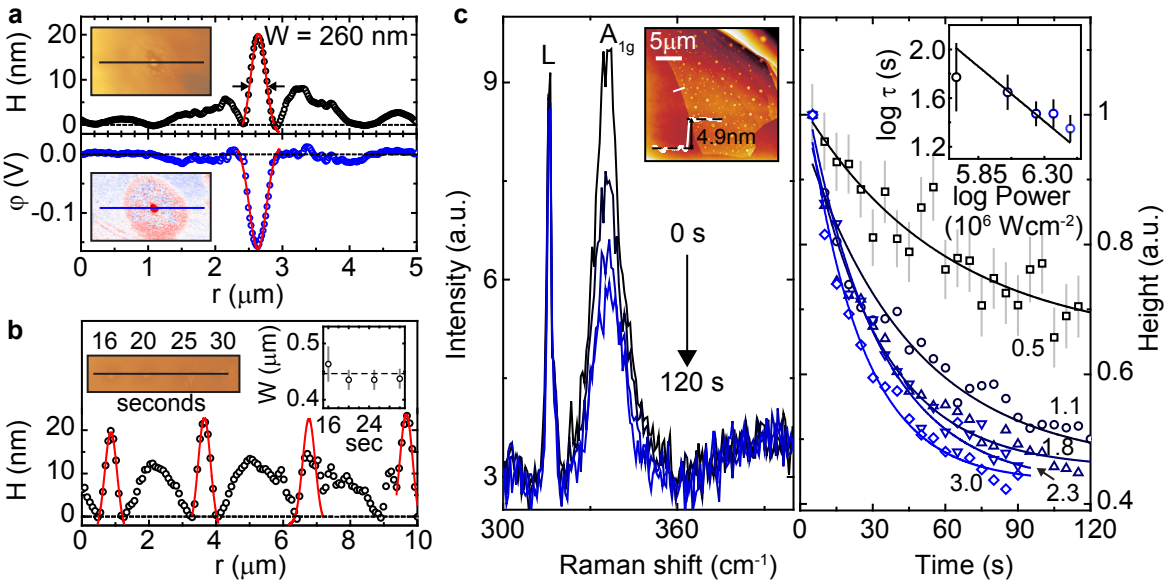


**Figure 7.5: Photo-oxidation dynamics study.** **a**, AFM topography (top) and phase signal (bottom) of an 80 nm-thick flake exposed to intense laser light ($\lambda = 375$ nm, P = 1.5 MW/cm$^2$) for 10 seconds, a Gaussian peak can be fitted with a FWHM of 260 nm. **b**, AFM topography of laser-irradiated spots for different exposure times ($\lambda = 473$ nm, P = 4.3 MW/cm$^2$). Inset: FWHM of the Gaussian fits as a function of exposure time, dashed line marks the average value of 446 nm. **c**, Left: time evolution of the $HfS_2$ $A_{1g}$ mode, upon intense laser exposure ($\lambda = 514$ nm, P = 3.0 MW/cm$^2$) in a 4.9 nm thick flake, shown in the inset. The peak named L corresponds to a spurious laser line. Right: normalized $A_{1g}$ peak height as a function of time for different incident laser powers (0.5 - 3.0 MW/cm$^2$), solid lines mark monoexponential decays; Inset: log-log plot of decay time $\tau$ versus incident power density, solid line marks a slope of $-1$.

optical transition above the bandgap can make an electron ready to be transferred to the oxygen empty states, making the photo-oxidation reaction highly feasible across the whole visible range, explaining the instability of few-layer $HfS_2$ in atmospheric conditions.

The CT reaction starts with a photon of energy $\hbar\omega$ impinging on $HfS_2$, which produces an optical excitation, leaving the material in an excited state: $HfS_2 + \hbar\omega \longrightarrow HfS_2{}^*$. This state provides the carriers for the CT reaction at the surface according to:

$$HfS_2{}^* + O_2(aq) \longrightarrow HfS_2 + O_2{}^{\cdot -}(aq) + h^+, \tag{7.2}$$

the oxygen radical ion $O_2{}^{\cdot -}(aq)$ can then react with the $HfS_2$ and, upon cleavage of the Hf−S bond, bind to the Hf sites:

$$Hf + 2S + 3O_2{}^{\cdot -}(aq) + 3h^+ \longrightarrow HfO_2 + 2\,SO_2(g). \tag{7.3}$$

Therefore the total reaction can be written as:

$$HfS_2(s) + 3O_2(aq) + \hbar\omega \longrightarrow HfO_2(s) + 2SO_2(g). \tag{7.4}$$

The energy cost for the reaction in equation (7.4), considering the formation of monoclinic $HfO_2$, was calculated to be of $-11.58$ eV per $HfS_2$ molecule, making it very favourable. The feasibility of the proposed reaction was verified by simulating the crystal structure of the different compounds and calculating the energy cost per reaction, as detailed in figure 7.6b and in table 7.3. The energy cost was calculated as $E_R = E_{\text{reagents}} - E_{\text{products}}$.

The possibility of the formation of two-dimensional (2D) $HfO_2$, as opposed to monoclinic 3D $HfO_2$, was also considered. Such material is given by the substitution of each S by O in the 2D precursor. However, calculations show that the proposed reaction in equation (7.4) has an energy cost of $-10.90$ eV for 2D $HfO_2$, a difference $\Delta E = 0.68$ eV as compared to monoclinic $HfO_2$, which makes the formation of 2D $HfO_2$ not favourable. In the same way, the formation of cubic $HfO_2$, has a $\Delta E = 0.30$ eV as compared to monoclinic $HfO_2$. The findings of the DFT modelling are also consistent with the observed Raman spectrum (see figure 7.3c and table 7.2). Therefore, it is possible to conclude that the photo-oxidation of $HfS_2$ in ambient conditions leads to

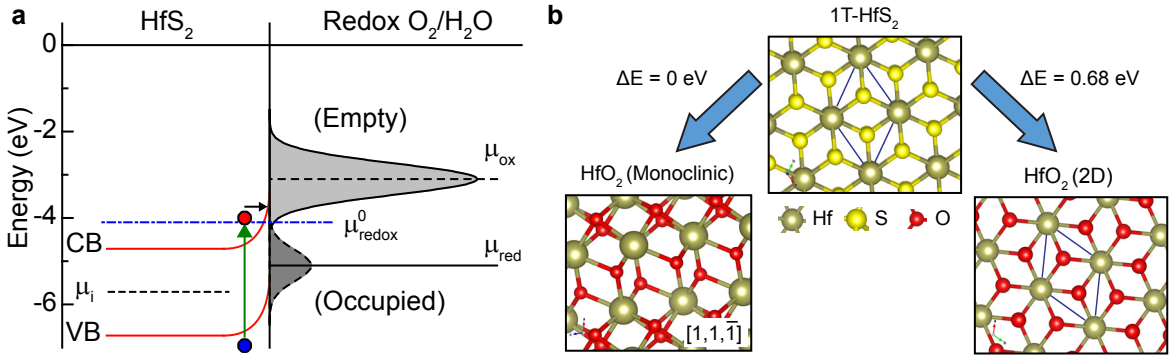


**Figure 7.6: Charge-Transfer model and crystal structures of $HfO_2$** **a**, Energy diagram of multi-layer $HfS_2$ in contact with the redox couple $O_2/H_2O$ present in air in atmospheric conditions. The density of states (DOS) of the redox couple is calculated according to ref. 34: the chemical potentials of the oxidizing and reducing species are $\mu_{ox} = -3.1$ eV and $\mu_{ox} = -5.1$ eV, respectively; the chemical potential of the oxygen acceptor state is $\mu^0_{redox} = -4.1$ eV. The intrinsic work function of $HfS_2$ is $\mu_i = -5.7$ eV with $E_g = 1.96$ eV. Green vertical arrow represents the absorption of a photon. **b** Simulated crystal structure of octahedral $HfS_2$, monoclinic $HfO_2$ cut along the $[11\bar{1}]$ face and 2D $HfO_2$. The energy difference for the reactions, $\Delta$E, is calculated with respect to the formation of monoclinic $HfO_2$ (E = −11.58 eV). Unit cell highlighted in blue.

**Table 7.3:** Reactions energetics

| Reaction | Energy cost (eV) | Energy cost (eV) per $HfS_2$ | $\Delta E$ (eV)[a] per $HfS_2$ |
|---|---|---|---|
| $HfS_2 + 3\,O_2 \longrightarrow HfO_2 + 2\,SO_2$[b] | -11.58 | -11.58 | 0 |
| $32\,HfS_2 + (32 + 64)\,O_2 \longrightarrow Hf_{32}O_{64} + 64\,SO_2$[c] | -370.55 | -11.58 | 0 |
| $HfS_2 + 3\,O_2 \longrightarrow HfO_2(2\,D) + 2\,SO_2$[f] | -10.90 | -10.90 | 0.68 |
| $HfS_2 + 3\,O_2 \longrightarrow HfO_2(\text{cubic}) + 2\,SO_2$[g] | -11.28 | -11.28 | 0.30 |

[a]Compared to lowest energy reaction; [b]$1 \times 1 \times 1$ Primary unit cell of monoclinic $HfO_2$; [c]Large $2 \times 2 \times 2$ unit cell of monoclinic $HfO_2$; [f]Energy cost to produce 2D $HfO_2$; [g]Energy cost to produce cubic $HfO_2$;

the formation of monoclinic $HfO_2$, embedded in the 2D matrix of the few-layer $HfS_2$.

### 7.4.2 *MGT theory of CT reaction*

Marcus-Gerischer theory (MGT)[34] can be used to estimate the rate of change of the pristine material composition, based on the rate of charge transfer from the $HfS_2$ to the $O_2$(aq)[32]:

$$\frac{d\Theta}{dt} \propto \Theta\Phi_{ph}[O_2]\exp\left[-\frac{\left(\frac{E_g}{2}+E_i-E^0_{F,red}-\lambda\right)^2}{4k_bT\lambda}\right], \tag{7.5}$$

where $\Theta$ is the initial amount of pristine material, $\Phi_{ph}$ is the laser flux, $[O_2]$ is the oxygen concentration, $E_g$ is the direct gap energy, $E_i$ is the intrinsic Fermi level, $E^0_{F,red}$ is the energy of the oxygen acceptor state ($\sim 3.1$ eV) with respect to the vacuum level and $\lambda$ is the renormalization energy of oxygen in water ($\sim 1$ eV)[34]. The solution of equation (7.5) gives:

$$\Theta = \Theta_0 \exp\left[-\Phi_{ph}\Gamma t\right], \tag{7.6}$$

where $\Gamma = [O_2]\exp\left[-\left(E_g/2+E_i-E^0_{F,red}-\lambda\right)^2/4k_bT\lambda\right]$ and $\Theta_0$ is the initial amount of material. Equation (7.6) shows that the oxidation has an exponential dependence over time with a time constant $\tau \propto \Phi_{ph}^{-1}$. This is verified in figure 7.5c where the intensity of the Raman $A_{1g}$ mode of $HfS_2$, an indication of the amount of pristine material present in the sampling volume $\Theta$, is plotted against time for different laser fluxes. Monoexponential decay fits give a decay time $\tau$ with the expected power dependence (figure 7.5c, inset).

## 7.5 PHOTORESPONSE AND STRAIN IN PHOTO-OXIDISED $HfS_2$

SPCM mapping was employed in order to study the photoresponse of a $HfS_2$ photodetector in a field effect transistor (FET) configuration, as shown in figure 7.7a. The device was fabricated on a doped Si substrate capped with 285 nm of thermally-grown $SiO_2$. Contacts were defined via electron-beam lithography, as described in appendix A.2. Figure 7.7c,d show the SPCM maps before and after photo-oxidation

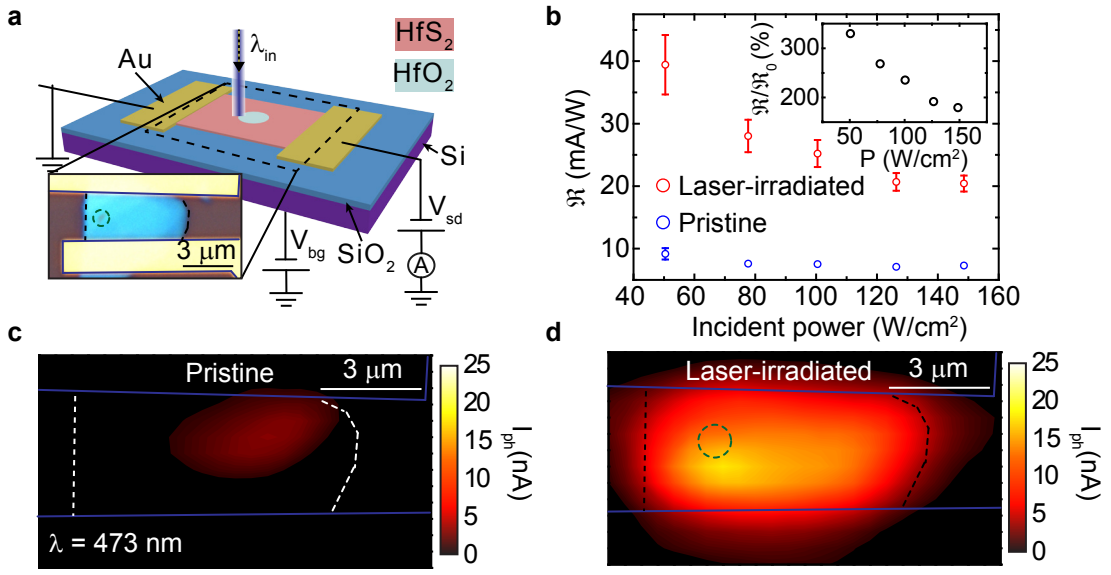


**Figure 7.7: Photo-response characterisation of $HfS_2/HfO_2$ device.** **a**, Schematic diagram of the device and SPCM mapping. Inset: optical micrograph of the device, after laser-irradiation of a single spot (green dashed circle). **b**, Responsivity before (blue, $\mathfrak{R}_0$) and after (red, $\mathfrak{R}$) laser-assisted oxidation as a function of incident optical power. Inset: ratio $\mathfrak{R}/\mathfrak{R}_0$. **c** and **d**, SPCM maps of the device before and after laser-irradiation acquired with: $V_{sd} = -5$ V, $V_{bg} = 50$ V, $\lambda = 473$ nm, $P = 150$ W/cm$^2$ and 0.5 $\mu$m steps.

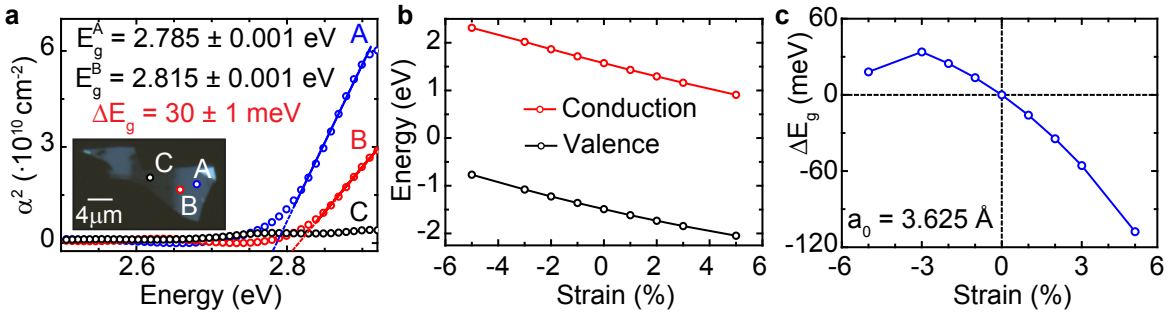


**Figure 7.8: Photo-oxidation-induced strain in $HfS_2$.** **a**, Absorption coefficient $\alpha^2$ of: (A) $HfS_2$ away and (B) close to the oxidised area and (C) $HfO_2$. Extrapolated direct bandgap: $E_g^A = 2.785 \pm 0.001$ eV and $E_g^B = 2.815 \pm 0.001$, $\Delta E_g = 30 \pm 1$ meV. Inset: optical micrograph of the flake with the measured regions highlighted. **b**, Calculated valence and conduction bands of $HfS_2$ at the $\Gamma$ point, as a function of strain. **c**, Calculated direct bandgap energy shift $\Delta E_g$ as a function of strain. Relaxed lattice constant of $HfS_2$: $a_0 = 3.625$ Å.

of a single spot in the channel, where an enhancement of the photoresponse close to the laser-oxidised area (green circles in figure 7.7a,d) was observed. Strikingly, the responsivity of the device is enhanced by $\sim 350, \%$ at low powers and $\sim 200\,\%$ at the saturation power (120 W/cm$^2$), as shown in figure 7.7b.

The observed enhancement of the photoresponse, localized in the proximity of the oxidised area, suggests that the presence of the oxide affects the $HfS_2$. Indeed, strain induced by the lattice mismatch between the two materials, is the key factor. As shown from calculations (see figure 7.6b) The $[1, 1, \bar{1}]$ cleavage plane of monoclinic $HfO_2$ has a spatial arrangement of Hf atoms commensurate to that of the basal plane of $HfS_2$, with an Hf-Hf distance of 3.426 Å. Since the Hf-Hf distance in $HfS_2$ is 3.625 Å, a transition between these two structures is likely to introduce an average 2.7% compressive strain in the $HfS_2$ (and extensive in the$HfO_2$) at the interface between the two materials. This would result in a change in the bandgap of $HfS_2$ of $\sim 30$ meV, as shown in figure 7.8c from first principles calculations. A measurement of the absorption coefficient $\alpha$ of $HfS_2$ (see section 3.3.2) confirms such hypothesis. In figure 7.8a, the measured $\alpha$ is shown together with the extrapolated direct bandgap, in the region far from the laser-written oxide (A), $E_g^A = 2.785 \pm 0.001$ eV, and close to it (B), $E_g^B = 2.815 \pm 0.001$ eV. A difference of $\Delta E_g = 30$ meV is observed, compatible with a 3% compressive strain in the $HfS_2$. The absorption coefficient measured in the centre of the oxidised area is

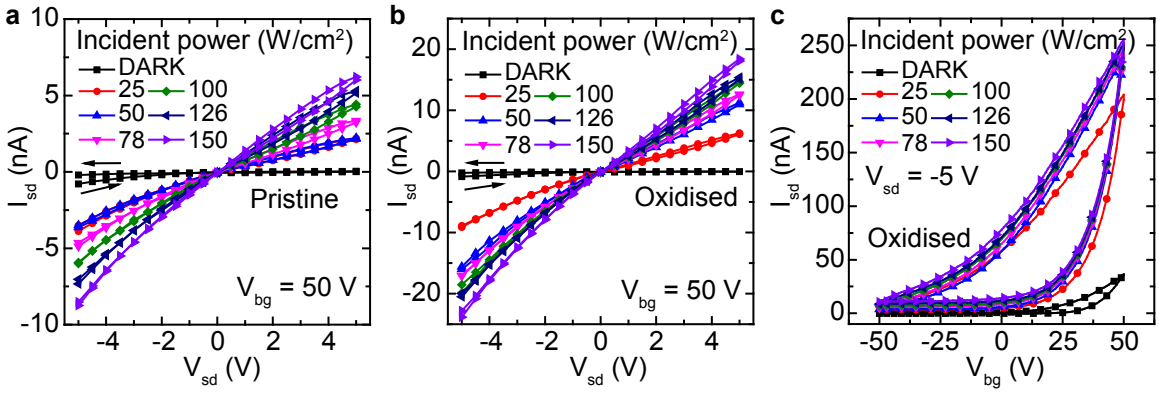


**Figure 7.9: Electrical characteristic of $HfS_2/HfO_2$ devices.** **a**, Current-voltage ($I_{sd}$-$V_{sd}$) characteristic of the device shown in figure 7.7, before laser-assisted oxidation in the dark and for different incident optical powers ($\lambda = 473$ nm, $V_{bg} = +50$ V). **b**, Current-voltage characteristic of the same device after laser-assisted oxidation. **c**, Gate voltage dependence of the photocurrent for the same device, after laser-assisted oxidation, $V_{sd} = -5$ V.

close to zero, showing that the direct absorption edge lies $> 2.9$ eV.

For completeness the electrical characterization of the device is shown in figure 7.9. Figure 7.9a shows the current-voltage ($I_{sd}$-$V_{sd}$) characteristic before the photo-oxidation at different incident optical powers and figure 7.9b shows the same curves acquired after the photo-oxidation. Sweeping the $V_{sd}$ in both direction, no significant hysteresis is observed. In figure 7.9c the gate voltage $V_{bg}$ sweep, as a function of incident optical power, is shown for the same device, after photo-oxidation. In this case a very large hysteresis is observed, due to the contamination of the device in ambient conditions. The observed hysteresis is in agreement with previous results[30].

Both the SPCM and electrical measurements were performed in the setup described in section 3.5: the electrical signal from the device was amplified with a *DL* Model 1211 current preamplifier and measured with an *Ametek* Model 7270 DSP Lock-in amplifier. The locking frequency was provided by the function generator which modulated the lasers. The bias and gate voltages were provided by a *Keithley* 2400 SourceMeter.

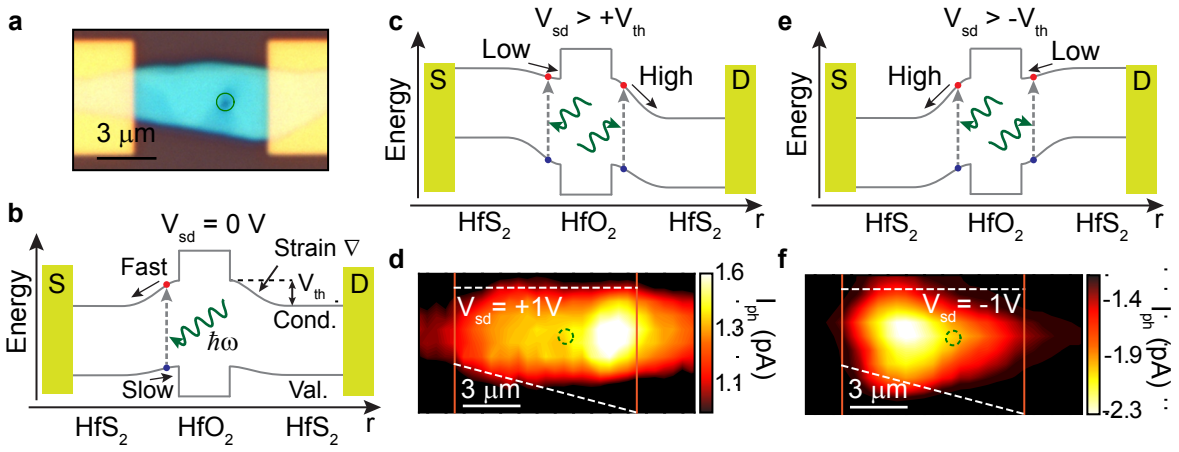


**Figure 7.10: Charge funnel effect in $HfS_2/HfO_2$ photodetectors.** **a**, Optical micrograph of the device, the oxidised region is highlighted in green. **b**, Band diagram of a device subject to strain induced by local oxidation, with $V_{sd} = 0$ V. "Fast" and "slow" indicate the drift velocity of the charges due to the local electric field. **c**, Band diagram of the device under $V_{sd} > +V_{th}$. **d**, SPCM map of the device under $V_{sd} = +1$ V. **e** and **f**, Band diagram and SPCM map of the device under $V_{sd} = -1$ V $< V_{th}$.

## 7.6 CHARGE-FUNNEL EFFECT IN STRAINED $HfS_2$

The role of strain in the enhanced photoresponse is studied in a second device, where a single spot of oxide is formed in the channel (see figure 7.10a). Figure 7.10b shows the band alignment in such device for an applied bias $V_{sd} = 0$ V, considering direct transitions at Γ. The effect of strain in the conduction and valence band of $HfS_2$ at the Γ point is shown in figure 7.8b. Excited electron-hole pairs, in the proximity of the strained area, will be efficiently separated by the built-in field created by the strain gradient and "funnelled" towards the electrodes, giving an enhanced photoresponse[8;9]. In this case, both sides of the strained junction will give equal contribution. The application of a bias $V_{sd} > +V_{th}$ between the electrodes, where $V_{th}$ is the difference between the conduction band energy at the maximum strain point and its value in the untrained region, will result in the situation depicted in figure 7.10c, where one side of the strained interface will show a larger photoresponse due to the steeper gradient. This is indeed observed in the SPCM map shown in figure 7.10d. Reversing the bias, i.e. $V_{sd} > -V_{th}$, the same behaviour is expected but on the other side of the oxidised

area, as shown in figure 7.10e and demonstrated in figure 7.10f. Therefore, it is possible to switch the position of photoactive region by simply reversing the bias voltage.

## 7.7 SUMMARY AND OUTLOOK

In summary, the controlled photo-oxidation of ultrathin $HfS_2$ was studied showing that charge-transfer between $HfS_2$ and aqueous oxygen in air is the leading mechanism for oxidation and a model based on MGT theory was experimentally verified. These findings indicate that the photo-oxidation process is readily controllable, with the oxidation resolution determined by the spot size of the focused laser beam. This controlled oxidation has been then used to modulate the bandgap of $HfS_2$ through local strain induced by the lattice mismatch between the oxide and the pristine material. A charge-funnel effect was then demonstrated in such strain-engineered photodetector which showed an improved responsivity up to 350% compared to the pristine device and the ability to switch on and off the photoactive region simply with the applied bias. These results open the route towards the exploitation of strain-engineered devices for high-efficiency energy harvesting and sensing applications, with the ability to overcome the intrinsic limitations of current solar cells. In the future such devices could be incorporated in emerging wearable electronics technologies[35] and smart buildings, creating a new paradigm in energy efficiency.

# BIBLIOGRAPHY


[1] Qing Hua Wang, Kourosh Kalantar-Zadeh, Andras Kis, Jonathan N. Coleman, and Michael S. Strano. Electronics and optoelectronics of two-dimensional transition metal dichalcogenides. *Nat Nano*, 7(11):699–712, Nov 2012.

[2] Andreas Pospischil and Thomas Mueller. Optoelectronic devices based on atomically thin transition metal dichalcogenides. *Applied Sciences*, 6(3):78, 2016.

[3] Kin Fai Mak, Changgu Lee, James Hone, Jie Shan, and Tony F. Heinz. Atomically thin $MoS_2$: A new direct-gap semiconductor. *Phys. Rev. Lett.*, 105:136805, Sep 2010.

[4] Ozgur Burak Aslan, Daniel A. Chenet, Arend M. van der Zande, James C. Hone, and Tony F. Heinz. Linearly polarized excitons in single- and few-layer $ReS_2$ crystals. *ACS Photonics*, 3(1):96–101, 2016.

[5] Y. J. Zhang, T. Oka, R. Suzuki, J. T. Ye, and Y. Iwasa. Electrically switchable chiral light-emitting transistor. *Science*, 344(6185):725–728, 2014.

[6] Kin Fai Mak and Jie Shan. Photonics and optoelectronics of 2D semiconductor transition metal dichalcogenides. *Nat Photon*, 10(4):216–226, Apr 2016.

[7] William Shockley and Hans J. Queisser. Detailed balance limit of efficiency of p-n junction solar cells. *Journal of Applied Physics*, 32(3):510–519, 1961.

[8] Ji Feng, Xiaofeng Qian, Cheng-Wei Huang, and Ju Li. Strain-engineered artificial atom as a broad-spectrum solar energy funnel. *Nat Photon*, 6(12):866–872, Dec 2012.

[9] Pablo San-Jose, Vincenzo Parente, Francisco Guinea, Rafael Roldán, and Elsa Prada. Inverse funnel effect of excitons in strained black phosphorus. *Phys. Rev. X*, 6:031046, Sep 2016.

[10] Andres Castellanos-Gomez, Rafael RoldÃ¡n, Emmanuele Cappelluti, Michele Buscema, Francisco Guinea, Herre S. J. van der Zant, and Gary A. Steele. Local strain engineering in atomically thin $MoS_2$. *Nano Letters*, 13(11):5361–5366, 2013.

[11] Hong Li, Alex W. Contryman, Xiaofeng Qian, Sina Moeini Ardakani, Yongji Gong, Xingli Wang, Jeffrey M. Weisse, Chi Hwan Lee, Jiheng Zhao, Pulickel M. Ajayan, Ju Li, Hari C. Manoharan, and Xiaolin Zheng. Optoelectronic crystal of artificial atoms in strain-textured molybdenum disulphide. *Nature Communications*, 6:7381, Jun 2015. Article.

[12] Cicek Boztug, José R. Sánchez-Pérez, Francesca Cavallo, Max G. Lagally, and Roberto Paiella. Strained-germanium nanostructures for infrared photonics. *ACS Nano*, 8(4):3136–3151, 2014.

[13] T.-H. Cheng, K.-L. Peng, C.-Y. Ko, C.-Y. Chen, H.-S. Lan, Y.-R. Wu, C. W. Liu, and H.-H. Tseng. Strain-enhanced photoluminescence from Ge direct transition. *Applied Physics Letters*, 96(21), 2010.

[14] M. El Kurdi, H. Bertin, E. Martincic, M. de Kersauson, G. Fishman, S. Sauvage, A. Bosseboeuf, and P. Boucaud. Control of direct band gap emission of bulk germanium by mechanical tensile strain. *Applied Physics Letters*, 96(4), 2010.

[15] Changgu Lee, Xiaoding Wei, Jeffrey W. Kysar, and James Hone. Measurement of the elastic properties and intrinsic strength of monolayer graphene. *Science*, 321(5887):385–388, 2008.

[16] Simone Bertolazzi, Jacopo Brivio, and Andras Kis. Stretching and breaking of ultrathin $MoS_2$. *ACS Nano*, 5(12):9703–9709, 2011.

[17] Jie Guan, Wenshen Song, Li Yang, and David Tomanek. Strain-controlled fundamental gap and structure of bulk black phosphorus. *Phys. Rev. B*, 94:045414, Jul 2016.

[18] Jorge Quereda, Pablo San-Jose, Vincenzo Parente, Luis Vaquero-Garzon, Aday J. Molina-Mendoza, Nicolas Agrait, Gabino Rubio-Bollinger, Francisco Guinea, Rafael Roldán, and Andres Castellanos-Gomez. Strong modulation of optical properties in black phosphorus through strain-engineered rippling. *Nano Letters*, 16(5):2931–2937, 2016.

[19] Yu-Ming He, ClarkGenevieve, SchaibleyJohn R., Yu He, ChenMing-Cheng, WeiYu-Jia, DingXing, Qiang Zhang, Wang Yao, Xiaodong Xu, Chao-Yang Lu, and Jian-Wei Pan. Single quantum emitters in monolayer semiconductors. *Nat Nano*, 10(6):497–502, Jun 2015. Letter.

[20] Gabriele Grosso, Hyowon Moon, Benjamin Lienhard, Sajid Ali, Dmitri K. Efetov, Marco M. Furchi, Pablo Jarillo-Herrero, Michael J. Ford, Igor Aharonovich, and Dirk Englund. Tunable and high purity room-temperature single photon emission from atomic defects in hexagonal boron nitride. *arXiv:1611.03515*, 2016.

[21] D.L. Greenaway and R. Nitsche. Preparation and optical properties of group IV-VI chalcogenides having the $CdI_2$ structure. *Journal of Physics and Chemistry of Solids*, 26(9):1445 – 1458, 1965.

[22] Lawrence E. Conroy and Kyu Chang Park. Electrical properties of the group IV disulfides, titanium disulfide, zirconium disulfide, hafnium disulfide and tin disulfide. *Inorganic Chemistry*, 7(3):459–463, 1968.

[23] R. Nitsche, H.U. Bálsterli, and M. Lichtensteiger. Crystal growth by chemical transport reactions-I. *Journal of Physics and Chemistry of Solids*, 21(3):199 – 205, 1961.

[24] Toshiki Iwasaki, Noritaka Kuroda, and Yuichiro Nishina. Anisotropy of lattice dynamical properties in $ZrS_2$ and $HfS_2$. *Journal of the Physical Society of Japan*, 51(7):2233–2240, 1982.

[25] A. Cingolani, M. Lugará, G. Scamarcio, and F. Lévy. The Raman scattering in hafnium disulfide. *Solid State Communications*, 62(2):121 – 123, 1987.

[26] M. Traving, T. Seydel, L. Kipp, M. Skibowski, F. Starrost, E. E. Krasovskii, A. Perlov, and W. Schattke. Combined photoemission and inverse photoemission study of $HfS_2$. *Phys. Rev. B*, 63:035107, Jan 2001.

[27] Filip A. Rasmussen and Kristian S. Thygesen. Computational 2D materials database: Electronic structure of transition-metal dichalcogenides and oxides. *The Journal of Physical Chemistry C*, 119(23):13169–13183, 2015.

[28] K. S. Novoselov, D. Jiang, F. Schedin, T. J. Booth, V. V. Khotkevich, S. V. Morozov, and A. K. Geim. Two-dimensional atomic crystals. *Proceedings of the National Academy of Sciences of the United States of America*, 102(30):10451–10453, 2005.

[29] Pierre E. Quintard, Pierre Barbéris, Andrei P. Mirgorodsky, and Thérèse Merle-Méjean. Comparative lattice-dynamical study of the raman spectra of monoclinic and tetragonal phases of zirconia and hafnia. *Journal of the American Ceramic Society*, 85(7):1745–1749, 2002.

[30] Sang Hoon Chae, Youngjo Jin, Tae Soo Kim, Dong Seob Chung, Hyunyeong Na, Honggi Nam,

Hyun Kim, David J. Perello, Hye Yun Jeong, Thuc Hue Ly, and Young Hee Lee. Oxidation effect in octahedral hafnium disulfide thin film. *ACS Nano*, 10(1):1309–1316, 2016. PMID: 26735305.

[31] Eunpa Kim, Changhyun Ko, Kyunghoon Kim, Yabin Chen, Joonki Suh, Sang-Gil Ryu, Kedi Wu, Xiuqing Meng, Aslihan Suslu, Sefaattin Tongay, Junqiao Wu, and Costas P. Grigoropoulos. Site selective doping of ultrathin metal dichalcogenides by laser-assisted reaction. *Advanced Materials*, 28(2):341–346, 2016.

[32] Alexandre Favron, Etienne Gaufres, Frederic Fossard, Anne-Laurence Phaneuf-L'Heureux, Nathalie Y-W Tang, Pierre L. Levesque, Annick Loiseau, Richard Leonelli, Sebastien Francoeur, and Richard Martel. Photooxidation and quantum confinement effects in exfoliated black phosphorus. *Nat Mater*, 14(8):826–832, Aug 2015.

[33] W. Jaegermann and D. Schmeisser. Reactivity of layer type transition metal chalcogenides towards oxidation. *Surface Science*, 165(1):143 – 160, 1986.

[34] R. Memming. *Semiconductor Electrochemistry*. Wiley, 2008.

[35] A. I. S. Neves, T. H. Bointon, L. V. Melo, S. Russo, I. de Schrijver, M. F. Craciun, and H. Alves. Transparent conductive graphene textile fibers. *Scientific Reports*, 5:9866, May 2015.

# 8

# FINAL REMARKS AND OUTLOOK

The results presented in this thesis demonstrate the use of graphene and transition metal dichalcogenides (TMDs) in novel optoelectronic applications. Intercalation of graphene with $FeCl_3$ has been shown to result in a material that can be arbitrarily tuned using laser-irradiation to form photo-active junctions. The investigation of the photo-response of these junctions showed a purely photovoltaic (PV) effect, for the first time, in an all-graphene detector thanks to the quenching of the thermoelectric contribution which stems from the enhanced cooling of hot carriers in graphene. For the same reason, these devices show an extraordinary linear dynamic range (LDR) up to 44 dB, more than 4500 times larger than other graphene photodetectors, that can operate at incident optical powers up to $10^4$ kW/cm$^2$ in the whole visible range, in the near-UV and at MIR wavelengths. The extended LDR, broadband operation and spatial extension of such junctions paves the way towards the development of atomically-thin, flexible devices for light detection in applications such as: laser-induced plasmas; ultra-violet (UV) photo-catalytic water sanitation processes; and high precision manufacturing. In such environments, these novel sensors could eliminate the need for attenuating optics in the detection of ultra-bright light signals with high spatial resolution.

Intercalated graphene, in the form of hexagonal domains, was also used to demonstrate the first all-graphene position-sensitive detector (PSD), which exploits the symmetry of the junctions formed by the intercalant at the folds in the graphene layers. These junctions show a linear and bipolar photo-response with respect to the laser position. Such photodetectors (PDs) could be potentially employed in flexible-electronic applications for sensing, such as in the detection of vibrations from buildings or machinery.

In both cases future work should focus on the enhancement of the responsivity of such photodetectors through the use of an increased number of intercalated graphene layers and optimisation of the de-intercalation process to maximise the chemical potential gradient at the p-p' junctions. Intercalation of $FeCl_3$ throughout large-area graphene films of a uniform layer number will be crucial for implementing these findings in practical applications. To this end, intercalation of large-area CVD-grown graphene has already been demonstrated (as discussed in chapter 4) and roll-to-roll processing of graphene is readily applicable to intercalated films. Therefore future work should be devoted to achieving full control over the number of graphene layers grown by CVD over large areas ($\sim m^2$).

Following the knowledge acquired with intercalated graphene, laser-irradiation has been used to tune the optoelectronic response of a semiconducting transition metal dichalcogenide (TMD). The controlled photo-oxidation of $HfS_2$ is studied and the formation of monoclinic $HfO_2$ in the two-dimensional (2D) matrix of the $HfS_2$ is demonstrated. This spatially-confined oxidation induces compressive strain in the $HfS_2$. Such strain leads to a spatially-varying bandgap which then enhances the responsivity of a photodetector (PD) by 350 % compared to the unstrained device. This enhancement arises from the so-called "inverse charge-funnel" effect, which is electrically measured for the first time in a layered semiconductor. This effect allows the photo-excited charges to be driven away from the excitation region, towards the electrodes, where they can be extracted more efficiently. This work represents the first step towards the realisation of PV cells which could overcome their intrinsic limitations in efficiency. Future work should be devoted to the study of this effect in similar materials in order to optimise the laser-oxidation process, both from an experimental and theoretical point of view. Of particular interest will be the study of the interface between the two materials in order to model the strain gradient at these interfaces. This would allow one to gain insight into the possible ways of increasing such induced strain. The growth of TMDs on a large-area is another field that would push the proposed devices into real-life applications although their instability in ambient conditions is still a critical factor which prevents, at the moment, their industrial exploitation. Therefore, further developments in encapsulation techniques are needed. As laser-irradiation is readily available in industry, this technique could be immediately employed to realise arrays of "funnel-type" photodetectors with ultra-high efficiency.

# Part IV

# Appendices

# A

# MATERIALS PREPARATION AND SAMPLE FABRICATION

## A.1 GRAPHENE PREPARATION AND TRANSFER

There are different methods to obtain graphene. The first and most direct approach is micro-mechanical cleavage of bulk graphite[1], also known as "tape method". This is the main technique used to produce graphene for the devices studied in this work.

Chemical vapour deposition (CVD) is used to produce large-area graphene[2] and hexagonal, single-crystal domains of high-quality graphene[3]. The most common precursor used in the CVD growth of graphene is methane ($CH_4$) which generally pyrolyses at 1100 °C or above over a wide range of pressure. Other common precursors are ethylene ($C_2H_6$) and acetylene ($C_2H_2$). To date, the CVD growth of graphene has been demonstrated on many polycrystalline metals such as Fe, Co, Ni, Cu, Ru, Rh, Ir, Pt, Au plus some compounds and alloys, such as Cu-Ni alloy[4] or Mo-Ni alloy[5]. CVD growth on metals, which yields to uniform, large area ($\sim$ cm$^2$) monolayer graphene (MLG) has been reported for the first time in 2009 on polycrystalline Cu foils[6], exploiting thermal catalytic decomposition of $CH_4$ and the low carbon solubility of Cu. Growth on Ni is known to give few-layer graphene (FLG), as studied in section 4.3. Here, large-area FLG grown on Ni (wafer of 100 mm purchased from *Graphene supermarket*) was transferred to glass substrates using poly(methyl methacrylate) (PMMA) as a support during the wet-etching of nickel in a $FeCl_3$ solution. The PMMA-supported graphene was subsequently transferred to ultra pure water, to a concentrated HCl solution for 1 hour and rinsed in ultra pure water. Finally, the stack of multilayer graphene/PMMA was transferred to glass substrates and, after 24 hours, the PMMA was removed with

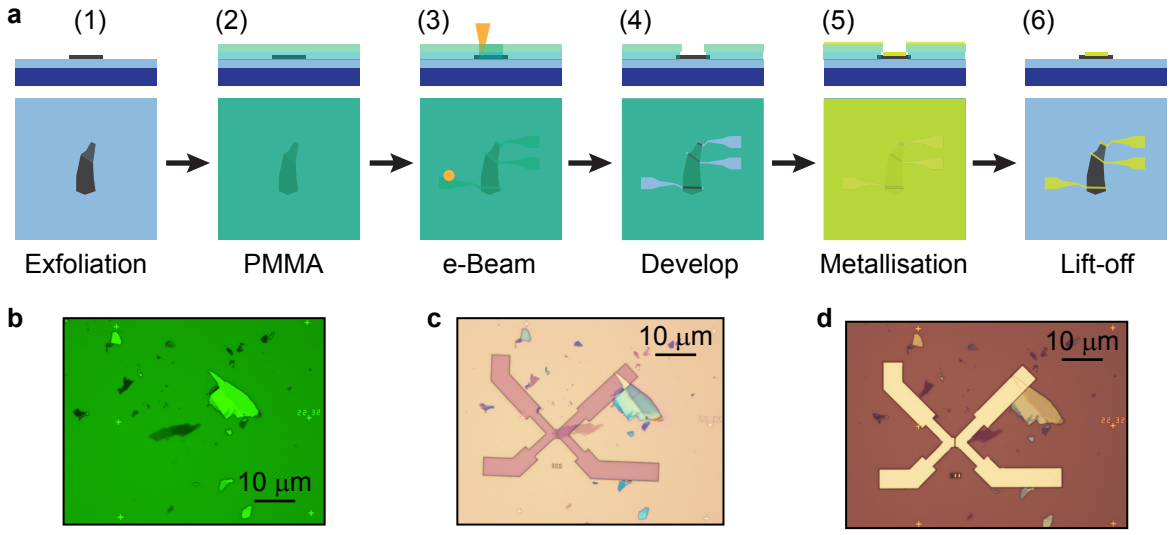


**Figure A.1: Schematic procedure of Electon-beam (e-beam) lithography.** **a**, (1) Deposition of graphene/transition metal dichalcogenides (TMDs); (2) Spin-coating of PMMA, two layers are used (see text); (3) Exposure to electron beam; (4) PMMA develop in appropriate solution; (5) Evaporation of metals (Cr, Au, Pt, etc.); (6) Lift-off in Acetone bath. **b**, Optical micrograph of exfoliated graphene on $Si/SiO_2$ using a green filter. **c**, Optical micrograph of the same flake after developing the PMMA and **d**, after metallisation with Cr/Au (5/50 nm) and lift-off.

Acetone.

## A.2 DEVICES FABRICATION

The devices presented in this work consist of a thin flake of graphene or $HfS_2$ deposited on top of a doped Silicon substrate (p-type) capped with 285 nm of $SiO_2$. After deposition, electric contacts to the material were defined via e-beam lithography, as illustrated in figure A.1a. A double-layer of PMMA is spin-coated on the substrate. This layer is formed by 300 nm of 950 K PMMA on top of 300 nm of 450 K PMMA, where the "K" number indicates the number of monomers in the polymer chain. The purpose of a double-layer is to obtain a step during the development phase, which allows easy lift-off after metallisation. The pattern is the defined via e-beam exposure using a *Nano Beam* NBL-3. The electrons are accelerated to 20 keV and have the energy to break

the polymer chains of PMMA. After, the sample is immersed in a developer solution (15 % Isopropanol (IPA) + 5 % Methyl isobutyl ketone (MIBK) + 1 % Methyl ethyl ketone (MEK)), which removes the exposed PMMA. After rinsing in IPA and drying with $N_2$ a metallisation step is performed using either e-beam od thermal evaporation of a double layer of Ti and Au typically 5 and 50 nm thick, respectively. The first metal is used as a sticking layer to the $SiO_2$, other common choices are Cr and Au and Al capped with either Pd or Au to avoid oxidation. After the metallisation stage the stack is lifted-off using an Acetone bath, leaving only the metal in the exposed regions. An example is shown in figure A.1b-d, where graphene is contacted using Cr/Au (5/50 nm). This technique allows a resolution below 10 nm.

# BIBLIOGRAPHY

[1] K. S. Novoselov, A. K. Geim, S. V. Morozov, D. Jiang, Y. Zhang, S. V. Dubonos, I. V. Grigorieva, and A. A. Firsov. Electric field effect in atomically thin carbon films. *Science*, 306:666, 2004.

[2] Thomas H. Bointon, Matthew D. Barnes, Saverio Russo, and Monica F. Craciun. High quality monolayer graphene synthesized by resistive heating cold wall chemical vapor deposition. *Advanced Materials*, 27(28):4200–4206, 2015.

[3] Ali Mohsin, Lei Liu, Peizhi Liu, Wan Deng, Ilia N. Ivanov, Guoliang Li, Ondrej E. Dyck, Gerd Duscher, John R. Dunlap, Kai Xiao, and Gong Gu. Synthesis of millimeter-size hexagon-shaped graphene single crystals on resolidified copper. *ACS Nano*, 7(10):8924–8931, 2013.

[4] Rebecca S. Edwards and Karl S. Coleman. Graphene film growth on polycrystalline metals. *Accounts of Chemical Research*, 46(1):23–30, 2013.

[5] Boya Dai, Lei Fu, Zhiyu Zou, Min Wang, Haitao Xu, Sheng Wang, and Zhongfan Liu. Rational design of a binary metal alloy for chemical vapour deposition growth of uniform single-layer graphene. *Nat Commun*, 2:522, Nov 2011.

[6] Xuesong Li, Weiwei Cai, Jinho An, Seyoung Kim, Junghyo Nah, Dongxing Yang, Richard Piner, Aruna Velamakanni, Inhwa Jung, Emanuel Tutuc, Sanjay K. Banerjee, Luigi Colombo, and Rodney S. Ruoff. Large-area synthesis of high-quality and uniform graphene films on copper foils. *Science*, 324(5932):1312–1314, 2009.

# B

# CORRECTION OF RESPONSIVITY SPECTRA FOR SUBSTRATE REFLECTIONS

As discussed in chapter 5, the presence of a reflecting $Si/SiO_2$ substrate affects the measured spectral responsivity of the $FeCl_3$-FLG photodetectors. As shown in figure 5.6c, a correction which accounts for these reflections was performed in order to examine the intrinsic spectral response of the laser-written p-p' junctions. Figure B.1a illustrates the model used for this correction which consists of considering an incident photon flux ($\Phi_0$) partially absorbed by a $FeCl_3$-FLG flake of transmittance $T$ and a transmitted remaining flux, $\Phi_t = T\Phi_0$. A portion of this transmitted flux ($\Phi_r = \Phi_t R$, where $R$ is the reflectance of $Si/SiO_2$) is reflected by the substrate and absorbed/transmitted by $FeCl_3$-FLG, leaving a flux $\Phi_{t'} = T\Phi_r$ reflected into the environment. Further reflections can be neglected due to the high transmittance of $FeCl_3$-FLG and define the spectral responsivity as $\mathfrak{R}(\lambda) = I_{ph}/\epsilon_0\Phi$. Hence, the photon flux incident on a supported $FeCl_3$-FLG detector is effectively $(\Phi_0 + \Phi_r)$ and the ratio between the measured ($\mathfrak{R}$) and intrinsic ($\mathfrak{R}_0$) responsivity may be evaluated using just $T$ and $R$:

$$\frac{\mathfrak{R}_0}{\mathfrak{R}} = \frac{\Phi_0}{\Phi_0 + \Phi_r} = \frac{1}{1 + TR}. \tag{B.1}$$

Figure B.1b shows the transmittance of a four-layer $FeCl_3$-FLG sample reproduced with permission from Ref. 1 and the reflectivity of the $Si/SiO_2$ substrate measured in the range $420 - 700$ nm. A simulation of the substrate reflectivity using TFCalc software (*Software Spectra Inc.*) shows excellent agreement with the experimental data, therefore allowing the extrapolation of the reflection coefficient from the simulated curve down to $\lambda = 375$ nm where no experimental data points are available. In the

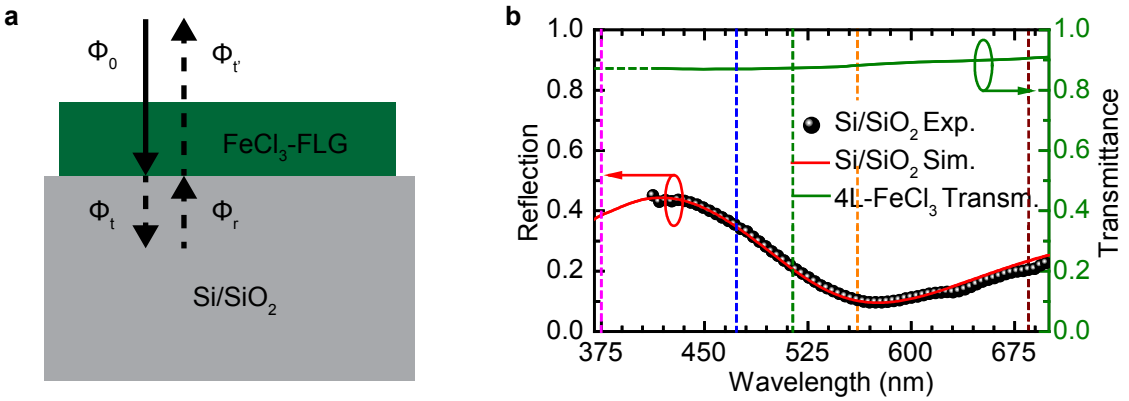


**Figure B.1: Correction of spectral responsivity for substrate reflections.** **a**, Substrate reflection correction of responsivity: solid arrow is the incoming light ($\Phi_0$), dotted lines represent the transmitted light through the $FeCl_3$-FLG ($\Phi_t$) and the reflected part by the $Si/SiO_2$ interface ($\Phi_r$). **b**, Reflectivity of Silicon substrate with 290 nm of $SiO_2$ on top: experimental values (black dots) in the region $420-700$ nm and computed curve (solid red line) between $370-700$ nm; the green line represents the transmittance of 4-layer $FeCl_3$-FLG (data from Ref. 1). Vertical dotted lines represent the laser wavelengths used in this work.

same way, the absorption coefficient of $FeCl_3$-FLG, for the same wavelength range, is extrapolated from the experimental data. The computed correction factors used in figure 5.6c are reported in table B.1.

**Table B.1: Corrections to responsivity due to substrate reflection.**

| $\lambda$ (nm) | $T$ | $R$ | $\Re_0/\Re$ |
|---|---|---|---|
| 375 | 0.872 | 0.385 | 0.749 |
| 473 | 0.870 | 0.355 | 0.764 |
| 514 | 0.874 | 0.207 | 0.847 |
| 561 | 0.883 | 0.102 | 0.917 |
| 685 | 0.906 | 0.234 | 0.825 |

# BIBLIOGRAPHY

[1] Ivan Khrapach, Freddie Withers, Thomas H. Bointon, Dmitry K. Polyushkin, William L. Barnes, Saverio Russo, and Monica F. Craciun. Novel highly conductive and transparent graphene-based conductors. *Advanced Materials*, 24(21):2844–2849, 2012.

# PUBLICATIONS

The ideas and data presented in this thesis are subject of the following publications:

- Adolfo De Sanctis, Gareth F. Jones, Dominque J. Wehenkel, Francisco Bezares, Frank H. L. Koppens, Monica F. Craciun and Saverio Russo. *Extraordinary linear dynamic range in laser-defined functionalized graphene photodetectors.* Science Advances 3:e1602617 (2017);

- Adolfo De Sanctis, Gareth F. Jones, Nicola J. Townsend, Monica F. Craciun and Saverio Russo. *An integrated and multi-purpose microscope for the characterization of atomically thin optoelectronic devices.* Review of Scientific Instruments 88, 055102 (2017).

- Adolfo De Sanctis, Matthew D. Barnes, Iddo Amit, Monica F. Craciun and Saverio Russo. *Functionalised hexagonal-domain graphene for position-sensitive photodetectors.* Nanotechnology, 28:124004 (2017);

- Thomas H. Bointon, Gareth F. Jones, Adolfo De Sanctis, Ruth Hill-Pearce, Monica F. Craciun and Saverio Russo. *Large-area functionalized CVD graphene for work function matched transparent electrodes.* Scientific Reports, 5:16464 (2015);

- Adolfo De Sanctis, Iddo Amit, Steven Hepplestone, Monica F. Craciun and Saverio Russo. *Strain-engineered energy funneling in a layered semiconductor.* (Under review in *Advanced Materials*);